Evaluating polyphenolic antioxidant protection of mitochondrial DNA in a variety of human skin models

Rebecca L. Hanna, BSc. (Hons)

Thesis submitted for the degree of Doctor of Philosophy

Department of Dermatological Sciences
Faculty of Medical Sciences, Institute of Cellular Medicine,
Newcastle University, UK.

September 2019

Abstract

Compromised skin barrier function negatively impacts up to 50% of our global population. Skin areas with compromised barrier integrity are affected more by environmental triggers such as sun exposure and environmental pollution which induce cellular oxidative stress, damage skin integrity and promote skin aging. At a sub-cellular level there are accumulative strand breaks to mitochondrial DNA (mtDNA). Limited repair mechanisms and proximity to the site of superoxide generation, make mtDNA a biomarker of oxidative damage in multiple human cell and tissue types.

This project optimised a long-range qPCR method to compare relative mtDNA damage between samples. An application of this methodology tested commercial antioxidants (AOXs) tetrahydrocurcumin (THC) and pterostilbene (PTERO) for their capacity to protect skin mtDNA from sun exposure in a wide range of human skin models; primary monocultures, skin equivalents, and whole skin ex-plants. The assay was also used to detect mtDNA damage between donor-matched basal cell carcinoma (BCC) and non-BCC facial skin.

In skin monolayer experiments, the mtDNA of foreskin-derived adult keratinocytes or differentiated keratinocytes was not protected by THC or PTERO. However the mtDNA of foreskin-derived adult reticular fibroblasts was protected by THC (but not PTERO), with greatest protection provided by a THC + PTERO combination.

Various technical protocols were developed in this thesis, including an in-house full thickness human skin equivalent using CELLnTEC medium. Skin equivalents have donor-matched layers and no scaffold material, so fibroblasts secrete and maintain their own dermal extracellular matrix. A majority of the skin equivalents were formed with foreskin-derived adult keratinocytes and reticular fibroblasts, but some trials were performed using the same cell types derived from adult facial skin. In-house (CELLnTEC) and commercial (Labskin™) skin equivalents, foreskin and facial ex-plant skin were also tested for mtDNA protection by THC/PTERO/combination within topically applied Physiogel™ base formulations. As the epidermis can be manually removed from Labskin™, the qPCR assay detected a high 64-fold range of mtDNA damage in this epidermis and in-house (CELLnTEC) skin equivalents. However, the qPCR assay sensitivity was reduced in thicker skin models such as whole Labskin™, foreskin and facial ex-plant skin. As such it was difficult to determine conclusive results from formulation testing in these models using the mtDNA qPCR assay.

It is anticipated that the mtDNA assay and human skin equivalent arising from this thesis will have wide-ranging applications. The data pertaining to THC/PTERO is indicative that these AOXs could enhance the GSK commercial Physiogel™ skin range designed for skin that is particularly reactive to environmental stressors such as sunlight.

Declaration

This thesis is submitted for the degree of Doctor of Philosophy. The research for this submission was performed in the Dermatological Sciences or Wolfson Building departments at the Institute of Cellular Medicine, under the academic supervision of Professor Mark Birch-Machin. All work is original and performed personally unless stated otherwise in the text. None of the material has been submitted previously for a degree or any other qualification at this university or any other institution.

Acknowledgements

This work was achieved through the support and funding provided by BBSRC and GlaxoSmithKline Consumer Healthcare. I would like to thank my industry supervisors for their guidance, approachability and friendly encouragement, Dr David Moore, Dr Xuying Wang, Dr Pallav Bulsara, Dr Jonathon Crowther, and Dr Robert Lucas.

Particular appreciation is reserved for Professor Mark Birch-Machin, who has been an incredible mentor and supervisor. I thank you for all I have learnt from your wisdom, enthusiasm, and knowledge. It's been a blessing that will serve me well through life.

This work would not have been possible without the technical expertise and guidance provided by several individuals at Newcastle University. For histology I particularly thank Dr Glyn Nelson and staff of the Bio-Imaging Unit, Ms Xin Xu of the Newcastle Central Biobank, and staff of Newcastle NODE molecular pathology. I thank Dr Peter Hanson for skin equivalent development, and Dr Kim Pearce for statistics. For ELISAs I thank Dr Lee Borthwick of the university fibrosis group, and his research technicians Mr Ben Barksby and Dr Alisha Chhatwal. I also thank my internal assessors Professor Fiona Oakley and Dr Simon Wilkinson who offered encouragement and technical expertise. Thank you to other members of dermatological sciences, in particular Ms Carole Todd, Dr Ashleigh O'Connell and Dr Tom Ewan. A thank you to Miss Maria Zakhour and Miss Agalya Amalanathan for the summer placement data that contributed to this thesis.

Thanks are extended to the group of Professor Marcus Cooke who hosted me for a month, sharing expertise in nDNA damage at Florida International University. I am grateful to the company Labskin™ (Innovenn, UK) for providing a free trial of skin equivalents for my research, and to CELLnTEC scientists who provided technical guidance by email relating to developing skin equivalents with their specialist medium. Thank you to Dr Ken Raj and Dr Graham Holliman of Public Health England who shared DNA samples from surgical patients in collaboration with consultant dermatologist Dr Sarah Felton of Oxford University Hospitals NHS Trust.

To my research group, I thank Dr Amy Bowman, Dr Eyman Rashdan, Dr Matt Jackson, Dr Khimara Naidoo, and future Drs - Ms Gewei Zhu, Ms Lizzie Ruddy, Ms Roisin Stout, and Ms Catherine Bonn. You have been so much fun, and I will miss you all dearly. The walls of photo memories speak for itself – so much joy!

Without the mentorship, guidance and friendship of Dr Anne Oyewole, I could not have reached this point. Thank you for always helping me to keep perspective, enjoy life, and do my best. Huge thanks are extended to my Newcastle family at Christ Church Heaton, with love and support from Lydia Chan, Hannah Graham, Anne Oyewole, and Iulia Udrescu-Clarke. Thank you for keeping me on track, sharing meals, hugs and happy memories.

Thank you to my loving family for always being there - Dad, Mum, Granny, Grandad, Nicole, Ryan, Vicki, Aoife, Ruari, Nyx and Rose.

Table of Contents

List of Figures and Tables

List of Abbreviations

3D	Three-dimensional
8-OHdG	8-hydroxy-2'-deoxyguanosine
Abs	Absorbance
ABTS	2,2′-Azinobis-(3-Ethylbenzthiazolin-6-Sulfonic Acid)
ALI	Air-liquid interface
ATP	Adenosine trisphosphate
β2M	Beta-2-microglobulin
β-carotene	Beta-carotene
BCC	Basal cell carcinoma
BER	Base excision repair
BME	Basal Medium Eagle
Bp	Base pair
BPE	Bovine pituitary extract
BSA	Bovine serum albumin
C	Cream (formulation)
Chr	Chromosome (nuclear)
ChrM	Mitochondrial chromosome
CI	Confidence intervals – 95%
COLA1	Collagen protein, type I, alpha 1
COLIPA	The European Cosmetic and Perfumery Association (Cosmetics Europe)
C_t	Cycle threshold
Cyt c	Cytochrome c
DAPI	4′,6-diamidino-2-phenylindole
ddH_2O	Double distilled water
D-loop	Dissociation loop region
DMEM	Dulbecco's Modified Eagle Medium
DMSO	Dimethyl sulfoxide
DNA	Deoxyribonucleic acid
e^-	Electron
ECM	Extracellular matrix
EDTA	Ethylenediaminetetraacetic acid
ELISA	Enzyme linked immunosorbent assay
ETC	Electron transport chain
FBS	Foetal bovine serum
Fe^{2+}	Iron (II)
$FeCl_3$	Ferric chloride
FFPE	Formalin-fixed paraffin embedded
Fitz	Fitzpatrick skin phototype scale
FN	Fibronectin
FRAP	Ferric reducing antioxidant power
FT	Full thickness (skin model comprising of epidermal and dermal layers)
GPx	Glutathione peroxidase
GSK	GlaxoSmithKline
HA	Hyaluronan

HCL	Hydrochloric acid
HDFn	Human Dermal Fibroblast Normal; Neonatal
H&E	Hematoxylin and Eosin
HEV	High-energy visible
HFF-1	Human Foreskin Fibroblast (neonatal)
HKGS	Human keratinocyte growth serum
HPLC	High Performance Liquid Chromatography
HPSF	High Purity Salt Free
H-strand	Heavy strand
H_2O_2	Hydrogen peroxide
IDTE	Tris-EDTA buffer - 10mM Tris, 0.1mM EDTA
IF	Immunofluorescence
IMS	Intermembrane space
IR	Infrared
kb	Kilobase
kDa	Kilodalton
L-strand	Light strand
MALDI-MS	Matrix-assisted laser desorption/ionization mass spectrometry
mAmp	Milliamp
MEM	Modified Eagle Medium
mtDNA	Mitochondrial DNA
MHz	Megahertz
MTT	3-(4, 5-dimethylthiazol-2-yl)-2, 5-diphentyltetrazolium bromide
MTS	3-(4,5-dimethylthiazol-2-yl)-5-(3-carboxymethoxyphenyl)-2-(4-sulfophenyl)-2H-tetrazolium, inner salt
NA	Numerical aperture
nDNA	Nuclear DNA
NAM	Niacinamide
NCR	Non-coding region
NDD	Non-descanned detector
NMR	Nuclear magnetic resonance spectrometry
NRF2	Nuclear factor erythroid-2-related factor 2
$^1O_2$	Singlet oxygen
O_2^-	Superoxide anion
OCT	Optimal cutting temperature compound
OH^-	Hydroxyl radical
P	Passage number
PAH	Polycyclic aromatic hydrocarbons
PBS	Phosphate buffered saline
PET	Polyethylene terephthalate
PFA	Paraformaldehyde
PM	Particulate matter
PMMA	Poly(methyl methacrylate)
PMT	Proton motive force

PSA	Penicillin-streptomycin-amphotericin B
PTERO	Pterostilbene
Q	Ubiquinone
qPCR	Quantitative polymerase chain reaction
RD	Reagent diluent
RHE	Reconstructed human epidermis
RIN	RNA integrity number
RNA	Ribonucleic acid
tRNA	Transfer ribonucleic acid
Redox	Reduction-oxidation
ROCK	Rho-associated protein kinase
ROS	Reactive oxygen species
SCC	Squamous cell carcinoma
SD	Standard deviation (of the mean)
SED	Standard erythemal dose
SEM	Standard error of the mean
SHG	Second Harmonic Generation
SOD	Superoxide dismutase
SPF	Sun protection factor
T	Tween 20
T_M	Melting temperature (of primers)
TBS	Tris buffered saline
TE	Trypsin-EDTA
TEAC	Trolox equivalent antioxidant capacity
THC	Tetrahydrocurcumin
TPTZ	2,4,6-Tri(2-pyridyl)-s-triazine
UVA1	Ultraviolet A1
UVA2	Ultraviolet A2
UVB	Ultraviolet B
UVC	Ultraviolet C
UVR	Ultraviolet radiation
VIS	Visible light

Chapter 1: Introduction

The EU Cosmetics Regulation (1223/2009/EEC) prohibits all cosmetic products tested, marketed and sold on the backbone of an animal model. Arising from a change in public opinion, such guidelines directly affect international industry trade and are beginning to influence foreign government policies (Bellas *et al.*, 2012). With academic funding bodies also calling for alternatives to animal models, this has influenced the research avenues of university institutions. In correlation there is a shift in the commercial availability of human skin equivalents, the resources to grow 'in-house' equivalents from donor tissue, and development of commercial assays for three-dimensional (3D) model systems. An overall precedence has been set for the human skin model market to continually evolve.

Human skin models (3D) are the most developed and understood of all *in-vitro* engineered tissues (Mathes *et al.*, 2014). As Figure 1-1 demonstrates, there are a range of human skin equivalent models, ranging in complexity from monoculture to equivalents, explants and perfused organ chips. The novel approach of this research project is that it incorporates a multi-comparative study through several *in vitro* models of varying biological complexity.

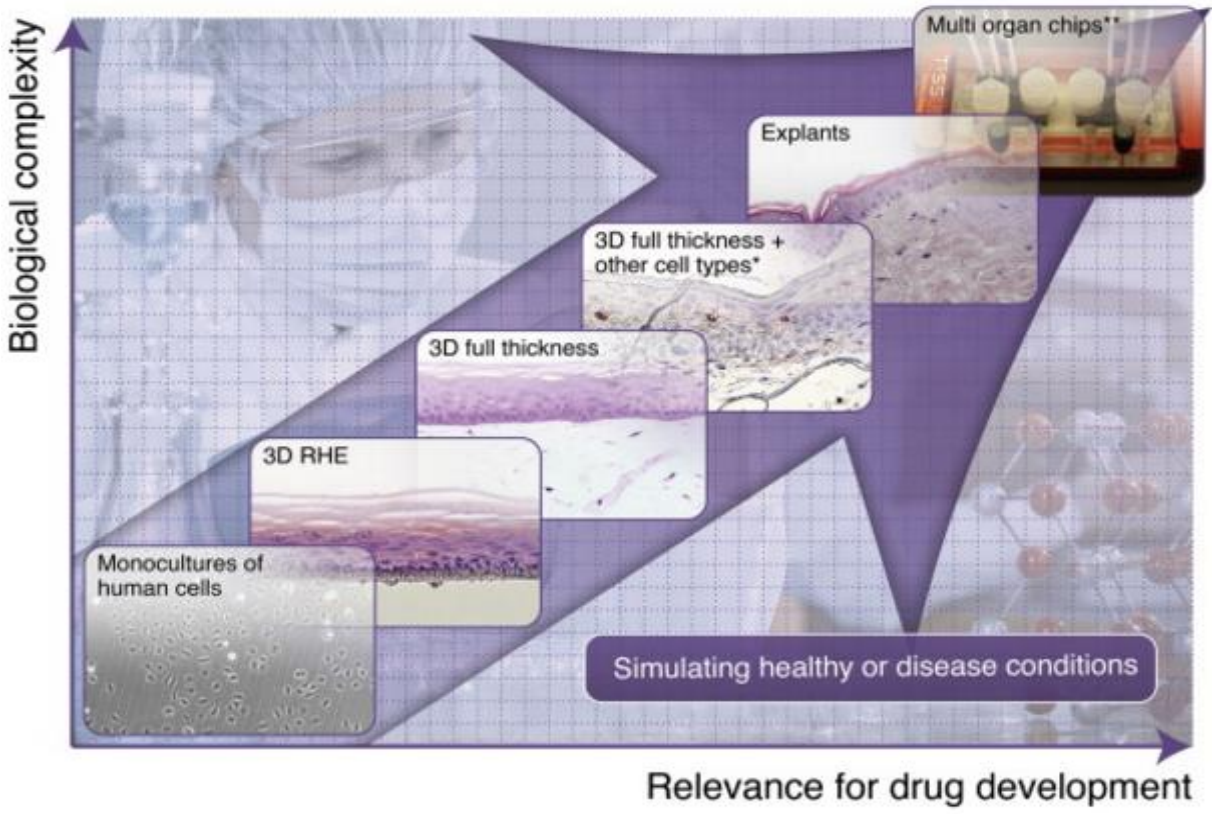

Figure 1-1: Relationship between *in vitro* model complexity and relevance for industrial drug development. RHE - reconstructed human epidermis, 3D - three-dimensional. Image source: Mathes *et al.* (2014)

1.1 Skin function

In its simplest terms, skin is our largest protective organ. It contains a multitude of interacting cells types, synergistically maintaining a dynamic homeostatic barrier against our external environment (Mathes *et al.*, 2014). As a perceptive interface, it influences responses (e.g. immunological) to physical, chemical and biological stimuli (Tobin, 2006; Działo *et al.*, 2016).

1.2 Skin architecture

A full thickness skin equivalent aims to recreate human skin structure, spanning core structural layers of epidermis and dermis. Physiological skin also contains a hypodermis, and connects to the fascial endoskeleton through extensive peripheral components of the neural, immune, lymphatic and circulatory systems (Wong *et al.*, 2016). A youthful and 'defined' skin appearance is synonymous with anchored tethering points, in particular ligaments of the head and face that weaken with age (Wong *et al.*, 2016).

It is important to consider skin architecture when establishing a representative 3D model that generates translational data. Skin is not homogenous across the entire body surface area, where adipose fat distribution, structure and density of hair, nerve endings and blood supply are highly variable (Tobin, 2006). The hands (palmer) and feet (plantar) are particularly adapted to enhanced environmental contact through the presence of keratinous nails, a strong and thickened retinacula system, and unique skin surface pattern (e.g. ridged for grip) (Wong *et al.*, 2016).

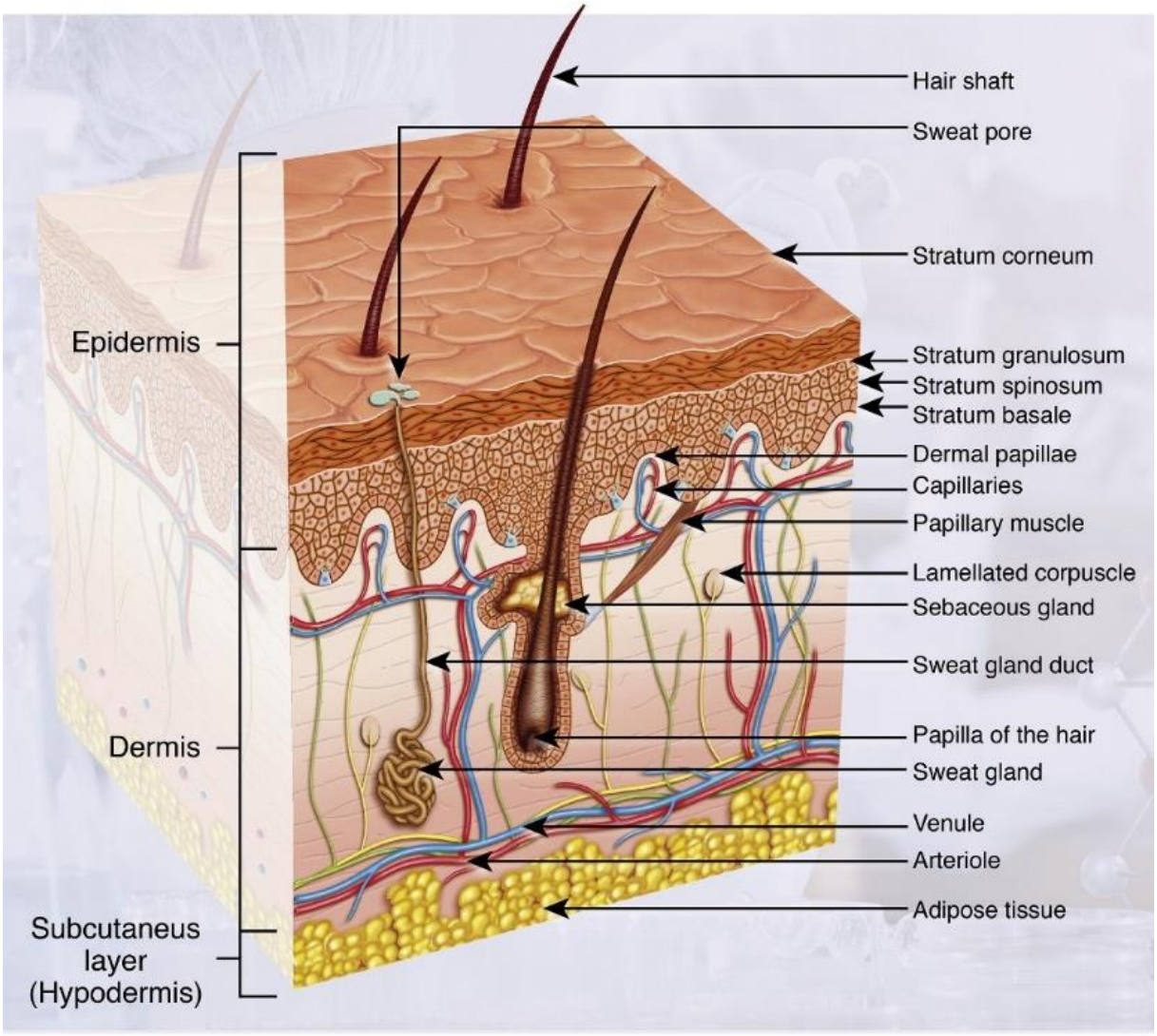

Figure 1-2: Schematic of human skin anatomy. There are three primary compartment sub-classes: epidermis, dermis, and subcutis (hypodermis). Peripheral components of the neural, immune and circulatory system are embedded throughout (e.g. sebaceous/sweat glands, capillaries etc.). Image source: Mathes *et al.* (2014)

1.2.1 Epidermis

Epidermal thickness varies across the body but also according to sex, ethnicity and environmental impact. However, it shares a common architecture of an outermost stratum corneum, followed by granulosum, spinosum and basale (Figure 1-2). Each are permeated by specialist cells with a protective function such as pigment producing melanocytes, Langerhans cells (immune - dendritic) and Merkal cells (neural - sensory) (Brohem *et al.*, 2011). Without vascular support they rely solely on diffusion from the dermal capillary network (MacNeil, 2007). Keratinocytes progressively differentiate and migrate upwards from a columnar layer of self-renewing proliferative cells in the stratum basale (MacNeil, 2007). When at the outermost stratum corneum, they have undergone keratinisation to form a protective outermost barrier. It is formed of approximately 15 layers of distinctive anuclear corneocytes embedded within a high volume of organised multilamellar lipids, such as ceramides and sphingolipids (Brohem

et al., 2011). This high lipid content is generated by the stratum granulosum, accounting for the firmness of the epidermis (Wong *et al.*, 2016). The stratum corneum continually sheds (desquamation), in synergy with keratinocyte proliferation (Mathes *et al.*, 2014).

1.2.2 Basement membrane

The stratum basale of the epidermal barrier layer is attached to the dermis by a specialist basement membrane, consisting of several forms of collagen fibre (MacNeil, 2007). These mainly include collagen IV, laminin, proteoglycans and glycosaminoglycans, alongside a host of growth factors and cytokines (Brohem *et al.*, 2011). Other proteins such as collagen VII anchor the dermal reticular lamina to the basal lamina of the basement membrane (Mikesh *et al.*, 2013). Key physiological processes such as wound healing, skin regeneration and homeostatic maintenance rely on epidermal-dermal interactions through this membrane (Brohem *et al.*, 2011). The culmination is a strong and flexible junction that also acts as a mechanical barrier against pathogens (Wong *et al.*, 2016).

1.2.3 Dermis

Like the epidermis, dermal thickness varies across the body, as well as between sexes and ethnicities. The dermis provides considerable strength and structural support to skin through its upper papillary layer of thin collagen fibres interspersed with elastic fibres, on top of a reticular layer composed of thicker collagen fibres (Wong *et al.*, 2016). The reticular layer has a densely packed collagenous mesh interlaced with branching elastin fibres, fibronectin and proteoglycans (Brohem *et al.*, 2011). Dermal fibroblasts aid synthesis and maintenance of the extra-cellular matrix (Brohem *et al.*, 2011). The most abundant collagens are fibril forming type I (80-90%), type III (10-20%) and lesser amounts of fibril-associated collagen VI, XII, and XIV (Mikesh *et al.*, 2013). Alongside dermal fibroblasts, the layer is also permeated by hair follicles, sweat and sebaceous glands, blood vessels and nerve endings (Tobin, 2006). The dermal matrix provides energy and nutrition to the epidermis, but also facilitates cellular proliferation and migration in wound healing (Brohem *et al.*, 2011). Sensations of touch, pain, itch, temperature and pressure are transmitted from this skin region (MacNeil, 2007).

1.2.4 Subcutis

Also known as the hypodermis, layers of connective tissue and adipose house both nerves and larger blood vessels. Like the epidermis, the thickness of this layer varies between individuals and is important for both temperature regulation and shock-absorbance (Mathes *et al.*, 2014). Relative to the epidermis and dermis, the hypodermis is considered less defined and understood (Wong *et al.*, 2016). Indeed, they are generally (if not always) absent from skin equivalents.

The cells types include fibroblasts, macrophages and adipocytes, with the overall tissue rich in fluid attracting hyaluronan, proteoglycans and glycosaminoglycans (Wong *et al.*, 2016).

1.3 Skin model systems: *ex-vivo* skin and *in-vitro* reconstructed skin equivalents

There are a host of human skin equivalent models available to purchase commercially or grown 'in-house' from widely published methodologies. Broadly they are divided into epidermal (reconstructed human epidermis (RHE)), dermal, or full-thickness (reconstructed human dermis, basement membrane, epidermis and stratum corneum) sub-types (Mathes *et al.*, 2014). At a cellular level they are primarily composed of human keratinocytes and fibroblasts, but additional cell types can be integrated (e.g. melanocytes, stem cells, Langerhans etc.) (Mathes *et al.*, 2014). Integration of appendage hair follicles, pores, or sweat/sebaceous glands are also a consideration (Mathes *et al.*, 2014). Nutrition is delivered to equivalents via culture media, although perfusion-based methodologies are being developed to replicate vascular input.

Commercial skin equivalents are widely used in academia, as well as pharmaceutical and biotechnological industries. The most commonplace are those produced by SkinEthic™ (L'Oréal, France), MatTek™ (MatTek Corporation, USA), Phenion™ (Henkel, Germany), and Labskin™ (Innovenn, UK). It is known that the epidermal equivalents of SkinEthic™ and MatTek™ use collagen/polycarbonate scaffolds (Groeber *et al.*, 2011). For full thickness equivalents, it is not definitively known that SkinEthic™/MatTek™ skin equivalents are scaffold-free, but those from Phenion™ incorporate bovine collagen I scaffold (Groeber *et al.*, 2011) and Labskin™ dermis is formed of polymerised fibrin (Bojar, 2015). Most published methodologies develop a viable dermis by seeding fibroblasts into a collagen scaffold or hydrogel (Zhang and Michniak-Kohn, 2012; Mathes *et al.*, 2014). Some scaffold/gel materials are biodegradable, and can be human- or animal-derived (Mathes *et al.*, 2014), where the scaffold degrades as proliferating cells produce an extracellular matrix (Zhang and Michniak-Kohn, 2012). It would be difficult to determine if the scaffold itself or degraded particulates have an effect on the cellular microenvironment (cell signalling etc.).

CELLnTEC (CnT; Switzerland; www.cellntec.com) have produced a fully defined medium range called 'CnT Prime' that allows for co-culture of keratinocytes and fibroblasts, and eliminates the need for a scaffold. The fibroblast media (product CnT-PR-F) has <1% animal serum but a combination of cell-specific growth factors that support fibroblast production of an extracellular dermal matrix over 10 days. When keratinocytes are seeded onto the dermis, they remain for 3 days in a co-culture 'airlift' media (product CnT-PR-FTAL) designed to encourage equal growth of both cell types whilst maintaining the correct phenotype. When the keratinocytes are raised to the air-liquid interface for 12 days, the equivalents continue to be

maintained with the ‘airlift’ medium throughout. The only technical difficulty with this method is that it incorporates no antibiotics or antifungals in the cell media, and details not to use them in the supplied protocol.

1.4 Mitochondria

1.4.1 Mitochondrial function

Mitochondria are dynamic, double-membraned organelles that exist in varying quantities per cell type (Kandola *et al.*, 2015). They are pivotal to cellular energy (ATP) biogenesis, supplying up to 90% of the required quota using electron transport chains (ETC; see Figure 1-4). Energy production is maximised by arranging ETC complexes in a densely folded inner membrane (cristae) (Oyewole and Birch-Machin, 2015). Mitochondria are integral to multiple cell-signalling cascades, with certain proteins (GTPases, kinases, phosphatases etc.) co-ordinating mitochondrial function with the regulation of metabolism, cell-cycle control, anti-viral response and apoptosis (McBride *et al.*, 2006; Panich *et al.*, 2016). They also dynamically interact intracellularly, transferring contents through fission-fusion and appropriately cleansing their pool through target-specific mitophagy (Kandola *et al.*, 2015).

1.4.2 Mitochondrial genome (mtDNA)

Each mitochondrion contains approximately 2 to 10 copies of a 16.5kb mtDNA genome (Kandola *et al.*, 2015). It is a double stranded circular molecule with an outer (heavy) and inner (light) strand of nuclei acid, which contain genes for two ribosomal RNA (rRNA), 22 transfer RNA (tRNA), and sub-units of electron transport chain (ETC) complexes I, III, IV and V (Schon *et al.*, 2012; Kandola *et al.*, 2015). The D-loop region contains promotors for the initiation and control of mtDNA replication and transcription (Li *et al.*, 2012; Gammage and Frezza, 2019)

Whilst nDNA has histone arrangement and additional protective/reparative mechanisms, mtDNA is vulnerable to oxidative stress-induced strand breaks. Due to the polyploid nature of mtDNA, damage can accumulate to a threshold before functional decline is seen (Birch-Machin and Swalwell, 2010). The mtDNA content, lesions, methylation, deletions and mutations are widespread biomarkers of disease and ageing (Wallace, 2010; Tulah and Birch-Machin, 2013). This is particularly true of highly metabolic or proliferative tissues (which require more energy and have increased numbers of mitochondria and mtDNA), such as the nervous, muscular and endocrine systems (Hudson *et al.*, 2016).

Relative to nDNA, mtDNA has limited repair capacity but both genomes share a communicative role in mtDNA replication and maintenance. Wisnovsky *et al.* (2016) report that mtDNA have components of the base excision repair (BER) pathway, but even nDNA assistance cannot appear to repair double strand breaks. Mutations in nDNA can therefore affect the repair of mtDNA, although mitochondria can be recycled by mitophagy or the entire cell recycled by apoptosis (Kazak *et al.*, 2012).

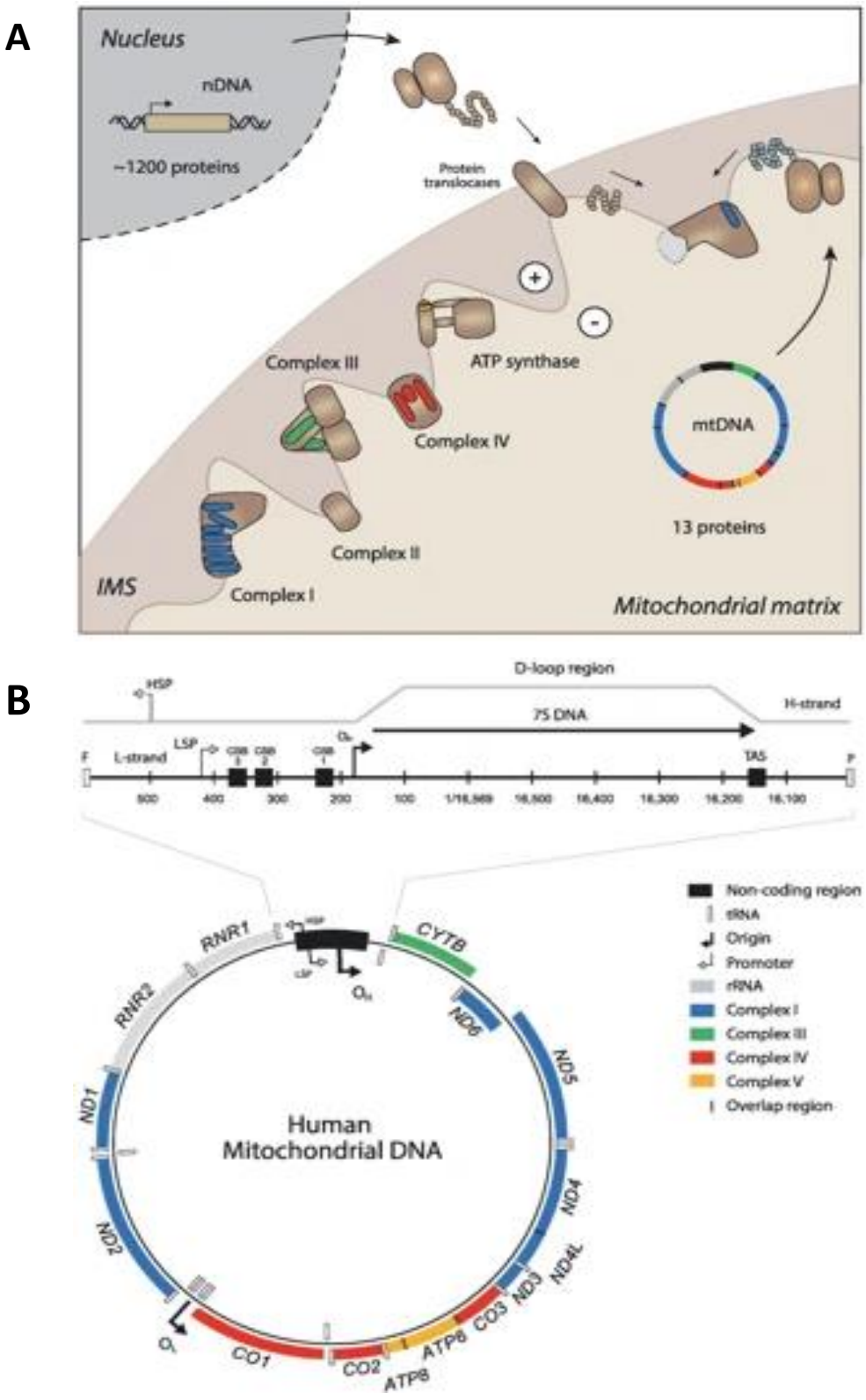

Figure 1-3: Schematic of human mitochondrial DNA. (A) An electron transport chain (ETC) originates from the nuclear and mitochondrial genomes, which together orchestrate the assembly, regulation and expression of its functional components. Nuclear encoded proteins are imported through membrane embedded protein translocases in the intermembrane space (IMS) adjacent to the mitochondrial matrix. Nuclear encoded components are brown (e.g. complex II), and coloured portions correlate to their mitochondrial genome coding region (e.g. complexes I, III, IV, V). (B) The mitochondrial genome has eleven mRNAs (grey) which encode 13 ETC polypeptides and are expressed by 22 tRNAs. Proteins are inserted into the inner mitochondrial membrane by mitochondrial ribosomes. The displacement loop (D-loop) contained a non-coding region (NCR) and is expanded to show the HSP/LSP promotors for mtDNA transcription of the respective heavy (H-) strand and light (L-) strands, alongside the O_H promotor for mtDNA replication. Image sourced from Gammage and Frezza (2019).

1.4.3 Reactive oxygen species (ROS) and oxidative stress

ROS are an endogenous bi-product of cellular metabolic processes, with the largest amounts arising from mitochondrial driven respiration (Panich *et al.*, 2016). However exogenous environmental factors can also drive excessive ROS production, such as ultra violet radiation (UVR), air pollutants, and household/agricultural chemical compounds (Poljšak and Fink, 2014). Examples of ROS include free radicals (superoxide anion - O_2^-, hydroxyl radical - OH, and non-radicals (singlet oxygen - $^1O_2$, hydrogen peroxide - H_2O_2) (Panich *et al.*, 2016). Indeed ROS aid physiological processes such as phagocytosis (immunity), intracellular signalling cascades and general survival of cells such as neurons, fibroblasts, smooth muscle cells, and skin keratinocytes (Panich *et al.*, 2016). Paradoxically, the ROS that aid cellular survival, ultimately induce senescence via oxidative stress.

During aerobic respiration (Figure 1-4), electron leakage at the ETC results in mitochondrial superoxide (O_2^-) formation (Oyewole and Birch-Machin, 2015).Catalysed to H_2O_2 by endogenous SOD enzyme, any H_2O_2 surplus to cellular function is quenched by GPx enzyme to form water. However, Fenton reaction with endogenous metal ions (e.g. Fe^{2+}) produce highly reactive radicals that put cells under oxidative stress, inducing damage to intracellular structures such as mtDNA (Oyewole and Birch-Machin, 2015). Non-radical H_2O_2 is membrane permeable and contributes to oxidative stress cell damage (Panich *et al.*, 2016).

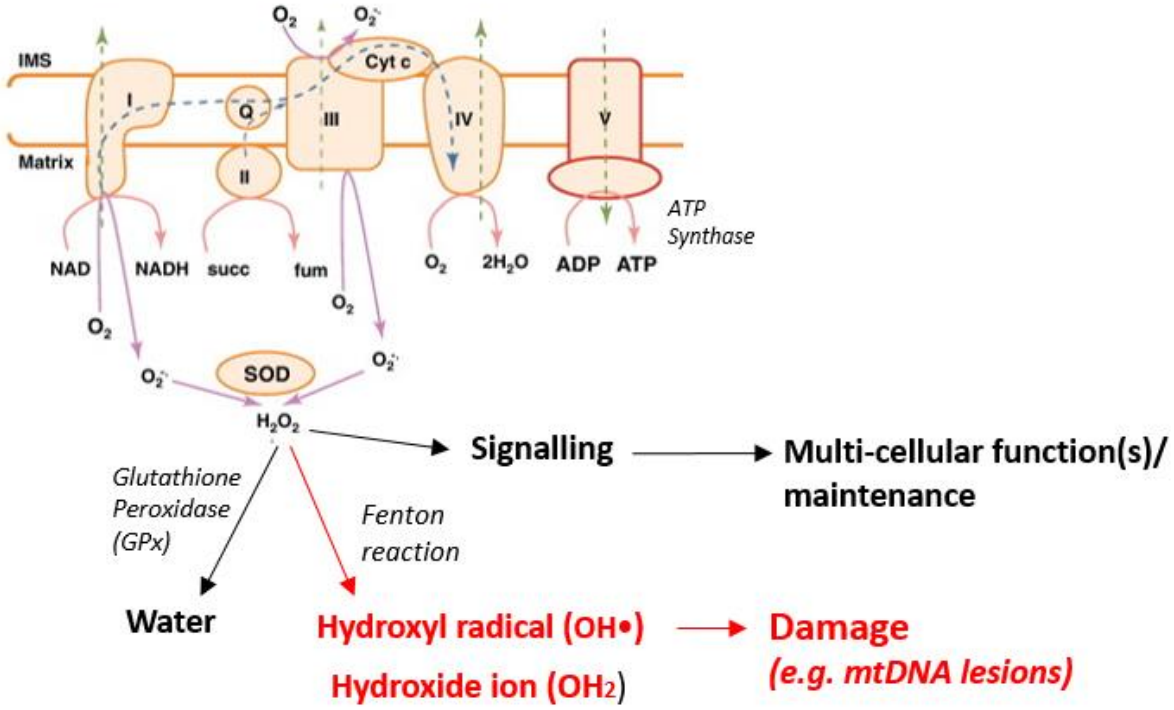

Figure 1-4: Schematic of mitochondrial electron transport chain (ETC) and reactive oxygen species (ROS) generation. Within the inner mitochondrial membrane, a series of fuel oxidation stages occur in protein complex I and II which result in an electron transfer (e^-; blue dotted line) to ubiquinone (Q) and a reduction at complex III. Cytochrome c (Cyt c) carries electrons between respiratory complexes III and IV, to the terminal O_2 acceptor. Proton motive force (PMT) drives ATP synthesis at complex V, thorough use of the generated proton gradient (green lines). PMT can also induce electron leakage, which reacts with O_2 to form superoxide anions (O_2^-). These are catalysed to H_2O_2 by superoxide dismutase (SOD), which can be used in signalling pathways or further catalysed to water by GPx. Unquenched H_2O_2 can react with metal ions (Fenton reaction), resulting in an oxidative stress-induced cellular damage. Image adapted from Kandola *et al.* (2015) and Mailloux and Harper (2012).

Oxidative stress is thought to be a major contributor of the mtDNA damage and this tends to induce random strand breaks. The mtDNA genome is close to the site of ROS production and multiple copies exist within each cell. These factors make mtDNA particularly vulnerable to the effects of oxidative stress, exacerbated further by the fact that mtDNA has limited repair mechanisms and lacks protective histones (Anderson *et al.*, 2014). Berneburg *et al.* (2000) reported that the mutation frequency of mtDNA is approximately 50-fold higher than nDNA. As the integrity of mtDNA is essential for mitochondrial function, the accumulation of mutations can result in dysfunctional mitochondrial subunits (Anderson et al., 2014). The dysfunctional mitochondria are thought to contribute to increased ROS production, leading to further oxidative damage to mitochondria in a continuous cycle illustrated in Figure 1-5 (Birch-Machin and Bowman, 2016; Naidoo *et al.*, 2018).

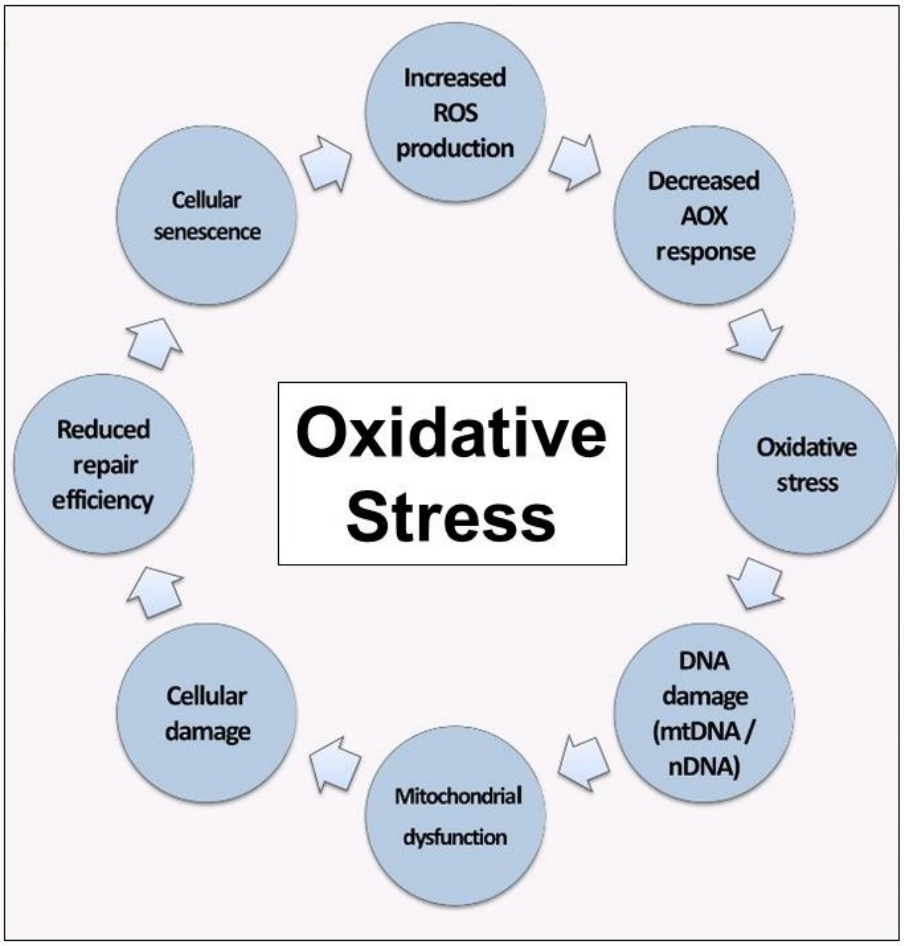

Figure 1-5: Oxidative stress and mitochondrial theory of ageing. Oxidative stress arises from an imbalance between an increase in reactive oxygen species (ROS) and decrease in antioxidant (AOX) response. These reactive species cause damage to both nuclear and mitochondrial genomes but accumulates in the mtDNA due to proximity and limited repair mechanisms. Beyond a threshold, mitochondrial becomes dysfunctional which reduces energy production and impacts cellular function and repair, as well as increasing the likelihood of cellular senescence. Furthermore, dysfunctional mitochondria produce greater levels of ROS. The mitochondrial theory of ageing proposes that this cascade of events at cellular level results in biological ageing. Image adapted from Naidoo *et al.* (2018)

1.5 Environmental skin stressors

Whilst our skin is designed to protect from environmental impact, some stressors (e.g. sunlight) remain capable of penetration and individuals with compromised skin barrier integrity are at risk of enhanced penetration of environmental stressors such as sunlight/pollutants (Figure 1-6). Indeed new fields of research are emerging that show a synergistic photoactivation of sunlight on environmental stressors such as pollution (Laurent, 2018). Sunlight is an electromagnetic spectrum of varying wavelengths that include visible light (VIS; ~42-43%), ultraviolet (UV; ~3-5%) and infrared radiation (IRR; ~52-55%). UV is subdivided into UVA1 (320-340nm), UVA2 (340-400nm), UVB (280-320nm), and UVC (100-280nm), where UVC is filtered by ozone and does not reach skin. While UVB/UVA2 penetrate the epidermis (keratinocytes, melanocytes, Langerhans), UVA1 penetrates deeper to the dermis (fibroblast, vascular and connective tissue), and IRR/VIS penetrate even deeper. The effects of IRR, VIS and artificial blue light (HEV) from devices are new emerging areas of interest in sun protection. Naidoo *et al.* (2018) reviews the effects of sunlight on photoageing, with emphasis on the role of mitochondria as outlined in section 1.4.3. The shorter wavelengths of UV are known to cause extensive mutagenic and cytotoxic damage to both genomes and other components of skin cells (e.g. lipids, proteins) (Tulah and Birch-Machin, 2013). This can result in skin erythema, sunburn and cancers such as localised (non-melanoma) basal/squamous cell carcinoma (BCC/SCC), or melanoma. Intermittent sun-exposure (e.g. holidays) is more associated with BCC and melanoma, whereas accumulative lifetime sun exposure is associated with SCC (Kimlin and Guo, 2012).

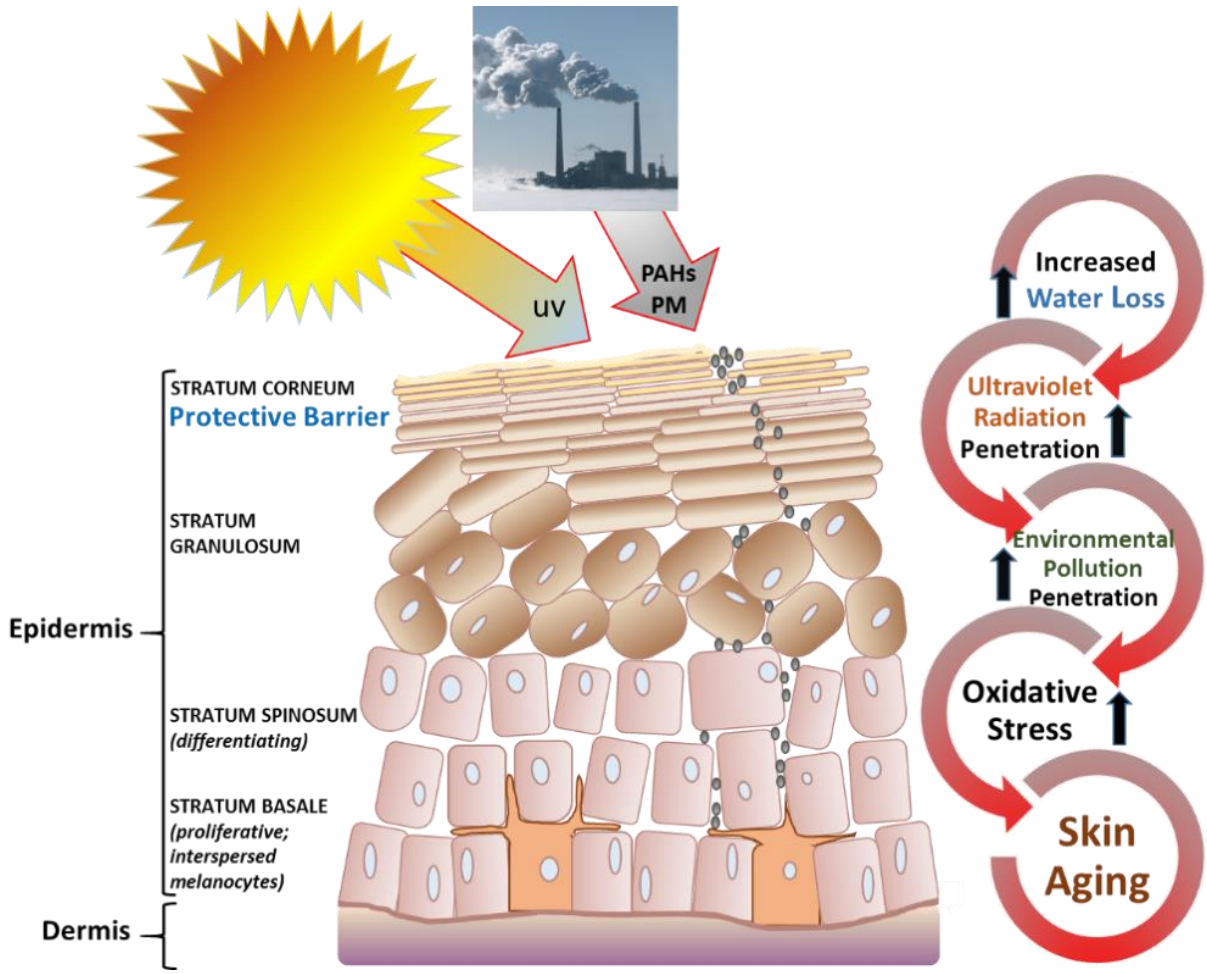

Figure 1-6: Effect of environmental stressors on skin. Skin has an increased risk of damage by environmental stressors such as ultraviolet radiation (UV) and environmental pollution (PAHs; PM). Areas of compromised barrier obtain deeper particle/UV penetration, inducing oxidative stress, inflammation, further dehydration, and overall skin aging. *PAHs, polyaromatic hydrocarbons; PM, particulate matter; UV, ultraviolet*

1.6 Antioxidants (AOXs) and chelators

The continual cellular proliferation/differentiation involved in skin self-renewal is maintained by a balance of redox homeostasis and regulation of ROS-mediated signalling (Panich *et al.*, 2016). Skin epidermis incorporates melanin as an endogenous tissue defence mechanism against UV-mediated oxidative stress (Tan *et al.*, 2015). As outlined in Figures 1-3 and 1-7, there are also endogenous enzymatic AOXs, non-enzymatic AOX support systems, and iron chelators that together maintain an optimal level of intracellular ROS (Panich *et al.*, 2016). Indeed AOXs/chelators are used to treat oxidative damage related illnesses, such as cardiovascular and neurodegenerative diseases (Rahal *et al.*, 2014).

1.6.1 Mechanisms of action

It has been widely seen in the literature that a combination of plant derived (phyto) AOXs such as vitamin E, vitamin C, β-carotene are required to have a biologically relevent effect (Działo *et al.*, 2016). This is commonly found in nutritional recommendation of a varied diet, but is also of importance to skincare. Strategic combination is based on an understanding of their mechanism of action and which cytosolic pathways they influence.

The mechanism of action and protective effects of cytosolic AOXs have been well derived. More recently, mitochondria-targeted antioxidants are gaining traction from their ability to cross the mitochondrial phospholipid bilayer and sequester reactive oxygen species at their source (Oyewole and Birch-Machin, 2015). Tiron is a potent mitochondria-targeting chelator, qualifiying as an ideal experimental positive control (Oyewole *et al.*, 2014).

1.6.2 Niacinamide

Niacinamide (or nicatinamide) is widely used in both clinical dermatology and consumer skin-care products as a topical (~1-5%) and oral treatment (Forbat *et al.*, 2017). It is a water-soluble amide isotype of vitamin B3 (niacin) that is acquired through the diet, and essential for skin, oral and digestive health (Forbat *et al.*, 2017). The mechanism of action is well derived, where it is an essential catalyst for anti-inflammatory and nDNA repair pathways, and converts to co-enzymes essential for mitochondrial energy metabolism (Forbat *et al.*, 2017). It has been trialled for blistering, acne, hyperpigmentation, pruritus (itch), rosacea, dermatitis, and anti-ageing effects.

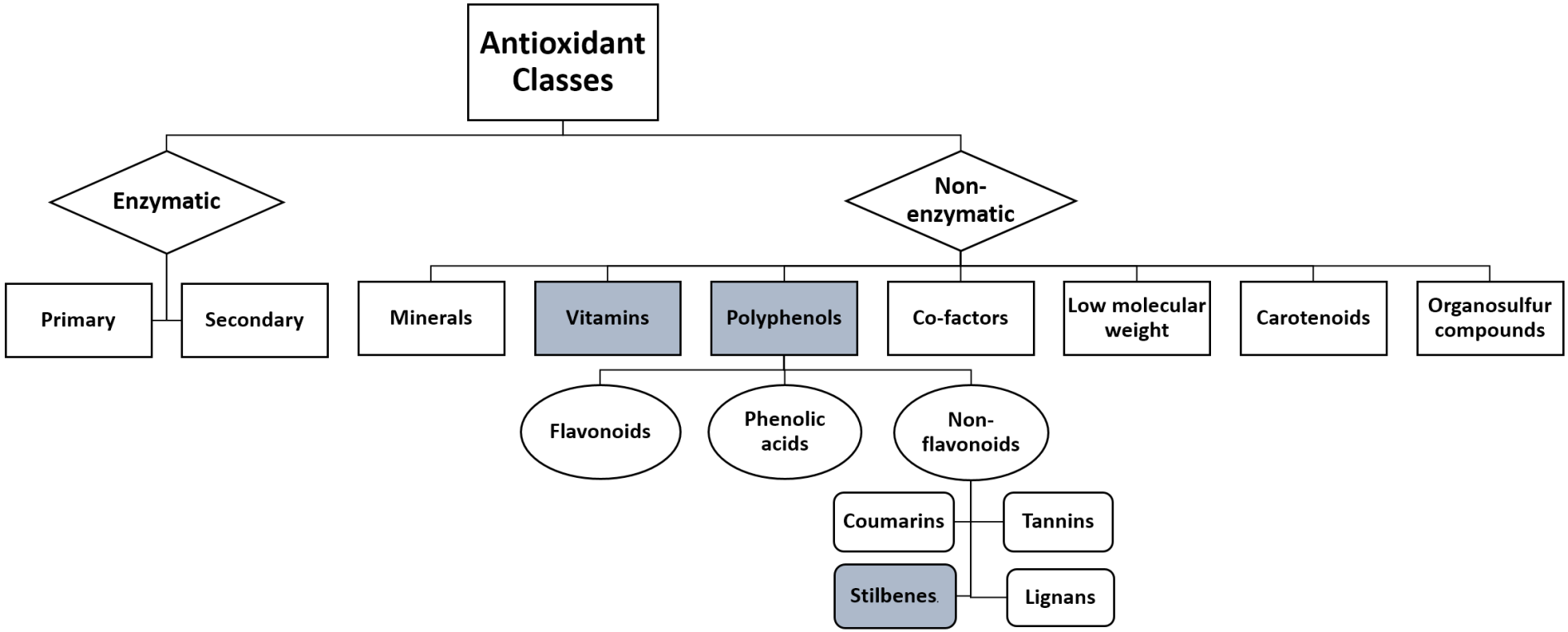

Figure 1-7: Schematic of antioxidant (AOX) classes. AOXs are categorised as enzymatic or non-enzymatic, with each containing a multitude of sub-classes. AOX classes of interest to this study are highlighted in grey, with individual actives underlined as class examples.

1.6.3 Polyphenolic antioxidants (AOXs)

The AOXs of interest in this study are polyphenolic compounds tetrahydrocurcumin and pterostilbene (Figure 1-7). Polyphenolic compounds are widely found in plants and their benefits are extended to humans through diet and herbal medicines. Interestingly both are used in traditional Indian ayurvedic medicine, with pterostilbene found in native tree barks used to treat diabetes and cardiovascualar ailments (Kosuru *et al.*, 2016). Similarly tetrahydrocurcumin is a metabolite of the famous Indian spice tumeric, which is ingested and used topically. They are reported to powerfully scavenge free radicals by reducing one electron oxidants and free iron (Fe^{2+}) (Tückmantel *et al.*, 1999; Handique and Baruah, 2002). In the food and agriculture industries extensive research has been performed on the potent interaction of polyphenols with proteins, often forming percipitates of polyphenol-protein complexes that cause haze in clear beverages and are the basis of leather tanning (Siebert *et al.*, 1996; Siebert, 2009).

1.6.3.1 *Tetrahydrocurcumin (THC)*

THC is derived from yellow turmeric, where the active ingredient curcumin has a recognised role in alleviation of inflammatory skin conditions, enhancement of wound-healing and general antimutagenic properties (Kakkar *et al.*, 2018). The synthesis of THC incorporates hydrogenisation that increases physical stability at biological pH, bioavailability, hydrophillicity, AOX capacity, and creates a more aesthetically pleasing white colour (Okada *et al.*, 2001; Prasad *et al.*, 2014; Kakkar *et al.*, 2018). Unlike curcumin, the role of THC in skincare is relatively understudied with available literature advocating a role as a depigmenting agent. However a recent study by Kakkar *et al.* (2018) compared topical hydrogel formulation containing 'free' or lipid nanoparticles of THC. They applied the gels to the skin of an inflammatory wound mouse model and reported enhanced anti-inflammatory/antioxidant properties. The role of THC in suncare is relatively unknown, but hairless mice given topically applied curcumin had a delaysed onset of smaller and less frequent skin tumours from repeated UVB exposure (Phillips *et al.*, 2013). Okada *et al.* (2001) found that compared to curcumin, mice fed with a THC supplemented diet had reduced oxidative stress induced lipid peroxidisation and 8-hydroxy-2'-deoxyguanosine (8-OHdG) nDNA products in their kidney.

1.6.3.2 *Pterostilbene (PTERO)*

PTERO is a stilbene class of chemical secreted by various plants (e.g. blueberries, grapes, and some tree barks) in response to environmental stressors such as high UV exposure or microbial infection (Chen *et al.*, 2017). It is a methoxylated form of the widely studied and utilised resveratrol compound, but has a markedly increased bioavailability through enhanced lipophilicity, and longer half-life (Sirerol *et al.*, 2015; Yang *et al.*, 2017). Like resveratrol it has

proven AOX, anti-inflammatory and anti-microbial qualities, but interest in pterostilbene rose when it was reported to drive enhanced rates of autophagy and halt proliferation of cancer cells (Chen *et al.*, 2010; Chen *et al.*, 2017; Li *et al.*, 2017). The role of pterostilbene in suncare is relatively unknown, but 90% of hairless mice given topically applied pterostilene (delivered within liposome) were protected from UVB induction of skin tumour development, whereas all mice given resveratrol or placebo developed tumors (Sirerol *et al.*, 2015). In addition, pterostilbene treated mice had reduced inflammation and wrinkling at the site of UVB solar irradiation (Sirenko *et al.*, 2015). This research group patented the use of pterostilbene for prevention or treatment of skin damage (Estrela. J. and Aseni, M. 2009).

1.6.4 Antioxidant (AOX) concern surrounding prooxidant activity

Concern has arisen over certain polyphenolic compounds acting as prooxidants under certain conditions, e.g. flavinoid oxidation (Alanko *et al.*, 1999). Metodiewa *et al.* (1999) postulated that the positions and number of hydroxyl groups determined an AOX or proxidant status. It has been reported that curcumin (but not THC) had pro-oxidant activity with several cell types, including human gingival fibroblasts (Atsumi *et al.*, 2005; Aggarwal *et al.*, 2014). Some studies have reported factors such as time (duration), dose, biological age, and even daylight cycles influence the pro- or anti-oxidative status of reseveratrol, whereby the potent anticancer effects have been attributed to oxidative DNA strand breaks (de la Lastra and Villegas, 2007; Salehi *et al.*, 2018). Indeed vitamin E becomes a radical when it interacts with a free radical, and remains pro-oxidative if there is insufficient vitamin C to recycle it (Mehta and Gowder, 2015).

In skin, prolonged exposure to free radicals can overwhelm ROS defence mechanisms contributing to general skin aging, and influencing the development of cutaneous diseases or skin cancer (Godic *et al.*, 2014). The use of exogenous AOXs to tackle high levels of ROS are most beneficial before exposure to environmental stressors (e.g. UV). Incidentally, post-application may hinder ROS-mediated cell cycle control and apoptosis of damaged cells (with significantly mutated DNA) (Godic *et al.*, 2014). Establishing an optimal dosage is important, because exogenous AOXs in combination with endogenous AOXs should aim to re-balance (but not over-balance) the redox homeostasis of our skin (Kawagishi and Finkel, 2014).

1.7 Cosmeceutical formulation, skin barrier application and permeation

Whilst a majority of basic research identifies the interaction of AOXs with skin cells, the translation to a final product with appropriate dose and penetrative delivery is largely dependent on the formulation (Burke, K., 2018). Furthermore without a standardised measurement of efficacy for AOXs, there is concern they are too ‘untargeted’ to significantly reverse oxidative

stress (Oyewole and Birch-Machin, 2015). In addition, the economic viability of a product is tied to consumer experience of sensory qualities such as absorption, texture, colour and scent. To achieve these outcomes, cosmeceutical and sun protection active ingredients have been controversially moving towards nanoparticle containing formulations and target driven nanocarrier delivery systems which are well reviewed by Kaul *et al.* (2018). Although concerns have arose from the lack of long-term safety data surrounding nanoparticles and how it fits into current cosmetic legislation, it is recognised that this is a powerful tool for translating protective and synergistic effects seen with phenolic phytochemicals and *in vitro* cells to real world applications (Ganesan and Choi, 2016).

1.8 Project aims

GlaxoSmithKline Consumer Healthcare has a portfolio of product brands (e.g. Oilatum™, Zovirax™, Physiogel™ etc.) which aim to protect skin health and alleviate symptoms such as dryness, itch, and irritation. Topical cosmetic and 'over the counter' products contain active ingredients of various bio-functions. Understanding how these ingredients interact and behave is key to driving product development.

Human skin is exposed to daily oxidative stress from UV light, environmental pollution, and the ozone. It is therefore beneficial to understand the functional applications of AOX ingredients. This project aimed to initially demonstrate if phenolic AOXs tetrahydrocurcumin and pterostilbene could protect the mtDNA of keratinocytes and fibroblasts skin cells from environmental sun exposure. There are numerous publications relating to curcumin and resveratrol, but extremely limited studies on their enhanced synthetic derivatives which are likely to have better function in skin due to improved bioavailability and stability. Furthermore, there are no studies that use these derivatives in combination, making any findings highly novel. This work aimed to optimise a sensitive assay to detect protection of mtDNA, and to develop a representative full thickness skin equivalent grown without scaffold and with donor-matched layers where the fibroblasts secrete and maintain their own extracellular dermal matrix. Novel elements of this project included the transitional approach from pilot data (previously obtained in human cell line) to 2D primary cell monoculture, full-thickness skin equivalents, and whole skin ex-plants. This transition usually occurs in consecutive projects (and is published in consecutive papers), whereas this work proceeded synergistically.

Chapter 2: General Methods

2.1 Human skin cell culture

Cell culture medium referred to in the text was supplemented as follows. Unless stated otherwise, fibroblast medium was Dulbecco's Modified Eagles Medium (DMEM) containing 4.5g/L glucose, L-glutamine, sodium pyruvate and sodium bicarbonate (BE12-604F; Lonza) supplemented with 10% foetal bovine serum (FBS; F9665, Sigma) and 1% streptomycin-penicillin-amphotericin B (PSA; A5955, Sigma). Unless stated otherwise, keratinocyte medium was EpiLife™ (MEPI500CA, Thermo Scientific) supplemented with 1% human keratinocyte growth supplement (HKGS; S0015, Thermo Scientific) and PSA. The compositions of EpiLife™, HKGS and DMEM are included in the supplementary information, under sections 9.2.1-9.2.3 respectively. Working stock aliquots of all media supplements were stored at -20°C. Dulbecco's phosphate buffered saline (PBS) referred to in the text was 1X concentration and without calcium or magnesium. All primary cells were maintained at 37°C, 5% CO_2.

2.1.1 Human skin processing

Facial skin was kindly donated in collaboration with the dermatology surgical department of the Royal Victoria Infirmary and foreskin from the urology surgical department of the Freeman Hospital. All human tissue work adhered to the guidelines outlined by the Newcastle and North Tyneside Research Ethics Committee (Ref 08/H0906/95+5_Lovat) and the Newcastle upon Tyne Hospitals NHS Foundation Trust (trust approval for R&D project reference 4775).

Tissue was processed in chilled PBS supplemented with 2% PSA. Dispase enzyme was prepared by dissolving a 1g vial of Dispase (neutral protease, grade II; 942078001, Sigma) in 50ml PBS, and sterile filtered through a 0.22µm membrane before freezing 1ml aliquots at -20°C. All surgical equipment was cleaned with 70% ethanol and flame sterilised. Subcutaneous tissue and vasculature were removed from skin, before overnight incubation at 4°C with 1ml Dispase, 1ml PSA, and 8ml PBS-5% PSA.

2.1.2 Isolation and culture of adult skin-derived epidermal keratinocytes

2.1.2.1 *Foreskin source*

After Dispase incubation, epidermis was manually peeled from the dermis with surgical tweezers and incubated with Trypsin-EDTA (TE; T3924, Sigma) at 37°C for 5 minutes before being neutralised with DMEM, centrifuged (300 RCF, 5 minutes) and resuspended in keratinocyte medium. Flask media was changed within 24 hours. Flask size (cm^2) were adapted to tissue size, with cells from an average size sample seeded into a 175cm^2 flask. Cells ($\geq 1x10^6$) were cryopreserved at cell passage number 0 or 1 (P0/P1) in 1ml Synth-a-Freeze™ medium

(A1254201, Thermo Scientific). Thawed keratinocytes were cultured in EpiLife™ for monolayer experiments or CELLnTEC CnT-PR medium for human skin equivalents. Keratinocytes were detached with Accutase™ (A1110501, Thermo Scientific) because it was gentler than trypsin. They were used experimentally from cell passage number 1 to 3, as the proliferative capacity of adult (but not neonatal) skin-derived keratinocytes will reduce from passage number 4. Each experiment was performed in at least three independent donors.

Proliferative basale-like keratinocytes were differentiated into spinosum-like keratinocytes by growing the monolayers to 100% confluency in EpiLife™, and then further supplementing the medium with 1M $CaCl_2$ (PBS diluent, 0.22µm sterile filtered) to a final calcium concentration of 1.2mM. The keratinocytes were in high calcium medium for a further 5 days, with a medium change on day 3. Experiments were performed on the fifth day, with antioxidants prepared in high calcium medium.

2.1.2.2 *Facial skin source*

Facial skin keratinocytes were isolated and cultured as for foreskin aside from the following protocol alterations. A stock of 10mM Y-27632 dihydrochloride (P160 ROCK inhibitor; 1254, Tocris) was prepared by sterile filtering ddH_2O through a 0.22µm membrane and injecting the appropriate volume into the vial. Stock was stored in a screw top vial at 4°C. Prior to each medium change EpiLife™ was additionally supplemented with 0.1% ROCK inhibitor. Thawed facial keratinocytes no longer required ROCK inhibitor and were cultured in CELLnTEC CnT-PR medium for skin equivalents. The starting culture of viable keratinocytes from facial skin biopsies was very low because of the skin sample size (cm^2). As keratinocytes will not grow below a certain density, the optimisation in section 5.3.6 outlines how the inclusion of ROCK inhibitor was required to obtain a larger starter culture.

2.1.3 Isolation and culture of adult skin-derived reticular fibroblasts

2.1.3.1 *Foreskin source*

Small pieces of dermis were attached to a lightly scored 75cm^2 flask surface with the reticular layer facing downwards, before coated in 1ml 100% FBS and incubated overnight. Media was added the following morning. The tissue was fed 3 times weekly for 14 days with DMEM. The fibroblasts migrated out of the tissue and were spread out at day 14 by detaching with TE and neutralising with DMEM. Once the cells had readhered, the medium was replaced. Cells were cultured in 75cm^2 flasks and cryopreserved at P0 or P1 in 1ml freezing medium (90% complete DMEM, 10% DMSO). Thawed fibroblasts were cultured in complete DMEM for monolayer experiments, or CELLnTEC CnT-PR-F medium for human skin equivalents. In addition, they

were expanded and passaged once before seeded for experiments. They were used experimentally from cell passage number 2 to 6.

2.1.3.2 *Facial skin source*

Facial skin fibroblasts were isolated and cultured as for foreskin aside from the following protocol alterations. Small flasks (25cm^2) were coated in sterilised 0.1% gelatine (PBS diluent) before small pieces of dermis were attached. The P0 fibroblasts migrated out of the tissue but were not spread out at day 14. They were trypsinized at day 14 for cryopreservation in 1ml Synth-a-Freeze™. Additional information is found in section 5.3.6.

2.2 Induction of DNA damage

General DNA damage was induced by hydrogen peroxide or irradiation with a solar simulator lamp. The purpose was to induce a detectable amount of damage to the mtDNA genome, which could be detected by the comparative qPCR assay described in Chapter 3. This allowed for screening of antioxidant protection against the damage stimuli, as seen in Chapters 4 and 6.

2.2.1 Hydrogen peroxide

Experimental DNA damage was induced with 150µM hydrogen peroxide (H_2O_2), diluted from 30% w/w stock (H1009, Sigma) in non-supplemented cell specific medium. Stock was stored light protected at 4^{o}C. All H_2O_2 dosing was performed on cell monolayers grown in 3.2cm^2 dishes, which were PBS washed (to remove serum) before light protected incubation for 1 or 2 hours at room temperature. Cells were trypsinized, pelleted at 300 RCF and frozen at -20^{o}C.

2.2.2 Solar irradiation

Annual calibration of the solar simulator and filters was performed by the regional medical physics department of the Newcastle Upon Tyne Hospitals Trust, UK. They Newport solar simulator (Model 91282-1000) uses a xenon lamp with associated optics designed to give a uniform downwardly directed beam. The calibration report states that this model has been retrofitted with an infra-red heat filter and is broadly consistent with the current Newport Oriel® Sol-UV-6 model (see Figure 2.1). Calibration is performed to ensure it is spectrally compliant with the COLIPA irradiance response curve whereby ~59 seconds is a typical time to reach 1 standard erythemal dose (SED) which equates to 10mJ/cm^2 weighted (Diffey, 1991) at maximum output power. The calibration data in Table 2.1 detected 1.19 SED /min, comprised of 0% UVC, 7.8% UVB, and the remainder UVA. For experiments, solar radiation was performed with a with SED doses (Diffey, 1991) with the exposure time (seconds) calculated using an International Light Technologies radiometer-photometer (Model ILT1400-A serial

8524 with UVA sensor serial 867) and UQG optics VIS-IR light filter (Schott UG11 Glass-Type). This light filter was removed prior to full spectrum solar irradiation.

Measured Irradiance - no filter			
Irradiance	*(mw / cm2)*	*%*	*Calibration factor*
Total UV	15.079		1.263
UVC (250-280)	0.000	0.0	0.000
UVB (280-315)	1.182	7.8	0.099
UVA (315-400)	13.897	92.2	1.164
SED / min	1.191		

Table 2-1: Measured UV Irradiance of Newport solar simulator Measured value of total UV irradiance (and its components). The calibration factors are to convert the local broadband meter reading to UV irradiance. The lower portion of the table gives the number of standardised erythema (SED) doses (i.e. multiples of 10mJ/cm^2) delivered per minute**.**

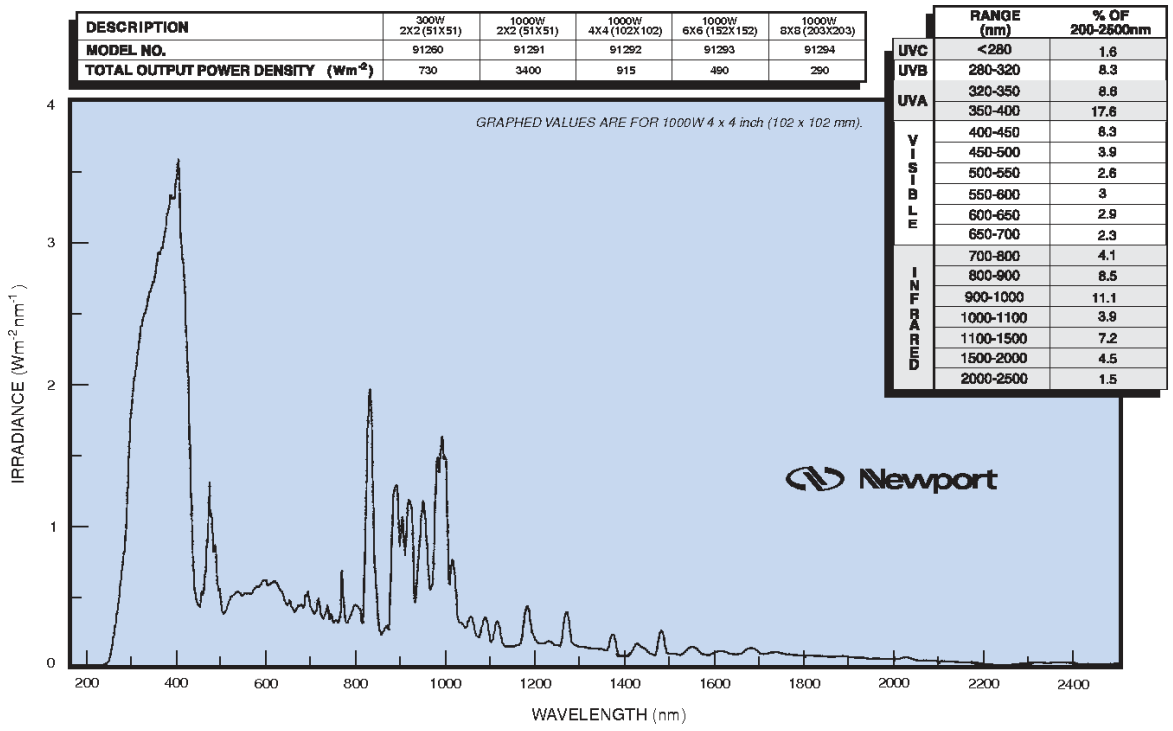

Figure 2-1: Newport Solar Simulator Online Spectral Irradiance Curve.

Cell monolayers were grown in 3.2cm^2 dishes and irradiated in phenol red-free non-supplemented DMEM with lids removed, because previous work in this research group have shown that supplements (e.g. serum) and phenol absorb some of the lamp irradiance and affect the dose provided to cells. Human skin equivalent and ex-plant models were irradiated in a similar manner except suspended within hanging inserts over medium so the stratum corneum remained dry (see sections 5.2 and 6.2). Non-irradiated controls were foil wrapped throughout solar irradiation.

Previous work in this research group has shown that UV solar irradiation increases cell monolayer adherence to tissue-culture coated plastic. As a result they require cell scraping as

well as trypsinisation immediately after solar irradiation. All non-monolayer experiments were rapidly chilled on wet ice (prior to processing) or snap-frozen on dry ice pending storage (see sections 5.2 and 6.2).

2.3 DNA extraction and quantification: *ex-vivo* tissue, human skin equivalent and cell models

Whole tissue and skin equivalents were thawed to room temperature and cut into small pieces with a scalpel before addition of tissue lysis buffer (ATL) and proteinase K of the QiaAMP™ DNA mini kit (Qiagen). Tissue homogenisation was performed within a rocking water bath (56^{o}C) for 3 hours (human skin equivalents) or overnight (whole tissue, approx. 18 hours). Cell pellets were thawed to room temperature before extraction. The extraction continued as outlined in the manufacturer's instructions for the QiaAMP™ DNA mini kit (Qiagen) and DNA quantified by NanoDrop ND-1000 spectrophotometer (Thermo Scientific). Isolated DNA was of high quality (A_{260}/A_{280} > 1.8) and stored at -20^{o}C with minimal freeze-thaw cycles.

2.4 RNA extraction and quantification: *ex-vivo* tissue, human skin equivalent and cell models

Whole tissue and skin equivalents were homogenised in chilled Precellys CKMix-50-R 2ml tissue lysing tubes with 600µl RLT buffer and 6µl β-mercaptoethanol, using a Precellys Evolution tissue homogeniser (Berlin Instruments) at the following settings: 0^{o}C temperature, 60 seconds at 6000rpm followed by 30 second pause for 6 cycles. The tubes were centrifuged at full speed for 30 seconds and the liquid transferred to RNAase-free eppendorfs. For human cell pellets, homogenisation was by Qiashredder as per manufacturer's instructions (Qiagen). The remainder of the extraction followed the Qiagen RNeasy mini kit protocol for animal tissue (inclusive of DNase I treatment step) and quantified using NanoDrop™ spectrophotometer. Isolated RNA was of high quality (A_{260}/A_{280} > 2.0) and stored at -80^{o}C with minimal freeze-thaw cycles. To maintain integrity, RNA was eluted into pre-chilled eppendorfs on wet ice and transferred to -80^{o}C for storage as fast as possible. Throughout homogenisation optimisation RNA integrity (RIN) was additionally assessed by Agilent RNA 6000 Nano Kit for bioanalyzer, whereby RIN>8.0 was of high quality. Protein acetone precipitation from RNeasy mini kit flow-through was possible, but with a significantly reduced yield to direct homogenisation (see section 2.5).

2.5 Protein extraction and quantification: *ex-vivo* tissue, human skin equivalent and cell models

Protein was extracted and stored in chilled RIPA buffer (150mM sodium chloride, 1% Triton X-100, 0.5% sodium deoxycholate, 50mM Tris, pH 8.0), freshly supplemented with 150µl cOmplete™ protease inhibitor cocktail (Roche) per 1ml RIPA. Protease inhibitor was made by dissolving one tablet in 1.5ml dH_2O and storing 150µl aliquots at -20°C. Cell pellets required no homogenisation, but whole skin and human skin equivalents were homogenised in RIPA-protease buffer within pre-chilled Precellys CKMIX-50-R tubes. The settings were as for RNA. Samples were incubated on wet ice for 20 minutes before centrifugation at maximum speed for 15 minutes at 4°C. Supernatant (containing protein lysate) was rapidly aliquoted on wet ice into pre-chilled eppendorfs and stored at -80°C with minimal freeze-thaw cycles. A small aliquot of protein was kept for quantification, which was performed using a BCA protein assay kit as per manufacturer's instructions with absorbance read at 562nm on SpectraMax 250 (Molecular Devices). Protein acetone precipitation from RNeasy mini kit flow-through was possible, but with a significantly reduced yield compared to direct homogenisation. The protocol is included online as a kit booklet supplement.

2.6 Human skin donors

Donor ID	Newcastle Hospital*	Surgical Site	Sex	Age**	Fitz. Skin Type	Biopsy Histology Block***
2624	RVI	Facial	Female	56	I-III	x1 FFPE
2625	RVI	Facial	Female	52	I-III	x1 FFPE
2626	RVI	Facial	Male	74	I-III	x1 FFPE
2683	RVI	Facial	Female	65	I-III	x1 FFPE
2720	RVI	Facial	Female	73	I-III	x1 FFPE
2727	RVI	Facial	Male	80	I-III	x1 FFPE
2729	RVI	Facial	Male	77	I-III	N/A
2731	RVI	Facial	Female	49	I-III	N/A
2732	RVI	Facial	Female	79	I-III	N/A
2733	RVI	Facial	Male	46	I-III	N/A
2734	RVI	Facial	Male	57	I-III	N/A
2735	RVI	Facial	Male	82	I-III	N/A
2736	RVI	Facial	Male	69	I-III	N/A
2737	RVI	Facial	Female	43	I-III	N/A
2742	RVI	Facial	Male	70	I-III	x1 FFPE
2746	RVI	Facial	Male	88	I-III	N/A
2747	RVI	Facial	Male	73	I-III	N/A
2748	RVI	Facial	Male	72	I-III	N/A
S1009F	Freeman	Foreskin	Male	50	I-IV	N/A
S1013F	Freeman	Foreskin	Male	51	I-IV	N/A
S1026F	Freeman	Foreskin	Male	unknown	I-IV	N/A
S1052F	Freeman	Foreskin	Male	53	I-IV	N/A
S1054F	Freeman	Foreskin	Male	27	I-IV	N/A
S1057F	Freeman	Foreskin	Male	51	I-IV	N/A
S1058F	Freeman	Foreskin	Male	59	I-IV	N/A
S1073F	Freeman	Foreskin	Male	65	I-IV	N/A
S1074F	Freeman	Foreskin	Male	28	I-IV	N/A
S1075F	Freeman	Foreskin	Male	unknown	I-IV	N/A
S1076F	Freeman	Foreskin	Male	unknown	I-IV	N/A
S1082F	Freeman	Foreskin	Male	unknown	I-IV	N/A
S1083F	Freeman	Foreskin	Male	unknown	I-IV	N/A
S1141F	Freeman	Foreskin	Male	40	VI	x1 FFPE
S1142F	Freeman	Foreskin	Male	17	I-IV	x1 FFPE
S1144F	Freeman	Foreskin	Male	80	I-IV	x1 FFPE
S1145F	Freeman	Foreskin	Male	51	I-IV	x1 FFPE
S1146F	Freeman	Foreskin	Male	76	I-IV	x1 FFPE
S1147F	Freeman	Foreskin	Male	53	I-IV	x1 FFPE
S1151F	Freeman	Foreskin	Male	35	I-IV	x1 FFPE
S1152F	Freeman	Foreskin	Male	77	I-IV	x1 FFPE
S1153F	Freeman	Foreskin	Male	45	I-IV	x1 FFPE
S1154F	Freeman	Foreskin	Male	44	I-IV	x1 FFPE
S1168F	Freeman	Foreskin	Male	33	I-IV	N/A
S1169F	Freeman	Foreskin	Male	26	I-IV	N/A
S1174F	Freeman	Foreskin	Male	22	I-IV	N/A

S1175F	Freeman	Foreskin	Male	48	I-IV	N/A
S1192F	Freeman	Foreskin	Male	64	I-IV	N/A
S1193F	Freeman	Foreskin	Male	76	I-IV	N/A
S1194F	Freeman	Foreskin	Male	48	I-IV	N/A
S1196F	Freeman	Foreskin	Male	40	I-IV	N/A
S1197F	Freeman	Foreskin	Male	56	I-IV	N/A
S1202F	Freeman	Foreskin	Male	85	I-IV	N/A
S1215F	Freeman	Foreskin	Male	49	I-IV	N/A
S1216F	Freeman	Foreskin	Male	22	I-IV	N/A
S1223F	Freeman	Foreskin	Male	50	I-IV	N/A
S1224F	Freeman	Foreskin	Male	76	I-IV	N/A
14525	Freeman	Foreskin	Male	56	I-IV	N/A
14526	Freeman	Foreskin	Male	48	I-IV	N/A
14527	Freeman	Foreskin	Male	67	I-IV	N/A
14534	Freeman	Foreskin	Male	43	I-IV	N/A
14551	Freeman	Foreskin	Male	41	I-IV	N/A
14552	Freeman	Foreskin	Male	27	I-IV	N/A
14563	Freeman	Foreskin	Male	21	I-IV	N/A
14566	Freeman	Foreskin	Male	77	I-IV	N/A
14567	Freeman	Foreskin	Male	40	I-IV	N/A

Table 2-2: Demographics of human skin donors obtained in collaboration with Newcastle upon Tyne Hospitals NHS Trust. *Newcastle Upon Tyne Hospitals Trust, UK; RVI dermatology and Freeman urology surgical departments **Age at time of surgery ***Formalin fixed biopsy stored in Newcastle Dermatology Biobank, UK. *Fitz. – Fitzgerald phototyping scale*

Chapter 3: Optimised detection of mitochondrial DNA damage

3.1 Chapter overview and aims

Intrinsic and extrinsic factors that induce cellular oxidative stress damage tissue integrity and promote ageing result in accumulative strand breaks to the mitochondrial DNA (mtDNA) genome. Limited repair mechanisms and proximity to superoxide generation make mtDNA a prominent biomarker of oxidative damage. Using human DNA, a long-range qPCR methodology has been optimised that sensitively detects mtDNA strand breaks relative to short mitochondrial and nuclear DNA (nDNA) housekeeping amplicons. The primers used are specific to the mtDNA genome, so total DNA (mt- and n-DNA) can be used because the housekeeping assay controls for mtDNA copy number variation between samples.

The assay provides a qualitative comparison of the amount of mtDNA damage relative to a control sample. The amount of fluorescence increases with each cycle as it makes more SYBR Green-bound mtDNA amplicons. If a sample has damaged regions within its mtDNA, it will require additional qPCR cycles to produce the same amount of fluorescent product (C_t). The damage detected across the 11kb region is non-specific and screens only for that significant enough to halt the DNA polymerase enzyme.

The reason why primers for 11kb mtDNA amplicons are used instead of covering the entire 16.5kb mtDNA, is because it is technically challenging to perform l6.5kb long-range qPCR in one reaction and robust primers already existed for this 11kb size region. Previous work in this research group performed 4 x 4kb qPCR assays to cover the entire mtDNA genome and found the amount of extra damage detected was not large enough to justify the extra time and reagents to perform multiple amplifications per sample. In addition, this assay amplifies intact 11kb regions so screening for a larger amplicon in a highly damaged sample would result in no qPCR product, and consequently no C_t data value.

Portions of this chapter formed a recently published method paper (Hanna *et al.*, 2019).

3.2 Chapter specific methods

3.2.1 Oligonucleotides

Primer sequences for all qPCR assays are as outlined in Table 3-1, alongside their respective published source. Sequence specificity was additionally verified using Sanger Institute Artemis, PrimerBLAST, and UCSC genome browsers. Primers for qPCR were synthesized by Eurofins Genomics, and reconstituted to 100µM in IDTE buffer (10mM Tris, pH 8, 0.1mM EDTA). Single use aliquots of working primers (10µM) were prepared in IDTE and stored at -20°C.

Primer Set		Base Sequence (5' to 3')	Nucleotide Numbers	T_M (±1°C)	Primer Efficiency (%)	Source
11,095bp (*mtDNA*)	DLB (*F*) OLA (*R*)	ATGATGTCTGTGTG GAAAGTGGCTGTGC GGGAGAAGCCCCG GCAGGTTTGAAGC	chrM: 282 + 5756	84	93.5*	Kleinle *et al.* (1997)
83bp *(mtDNA)*	IS1 *(F)* IS2 *(R)*	GATTTGGGTACCAC CCAAGTATTG AATATTCATGGTGG CTGGCAGTA	chrM: 16042 + 16124	80	93.5	Koch *et al.* (2001)
87bp *(mtDNA)*	DS1 F *(F)* DS1 R *(R)*	ACTACAACCCTTCG CTGACG GCGGTGATGTAGAG GGTGAT	chrM:3442 + 3528	82	92	Rothfuss *et al.* (2010)
93bp *(nDNA β2M gene)*	hB2M F2 *(F)* hB2M R2 (R)	GCTGGGTAGCTCTA AACAATGTATTCA CCATGTACTAACAA ATGTCTAAAATGGT	chr15: 39523 + 39617	79	102	Malik *et al.* (2011)

Table 3-1: Primer pair sequences for qPCR. Product melt temperature (T_M), primer efficiency (%) and published source are included. *Primer efficiency of 93.5% only within the dynamic linear range (see Figure 3-4). *Forward- F, Reverse- R*

3.2.2 Amplification of 11kb mtDNA amplicons using qPCR

Amplicons spanning 11kb of the 16.5kb mtDNA genome (Figure 3-1(A)) were amplified using a SYBR Green qPCR assay. This 11kb region spans 11 of the 13 genes encoding functional components of the electron transport chain (ETC) and a majority of the D-loop region which initiates mtDNA replication and transcription (Li *et al.*, 2012). It is technically challenging to perform l6.5kb long-range qPCR in one reaction and robust primers already existed for this 11kb size region. Previous work in this research group performed 4 x 4kb qPCR assays to cover the entire mtDNA genome and found the amount of extra damage detected was not large enough to justify the extra time and reagents to perform multiple amplifications per sample. SYBR Green I binds to double stranded mtDNA and fluoresces relative to a passive ROX reference dye. Fluorescence (ΔRn) increases exponentially to amount of amplicon and is measured at the end of each cycle. As illustrated in Figure 1(B) data is analysed according the comparative C_t method ($\Delta\Delta C_t$) whereby a more damaged sample will require more cycles to produce the same amount of amplicon product (Santos *et al.*, 2006). The method was performed on a 96 well StepOnePlus™ machine (Applied Biosystems), with mastermix composition and settings outlined in Tables 3-2 and 3-3. The Expand Long Range PCR System (Sigma) was used alongside SYBR Green I DNA dye (10,000X in DMSO; Lonza) and ROX passive reference dye (Applied Biosystems). To achieve 5X SYBR Green working concentration, a 1µl frozen aliquot was diluted in 2ml IDTE buffer as fluorescent dyes should not have more than two freeze-thaw cycles. Each sample was assayed in triplicate with a standard deviation threshold of ≤ 0.4 C_t. C_t threshold was manually adjusted to the linear range on StepOnePlus™ v2.3 software and melt curve analysis used to determine product size. The threshold was set at 1.25ΔRn for all 11kb qPCR experiments. A routine positive control was a previously run sample of known C_t value, and negative control was mastermix alone. If the machine was used throughout the day, it was important to shut down and reboot it prior to an overnight 11kb assay run in order to clear the memory cache and prevent overheating.

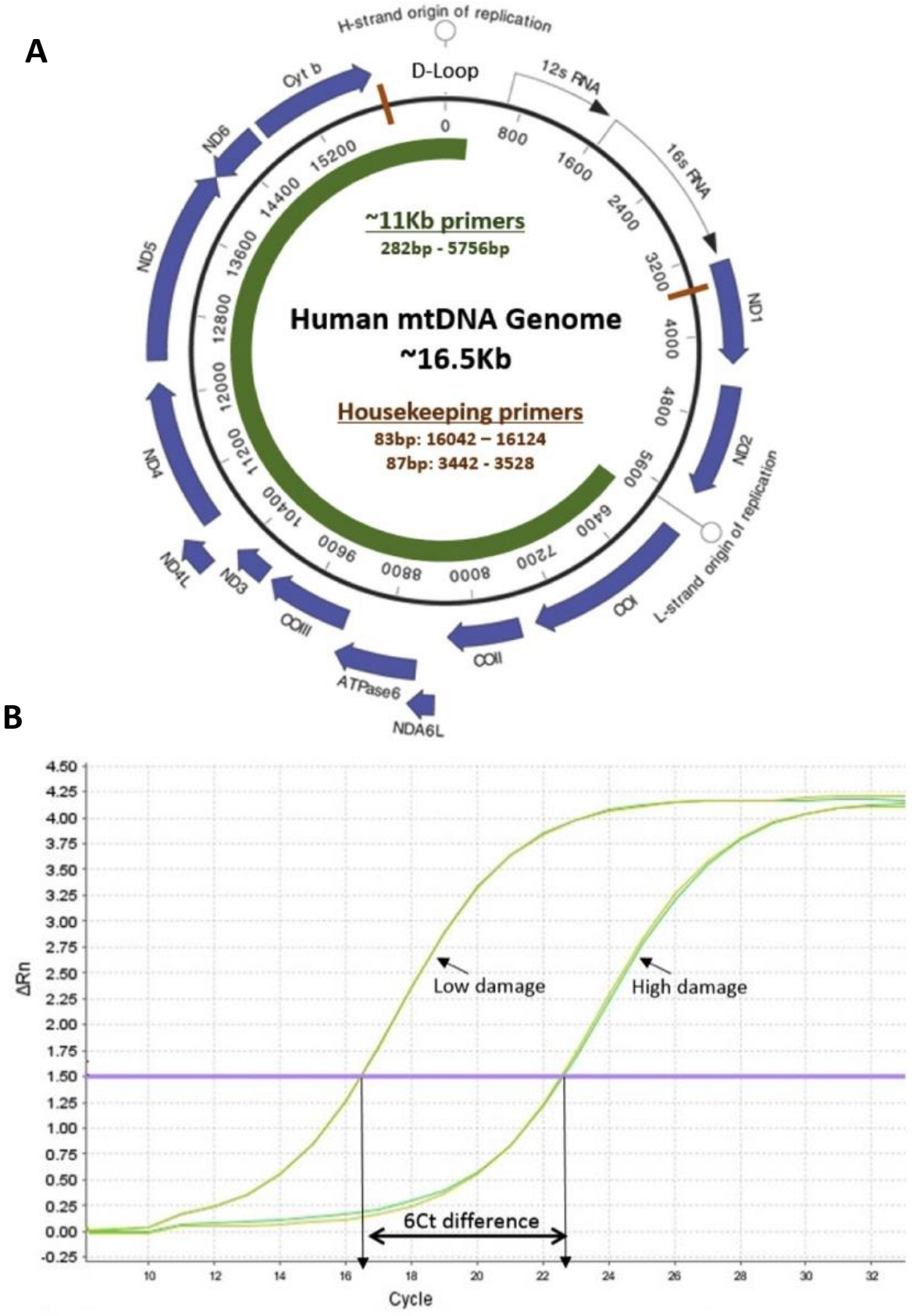

Figure 3-1: Summary of 11kb qPCR assay. (A) Schematic of the ~11kb region (green) amplified from each ~16.5kb human mtDNA genome. It is a circular molecule with an inner light (L) strand and outer heavy (H) strand. The 11kb region amplified contains 11 of 13 genes (blue arrows) encoding polypeptide components of the mitochondrial electron transport chain. It also covers a large portion of the non-coding D-loop control region. Small housekeeping regions are indicated in orange. (B) Amplification plot indicating C_t difference between a highly damaged and low damaged sample. Fluorescent threshold (1.5ΔRn) has been set within the linear range of exponential amplification. Image source: Hanna *et al.* (2019)

Mastermix Composition	Volume (µl)	Final Concentration
PCR grade H_20	12.7	N/A
Expand Long Template Buffer 2, with 27.5 mM $MgCl_2$ (10X concentrated)	2.0	1X Buffer (2.75mM $MgCl_2$)
PCR nucleotide mix (10mM dATP, dCTP, dGTP, and dTT)	1.0	500 µM
D1B primer (10µM; diluent: 10mM Tris, pH8, 0.1mM EDTA (IDTE))	0.6	0.3µM (300µM Tris, 0.3µM EDTA)
OLA primer (10µM; diluent: IDTE)	0.6	0.3 µM (300µM Tris, 0.3µM EDTA)
SYBR Green I (5X concentrated; diluent: IDTE)	0.4	0.1X Sybr Green I (300µM Tris, 0.3µM EDTA)
ROX passive reference dye (50X concentrated)	0.4	1X
Expand Long Template Enzyme Mix (5U/µl)	0.3	0.075U
Mastermix Total	18.0	
DNA (6ng/µl)	2.0	
Reaction Total	20.0	

Table 3-2: Reagents for 11kb qPCR assay

Stage	Temperature	Time (minutes)	Cycles
Initial Denaturation	94.0	2.00	1
Denaturation	94.0	0.15	10 *(Acquire at end of step)*
Annealing	60.0	0.30	
Extension	72.0	9.00	
Denaturation	94.0	0.15	25 *(Acquire at end of step)*
Annealing	60.0	0.30	
Extension	68.0	8.50 (+10 seconds per cycle)	
StepOnePlus Melt Curve Stage			

Table 3-3: Amplification settings for 11kb qPCR assay

3.2.3 Validation of 11kb mtDNA amplicons

During initial optimisation, amplified qPCR products were additionally analysed on a Gel-Red (Biotium) stained 0.8% w/v agarose gel and visualised using a Li-Cor Odyssey Fc system. Positive 11kb bands were cross-referenced with StepOnePlus melt curve analysis whereby each amplicon reached peak maximum at the same temperature. To establish the dynamic linear range and therefore optimal starting amount of DNA (ng), standard curves were simultaneously performed on one qPCR plate using untreated HDFn cell line, primary fibroblast and primary keratinocyte DNA. Each sample was serially diluted (1:2) from 100ng/µl to 3.125ng/µl. To identify the precise linear range, several smaller ranging standard curves were then performed (e.g. 20ng/µl to 5ng/µl). Linear regression analysis was used to calculate primer efficiency whereby $E = 2^{(-1/slope)}$ (Yuan *et al.*, 2006). Percentage efficiency (%) was calculated by (E-1) x 100.

3.2.4 Quality Control: Amplification of housekeeping amplicons

Small regions of mtDNA-specific (83bp or 87bp) and a single copy nDNA-specific β2M gene (93bp) were simultaneously amplified using a SYBR Green based qPCR assay. The method was performed on a 96 well StepOnePlus™ machine (Applied Biosystems), with mastermix

composition and settings outlined in Tables 3-4 and 3-5. Each sample was assayed in triplicate with a standard deviation threshold of ≤ 0.4 C_t. C_t threshold was manually adjusted to the linear range on StepOnePlus™ v2.3 software and melt curve analysis used to determine product size. The threshold was set at 7.5ΔRn for all housekeeping qPCR experiments. The standard curve for each primer pair were simultaneously performed on one qPCR plate using untreated primary fibroblast DNA. Each sample was serially diluted (1:2) from 100ng/µl to 1.56ng/µl. Linear regression analysis was performed as for 11kb standard curve.

Mastermix Composition	Volume (µl)	Final Concentration
PCR grade H_20	8.25	N/A
Forward primer (10µM)	1	0.4 µM
Reverse primer (10µM)	1	0.4 µM
SYBR® Green JumpStart™ Taq ReadyMix™ (2X)	12.5	1X
ROX passive reference dye (100X)	0.25	1X
Mastermix Total	23.0	
DNA	2.0	
Reaction Total	25.0	

Table 3-4: Reagents for 83bp/87bp/93bp housekeeping qPCR assay

Stage	Temperature	Time (minutes)	Cycles
Initial Denaturation	94.0	2.00	1
Denaturation	94.0	0.15	35 *(Acquire at end of step)*
Annealing	60.0	0.45	
Extension	72.0	0.45	
Final Extension	72.0	2.00	
StepOnePlus Melt Curve Stage			

Table 3-5: Amplification settings for 83bp/87bp/93bp housekeeping qPCR assay

3.3 Results

3.3.1 Validation of the 11kb qPCR strand break assay

3.3.1.1 *Mastermix optimisation*

SYBR Green I

A direct comparison with SYBR Green I diluted to 5X in 100% DMSO versus IDTE buffer (pH8) demonstrated that while both reactions worked, IDTE buffer produced superior melt curves and reduced replicate standard deviation (data not shown).

To determine if the mastermix final concentration of EDTA was low enough to avoid magnesium chelation, a direct comparison with commercial 10mM IDTE and Tri-HCL buffers was performed. Ultrapure 1M Tris-HCL pH8 (Invitrogen) was diluted to 10mM pH 7.7 using PCR grade water. There was no difference between the C_t values generated with either buffer (Figure 3-2) so IDTE was selected as a 10mM working buffer is commercially available.

Finally, a comparison was made between 5X and 10X SYBR Green I diluted in IDTE, and 5X in PCR grade water. It was found that SYBR Green was not water stable, and 10X SYBR Green was not able to detect C_t changes when DNA concentration was halved (data not shown). The DNA concentration standard curve was generated using a mastermix containing 5X SYBR Green I in IDTE pH 8 buffer (Figure 3-2).

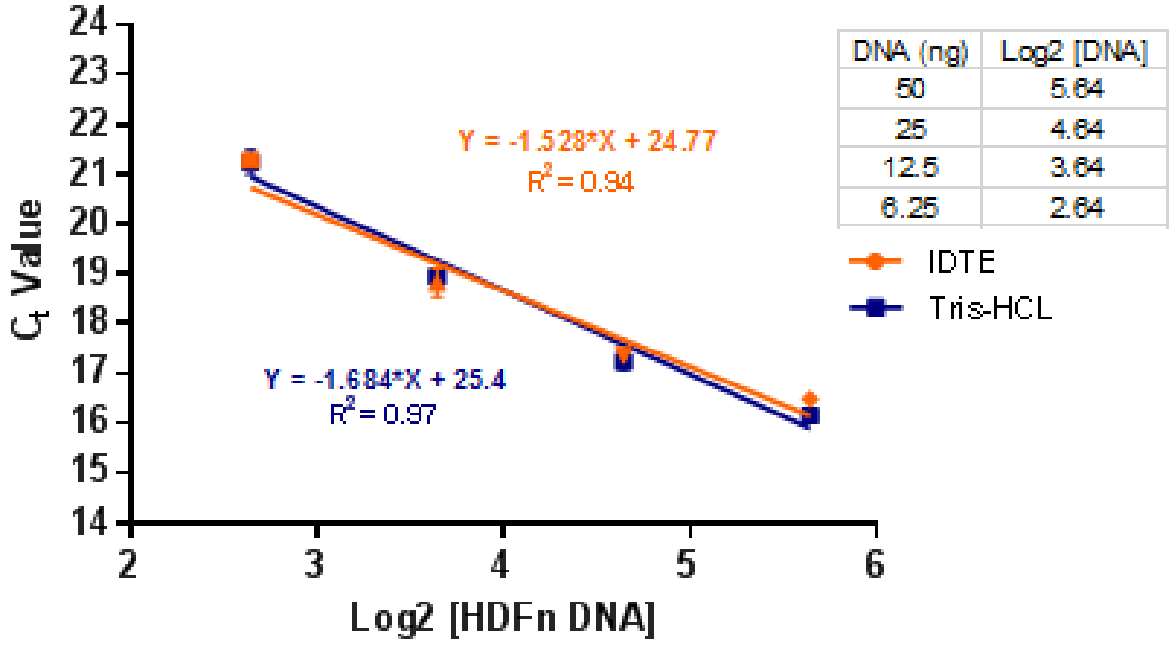

Figure 3-2: SYBR Green I diluent testing for 11kb qPCR assay mastermix. Partial standard curves (6.25-50ng DNA) for 11kb qPCR demonstrated no difference between C_t values obtained when the reaction mastermix contained SYBR Green I diluted in 10mM IDTE or Tris-HCL buffer. Data obtained from HDFn dermal fibroblast cell line DNA. Mean ± SD, N=1, n=3 per data point.

Oligonucleotides

Factors affecting primer integrity were investigated when primer dimer (melt curve temp. ~79) would intermittently increase in some plates.

Custom oligonucleotides from Eurofins Genomics were directly compared in three purification forms: 'optimised PCR primer', HPSF purified and HPLC purified (Figure 3-3). Whilst all primers were reconstituted to 100µM in IDTE buffer, a comparison of 10µM working primer diluents was performed using IDTE buffer or PCR grade water. It was found that only 'optimised PCR' and HPLC primers diluted in IDTE buffer detected $1C_t$ difference when the DNA concentration was halved. However only 'optimised PCR oligos' could detect the $1C_t$ difference with water diluent. HPSF oligos did not detect the difference in either diluent.

It was also found that primers were most stable stored as a concentrated 100µM stock, that 50µl working aliquots should be single use (to avoid freeze-thaw cycles) and they should be stored at -20°C for up to 4 weeks.

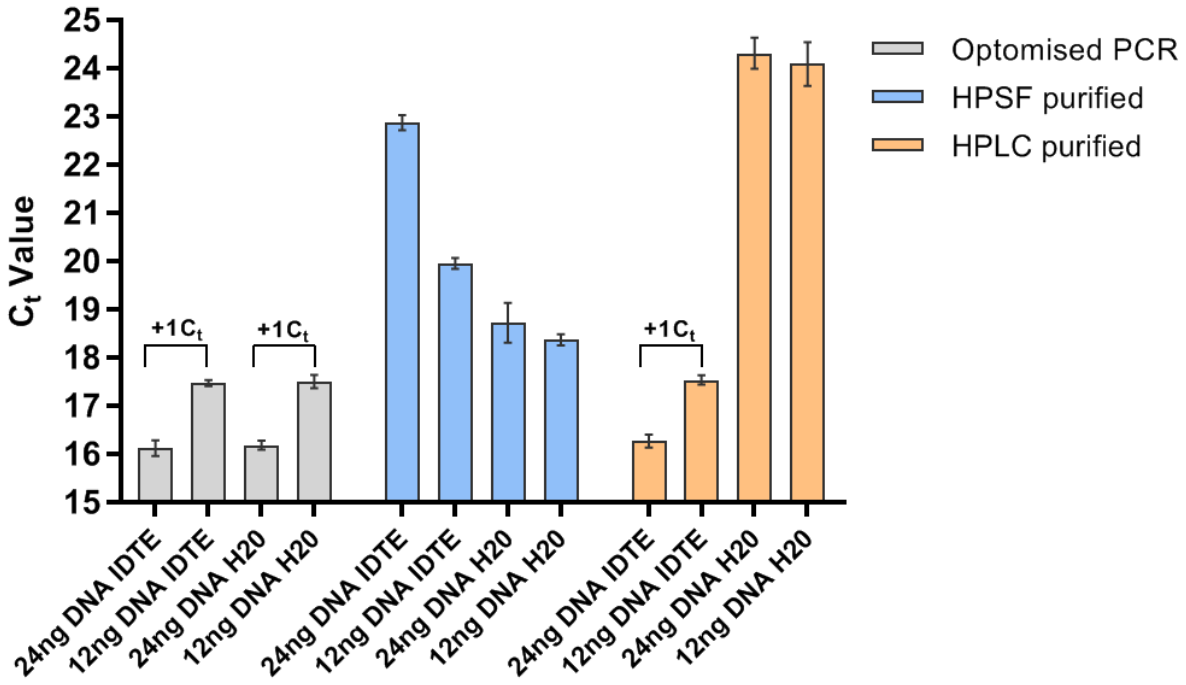

Figure 3-3: Effect of primer purification and diluent on 11kb qPCR assay. Primers synthesised in three purity forms ('optimised' PCR (left/grey), HPSF (middle/blue) and HPLC (right/orange)) were simultaneously compared in the 11kb qPCR, whereby a doubling of DNA concentration should correspond to a 1 C_t difference. 'Optimised' primers detected a 1 C_t difference when diluted in IDTE or PCR grade water. HPSF primers failed to detect the difference in both diluents, and HPLC detected only in IDTE buffer. Data obtained from adult foreskin-derived reticular fibroblast DNA (donor S1058F – male, age 59). Mean ± SD, N=1, n=3 per data point.

3.3.1.2 *Identification of a dynamic linear DNA range*

A series of mean standard curves evaluated the dynamic linear range and primer efficiency across a range of 6.25ng-200ng starting total DNA (Figure 3-2). A series of smaller standard curves (data not shown) narrowed the linear range too approximately 10-50ng, with 12ng selected as an optimal and economical DNA amount. Extending the regression analysis outside this range progressively reduced calculated primer efficiency (%) to 62%. However within this range (as indicated by dashed box), linear regression analysis determined a correlation coefficient (R^2) of 0.91 and primer efficiency of 93.5%. There was no difference seen between DNA extracted from different cell types, as demonstrated by the negligible error bars of Figure 3-4).

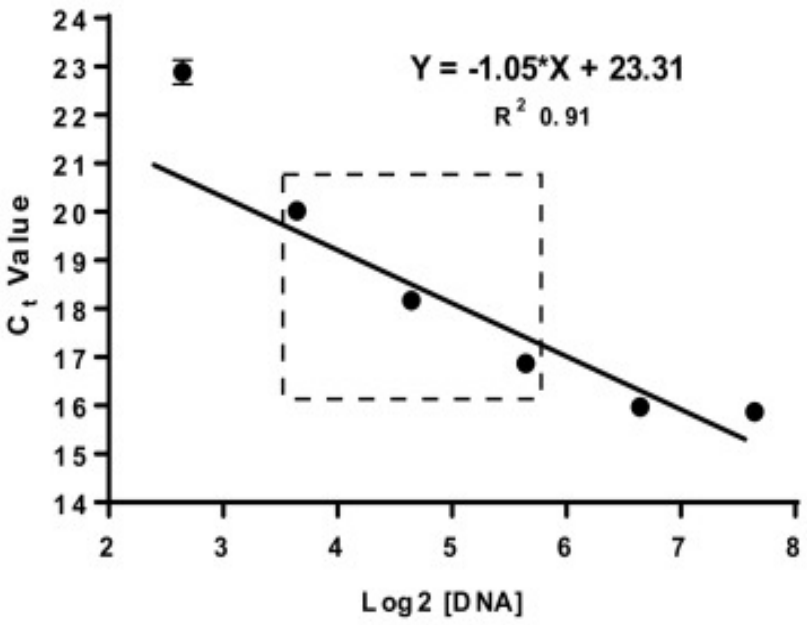

DNA (ng)	Log2 [DNA]
200	7.64
100	6.64
50	5.64
25	4.64
12.5	3.64
6.25	2.64

Figure 3-4: Mean standard curve for 11kb qPCR assay. The linear range lies between 10-50ng, whereby a doubling of DNA concentration corresponded to a 1 C_t difference. Data obtained from adult foreskin-derived reticular fibroblast DNA (donor S1057F – male, age 51), adult foreskin-derived keratinocyte DNA (donor S1058F – male, age 59) and HDFn dermal fibroblast cell line DNA. There was no variability between the donors, as evidenced by the negligible error bars. Mean ± SEM, N=3, n=9 per data point. Image source: Hanna *et al*. (2019)

3.3.1.3 *Clarification of the 11kb product amplification*

Positive 11kb bands were determined by StepOnePlus™ melt curve analysis whereby each amplicon reached peak maximum at the same temperature of 84°C±1 (Figure 3-5). Agarose gel analysis of all standard curve products (6-200ng) demonstrated 11kb bands. For samples with starting DNA ≤50ng, positive bands correlated to the correct size with absence of non-specific binding or primer- dimers (Figure 3-5). However, for 50-200ng the 11kb bands were accompanied by smears of unamplified DNA and bi-peak melt curves (data not shown).

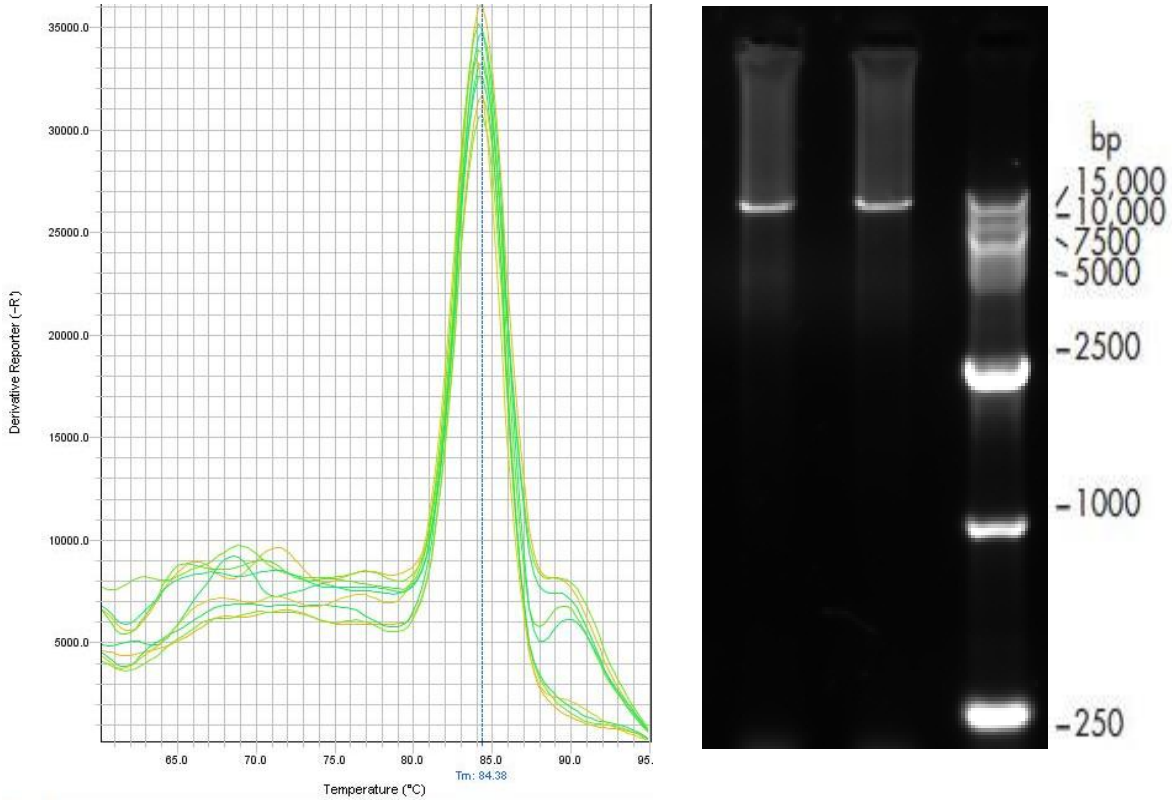

Figure 3-5: Melt curve analysis and agarose gel show positive 11kb amplicons. No evidence of non-specific binding or primer-dimer. Image source: Hanna *et al.* (2019)

3.3.1.4 *Determining equal amounts of starting mtDNA between samples and in relation to a nuclear DNA housekeeping gene*

To establish equal starting amounts of mtDNA between samples, small regions of mtDNA specific (83bp or 87bp) and a single copy nDNA β2M gene (93bp) were simultaneously amplified. The relative amount of mtDNA in treated versus untreated samples, was additionally normalised to the amount of β2M (93bp; gDNA) within those samples.

A comparative C_t method was used to determine the fold difference, whereby $2^{\Delta\Delta Ct} = 2^{\wedge}((Ct, mtDNA, untreated – C_t, nDNA, untreated)) - ((C_t, mtDNA, treated - C_t, nDNA, treated)$. All compared samples were between 1 C_t (±0.3) of each other. This is demonstrated in Figure 3-6 (D) showing equal amounts of starting mtDNA and nDNA in both solar irradiated and non-irradiated primary skin cells (see 2.2.2). If an experimental treatment increases or reduces the amount of intact mtDNA within the sample, the fold difference determines the ratio adjustment required between total DNA samples.

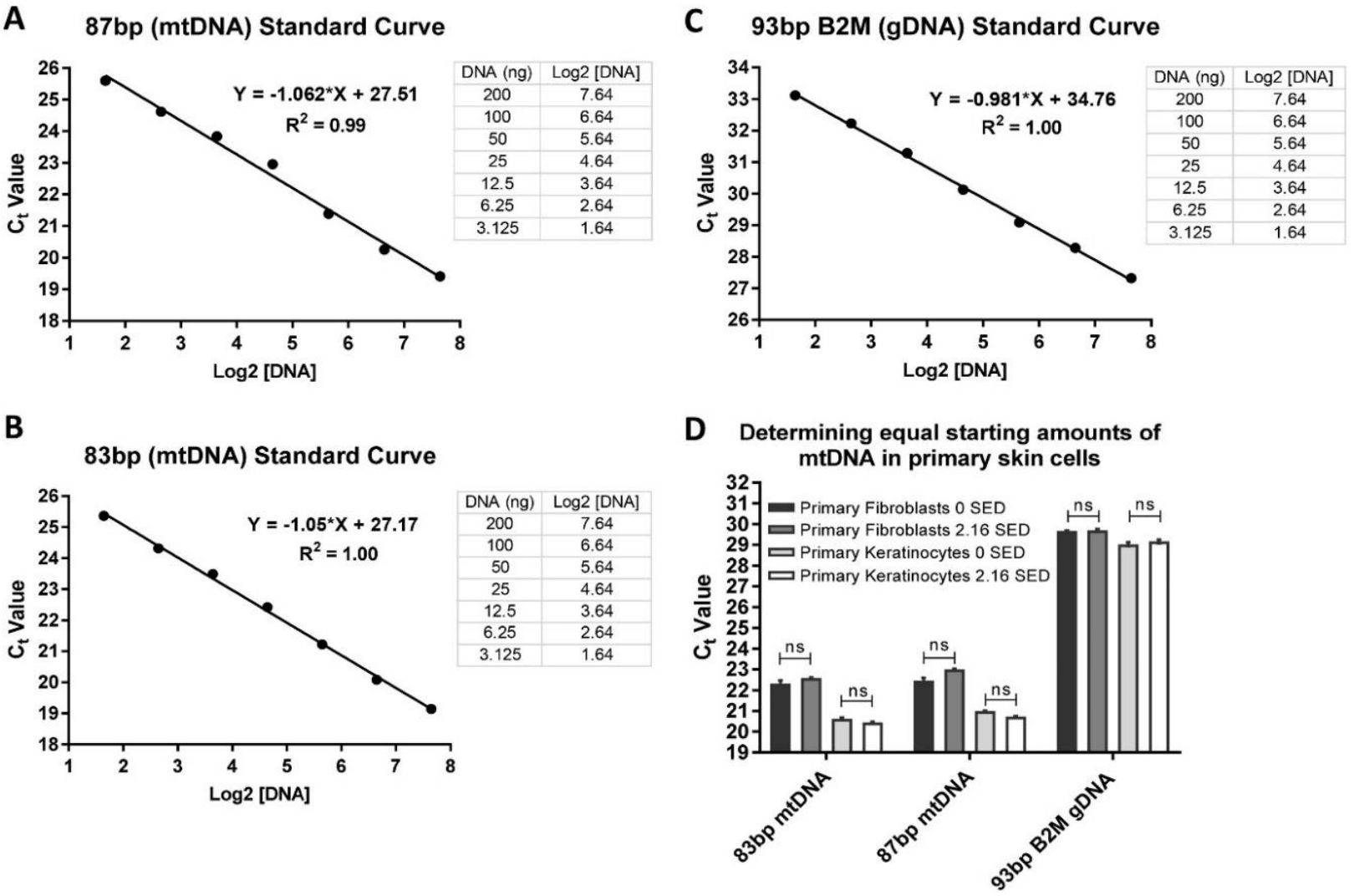

Figure 3-6: Standard curves of housekeeping qPCR assays. The dynamic linear range of each spanned 3-200ng. (D) Bar chart showing equal amounts of starting mtDNA in both solar irradiated and non-irradiated adult foreskin-derived skin cells. Keratinocyte donors used for solar irradiation treatment were S1174F (male, age 22), S1175F (male, age 48), and S1192F (male, age 64). Reticular fibroblast donors used for solar irradiation were S1141F (male, age 40), S1074F (male, age 28), and S1192F (male, age 64). Each sample (N) was performed in triplicate (n) and represented as mean ± SEM. Statistical difference determined by one-way ANOVA with Tukey's post-hoc test. ns $p>0.05$; N=3, n=9 per cell type. Image source: Hanna *et al.* (2019)

3.3.2 Sensitive detection of mtDNA strand breaks in H_2O_2/solar radiation treated human primary skin cells

Treatment of both human skin derived keratinocytes and fibroblasts by either hydrogen peroxide (H_2O_2) or solar simulated radiation (see 2.2.2) induced mtDNA strand breaks at significantly detectable levels, as determined by the modified 11kb qPCR assay. Relative to untreated cells there is approximately 16–36 fold (2^4–2^6) greater damage and this was not due to unequal amounts of starting mtDNA. The simultaneous housekeeping mtDNA and nDNA PCR assays not only confirmed equal loading of mtDNA in the assay, but that the treatment did not alter mtDNA content in relation to the nuclear gene. It is of interest that a similar degree of damage is induced in both skin types by both H_2O_2 and solar simulated light.

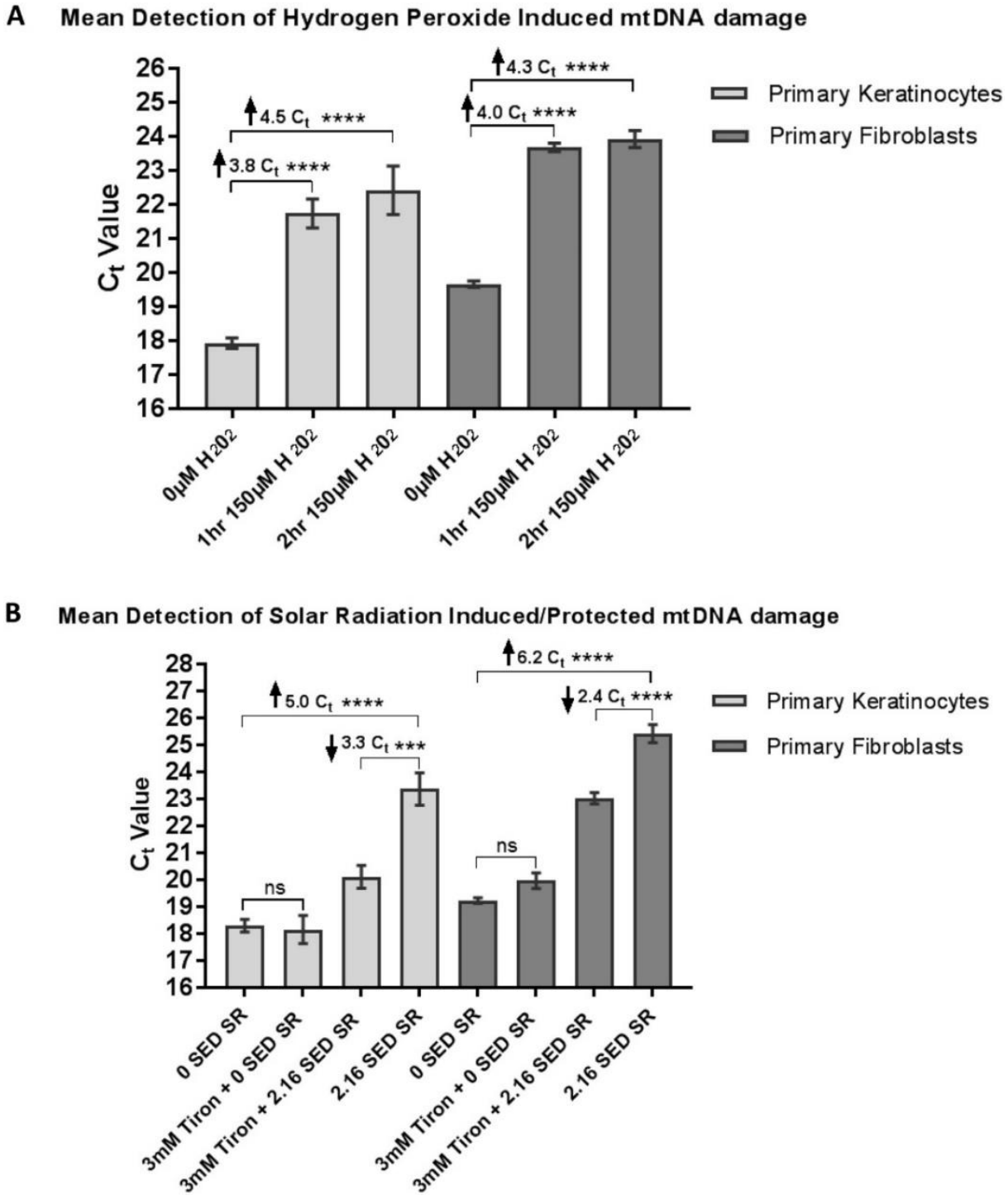

Figure 3-7: Detection of H_2O_2 (A) or solar radiation (B) induced mtDNA damage in human primary skin cells. Results generated from the DNA of three adult foreskin-derived keratinocyte or reticular fibroblast donors (N), treated with 150μM H_2O_2 (A) or 2.16 SED (standard erythema dose) complete solar simulated radiation (B). A dose of 2.16 SED is estimated to be the equivalent of 2 hours in the Mediterranean sun at noon during the summer months as an SED is 100 Joules per square meter. In addition, detection of mtDNA protection is demonstrated thorough pre-incubation with a mitochondria-permeable compound Tiron (PBS vehicle); Graph B). Keratinocytes donors used for H_2O_2 treatment were S1074F (age 28), S1083F (age unknown), and S1082F (age unknown). Keratinocyte donors used for solar irradiation treatment were S1174F (male, age 22), S1175F (male, age 48), and S1192F (male, age 64). Reticular fibroblast donors used for H_2O_2 treatment were S1073F (male, age 65), S1076F (male, age unknown), and S1075F (male, age unknown). Reticular fibroblast donors used for solar irradiation were S1141F (male, age 40), S1074F (male, age 28), and S1192F (male, age 64). Each sample (N) was performed in triplicate (n) and represented as mean ± SEM. Statistical difference determined by one-way ANOVA with Tukey's post-hoc test. **** $p < 0.0001$, *** $p = 0.0001$, ns $p > 0.05$; N=3, n=9 per cell type. Image source: Hanna *et al.* (2019)

3.3.3 11kb assay 16-32 times more sensitive than 1kb assay at detecting H_20_2-induced mtDNA damage in skin cells

To determine the increased sensitivity of amplifying an 11kb sized amplicon relative to 1kb, the same keratinocyte and fibroblast DNA samples were run on both assays consecutively. Figure 3-8 demonstrates there was approximately 4 C_t (16-fold) more damage detected by fibroblasts DNA in the 11kb assay, and approximately 5 C_t (32-fold) more in the keratinocyte DNA.

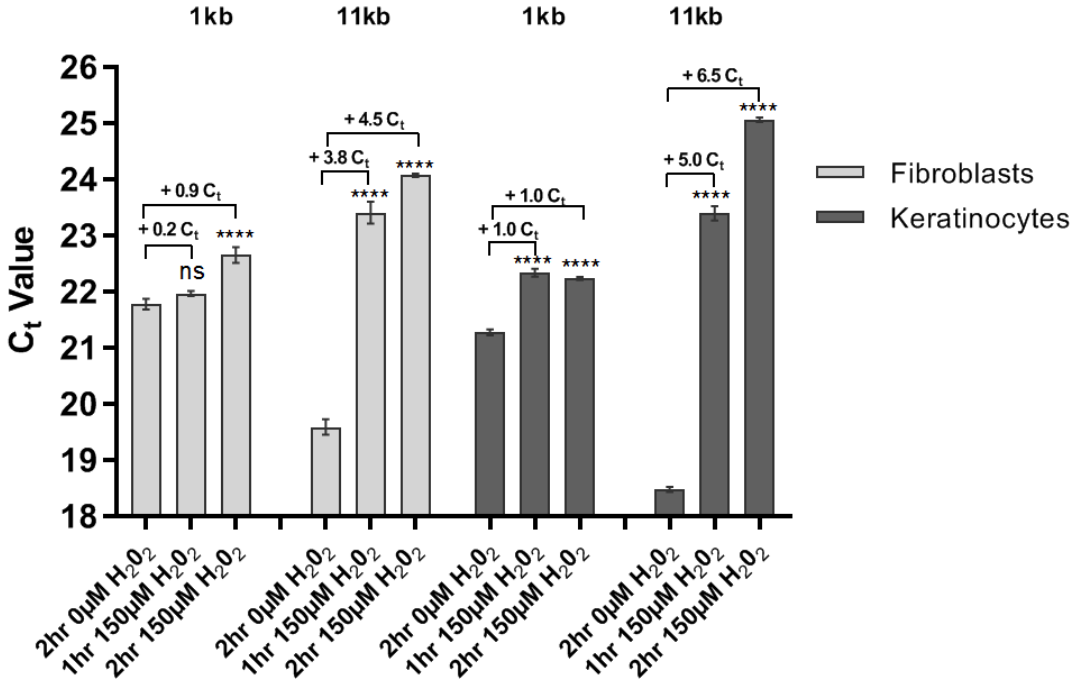

Figure 3-8: Comparison of 1kb and 11kb sensitivity in mtDNA detection. Detection of H_2O_2 induced mtDNA damage in human foreskin-derived skin cells is enhanced 16-32 fold with 11kb mtDNA amplicon, compared to <2-fold when an 1kb mtDNA region is amplified. Mean ± SD data generated from the DNA of adult foreskin-derived keratinocytes (S1075F - male, age unknown) or adult foreskin-derived reticular fibroblasts (S1073F - male, age 65). Each donor was treated with 0 or 150μM H_2O_2 for 1 or 2 hours. Statistical difference determined by one-way ANOVA with Tukey's post-hoc test. **** $p < 0.0001$, ns $p > 0.05$; N=1, n=3 per data point.

3.4 Discussion

This method improved on previously published versions of the 11kb assay arising from the Mark Birch-Machin research group (Ray *et al.*, 2000; Passos *et al.*, 2007), whilst adapting the method to a new qPCR machine. Firstly, there was a substantial 76% reduction in the amount of starting DNA (from 50ng to 12ng (per well)) and 60% reduction in reaction volume (from 50µl to 20µl). This was verified by standard dilution curves and melt curve analysis (Figures 3-2 and 3-3). This benefits applications where clinical samples are small and the DNA amount is limiting for multiple analysis, or where the economy of small sample volumes permits larger screening. Standard curves were used to determine qPCR efficiency for each primer pair, where 100% would equate to an amplicon product doubling per cycle (Taylor *et al.*, 2010). The dilutions where this occurs lie within the linear dynamic range and determines the optimal amount of starting template (ng) to use. Whilst a 10-fold dilution series is favoured in the literature, we used a 2-fold approach because the linear range for large amplicons is narrow. For this 11kb amplicon, the region of high efficiency (93.5%) spanned only 10-50ng and reduced to 62% outside this range. The 11kb standard curve data was indistinguishable when performed simultaneously on DNA from different cell types (primary or cell line). Whilst primers were reconstituted and diluted in IDTE buffer, the final EDTA concentration supported primer integrity without diminishing amplification. A direct comparison with PCR grade water was found to disrupt primer integrity over time, causing primer dimerization with melt temperatures of 79-80^{o}C. However IDTE buffer produced consistent 11kb products without artefact, observed as a single melt temperature peak of 84^{o}C.

The second improvement ensured equal mtDNA content within the context of total DNA samples through the simultaneous amplification of two small mtDNA specific amplicons from different regions of the mitochondrial genome as well as one from the single copy nuclear β2M gene. The use of these regions and their amplification conditions were verified by appropriate standard curves (Figure 3-6). The comparable C_t values obtained from both mtDNA specific regions (Fig. 3-6(D)) provided reassurance that the regions are not damaged or co-amplifying from nDNA (Malik *et al.*, 2011). Detecting mtDNA relative to nDNA eliminates dilution bias and validates C_t changes detected by the 11kb assay. A comparative C_t analysis ($2^{\Delta\Delta Ct}$) determines the fold difference between mtDNA and nDNA levels of untreated and treated samples. To avoid dilution error, the same diluted sample is used for sequential runs of housekeeping and 11kb assays.

The method primers can be experimentally used with DNA from any human tissue. An application of this methodology is demonstrated in detection of mtDNA damage following the separate treatment of human primary skin cells by hydrogen peroxide and solar simulated

radiation. Assay sensitivity is demonstrated through a 16–36 fold increase in detection of induced mtDNA strand breaks relative to untreated fibroblasts and keratinocytes (Figures 3-7 and 3-8). Figure 3-8 demonstrates that damage is present throughout the mtDNA genome, whereby amplifying an 11kb portion detects a lot more damage than a 1kb portion. Tiron was used to demonstrate localised mtDNA protection as it is a potent chelator, free radical scavenger, and mitochondrial membrane permeable (Yong *et al.*, 2012). Tiron pre-incubation correlated with a significantly reduced C_t value in both cell types, indicative of localised protection against solar radiation induced mtDNA damage (Figure 3-7).

Whilst the use of solar irradiation is an environmental stressor specific to skin, excess H_2O_2 is a bi-product of oxidative stress in an abundance of internal tissues (Halliwell *et al.*, 2000) and confirms the application of this optimised assay to study cell types particularly subjected to oxidative stress.

3.5 Summary of findings

- Optimisation of a long-range qPCR assay reduced starting DNA by 76% and reaction volume by 60%. Small clinical samples (ng) can now be screened.
- This assay amplifies 11kb of the 16.5kb human mitochondrial genome (mtDNA), and required additional cycles to produce the same number of amplicons if there is damaged mtDNA in the sample
- Long amplicons greatly increase the sensitivity of damage detection across mtDNA
- Mitochondrial DNA is a wide-ranging biomarker of oxidative stress, and these primers can be used in any human cell/tissue type
- The primers are specific to human mtDNA, so a total DNA sample can be used and both genomes can be analysed in the same sample (nDNA with a different assay)
- Housekeeping assays were additionally optimised to ensure that there is not mtDNA copy number variation between the total DNA samples
- Examples of oxidative stress induced damage detection are shown through H_2O_2 and solar simulated light treatment in human skin cells. Protection against damage was shown by pre-incubation with Tiron antioxidant.
- This methodology was published in *Mitochondrion* journal (Hanna *et al.*, 2019)

Chapter 4: Antioxidant (AOX) testing in acellular and human skin cell model systems

4.1 Chapter overview and aims

Commercial AOXs tetrahydrocurcumin (THC) and pterostilbene (PTERO) were tested for their capacity to protect the mtDNA of human skin cells from solar radiation (see 2.2.2). The aim was to investigate if in-house pilot data from Dr Matthew Jackson in human skin cell lines was reproduced in primary adult foreskin-derived keratinocytes/reticular fibroblasts, and how variable the response was between donors. The effect of solar radiation on acellular AOXs was also investigated to determine their photo-stability. These pre-incubation experiments are a direct application of the assay developed in Chapter 3, whereby a more damaged population of mtDNA will take additional qPCR cycles to amplify a large portion of intact mtDNA genomes. The positive control for the qPCR assay (Chapter 3) is a potent AOX/chelator called Tiron, which was used in all cell types as it crosses the mitochondrial membrane to act at the site of ROS production.

4.2 Chapter specific methods

4.2.1 AOX absorbance of UV-visible light using spectrometry

Absorbance of AOXs in UV-visible light (190-800nm) was detected using a Varian Cary 300 Bio UV-visible spectrophotometer with Cary WinUV software (Agilent Technologies). Samples were poured into a glass quartz dish for 2.16 SED solar irradiation (or foil protection; see 2.2.2), before immediate transfer to cuvette for analysis.

4.2.2 Making up AOXs and dosing cells

Tetrahydrocurcumin (THC; SabiWhite® 96%, SABINSA EUROPE) and pterostilbene (PTERO; PteroWhite® 90%, SABINSA EUROPE) were stored as dry powder and light protected at 4^{o}C. Tiron (product 89460, Sigma) was stored at room temperature in dry powder form. For experimental dosing, AOX stock solutions of 268mM THC and 234mM PTERO were made with 100% DMSO solvent, and 300mM Tiron with PBS solvent. All stock solutions were mixed by vortex until completely dissolved, and light protected within tinfoil. Working AOX solutions were prepared by diluting THC/PTERO 1:4000 or Tiron 1:100 with cell specific medium to obtain the experimental concentrations outlined in Table 4.1.

Cells were seeded into 3.2cm^2 dishes and adhered overnight. At 70-80% confluency, they were washed twice with PBS and dosed with AOX (Table 4-1), no AOX or 0.025% DMSO vehicle. They were incubated for 6 or 24 hours prior to being washed twice with PBS and irradiated as

outlined in 2.3.2. The incubation timepoints were recommended by GSK to obtain data surrounding the duration of protection, with consideration for future product application.

				Experimental Dose		
Compound	CAS No.	Derivative/Analog	Mw (g/Mol)	% (w/v)	µM	mg/ml
Tetrahydrocurcumin	36062-04-1	Curcumin	372.4	0.0025	67.0	0.025
Pterostilbene	537-42-8	Stilbenoid	256.3	0.0015	58.5	0.015
Tiron	270573-71-2	Vitamin E	314.2	0.944	3000	944

Table 4-1: AOX compound experimental doses

4.2.3 Trolox equivalent antioxidant capacity assay - FRAP

All buffers and reagents were stored at room temperature unless stated. Sodium acetate buffer (0.2M; pH 3.2) was prepared with sodium acetate trihydrate (57670, Sigma) in ddH_2O, and 40mM HCL was diluted from 12M stock in ddH_2O. On the day of experiment the following were prepared: 10mM TPTZ (4, 6,-tri [2-pyridyl]-s-triazine, Sigma) was prepared in 40mM HCL, and dissolved in a 50^oC waterbath. 20mM $FeCl_3$ was prepared from ferric chloride (FeCl3.6H_2O, Sigma) in ddH_2O.

Trolox standards and AOX stocks were prepared at 10X higher concentration, to account for the assay dilution factor. Consequently, Trolox (10mM) was dissolved in ddH_2O, pH adjusted to 7.2, and diluted to the following standards with ddH_2O: 0.5, 0.25, 0.125, 0.0625, 0.031, 0.016mM. As Niacinamide (NAM) is water soluble, 14.3mM (1600µg/ml) was prepared to obtain a 1.43mM experimental concentration. However to ensure the final vehicle concentration of THC/PTERO was 0.1%, 27mM THC (1mg/ml) and 23.5mM PTERO (600mg/ml) were each solubilised in 100% EtOH and then diluted 1:1000 with ddH_2O. Unlike the monolayer experiments in 4.2.2, EtOH was used instead of DMSO as AOX solvent because it is known to not affect the FRAP assay. There have been no historical differences seen in this research group between the use of DMSO or EtOH as an AOX solvent, as long as the final concentration is as low as possible (≤0.1%). The following combinations were tested simultaneously: THC, PTERO, THC+PTERO, NAM, NAM+THC+PTERO, 0.1% EtOH vehicle, and water vehicle. In addition, PTERO and NAM+THC+PTERO solutions were made in duplicate with half irradiated at 2.16 SED (see 2.3.2).

To prepare FRAP working solution, 25ml sodium acetate buffer (0.2M) was combined with 2.5ml TPTZ (10mM) and 2.5ml $FeCl_3$ (20mM). Using a clear, flat bottomed 96 well plate, 30µl Trolox standard, AOX or vehicle control were added to each well, followed by 270µl FRAP reagent and mixed. A duplicate plate was performed with 270µl ddH_2O in lieu of FRAP. Each condition was assayed in triplicates per plate (n=3), incubated for 30 minutes at room

temperature, and absorbance read at 592nm on a SpectraMax 250 (Molecular Devices). Three technical repeats were performed (N=3).

Raw data were blank corrected to their water or 0.1% EtOH vehicle control, and the mean of condition replicates calculated. Trolox equivalent (µM/ml) was extrapolated from the Trolox standard curve on the corresponding 96 well plate (within linear range R^2>0.95). The mean ± SD Trolox equivalent of three technical repeats was calculated for each AOX.

4.2.4 Aqueous One Cell Proliferation Assay (MTS)

Viability of treated cells were assessed using MTS (Promega) as per manufacturer's instructions. Cells were incubated with MTS in phenol red-free complete DMEM for 4 hours at 37^{o}C, 5% CO_2. Absorbance was read at 490nm using a SpectraMax 250 (Molecular Devices).

4.2.5 Data analysis of mitochondrial DNA protection

Mitochondrial DNA protection data was generated by the methods outlined in Chapter 3 for the 11kb and housekeeping assays. All samples for each donor were included on one qPCR plate, with housekeeping qPCR performed immediately beforehand to ensure equal starting levels of mtDNA across diluted samples.

Statistical analysis was performed with reference to Yuan *et al.* (2006) and performed on raw C_t values, whereby all non-irradiated controls were first grouped as a control column. Each donor was analysed individually. A one-way ANOVA with Tukey's post-hoc test was used to determine significance.

To generate a graph, C_t differences for each donor were converted to relative fold change ratio ($2^{\Delta Ct}$) and presented as mean±95% confidence intervals. The mean of controls was first subtracted from each treated condition ($\Delta C_t = \Delta C_{t\ (treated)} - \Delta C_{t\ (control)}$). In addition, the mean ± SD of grouped donor C_t values were used to illustrate variation and overall trend.

4.3 Results

4.3.1 AOX photo-stability test post 0, 2, 4, 6 or 8 SED complete solar irradiation: THC, PTERO, combination and Tiron

To determine the effect of solar irradiation on AOX photo-stability, each test compound was diluted in distilled water, irradiated in a dose dependent manner (0-8 SED) and analysed consecutively with a UV-VIS photo spectrometer (190-800nm; see 4.3.1). THC, PTERO, THC/PTERO 1:1 combination and Tiron were solubilized and diluted to the doses used for cell monolayer experiments (with water used in lieu of cell medium).

As seen in Figure 4-1 no AOXs absorbed in the visible light spectrum (400-800nm), and irradiation had no effect on Tiron or THC. The Tiron absorbance peak spanned UVB 275-291nm, and THC at the UVC-UVB border 279nm. However, whilst non-irradiated pterostilbene absorbed at the UVB-UVA border 316nm, all irradiated samples had a different absorbance peak at UVC (261nm) with a minimal secondary UVA peak (357nm). The irradiated THC and PTERO combination appear to merge/synergise around 279nm, with an increase in absorbance from ~0.4Abs to ~0.75Abs. In all cases the absorbance increased with increasing irradiation dose, and the vehicle did not have an absorbance value.

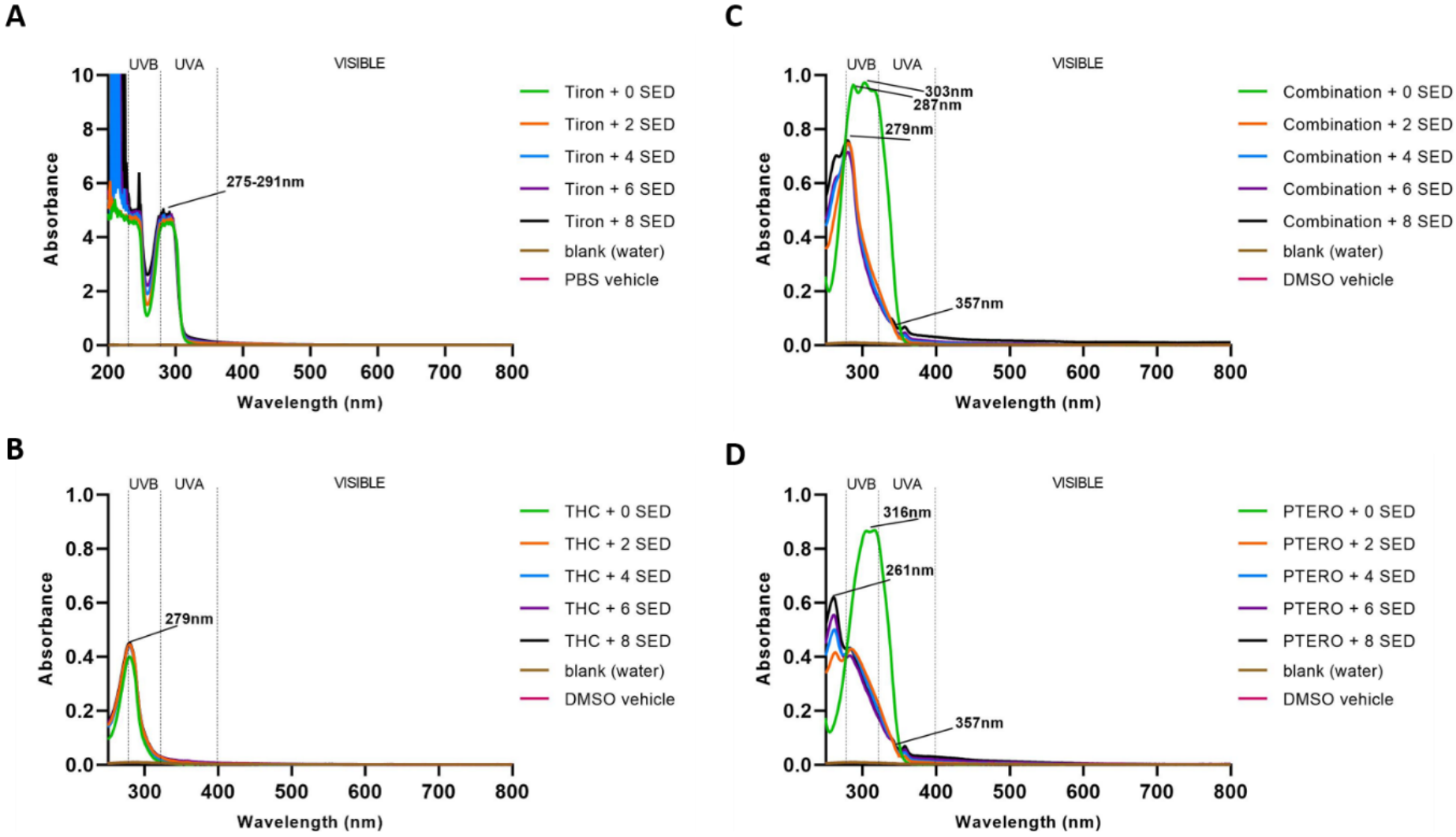

Figure 4-1: Antioxidant absorbance (Abs) within UV-VIS (190-800nm) light spectrum. Tiron (A; PBS solvent), tetrahydrocurcumin (B, DMSO solvent), pterostilbene + tetrahydrocurcumin combination (C; DMSO solvent) and pterostilbene (D; DMSO solvent), post solar irradiation with 0, 2, 4, 6 or 8 SED. The sterile distilled water diluent (ddH_2O), PBS and 0.025% DMSO vehicles did not absorb UV-VIS light. Traces were blank corrected to ddH_2O.

4.3.2 The effect of solar irradiation on AOX capacity using Trolox Equivalent FRAP assay

As PTERO was not photostable (Figure 4-1), the functional capacity of irradiated and non-irradiated AOXs was tested in a Trolox Equivalent FRAP assay by Miss Agalya Amalanathan (undergraduate student). PTERO was tested as non-irradiated and irradiated with 2.16 SED solar simulated light. In addition a combination of PTERO, THC and NAM was irradiated, to represent the AOXs that would be combined in formulation. NAM was water soluble but lacked ferric reducing capacity and tested negative in this assay. PTERO and THC were EtOH soluble, but both 0.1% EtOH and water vehicles gave the same 592nm absorbance value of approximately 0.1. EtOH was used instead of DMSO because it is known to not affect the assay, and no historical difference has been seen in this research group between the use of DMSO or EtOH as an AOX solvent, as long as the final concentration is as low as possible (ideally ≤0.1%). The AOX doses vary between compounds because the goal was not to compare their relative scavenging capacities, but rather represent their experimental doses in monolayer experiments (Chapter 4) and in test formulation (Chapter 6). NAM was included because GSK test formulations (Chapter 6) include this AOX, but this wasn't known during the design of earlier monolayer experiments.

The purpose of this experiment was to compare non-irradiated and irradiated samples. PTERO reducing capacity decreased only marginally upon irradiation. Whilst THC had a high AOX capacity, this was not significantly reduced when combined with PTERO and NAM, or when irradiated.

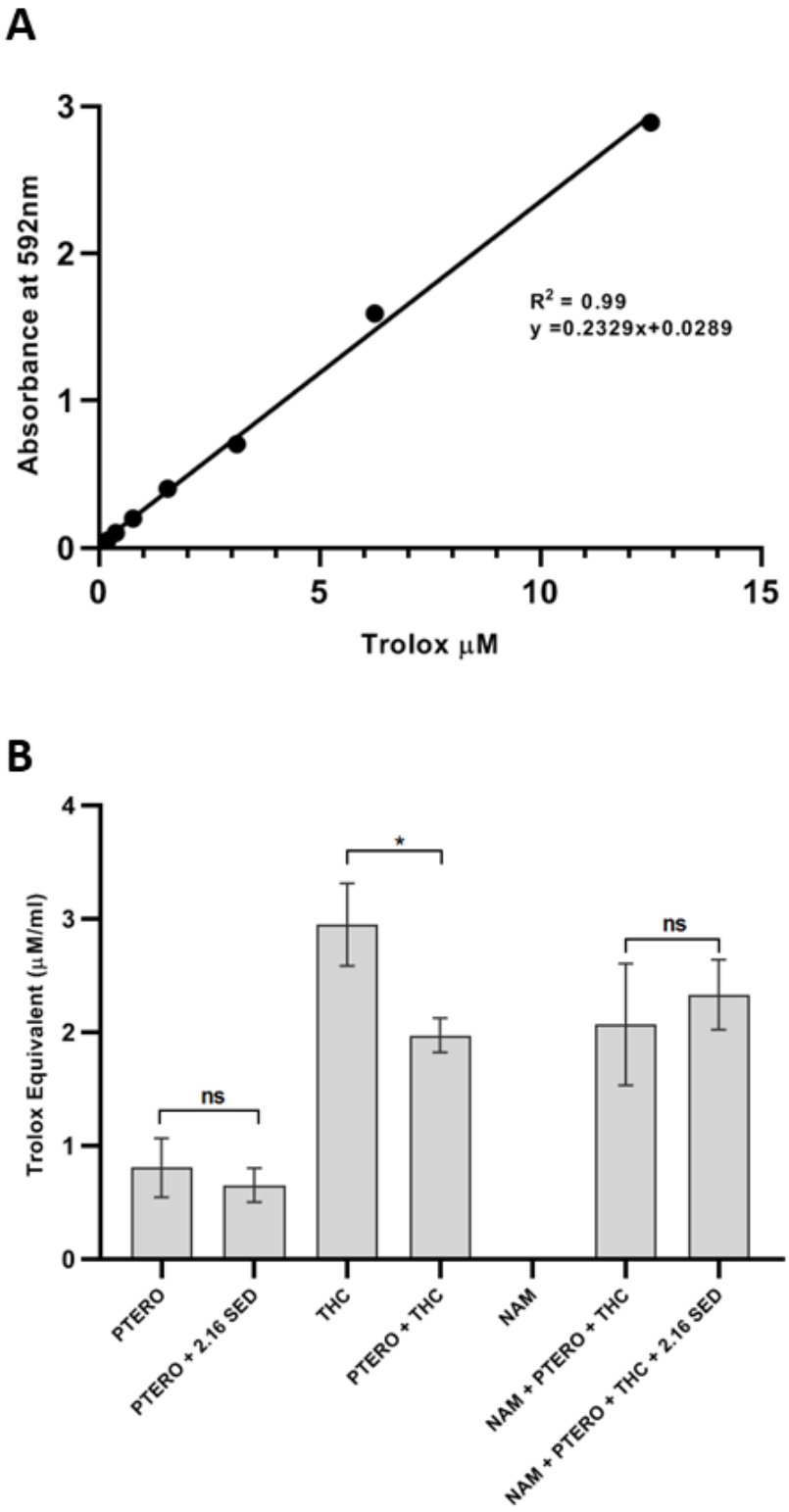

Figure 4-2: AOX capacity using Trolox Equivalent FRAP assay. A) Trolox Equivalent value was extrapolated for each AOX from a Trolox standard curve, where the linear range lay between 0.78-12.5μM. Sample absorbance at 525nm was blank corrected to 0.1% EtOH or water vehicle. B) The AOX concentrations are 16μM tetrahydrocurcumin (THC), 39μM pterostilbene (PTERO), and 1.3mM niacinamide (NAM). Irradiation performed as in 2.2.2 with a dose of 2.16 SED, whereby 1 standard erythemal dose (SED, J.m-2) is equivalent to an erythemal radiant exposure of 100 J.m-2. Mean ± SD, N=3, n=9. Statistical difference determined by unpaired two-tail Welch's t-test, *p=0.03, ns>0.05

4.3.3 NMR of tetrahydrocurcumin (THC) determined stock is stable for years

When THC protective effects were no longer observed in some fibroblast donors, NMR was performed at GSK (Weybridge, UK) to eliminate degradation as a causative factor. When more THC stock was required, a comparison was made between the original (3+ year) and new stock powders (Figure 4-3). GSK analysis determined minimal difference, with both samples representing pure THC.

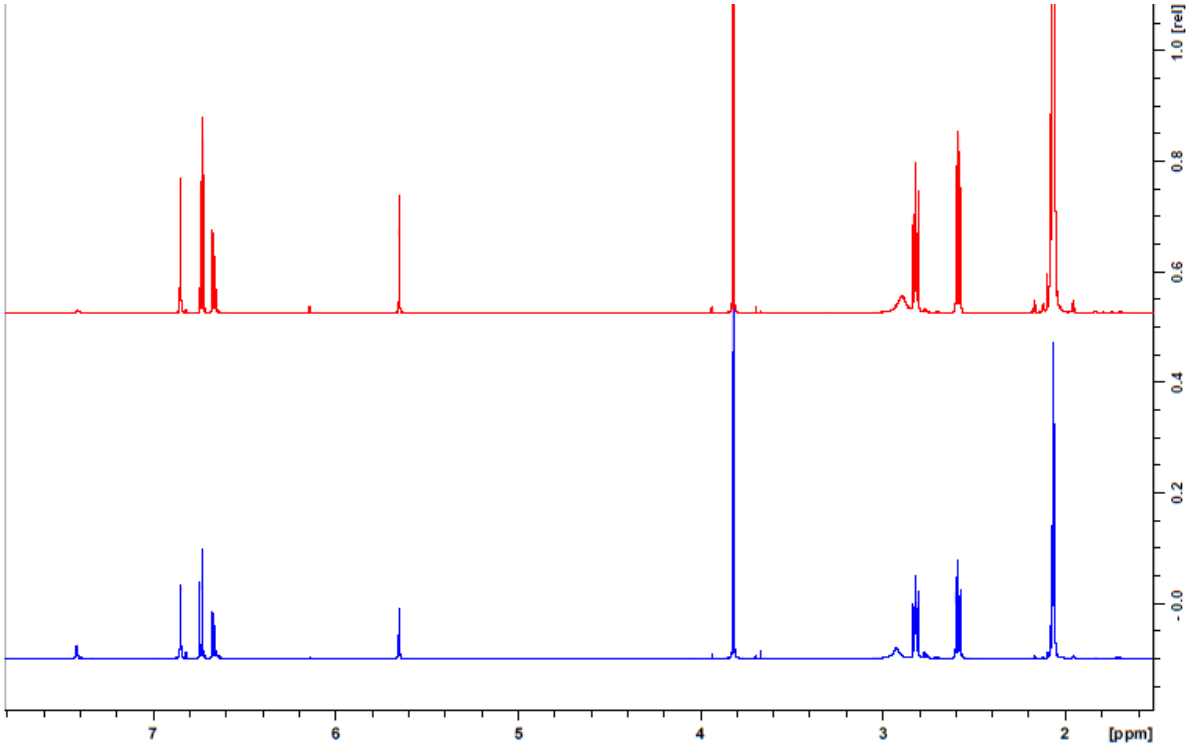

Figure 4-3: Comparative NMR of two tetrahydrocurcumin (THC) dry powder stocks. Samples were analysed at GSK. Negligible difference was seen between 3+ year old stock (blue) and a purchased re-supply (red), indicative of stability over time when stored light protected at 4ºC.

4.3.4 Determination of optimal H_2O_2 and solar irradiation doses for human foreskin-derived adult keratinocytes and reticular fibroblasts

The MTS viability assay was used to determine the optimal H_2O_2 dose for adult foreskin-derived keratinocytes and reticular fibroblasts, in order to damage mtDNA without inducing apoptosis (Figure 4-4). Previous in-house data demonstrated that 1 hour is an optimal time to incubate with H_2O_2 for the purposes of inducing mtDNA damage that can be detected by qPCR assay (chapter 3). For keratinocyte donors, a significant reduction in viability was induced with ≥300µM H_2O_2, whereas for reticular fibroblast donors this was ≥750µM H_2O_2. From this data a conservative dose of 150µM H_2O_2 was selected to induce mtDNA damage in both cell types. A dose response for solar simulated irradiation was not performed, as 2.16 SED was previously optimised as an in-house dose for human skin cell monolayer cultures.

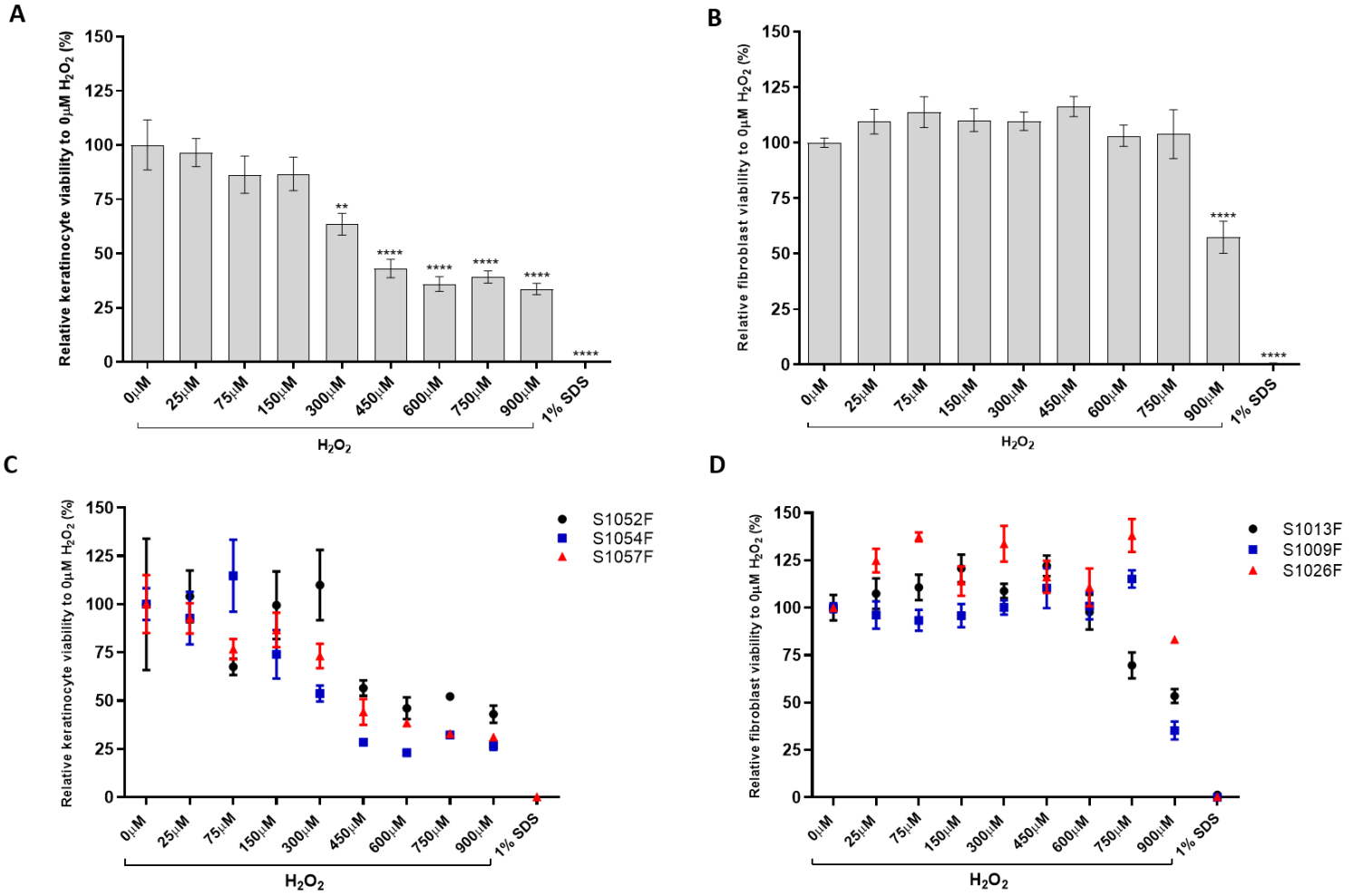

Figure 4-4: Dose response viability of human foreskin-derived adult keratinocytes and reticular fibroblasts to H_2O_2 treatment. Skin cells were incubated with H_2O_2 for 1 hour with viability calculated relative to 0µM H_2O_2. Keratinocytes viability significantly reduced ≥300µM H_2O_2 (A), and reticular fibroblasts ≥900µM H_2O_2 (B). There was donor variability in sensitivity to H_2O_2 treatment. Mean ± SEM data generated from three adult donors per cell type: A/C) S1052F – male, age 53, S1054F – male, age 27, S1057F – male, age 51; B/D) S1013F – male, age 51, S1009F – male, age 50, S1026F – male, age unknown. 1% SDS provided positive control cell death in both cell types. Statistical difference to 0µM H_2O_2 determined by one-way ANOVA with Dunnett's post-hoc test. ****p< .0001, **p=.002, ns p>.05; N=3, n=12

4.3.5 Determining optimal AOX and vehicle doses for human foreskin-derived adult keratinocytes and reticular fibroblasts

The MTS viability assay was used to determine the optimal AOX and vehicle dose for adult foreskin-derived keratinocytes and reticular fibroblasts (Figure 4-5). Dose ranges were based around previously obtained GSK data in skin cell lines. Viability was maintained in both cell types in all tested conditions except keratinocytes + 6mM Tiron. A dose of 58.5µM PTERO and 67µM THC were selected for experiments of both cell types. On the basis of the keratinocyte data, fewer conditions were tested on reticular fibroblasts. A 0.025% DMSO vehicle was acceptable for both cell types. A positive control of 3mM Tiron was selected for its localised mtDNA protection as published by Oyewole *et al.* (2014), although retrospectively a lower dose of ~1-1.5mM would have been preferable for keratinocytes to ensure there was no pro-oxidant activity. However the inclusion of Tiron in these experiments is only a control measure to ensure the qPCR assay is detecting mtDNA damage.

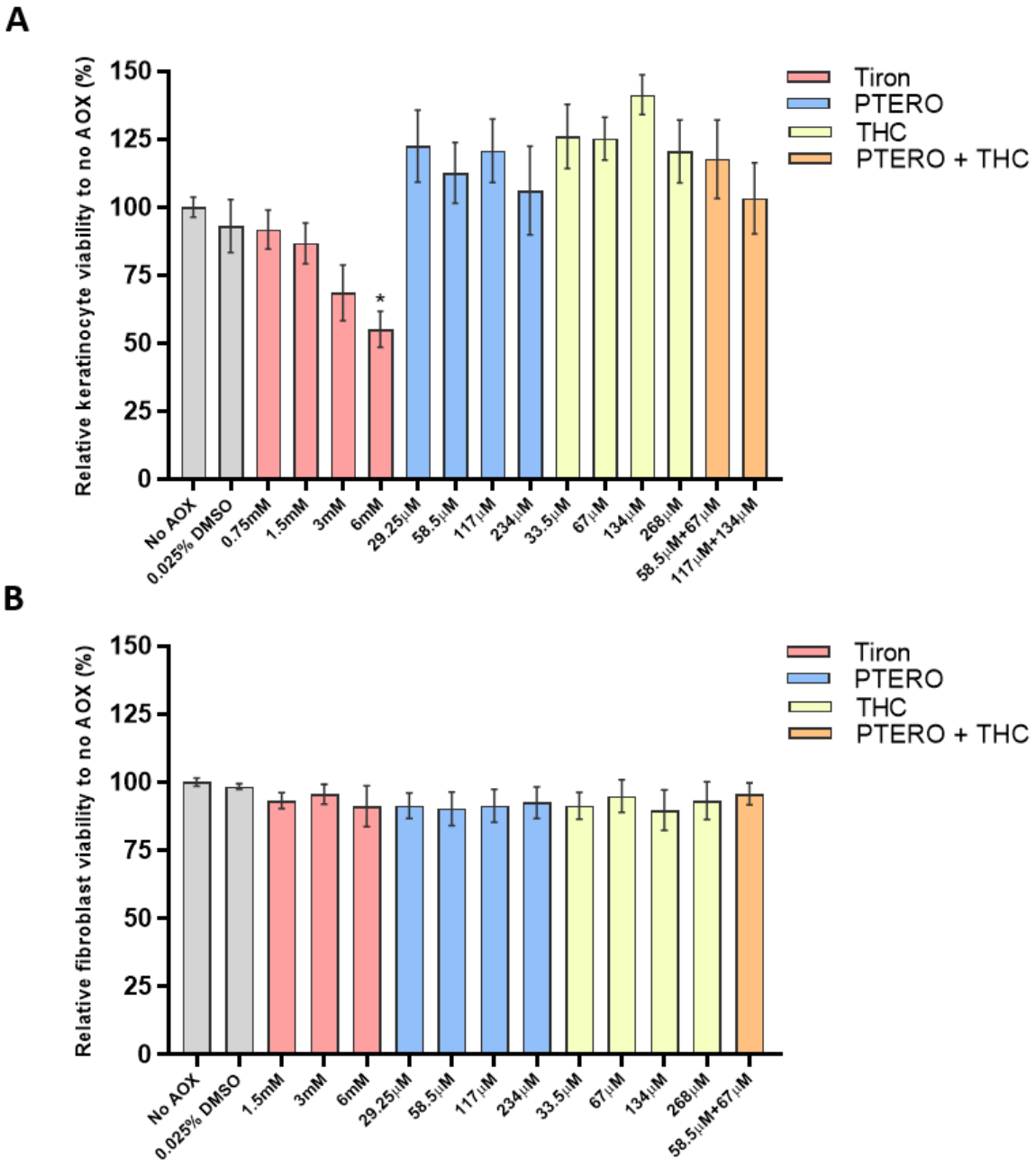

Figure 4-5: Relative viability of human foreskin-derived adult keratinocytes and reticular fibroblasts after 24-hour incubation with AOX or DMSO vehicle. Skin cells were incubated for 24 hours with dose(s) of DMSO vehicle, Tiron, pterostilbene (PTERO), tetrahydrocurcumin (THC), or PTERO/THC 1:1 combination. Relative viability of both cell types was maintained at all experimental doses except for keratinocytes with 6mM Tiron. Mean ± SEM data generated from three adult donors per cell type: A) S1215F – male, age 49, S1223F – male, age 50, S1224F – male, age 76, and B) S1202F – male, age 85, S1194F – male, age 48, S1196F – male, age 40. Statistical difference to no AOX determined by one-way ANOVA with Dunnett's post-hoc test. *=.002, ns p>.05; N=3, n=9

4.3.6 Determining the capacity of AOX pre-incubation to protect human foreskin-derived adult cell monolayers from solar light induced mtDNA damage

The 11kb qPCR assay described in Chapter 3 was used to determine if AOXs tetrahydrocurcumin (THC) and pterostilbene (PTERO) could protect human foreskin-derived cells from solar simulated radiation induced mtDNA damage. The housekeeping mtDNA qPCR assay (Chapter 3) confirmed equal loading of mtDNA, and that the treatments did not alter mtDNA content. Adult male foreskin donors of various ages were used to isolate epidermal keratinocytes, differentiated keratinocytes and dermal reticular fibroblasts. The cells were incubated for 6- or 24-hours with AOXs, with these timepoints recommended by GSK to obtain data surrounding the duration of protection, with consideration for future product application.

4.3.6.1 *Human foreskin-derived adult keratinocytes pre-incubated with THC or PTERO were not protected from solar light induced mtDNA damage*

Human keratinocytes (basale-like) derived from four adult foreskin donors were pre-incubated for 6 hours (Figure 4-6) and 24 hours with THC or PTERO and irradiated with 2.16 SED solar light. Neither test compound protected mtDNA, but the positive control Tiron protected all donors. The mtDNA of non-irradiated cells were unaffected by AOX or vehicle incubation and were grouped as controls for data analysis. Protection was also not seen with 24 hours pre-incubation (data not included).

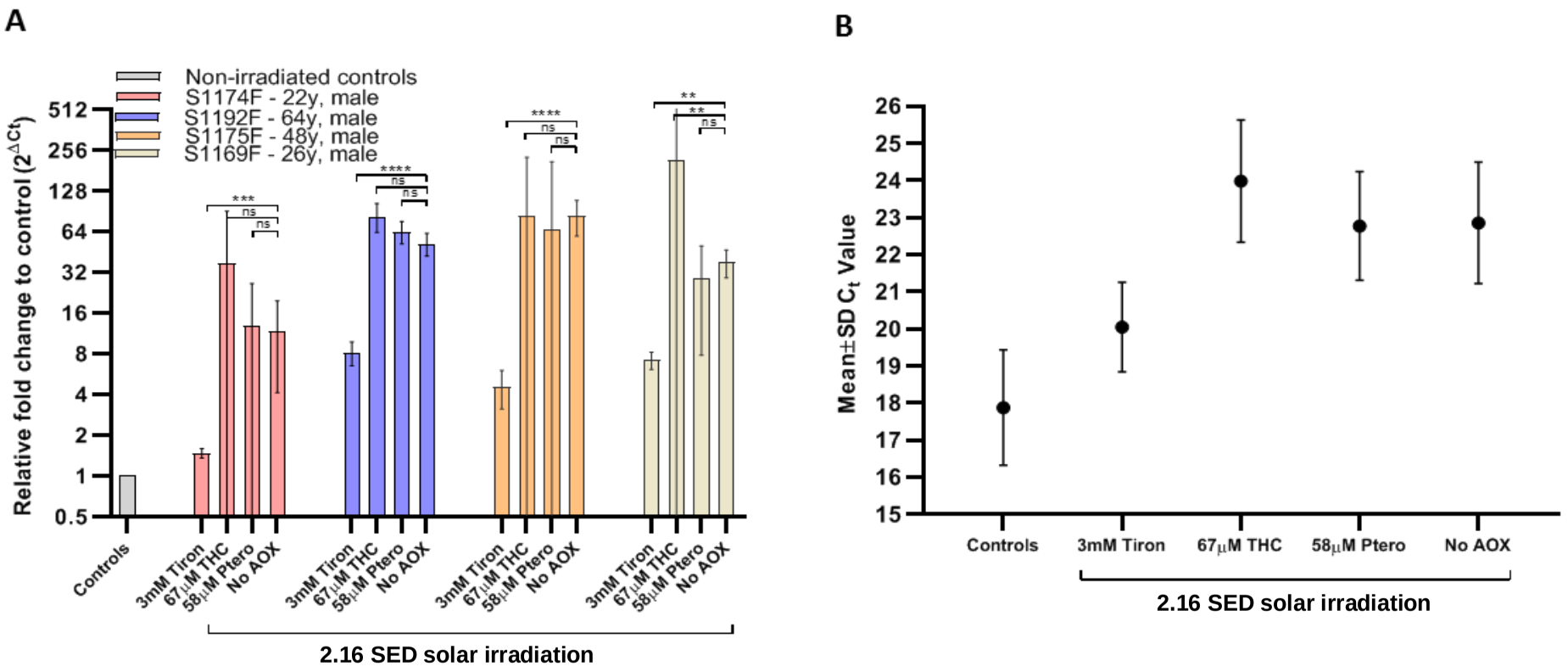

Figure 4-6: Human foreskin-derived adult keratinocytes pre-incubated with THC or PTERO for 6 hours were not protected from mtDNA damage induced by 2.16 SED complete solar irradiation. Relative fold change to grouped non-irradiated controls for each donor (A; mean ± 95% CI, N=1, n=3). Irradiation performed as in 2.2.2 with a dose of 2.16 SED, whereby 1 standard erythemal dose (SED, J.m-2) is equivalent to an erythemal radiant exposure of 100 J.m-2. Statistical difference for each donor determined by one-way ANOVA with Tukey's post-hoc test on raw C_t value data. Overall trend and donor variation represented by grouped raw data, whereby a higher C_t corresponds to greater mtDNA damage (B; C_t value ± SD, N=4, n=12). ****p<.0001, ***p<.001, ** p>.001, ns p>.05

4.3.6.2 *Human foreskin-derived adult differentiated keratinocytes pre-incubated with THC or PTERO were not protected from solar light induced mtDNA damage*

Human differentiated keratinocytes (spinosum-like) derived from four adult foreskin donors were pre-incubated for 6 hours (Figure 4-7) and 24 hours with THC or PTERO and irradiated with 2.16 SED solar light. Overall neither test compound protected mtDNA, although there was significant protection in one donor (S1194F – male, age 48) who had a much larger damage baseline than other donors. The method of differentiating keratinocytes means they are no longer a monolayer culture, and the mtDNA proportion damaged by 2.16 SED is relatively low at ~4-fold. The same results were seen with positive control Tiron, which also showed protection only for the S1194F donor. The mtDNA of non-irradiated cells were unaffected by AOX or vehicle incubation and were grouped as controls for data analysis.

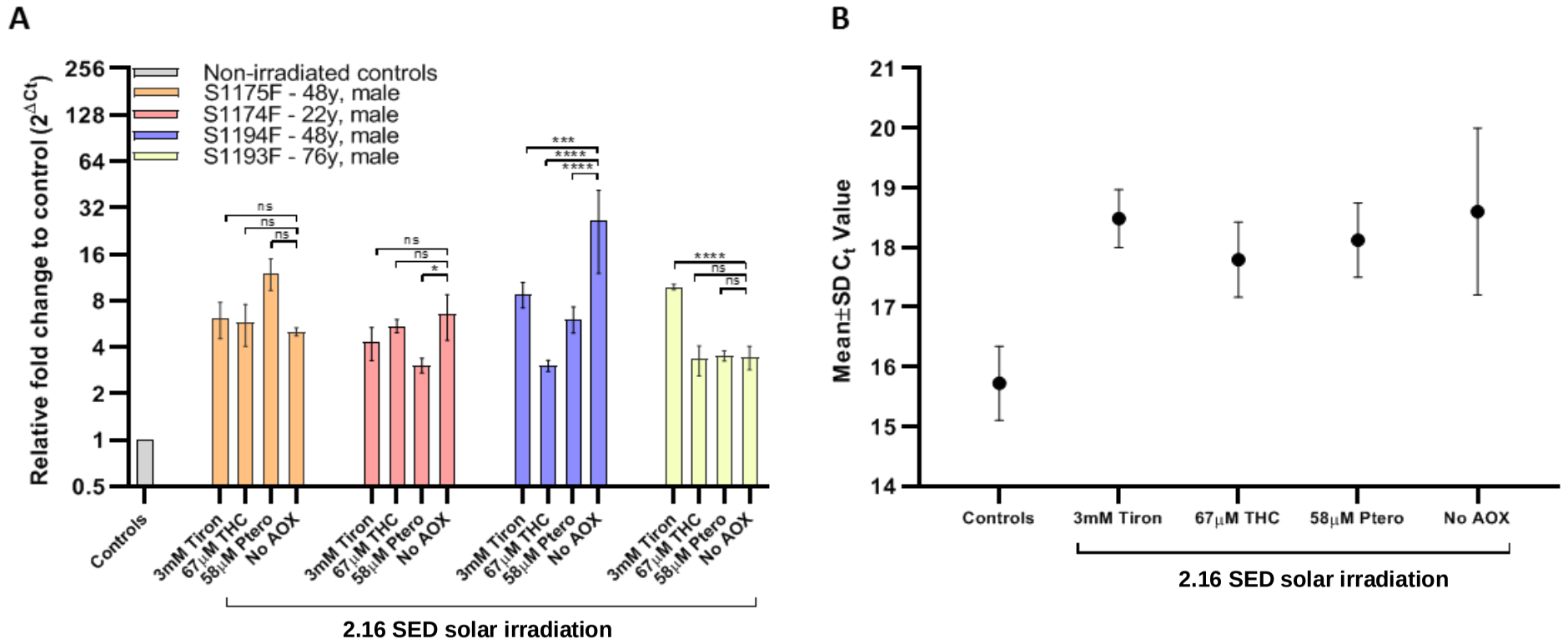

Figure 4-7: Human foreskin-derived adult differentiated keratinocytes pre-incubated with THC or PTERO for 6 hours were not protected from mtDNA damage induced by 2.16 SED complete solar irradiation. Relative fold change to grouped non-irradiated controls for each donor (A; mean ± 95% CI, N=1, n=3). Irradiation performed as in 2.2.2 with a dose of 2.16 SED, whereby 1 standard erythemal dose (SED, J.m-2) is equivalent to an erythemal radiant exposure of 100 J.m-2. Statistical difference for each donor determined by one-way ANOVA with Tukey's post-hoc test on raw C_t value data. Overall trend and donor variation represented by grouped raw data, whereby a higher C_t corresponds to greater mtDNA damage (B; C_t value ± SD, N=3, n=12). ****p<.0001, ***p<.001, * p>.01, ns p>.05

4.3.6.3 *Human foreskin-derived adult reticular fibroblasts pre-incubated with THC (but not PTERO) were protected from solar light induced mtDNA damage*

Human dermal fibroblasts derived from three adult foreskin donors were pre-incubated for 6 hours (Figure 4-8), 12 hours and 24 hours with THC or PTERO, and irradiated with 2.16 SED solar light. Both THC and positive control Tiron protected 2 of 3 donors, although donor S1168F (male – age 33) had a lower damage baseline. Donor S1074F (male – age 28) had significant protection for both THC and pterostilbene, but also a high damage baseline. Protection for all antioxidants except Tiron was no longer seen at 12 hour and 24 hours (data not included). The mtDNA of non-irradiated cells were unaffected by AOX or vehicle incubation and were grouped as controls for data analysis.

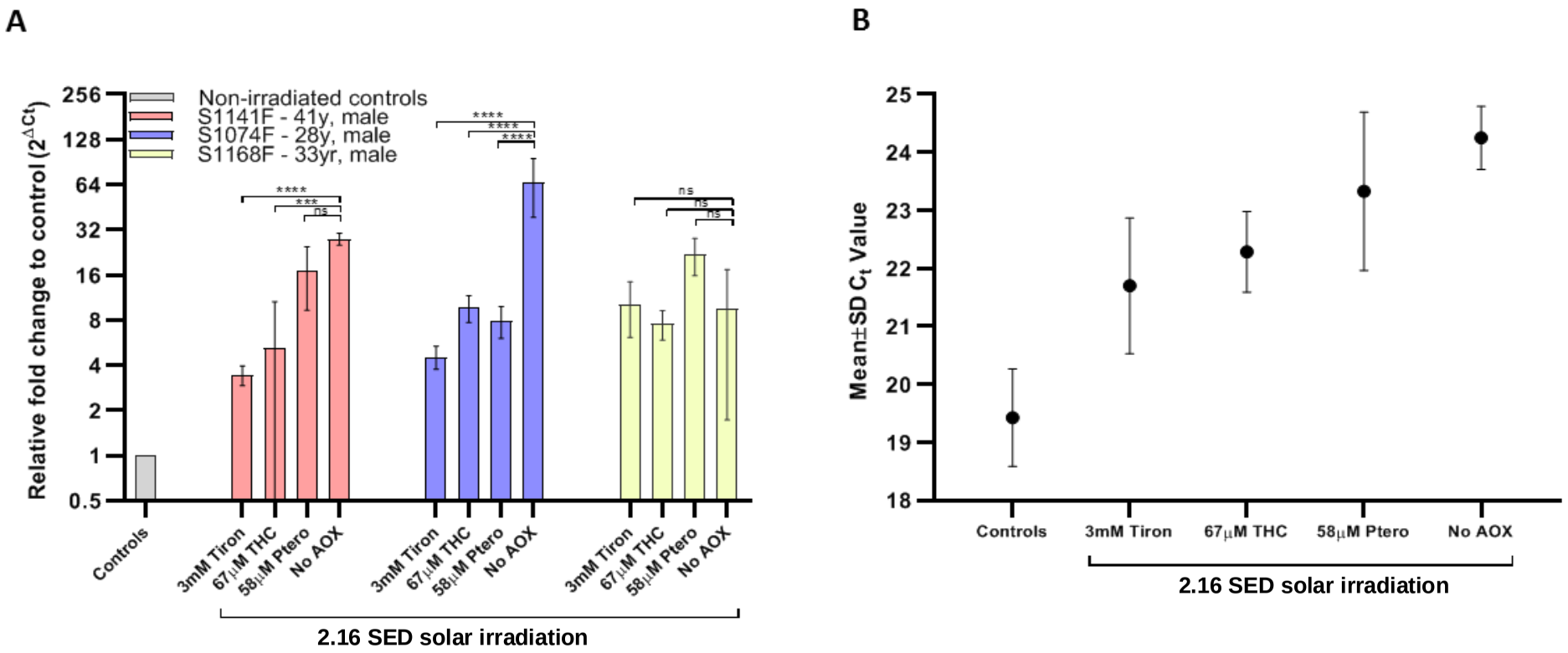

Figure 4-8: Human foreskin-derived adult reticular fibroblasts pre-incubated with THC (but not PTERO) for 6 hours were protected from mtDNA damage induced by 2.16 SED complete solar irradiation. Relative fold change to grouped non-irradiated controls for each donor (A; mean ± 95% CI, N=1, n=3). Irradiation performed as in 2.2.2 with a dose of 2.16 SED, whereby 1 standard erythemal dose (SED, J.m-2) is equivalent to an erythemal radiant exposure of 100 J.m-2. Statistical difference for each donor determined by one-way ANOVA with Tukey's post-hoc test on raw C_t value data. Overall trend and donor variation represented by grouped raw data, whereby a higher C_t corresponds to greater mtDNA damage (B; C_t value ± SD, N=3, n-9). ****p<.0001, ***p<.001, ns p>.05

4.3.6.4 *Human foreskin-derived adult reticular fibroblasts pre-incubated with THC and PTERO combination were protected more from solar light induced mtDNA damage*

Human dermal fibroblasts derived from three adult foreskin donors were pre-incubated for 6 hours (Figure 4-9) with THC or THC+PTERO combination and irradiated with 2.16 SED solar light. Both THC, THC+PTERO combination and positive control Tiron protected 2 of 3 donors. Both THC+PTERO combination and Tiron gave similarly high levels of protection. The THC+PTERO combination protected mtDNA greater than THC alone. The protective effects seen with THC were consistent with those seen in Figure 4-8, confirming that this result were reproduced in 4 of 6 donors overall. The mtDNA of non-irradiated cells were unaffected by AOX or vehicle incubation and were grouped as controls for data analysis.

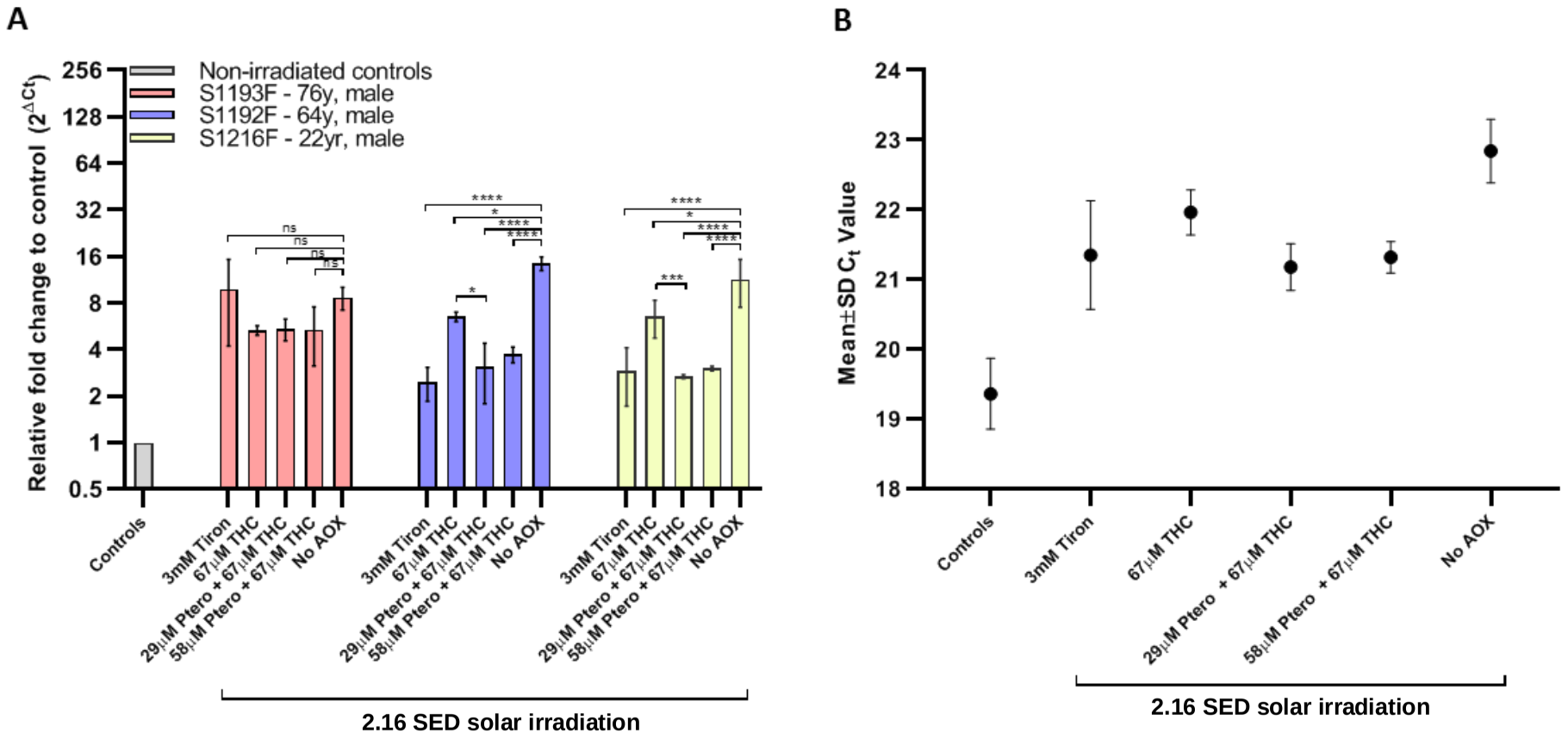

Figure 4-9: Human foreskin-derived adult fibroblasts pre-incubated with THC and PTERO combination for 6 hours received greater mtDNA protection than THC alone, when exposed to 2.16 SED complete solar irradiation. Relative fold change to grouped non-irradiated controls for each donor (A; mean ± 95% CI, N=1, n=3). Irradiation performed as in 2.2.2 with a dose of 2.16 SED, whereby 1 standard erythemal dose (SED, J.m-2) is equivalent to an erythemal radiant exposure of 100 J.m-2. Statistical difference for each donor determined by one-way ANOVA with Tukey' s post-hoc test on raw C_t value data. Overall trend and donor variation represented by grouped raw data, whereby a higher C_t corresponds to greater mtDNA damage (B; C_t value ± SD, N=3, n=9). ****p<.0001, ***p<.001, *p>0.01, ns p>.05

4.4 Discussion

Curcumin and resveratrol are widely published and recognised AOXs, yet their synthetically enhanced derivatives tetrahydrocurcumin (THC) and pterostilbene (PTERO) are significantly less investigated. There are no publications on the mtDNA effects of these compounds, a potent biomarker of ageing and damage in tissues such as skin. In this chapter commercial AOXs tetrahydrocurcumin (THC) and pterostilbene (PTERO) were tested for their capacity to protect the mtDNA of human skin cells from solar irradiation. The aim was to investigate if in-house pilot data from Dr Matthew Jackson in human skin cell lines was reproduced in primary adult foreskin-derived keratinocytes/reticular fibroblasts, and how variable the response was between donors. The effect of solar light on acellular AOXs was also investigated to determine their photo-stability. These pre-incubation experiments are a direct application of the assay developed in Chapter 3, whereby a more damaged population of mtDNA will take additional qPCR cycles to amplify a large portion of intact mtDNA genomes. As such, Tiron (a potent chelator) was used as an experimental positive control in all cell types.

THC and PTERO were tested acellularly for AOX scavenging capacity and photo-stability in solar simulated light. Throughout the literature, absorbance traces of AOXs in the UV-visible light range are commonplace. Sirerol *et al.* (2015) also report PTERO absorbance in the UVB range (275, 290, 305nm; 1mM), yet the effect of solar light on the stability and chemical structure of AOXs is rarely reported. This is an important consideration for the efficacy and safety of AOXs included in skin products as the consumer will be exposed to daylight. It was evident that PTERO irradiated with complete solar light was not photostable (Figure 4-1), which supports a similar finding by Silva *et al.* (2013) who found the amount and rate of trans-resveratrol degradation was highest after exposure to the combined UV-VIS (200-600nm) spectrum, rather than UV (254nm) or VIS (≥365nm) in isolation. In addition, they reported that the conversion to intermediates (e.g. cis-resveratrol) was proportionate to the solar light intensity, which loosely compares to Figure 4-1 where peak height increased with irradiation dose (2-8 SED). To hypothesize the structure of the PTERO photoproduct that absorbed at 262nm/376nm (Figure 4-1), Dr Robert Lucas of GSK produced a diagram depicting a possible chemical reaction in supplementary chapter 9.2.4 which suspects PTERO conversion to a pro-oxidant via production of ROS. It is extremely likely that the mechanism of action/efficacy of PTERO would be reduced, unless formulated encapsulated (e.g. within liposomes (Sirerol *et al.*, 2015)) or with sunscreen UV filters. The irradiated AOXs were tested in the FRAP assay and no difference between non-irradiated counterparts were found. However Sirerol *et al.* (2015) concurred with others in the literature that resveratrol/pterostilbene are not iron chelators and had weak radical scavenging capacity when tested with the 2,2′-Azino-bis(3-

Ethylbenzothiazoline-6-Sulfonic Acid) (ABTS) enzymatic assay which measures how strongly an AOX can quench ABTS radicals. This infers that PTERO functions involve a biological mechanism, and therefore the intracellular effect(s) of a photo-modified PTERO remains an open question. Nevertheless, it is worth noting that encapsulated antioxidants such as liposome-PTERO have shown remarkable protective effects against the production of skin cancer tumours in UVB treated hairless mice (Sirerol *et al.*, 2015). Further considerations for AOX formulation and whole skin application are discussed in Chapter 6.

To investigate if pilot data AOX pre-incubation could protect foreskin-derived adult skin cells from solar light induced mtDNA damage, THC and PTERO were tested with three or four donors of basale-like proliferative keratinocytes, spinosum-like differentiated keratinocytes or reticular fibroblasts. It wasn't feasible to donor-match the skin cell types for monolayer experiments, although this a prioritised factor for human skin equivalents in chapter 5. The experiments were performed at 6- and 24-hour time-points, with protective effects seen at 6-hours in some donors (Figures 4-6 to 4-9). Although both derivatives are more stable than their respective curcumin/resveratrol, it is likely the polyphenol antioxidants had completely metabolised by 24-hours through cutaneous phase II metabolic enzymes (Manevski *et al.*, 2015; Kosuru *et al.*, 2016).

No protection was seen with either AOX in foreskin-derived adult keratinocytes (0 of 4 donors; Figure 4-6), and protection was seen with both AOXs in 1 of 4 donors of differentiated spinosum-like keratinocytes (Figure 4-7). THC (but not PTERO) protected foreskin-derived adult reticular fibroblasts from 2 of 3 donors, but a combination gave greater protection in reticular fibroblasts from a further 2 of 3 donors (Figures 6-8, 6-9). A study by Trivedi *et al.* (2017) pre-incubated a human foreskin fibroblast cell line (HFF-1) with 0.1-1µg/ml THC and found they were protected from apoptosis when stressed with 200mJ/cm^2 (20 SED) UVB. Whilst the protective effects correlate with our findings, a dose of 20 SED is experimentally effective but not translational to real-world skin exposure. As such the biologically targeted qPCR assay shows how fibroblasts have protected mtDNA from an equivalent dose of 2-hours Mediterranean sun exposure (2.16 SED), without the induction of apoptotic pathways. In addition it was surprising that they reported a toxicity dose of 10µg/ml THC for HFF-1 cell line, when primary fibroblasts still had ~100% viability when dosed with 268µM (718 µg/ml) THC (Figure 4-5). This raises uncertainty about the use of HFF-1 cell line for experiments of this nature, suggesting that there are functional differences in HFF-1 and HDF cells. Costa-Almeida *et al.* (2015) directly compared the behaviour of HFF-1 and HDF fibroblasts in endothelial cell co-culture for their capacity to influence the formation of capillary-like structures. Despite both populations being foreskin-derived fibroblasts, HFF-1 fibroblasts failed

to secrete extracellular matrix (ECM) proteins (e.g. collagen I) necessary for this purpose. However it was interesting that Trivedi et al., (2017) reported that the culture medium of 1µg/ml THC-treated HFF-1 cells had higher levels of extracellular matrix proteins (collagen, elastin and hyaluronic acid), and enhanced wound healing response to scratch-test.

The data in Figures 6-8 and 6-9 demonstrate an enhanced protection of mtDNA in skin fibroblasts when PTERO was combined with THC (but not alone), which appears indicative of two different mechanisms of action in these skin cell types. It suggests that THC may work in a manner related to mitochondria, and the effects of PTERO indirectly enhance these effects. Kosuru *et al.* (2016) reviews the proposed mechanisms of action of PTERO, with emphasis on its recognised anticancer effects. Although most studies were performed on cancer cell lines or mouse models, there are recurrent suggestions that PTERO (like many polyphenols) helps to upregulate endogenous antioxidant enzymes via activation of the NRF2 pathway (Kosuru *et al.*, 2016; Dinkova-Kostova & Abramov, 2015). This pathway is synonymous in skin research for its role in the suppression of solar UV photo-damage (Rojo de la Vega *et al.*, 2017). A recent study by Zhou *et al.* (2019) investigated the role of PTERO on the NRF2 pathway in a keratinocyte cell line (HaCaT) that they stressed with arsenic. They found a dose of 60µM PTERO significantly reduced HaCaT viability using the MTT assay, yet this was not seen in foreskin-derived adult keratinocytes from three different donors when dosed with ≥200µM PTERO (Figure 4-5). Zhou *et al.* (2019) reported PTERO increased mitochondrial membrane potential and upregulated mitochondrial enzymes, which together decreased cellular ROS levels. These findings correlate with the studies outlined in two review articles of PTERO mechanisms of action (Kosuru *et al.*, 2016; Chen *et al.*, 2017). A resonating point from Kosuru *et al.* (2016) is that a low concentrations of PTERO drove protective anti-oxidant effects, and that high concentrations had a pro-oxidant effect by increasing ROS as a means of inducing apoptosis and preventing carcinogenesis. Whilst the doses of AOXs used in Figures 6-5 to 6-9 were selected for being high (but non-toxic), a lower dose of PTERO was included in Figure 6-9 to investigate if this in-fact had a greater protective effect. As halving the dose did not enhance or diminish the protective effects seen in Figure 6-9, future studies on AOX efficacy should aim to find the lowest effective dose.

Similar to PTERO and resveratrol, much of the mechanistic literature available for THC, curcumin and curcuminoids study their role in cancer or ischemic injury. The proposed mechanisms of action are similar to PTERO, as well as emphasis on a low dose for AOX effect. To investigate the antiproliferative effects of THC in relation to the cell-cycle, Ayli *et al.* (2010) used doses of 50-200µM THC on 18mJ/cm^2 (1.8 SED) UVB treated foreskin-derived neonatal keratinocytes. Their THC doses roughly correlate with the 67µM THC used in this thesis on

foreskin-derived adult keratinocytes. Whilst this study does not address mechanisms outside of the cell-cycle, it does confirm that the antiproliferative effects reported in other models also extends to skin keratinocytes. It also reproduced some data by Dujic *et al.* (2007) who reported UVA or VIS photoactivation of low level curcumin in HaCaT keratinocyte cell line was required to stimulate antiproliferative effects. This is a consideration for product design and future work, whereby photoactivation of AOXs would be protected against by the presence of UV filters.

Current literature does not mention mtDNA in relation to either THC or PTERO, nor their combination. Whilst some information exists relating to mechanisms of action that affect mitochondrial activity and redox pathways, the protection of skin fibroblast mtDNA from solar light induced damage is novel and worthy of future study.

4.5 Summary of findings

- THC and PTERO absorbed UVB, but PTERO was not photostable upon irradiation with solar simulated light (UV-VIS-IR; see 2.2.2)
- The FRAP assay was insufficient at determining the functional difference between intact and photo-modulated PTERO
- AOX powders remained stable for years when stored light-protected at 4^{o}C
- Human foreskin-derived adult keratinocytes/reticular fibroblasts had variable levels of sensitivity to AOX dose and damage stimulus (e.g. H_2O_2). Overall, fibroblasts were more robust than keratinocytes.
- Human foreskin-derived adult keratinocytes pre-incubated with THC or PTERO for 6 hours were not protected from mtDNA damage induced by 2.16 SED complete solar irradiation
- Human foreskin-derived adult differentiated keratinocytes pre-incubated with THC or PTERO for 6 hours were not protected from mtDNA damage induced by 2.16 SED complete solar irradiation
- Human foreskin-derived adult reticular fibroblasts pre-incubated with THC (but not PTERO) for 6 hours were protected from mtDNA damage induced by 2.16 SED complete solar irradiation
- Human foreskin-derived adult reticular fibroblasts pre-incubated with THC and PTERO combination for 6 hours received greater mtDNA protection than THC alone, when exposed to 2.16 SED complete solar irradiation
- Protective effects were not seen for any cell type when pre-incubated with THC and PTERO for 24 hours (data not included)

Chapter 5: Development of a full thickness human skin equivalent

5.1 Chapter overview and aims

CELLnTEC Advanced Cell Systems AG (Switzerland) produce commercial media for the development of full thickness human skin equivalents, with ingredients endogenous to the human cellular environment, and elimination of scaffold materials. This system was trialled with in-house donor-matched keratinocytes and fibroblasts from adult foreskin donors. The primary aim of this chapter was to characterise this model, compare it to a commercial model (Labskin™), and assess its suitability for various experiments. Pilots were designed to determine where the commercial protocol could be flexible, e.g. scaling model size or tissue site. A secondary aim was to investigate the use of facial cells in lieu of traditional foreskin derived cells and determine the degree of influence that tissue site has on the models produced.

5.2 Chapter specific methods

5.2.1 Human skin equivalents: full thickness and scaffold-free

5.2.1.1 *Model establishment*

Human skin keratinocytes and fibroblasts were isolated and cultured from foreskin and facial skin samples as outlined in section 2.1.

Skin models were grown according to the CELLnTEC online protocol (http://CELLnTEC.com/wp-content/uploads/pdf/FT_Skin_Model_Protocol.pdf) using CELLnTEC specialist medium (CnT-PR, CnT-PR-F, and CnT-PR-FTAL) alongside ThinCert™ 0.4µm PET transparent hanging inserts (see Table 5-1). Media was thawed at 4°C, light protected and aliquoted into 50ml tubes. If surplus to experimental requirements, these were stored at -20°C and thawed as required at 4°C. Light protected media aliquots were warmed briefly at room temperature before use and free from antibiotics/antifungals.

Cell densities and medium volume were scaled according to size and outlined in Table 5-1.

Insert / Plate size	Insert surface area (mm^2)	Volume inside insert (µl)	Volume outside insert (µl)	Fibroblasts per insert	Keratinocytes per insert	Greiner Insert Code
24 well	33.6	350	700	14,000	35,000	662640
12 well	113.1	1000	2000	50,000	120,000	665640
6 well	452.4	2000	4000	200,000	840,000	657640

Table 5-1: Cell seeding densities and media volume as scaled for 24, 12 and 6 well CELLnTEC skin models

In order to donor-match epidermal and dermal layers, cryopreserved keratinocytes were thawed approx. 7-10 days prior to seeding onto the fibroblast dermal layer.

Models were raised to the air liquid interface using CELLnTEC 12-well spacer plates (CnT-SP), or single use Greiner ThinCert™ 6 well (657110) or 12 deep well plates (665110). For 24-well models' inserts were placed inside 12-well inserts and raised as for 12-well plates. As ThinCert™ plates have increased depth (e.g. 4ml volume/12 well), media was reduced to 'half feeds' (i.e. 2ml was replaced per well).

At all stages empty wells were filled with the same volume of PBS to prevent unequal evaporation.

5.2.1.2 *Model harvest*

Models were generally quartered, with two quadrants embedded in OCT and/or paraffin blocks for histology and the others snap-frozen in liquid nitrogen before storage at -80^{o}C.

5.2.2 Epidermal skin equivalent

As cryopreserved keratinocytes are not routinely used for in-house equivalents, they were additionally seeded for reconstructed epidermis (RHE) models according to an in-house published method (Forrester *et al.*, 2014). Keratinocytes (1x10^{6}/model) were seeded into 12mm 0.4µm PCF inserts (Millipore) placed in 6-well plates. EpiLife™ medium was as outlined in section 2.1, but additionally supplemented with 0.22µm sterile filtered 1M $CaCl_2$ (PBS diluent; Sigma) to a final calcium concentration of 1.5mM. The equivalents were maintained overnight in high calcium medium, before grown at the air-liquid interface for 14 days in high calcium medium freshly supplemented with 0.22µm sterile filtered 5µg/ml ascorbic acid (ddH_2O diluent; Sigma). Media was changed three times weekly.

5.2.3 Histology and immunostaining

Human skin biopsies from adult foreskin or facial sites and human skin equivalent models were sandwiched between two biopsy foam pads, placed within tissue embedding cassettes (~1mm^2 holes), and fixed overnight in 10% formalin (Sigma). The small cassette holes ensured tissue was not lost during processing/embedding. All tissue processing, paraffin embedding, and sectioning was completed at the Newcastle Molecular Pathology Node, UK.

All OCT embedding and cryosectioning was performed in-house. OCT blocks were stored at -80^{o}C, and cryosections were air-dried for >1 hour before immediate staining or storage for up to 1 month at -20^{o}C.

All non-fluorescent images were acquired at 40X magnification with Leica SCN400 Brightfield Slide Scanner and Autoloader system at Newcastle University Central Biobank, UK. All fluorescent images were acquired at Newcastle Bio-Imaging Unit, UK.

5.2.3.1 *Haematoxylin and Eosin (H&E)*

Some H&E staining was performed at the Newcastle Molecular Pathology Node. In-house staining was performed as follows. Paraffin embedded 5µm sections were baked at 60°C overnight, cooled and passed through 90%, 100% ethanol, Histoclear™ (15 minutes), 100, 90 and 70% ethanol. OCT embedded 7µm sections were air-dried at room temperature for 30mins and rinsed with distilled water. Paraffin or OCT were then incubated with haematoxylin (30 seconds) and eosin (10 seconds), washed with tap water, passed through 70, 90 and 100% ethanol and mounted with DPX (06522, Sigma).

5.2.3.2 *Oil red O (with optional haematoxylin)*

OCT cryosections (10µm) were air-dried at room temperature for 30 minutes. Initial attempts to make Oil red O from powder was time-consuming and provided negative staining. Oil red O solution (0.5% isopropanol; Sigma) was then purchased and used as a single use stain. Slides were rinsed in distilled water (1 minute), fixed in 10% formalin (1 minute) and rinsed in 60% isopropanol before 30-minute incubation in Oil red O solution. They were briefly rinsed in tap water before counterstain in haematoxylin (optional; 15 seconds). They were rinsed in tap water and mounted with Aquatex™ (108562, Sigma).

5.2.3.3 *Fluorescent staining: collagen I, collagen IV, fibrillin, cytokeratin 14*

OCT cryosections (8µm) were air-dried at room temperature for 30mins, rinsed in PBS, fixed in 4% PFA for 10 minutes, and permeabilised in 0.2% Triton X-PBS for 10 minutes. Rabbit and mouse antibody co-staining included 30 minutes blocking in PBS-2% BSA (a9647, Sigma) supplemented with 2% goat serum (G9023, Sigma) and 2% donkey serum (D9663, Sigma). All primary and secondary antibodies were diluted in PBS-2% BSA. For multi-staining rabbit and mouse species, primary antibodies were incubated together humidified overnight at 4°C at the following dilutions: collagen I (1:1000, rabbit, ab34710, Abcam), collagen IV (1:1000, mouse, ab6311, Abcam), fibrillin (1:1000, mouse, mab1919, Millipore), cytokeratin 14 (1:200, rabbit, PA5-16722, Invitrogen – kindly gifted by Dr Pawan Gulati of Newcastle University). Slides were washed 3 x 10 minutes in PBS-T on a rocker at room temperature. Secondary antibodies were incubated together at room temperature for 1 hour as the following dilutions: donkey anti-mouse-Alexa594 (1:2000, A1203, Thermo) and goat anti-rabbit-Alexa647 (1:2000, A21244, Thermo). Slides were washed light protected 3x10minutes in PBS-T, incubated for 15 minutes

in 1µg/ml DAPI (PBS diluent), rinsed in PBS and passed through distilled water to removed salts before mounting with ProLong Fade Diamond (Thermo). After overnight curing the edges were varnish sealed and slides stored light protected at 4°C.

Imaging was performed at Newcastle Bio-Imaging Unit with Dr Glyn Nelson. Initial studies on autofluorescence used Zeiss AxioImager with Apotome, but later changed to Zeiss LSM800 confocal imaging for labelled staining. Negative controls were performed on all imaged samples to test for autofluorescence and non-specific labelling. Zeiss LSM800 images were captured with a 20x (0.8 NA) or a 40x (1.3 NA) lens, running Zen Blue v2.3 software (Zeiss). For multicolour fluorescence each channel was captured sequentially with the following excitation (ex.) /emission (em.) wavelengths: DAPI ex.405nm/em.400-580nm, Alexa Fluor 594 ex.561nm/em. 580-650nm, and Alexa Fluor 647 ex.640nm/em.546-700nm. Pixel density was maintained at Nyquist resolution for optimal imaging conditions. Post-acquisition, 3D stacks were rendered as maximum intensity projections to show the fluorophore distribution throughout the section.

5.2.3.4 *Multiphoton label free imaging of CELLnTEC human skin equivalent*

A 50µm cryosection was rinsed with distilled water and mounted with ProLong Fade Diamond with DAPI (Thermo). Images were acquired by Dr Glyn Nelson of Newcastle Bio-Imaging Unit on a Zeiss LSM880 confocal microscope equipped with non-descanned detection (NDD) on an epi port. For two photon imaging, excitation of DAPI was performed with a Coherent Discovery laser (80 MHz, ~100fs pulses) tuned to 760nm whilst sequential second-harmonic generation (SHG) signal from collagen and sample autofluorescence were excited using the dedicated 1040 nm output line. Emissions were detected using a 445-485nm bandpass for DAPI, 515-525nm bandpass for SHG and 570-610nm bandpass for autofluorescence using NDD detectors.

5.2.4 Protein ELISA: human pro-collagen I, fibronectin and hyaluronan

Medium collected for ELISA was immediately stored on wet ice before storage at -80°C. Samples were thawed on wet ice for protein ELISA analysis of human pro-collagen I (COLA1), fibronectin (FN) and hyaluronan (HA). ELISAs were performed in the lab of Dr Lee Borthwick at Newcastle University using R&D Systems DuoSet ELISA kits DY6220-05, DY3614-05, and DY1918-05. ELISAs were scaled down to half-area 96 well plates (675061, Greiner) with 25µl well volumes. The reagent diluent (RD) for COLA1/FN was 1% BSA-PSA and HA was 5% PBS-Tween. Capture antibodies were diluted 1:100 in PBS and incubated overnight at 4°C. All incubations were on a rocker, and at room temperature unless stated otherwise. All washes were performed using PBS-0.05%Tween (PBS-T) on a Wellwash™ microplate plate washer (Thermo). Plates were blocked in RD for 1 hour and incubated with samples/standard for

2hours. To determine sample dilution, standard curves for each kit standard were performed on suspected high protein samples with a serial 1:4 dilution: neat, 1:4, 1:16: 1:256, 1:1024, 1:4096 and 1:26,382. Sample dilutions were performed in U-bottomed plates and mixed thoroughly on a plate shaker. Samples were diluted in RD: 1:2000 (COLA1/FN) and 1:1000 (HA). Detection antibody was diluted 1:100 in RD and incubated for 2 hours. Streptavidin-HRP was prepared per kit instructions and incubated for 20 minutes in the dark. Substrate Reagent (DY999, R&D Systems) was prepared per kit instructions and incubated for maximum 20 minutes in the dark (checked visually every 5 minutes for colour gradient). Stop solution (1M H_2S0_4) was rapidly applied to prevent saturation, and plates read at 450nm using Filtermax F5 microplate reader with Softmax pro 6 software. The Kit standards were used on every ELISA plate, and each sample/standard was in duplicate.

5.2.5 Western blot: human collagen I

Cell pellets were lysed and quantified as outlined in 2.6. Protein lysate was thawed on ice, prepared with 4X Laemmli sample buffer and denatured at 95^{o}C for 5 minutes. Electrophoresis was performed with the XCell SureLock Mini-Cell System (Thermo). Each protein lysate sample was run in triplicate (10µg/lane) alongside PageRuler Prestained Protein Ladder (10-180kDa; Thermo) on NuPage Novex 4-12% BIS-Tris gel(s) for 40 minutes (200v) with 1X NuPage MES SDS Running buffer (ddH_2O diluent; Thermo) and 500µl NuPage Antioxidant (Thermo). Wet-transfer to PVDF membrane was performed for 1 hour (100v) using Bio-Rad Mini-PROTEAN Tetra System, and cold 1X NuPage Transfer Buffer (1L: 50ml 20X NuPage, 1ml NuPage Antioxidant, 100ml 100% Methanol, 849ml ddH_2O).

Unless stated all washes or incubations were performed whilst rocking at room temperature, with washes performed in 1X TBS-0.1%Tween (TBS-T) buffer for 15 minutes. Membrane was washed and blocked in 5% milk-TBS-T for 1 hour. The blot was cut between 55-70kDa, with the top half incubated overnight at 4^{o}C in collagen I primary antibody (ab34710, Abcam, 1:500 in 1% milk-TBS-T) and the lower half in GAPDH (#2118, Cell Signalling Technologies, 1:10,000 in 5% milk-TBS-T). HRP goat anti-rabbit (peroxidase) secondary antibody was incubated for 1 hour (1:20,000 in 5% milk-TBS-T, Vector Labs). There were three washes in TBS-T after each antibody incubation, before development with Supersignal West Dura ECL Substrate (Thermo) and chemiluminescent imaging on LI-COR Odyssey.

5.3 Results

5.3.1 Pilot study #1: Two donor trial of CELLnTEC full thickness skin model

In the first pilot study, keratinocytes and reticular fibroblasts isolated from two adult foreskin donors (S1073F/S1074F, see Table 2-2) were used to grow donor-matched and scaffold-free full thickness models (12 well size, n=2 per donor). Cells were isolated and expanded as outlined in section 2.1 and switched to CELLnTEC medium when seeded into inserts. The CELLnTEC protocol was followed including omission of antibiotics/antifungals. The fibroblasts had not been frozen and were seeded into inserts as passage number 2 cells with frequent doublings. The keratinocytes had been cryopreserved to ensure low passage number when thawed, expanded in EpiLife™ and seeded onto the dermis layer at day 10 (in Airlift medium). As in-house frozen keratinocytes are not generally used for human skin equivalent models and this was a new methodology, cells were simultaneously seeded for epidermal models according to an in-house established method (supplementary Figure 9.3). The keratinocytes successfully formed full thickness models (Figure 5-1).

Upon completion no contraction was evident and a visible dry stratum corneum was evident. Initial histological assessment are shown in Figure 5-1 which visually compare well to the CELLnTEC promotional image established with neonatal cells from different donors (supplementary Figure 9.3). To determine the layer thickness of online promotional images, CELLnTEC were contacted for scale bar information who stated that the PET membrane is ~10µm (supplementary Figure 9.3). The model histology of both donors shows a keratinised stratified epidermis attached to a thicker dermal layer, and a dermo-epidermal junction is visible (Figure 5-1). The dermis of S1074F (age 28) was markedly thicker than that of S1073F (age 65), which may correlate to age or innate donor variability.

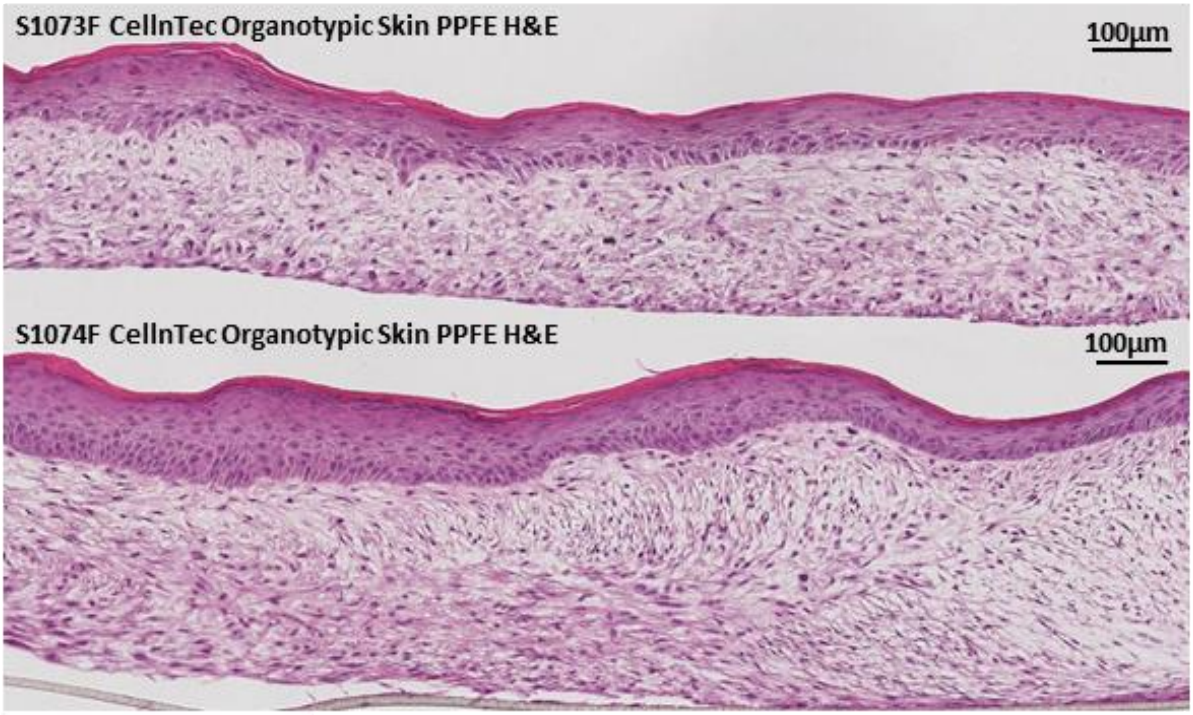

	CellnTec FT Organotypic Skin Model			*Ex-vivo* Adult Human Foreskin		
	Promo Image	**S1073F**	**S1074F**	**S1141F**	**S1142F**	**S1145F**
Stratum Corneum (mm)	0.006	0.005-0.011	0.006-0.017	0.005-0.014	0.07-0.014	0.07-0.015
Epidermis (mm)	0.075	0.042-0.105	0.047-0.117	0.023-0.136	0.069-0.138	0.052-0.138
Dermis (mm)	0.119	0.142-0.210	0.259-0.370	N/A	N/A	N/A
Dermis-Hypodermis (mm)	N/A	N/A	N/A	0.075-0.900	0.455-0.564	0.364-0.500
Total (mm)	0.200	0.189-0.325	0.311-0.505	0.103-1.050	0.594-0.716	0.486-0.653

Figure 5-1: Histological H&E staining of skin equivalents developed using CELLnTEC commercial medium and foreskin-derived adult keratinocytes and reticular fibroblasts. Models grown from foreskin-derived and donor-matched adult keratinocytes and reticular fibroblasts of S1073F (male – age 65) and S1074F (male – age 28). Models have formed a keratinised stratified epidermis attached to a thicker dermal layer. The dermal ECM was secreted by the fibroblasts, without use of an artificial scaffold. A dermo-epidermal junction is visible, and fibroblasts are evident within the dermal layer. Measurements (mm) of stratum corneum, epidermis and dermis have been calculated using the scale bars for both models, alongside the CELLnTEC promotional image (see supplementary Figure 9.3 or CELLnTEC.com) and three ex-vivo whole foreskin donors (S1141F – male, ag 40, S1142F – male, age 17, S1145F – male, age 51; see supplementary Figure 9.4). Identifying where the dermis met hypodermis in ex-vivo whole skin could not be performed confidently by eye, so they were measured together (see 9.2.8). Reference skin from S1073F and S1074F was unavailable. H&E staining was performed on three sections per model from each FFPE and OCT block. Images shown are one FFPE section per donor, with FFPE providing better imaging than OCT.

5.3.1.2 *Optimisation of multicolour immunofluorescence staining protocol*

To characterise the biological relevance of human skin equivalent models, skin biomarkers were optimised for multistaining. Emphasis was placed on extracellular matrix proteins, as the dermal matrix in CELLnTEC models is entirely derived from adult fibroblasts. Optimisation was performed in the stages outlined in Figure 5-2.

Control	Sample preparation	Useful for
Autofluorescence	• Fixation • Permeabilization • Blocking	Analyzation of cellular autofluorescence. Threshold for microscopy in direct IF.
Secondary antibody (only indirect IF)	• Fixation • Permeabilization • Blocking • Secondary antibody • (If desired: nucleus staining)	Unspecific binding of secondary antibody. Threshold for microscopy in indirect IF.
Multicolour IF	• Fixation • Permeabilization • Blocking • Only 1 first antibody • (Indirect IF: secondary antibody) • (If desired: nucleus staining)	Compare single staining to multicolour image: Check for crosstalk of the selected fluorochromes. Check if first antibodies affect each other in epitope binding.

Figure 5-2: Optimisation conditions used for individual and multicolour immunofluorescent (IF) labelling of frozen OCT embedded tissue. Table source: https://www.leica-microsystems.com/science-lab/how-to-prepare-your-specimen-for-immunofluorescence-microscopy/

As skin is highly autofluorescent, a spectral analysis was performed on frozen sections of CELLnTEC models grown from foreskin-derived and donor-matched adult keratinocytes and reticular fibroblasts of S1073F (male – age 65) and S1074F (male – age 28). The effect of fixative (4% PFA, 100% cold acetone, 100% cold methanol, or cold acetone: methanol) was found to have a positive effective on autofluorescence with mild quenching of high signal (data not shown). Whilst skin autofluoresces strongly across the spectrum (with a particularly strong signal in the green region), green region autofluorescence was not as strong as whole skin and could be corrected for with imaging settings. However as seen in Figure 5-3, far red dyes were the best option for human skin equivalents, and 4% PFA fixative was selected for its likelihood to be suitable for many primary antibodies (see supplementary Figure 9.2 which compares fixatives for IF staining).

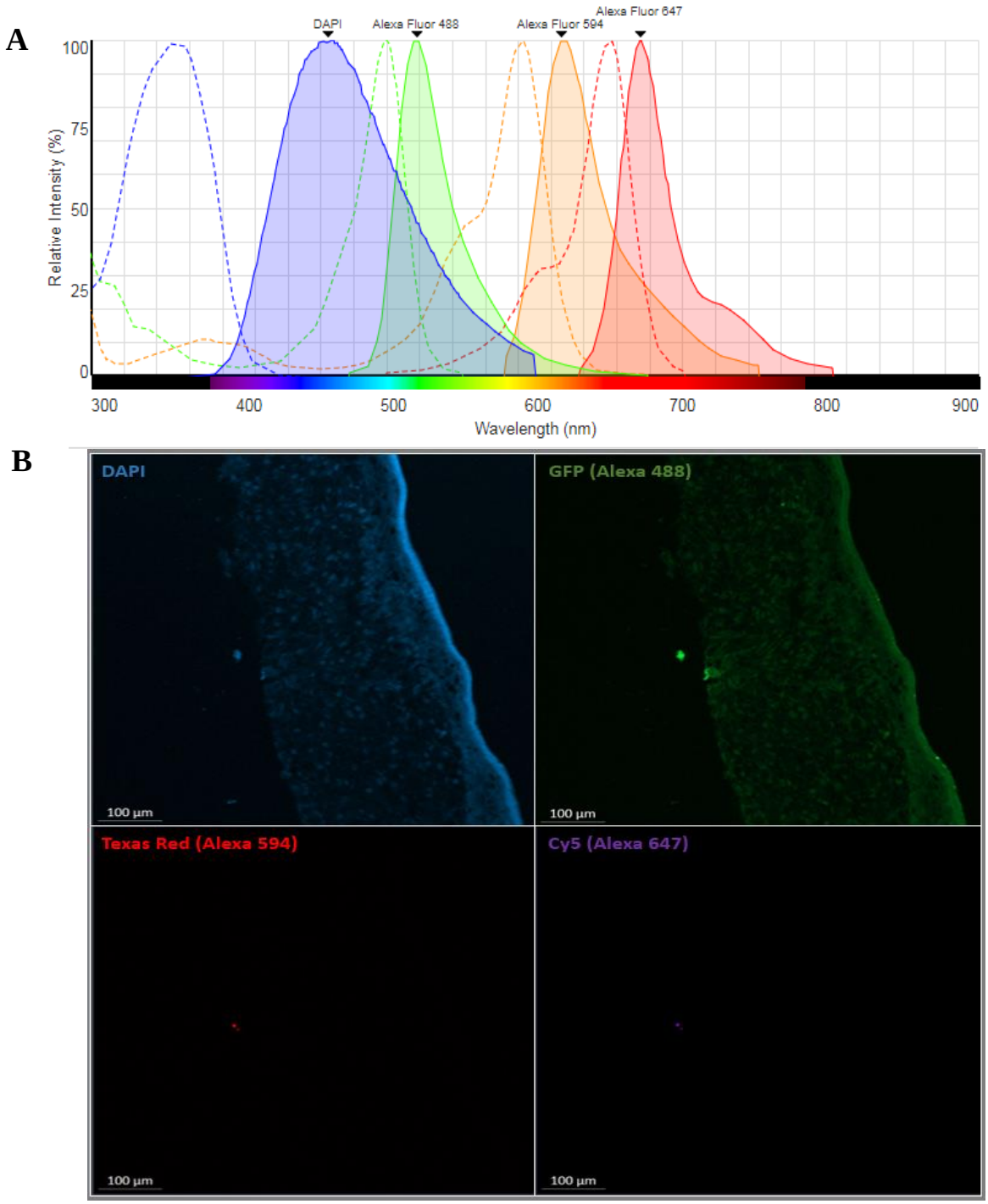

Figure 5-3: Determination of suitable fluorophores for IF labelling of CELLnTEC skin equivalents. A: Schematic of excitation (dashed) and emission (solid) spectra for Alexa Fluor -488, -594, -647, and DAPI. Both -488 and DAPI excite in the green region of the spectra, where skin autofluorescence emits strongly. Image source: Florescence SpectraViewer on ThermoFisher.com. B: CELLnTEC human skin equivalent OCT cryosections (7µm) were 4% PFA fixed and tested for autofluorescence in four light channels. Model used was derived from adult skin cells of donor S1074F (male – age 28). Autofluorescent signal was negligible in >600nm wavelengths where far right dyes (Alexa Fluor 594 and 647) emission spectra lie. Scale bars 100µm.

S1074F human skin equivalent sections were also used for optimisation in the following experimental conditions (performed simultaneously): donkey anti-mouse Alexa-Fluor 594 secondary antibody (no primary antibody, blocked with donkey serum and BSA), goat anti-rabbit Alexa-Fluor 647 secondary antibody (no primary antibody, blocked with goat serum and BSA), one primary antibody per section with species appropriate secondary antibody, and rabbit: mouse combinations of primary antibodies (with both serums and secondary antibodies). Starting dilutions were selected from publications and/or company recommendations and diluted 1:2 if the signal was strong but with some noise. Concentrations of BSA, serum, Triton-X, and washing buffers were selected from recommended ranges and published protocols. They did not require additional optimisation and worked well for all conditions tested, with no non-specific binding found. It was recommended by a histology technician that OCT-embedded tissue sections mounted onto slides should only be stored at -20^{o}C for 1 month before IF staining was performed. Tissue integrity was best preserved for long term storage within the OCT block at -80^{o}C. During optimisation Brightfield was used in lieu of DAPI to ensure the channels of interest had clean and specific signal. In later imaging it was found that DAPI staining should be performed before mounting, as DAPI-containing mountant created substantial background artefact. To achieve a wide field of view, images were initially acquired in single plane and stitched as tiles. However, as skin models are 3D structures it was necessary to generate images by compressing z-stack because a single plane could not be in focus across the entire surface area.

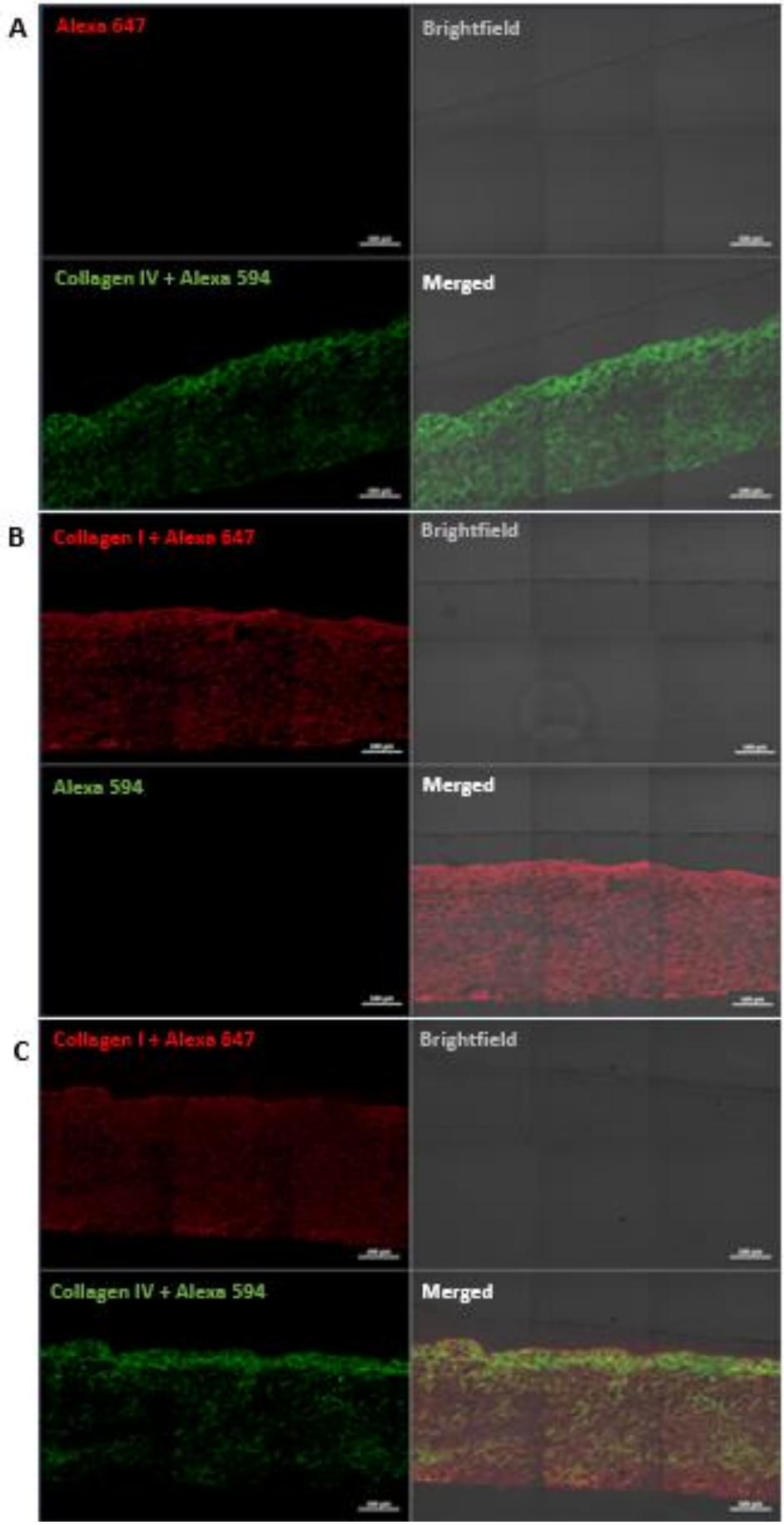

Figure 5-4: Optimisation of multi-label immunofluorescence on CELLnTEC method derived human skin equivalents. Combinations of single (A/B) and combined (C) collagen I and IV (mouse/rabbit) antibodies were used. Scale bars 100µm.

5.3.1.3 *Fluorescent imaging of collagen I, collagen IV, fibrillin and cytokeratin 14 in CELLnTEC and Labskin™ models*

CELLnTEC models grown from foreskin-derived and donor-matched adult keratinocytes and reticular fibroblasts of S1073F (male – age 65) and S1074F (male – age 28), and Labskin™ (batch 190103) were simultaneously multi-stained with rabbit and mouse primary antibodies combined as collagen I and IV, or fibrillin and cytokeratin 14. DAPI was included for cellular localisation, but the borrowed aliquot used failed to stain some sections and a new stock should have been made or purchased. Autofluorescence was quenched sufficiently in CELLnTEC models that negligible or no adjustment was required to the DAPI, -594, and -647 channel histograms.

In CELLnTEC models, the amounts of collagen I, IV and fibrillin demonstrated an extensive extracellular matrix. Collagen I was abundant (red), and collagen IV was present throughout the dermis, but more concentrated towards the basement membrane (green, Figure 5-5).

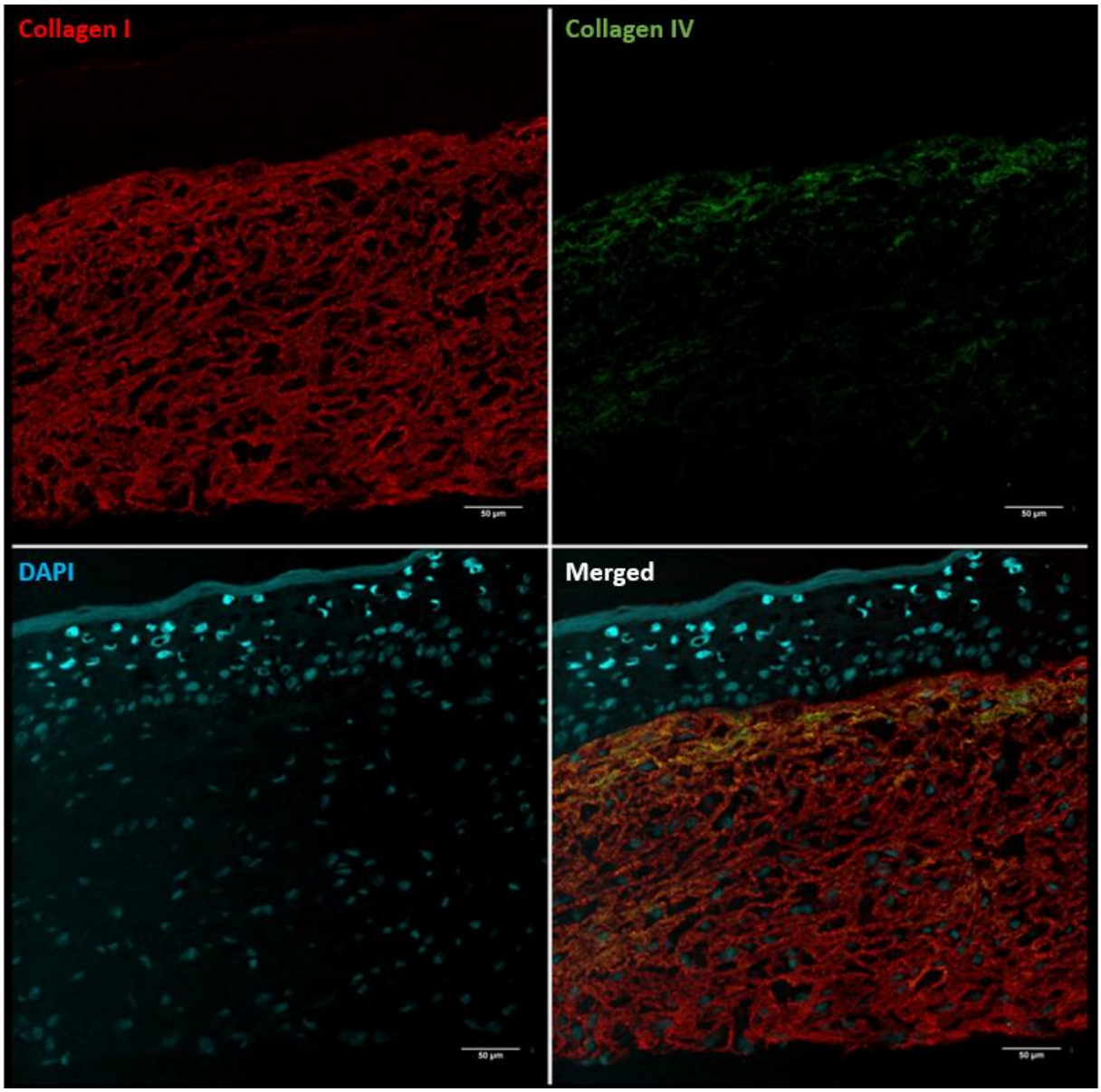

Figure 5-5: Multi-labelling of extracellular matrix proteins collagen I and collagen IV on CELLnTEC method derived human skin equivalent. Model used donor-matched keratinocytes and reticular fibroblasts derived from adult foreskin (donor S1074F – male, age 28). DAPI nuclear staining included for cellular localisation. Abundant collagen I (red) is present in the dermis layer, with collagen IV (green) more concentrated around the basement membrane. Scale bars 50µm.

Higher magnification (40X) of the collagen and fibrillin demonstrated a structured 3D matrix around fibroblasts. Cytokeratin 14 stained strongly throughout the entire reconstructed epidermis.

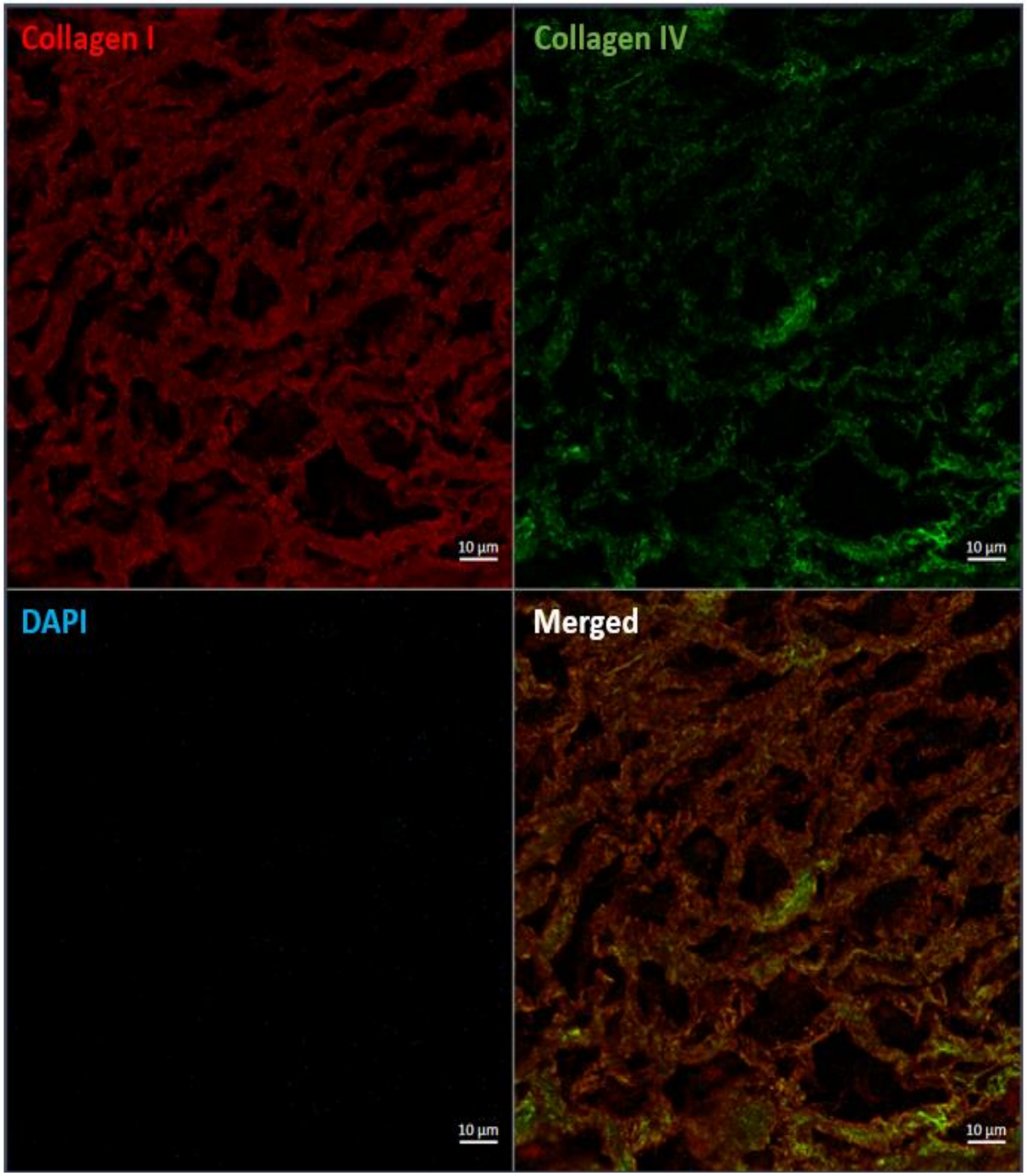

Figure 5-6: High magnification (40X) confocal imaging of multi-labelled extracellular matrix proteins Collagen I and Collagen IV on CELLnTEC method derived human skin equivalent. Model used donor-matched keratinocytes and reticular fibroblasts derived from adult foreskin (donor S1074F – male, age 28). DAPI failed to stain fibroblast nuclei on this section, though the 3D matrix is arranged around them. It wasn't a priority to repeat due to time constraints. Scale bars are 10µm.

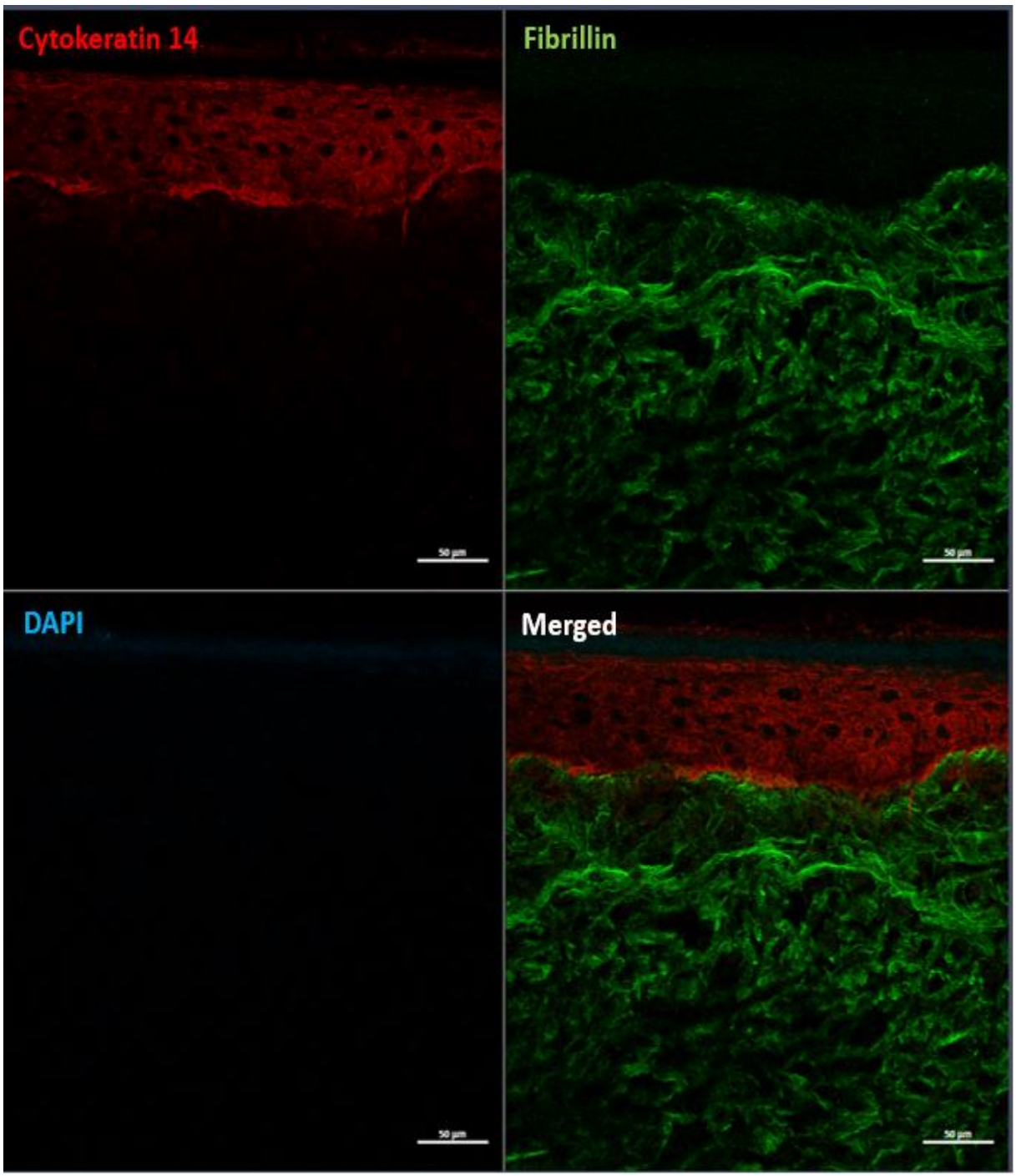

Figure 5-7: Multi-labelling of extracellular matrix protein Fibrillin and epidermal marker Cytokeratin 14 on CELLnTEC method derived human skin equivalent. Model used donor-matched keratinocytes and reticular fibroblasts derived from adult foreskin (donor S1074F – male, age 28). DAPI failed to stain fibroblast nuclei on this section, but it wasn't a priority to repeat due to time constraints. Abundant fibrillin is present in the dermis layer, with cytokeratin 14 specific to epidermis. Scale bars are 50µm.

Labskin™ cryosections were cut and stained with CELLnTEC models. Autofluorescence extended to the far-red channel -594, particularly in relation to the fibrin gel scaffold (data not shown, as corrected for using unstained control sections). This did not extend to the wavelength of Alexa-647. Negative controls were used to correct for -547 autofluorescence in stained sections. However, after correction no positive signal remained for collagen IV or fibrillin extracellular matrix proteins. DAPI revealed sparse fibroblast numbers in the thick dermal compartment, but no evidence of secreted extracellular matrix within the fibrin gel scaffold. In addition, both cytokeratin 14 and collagen I stained -647 positive in the epidermal compartment.

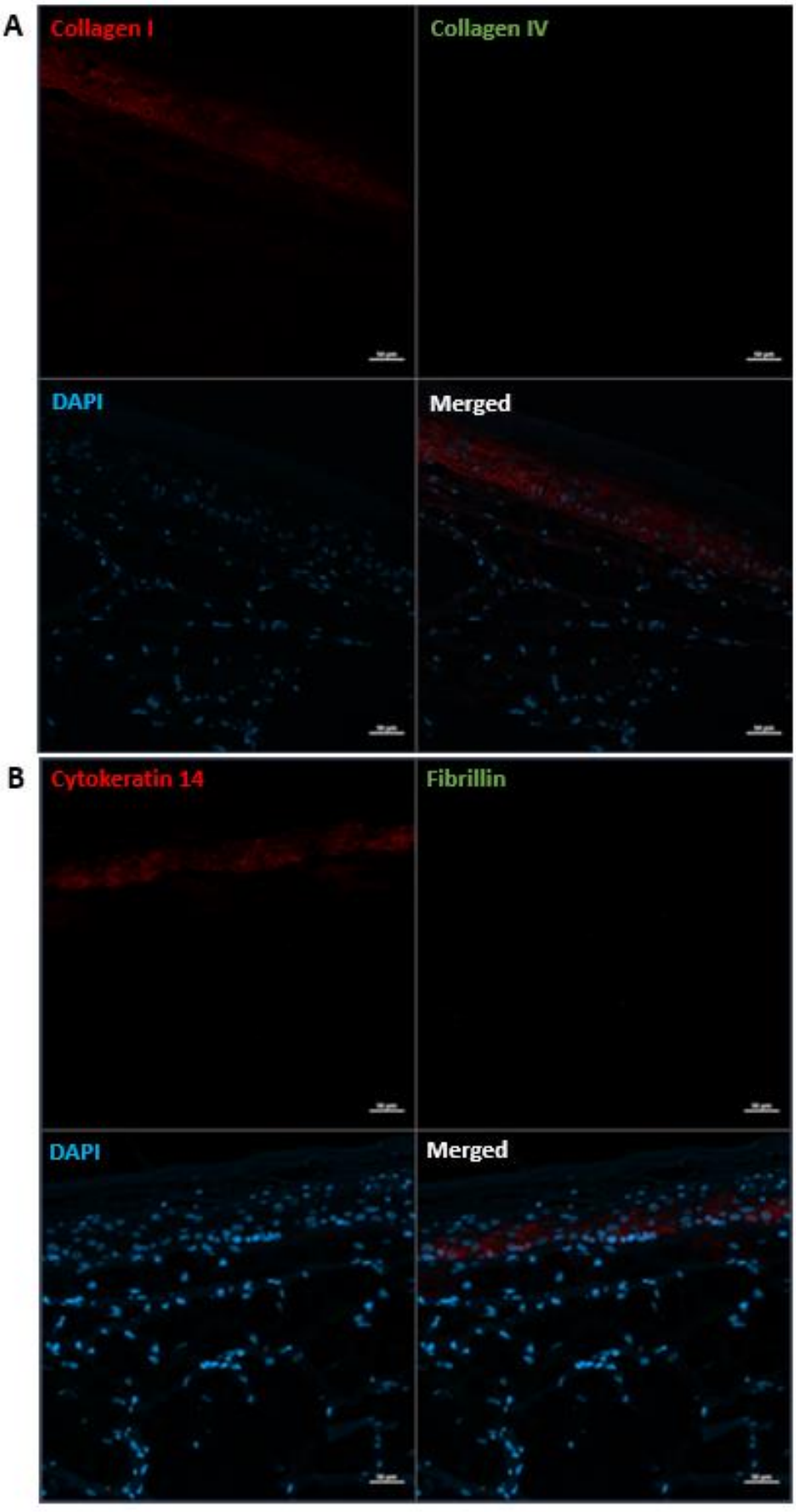

Figure 5-8: Labskin™ immunostaining of collagen I and collagen IV (A), or fibrillin and cytokeratin 14 (B). DAPI nuclear staining included for cellular localisation. Extracellular matrix proteins collagen IV and fibrillin were not present, and collagen I was in the epidermis instead of dermis. Epidermal cytokeratin 14 stained positive. Scale bars 50µm.

5.3.1.4 *Label free structural imaging using multiphoton microscopy*

Ex-vivo skin and human skin equivalents are strongly autofluorescent in the green region of the spectrum (see Figure 5-3). To determine if this signal was strong enough to enable label free imaging, a 50µm cryosection of a CELLnTEC media derived model was mounted with pro-long fade diamond with DAPI. The model used was formed using donor-matched keratinocytes and reticular fibroblasts derived from adult foreskin (donor S1074F – male, age 28). Dr Glyn Nelson (Newcastle University) generated some test images with one, two and three photon excitations. In addition, he used second harmonic generation to generate label free imaging of structures (specifically collagen at 515-525nm), with autofluorescence (570-610nm) functioning as a background 'counter stain' alongside nuclear stain DAPI (445-485nm).

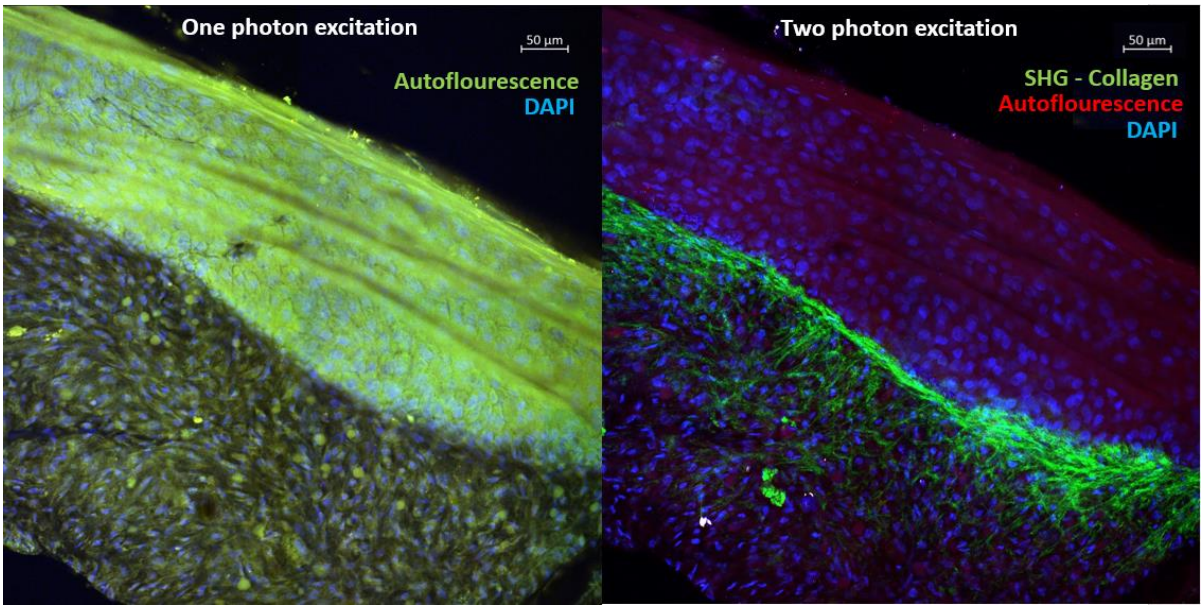

Figure 5-9: Label free multiphoton microscopy of CELLnTEC method derived human skin equivalent. One photon excitation of autofluorescence produced a strong positive signal at 570-610nm (green region). Two photon excitation identified collagen structures, with a strong signal concentrated towards the top of the dermal compartment. DAPI was included as a positive control signal and cellular localisation. Scale bars 50µm.

5.3.2 Pilot study #2: Investigation of CELLnTEC model longevity, XP3 maintenance medium trial, and induction of solar light mtDNA damage

In the second pilot study, keratinocytes and reticular fibroblasts isolated from three adult foreskin donors (S1141F – male, age 40, S1142F – male, age 17, S1145F - male, age 51) were used to grow donor-matched and scaffold-free full thickness human skin equivalents with CELLnTEC medium (12 well size, n=12 per donor). Reference H&E histology for these donors is available in supplementary Figure 9.5. To investigate the culture duration of formed human skin equivalents (at day 28), twelve were grown per donor to investigate their integrity at four harvest time-points (days 0, 4, 8 and 12). There were three skin equivalents at each harvest to

investigate model variation. When the skin equivalents were almost formed, there was a problem with contraction as illustrated in Figure 5-11 D+E. Whilst almost all had some puckering contraction that created a thicker outer 'roll' and non-uniform shape (E), 2 of 36 had severe contraction that rendered them unusable (D).

Whilst CELLnTEC medium is used to develop human skin equivalents, the company doesn't recommend a medium to maintain the fully formed equivalents or indicate how long they can remain viable for experiments to be performed. When contacted they suggested a trial of CELLnTEC CnT-XP3 medium may be suitable as it was designed for extended ex-plant culture of up to 10 days. As CnT-XP3 medium contained phenol, the first visual observation was made that equivalents formed with the skin cells of the 17-year-old donor (S1142F) were metabolising the medium much quicker than that of the 40-year-old donor (S1141F). The medium would be yellow within 24 hours, as conveyed in Figure 5-10 C.

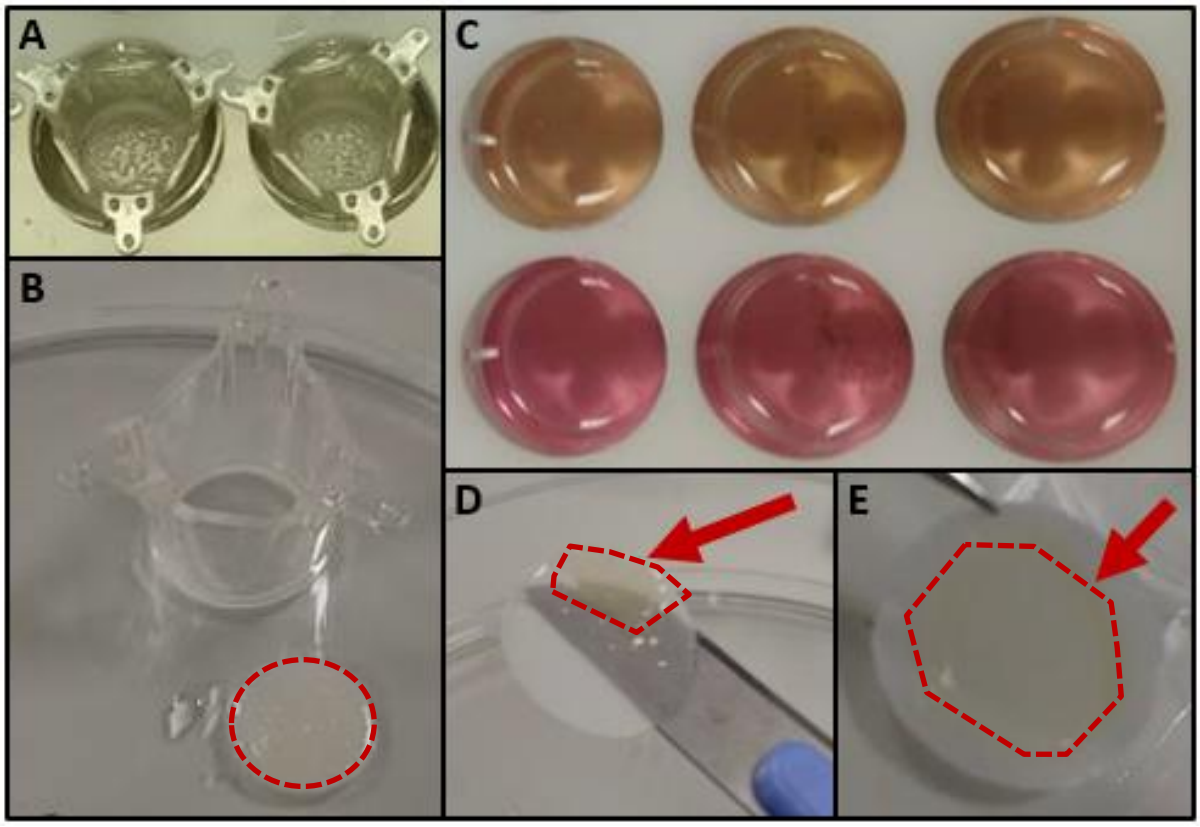

Figure 5-10: Photographs of CELLnTEC human skin equivalents pilots #1 and #2. A+B: pilot #1 of skin equivalents grown using donor-matched foreskin-derived adult skin cells from donors S1073F (male – age 65) or S1074F (male – age 28), which had a dry stratum corneum and no contraction. C: pilot #2 involved the transition of fully formed skin equivalents to a culture medium CnT-XP3 that contains. This demonstrated for the first time that metabolic capacity of skin equivalents would differ between donors, with the yellow wells showing medium from a 17 year-old donor (S1142F) and the red wells show how the medium from a 40-year-old donor (S1141F) hasn't changed in the same time-frame (24 hours). D+E: pilot #2 skin equivalents had contraction/shrinkage of various distances from the insert edge. Only 2 of 36 skin equivalents were as severe as the equivalent shown in 'D', which was experimentally unusable.

In pilot #1 there was inter-donor variability in established skin equivalents, whereby those derived from a younger donor had a thicker dermal layer (Figures 5-1). However, an association between skin donor age and 'better-formed' skin equivalents was not clearly seen in pilot #2. In fact there was a missing or fragmented epidermal layer in the H&E stained FFPE sections of most skin equivalents derived from donor S1141F (male – age 40; Figure 5-13) or S1142F (male – age 17; Figure 5-14). It was unclear if the epidermis had failed to form correctly or it was an artefact of histological processing. S1141F was the only foreskin donor used with a Fitz. type V phototype, but it is unclear if this was a contributing factor to sub-optimal skin equivalents.

The largest number of histologically-intact skin equivalents were those developed with foreskin-derived cells from donor S1145F (male – age 51; Figure 5-12). However an important observation was made that the dermis progressively thinned throughout 12 days in culture, whilst the stratum corneum appeared to continue progressively thicken (Figure 5-12). This is an indication that the skin equivalent does not undergo desquamation.

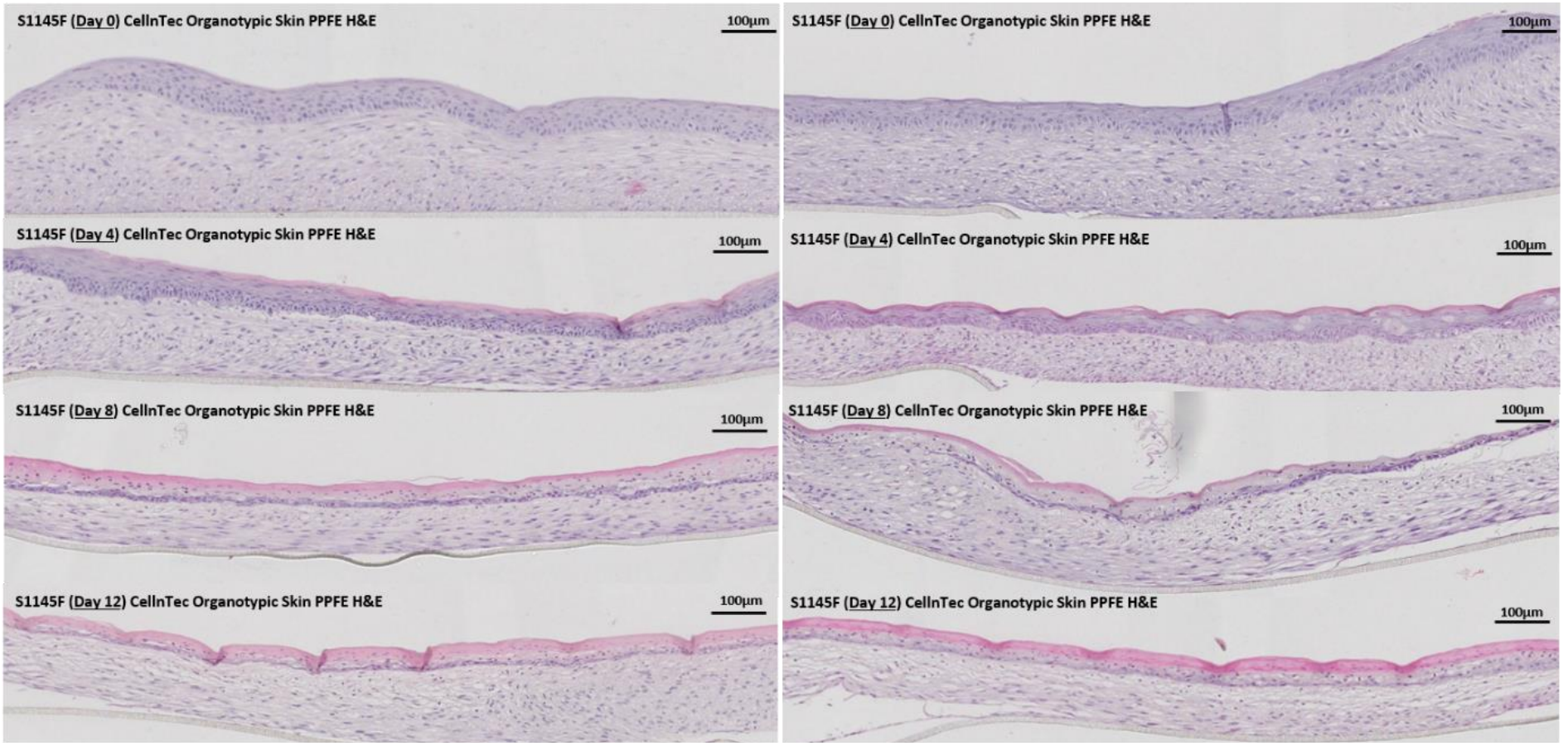

Figure 5-11: Histological H&E staining of skin equivalents developed using CELLnTEC commercial medium and foreskin-derived adult keratinocytes and reticular fibroblasts from donor S1145F. Twelve skin equivalents were formed from donor-matched adult keratinocytes and reticular fibroblasts of foreskin donor S1145F (male – age 51). Models have formed a keratinised stratified epidermis attached to a thicker dermal layer. The dermal ECM was secreted by the fibroblasts, without use of an artificial scaffold. A dermo-epidermal junction is visible, and fibroblasts are evident within the dermal layer. Once full-formed (Day 0), skin equivalents were maintained using CELLnTEC commercial XP3 medium, and three skin equivalents were harvested at days 4, 8 and 12. Imaging of two skin equivalents per time-point are included. The stratum corneum continued to thicken over time in culture. H&E staining was performed on three sections per FFPE-embedded skin equivalent. H&E staining of an ex-vivo biopsy from foreskin donor S1145F is in supplementary Figure 9.5. Scale bars 100µm, N=3, n=9

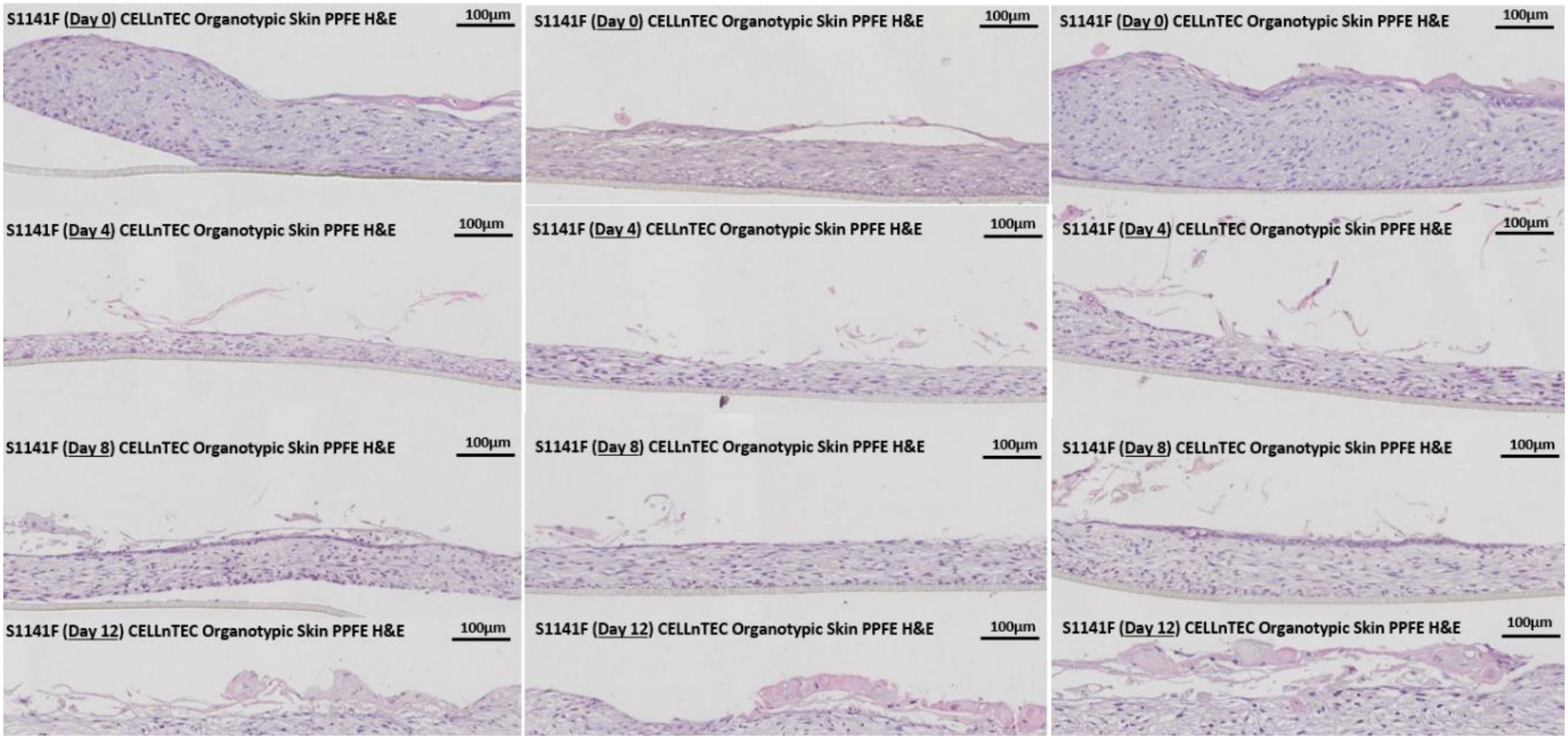

Figure 5-12: Histological H&E staining of skin equivalents developed using CELLnTEC commercial medium and foreskin-derived adult keratinocytes and reticular fibroblasts from donor S1141F. Twelve skin equivalents were formed from donor-matched adult keratinocytes and reticular fibroblasts of foreskin donor S1141F (male – age 40). Models have formed a keratinised stratified epidermis attached to a thicker dermal layer. The dermal ECM was secreted by the fibroblasts, without use of an artificial scaffold. A dermo-epidermal junction is visible, and fibroblasts are evident within the dermal layer. Once full-formed (Day 0), skin equivalents were maintained using CELLnTEC commercial XP3 medium, and three skin equivalents were harvested at days 4, 8 and 12. Imaging of three skin equivalents per time-point are included. H&E staining was performed on three sections per FFPE-embedded skin equivalent. H&E staining of an ex-vivo biopsy from foreskin donor S1141F is in supplementary Figure 9.5. Scale bars 100µm, N=3, n-9

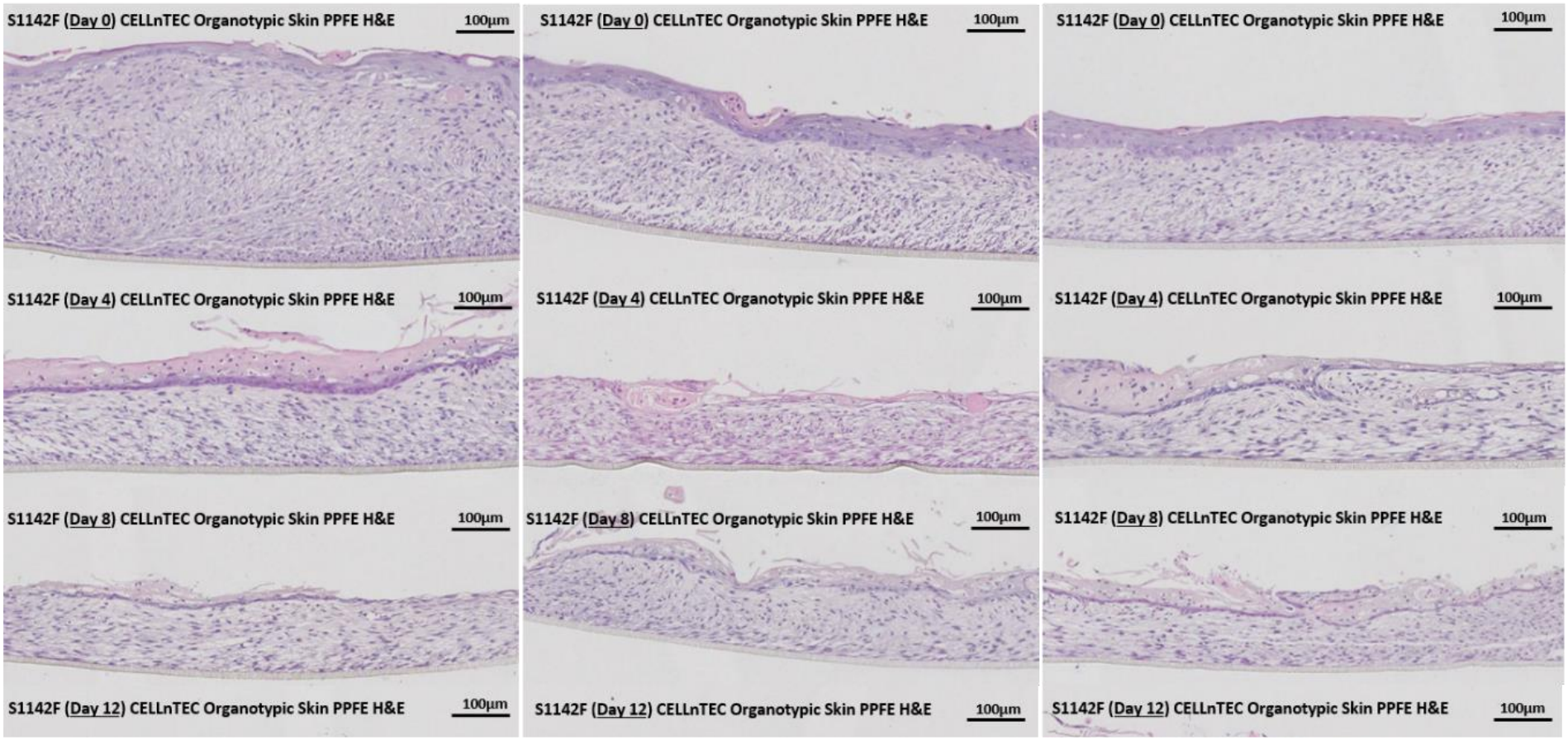

Figure 5-13: Histological H&E staining of skin equivalents developed using CELLnTEC commercial medium and foreskin-derived adult keratinocytes and reticular fibroblasts from donor S1142F. Twelve skin equivalents were formed from donor-matched adult keratinocytes and reticular fibroblasts of foreskin donor S1142F (male – age 17). Models have formed a keratinised stratified epidermis attached to a thicker dermal layer. The dermal ECM was secreted by the fibroblasts, without use of an artificial scaffold. A dermo-epidermal junction is visible, and fibroblasts are evident within the dermal layer. Once full-formed (Day 0), skin equivalents were maintained using CELLnTEC commercial XP3 medium, and three skin equivalents were harvested at days 4, 8 and 12. H&E imaging of three skin equivalents per time-point are included. H&E staining was performed on three sections per FFPE-embedded skin equivalent. H&E staining of an ex-vivo biopsy from foreskin donor S1142F is in supplementary Figure 9.5. Scale bars 100µm , N=3, n=9

In pilot #2, an additional two skin equivalents were developed from donors S1141F and S1142F to test the induction of mtDNA damage through solar simulated irradiation. The 2.16 SED dose given to cell monolayers (see Chapter 4) induced a similar amount of mtDNA damage in the 3D skin equivalents of both donors. The 11kb assay (Chapter 3) was used to determine a 4 C_t or 32-fold (2^4) induction of mtDNA damage, as seen in Figure 5-14. The DNA yield per quadrant of a 12-well skin equivalent was ~7-11µg for S1141F and ~8µg for S1142F.

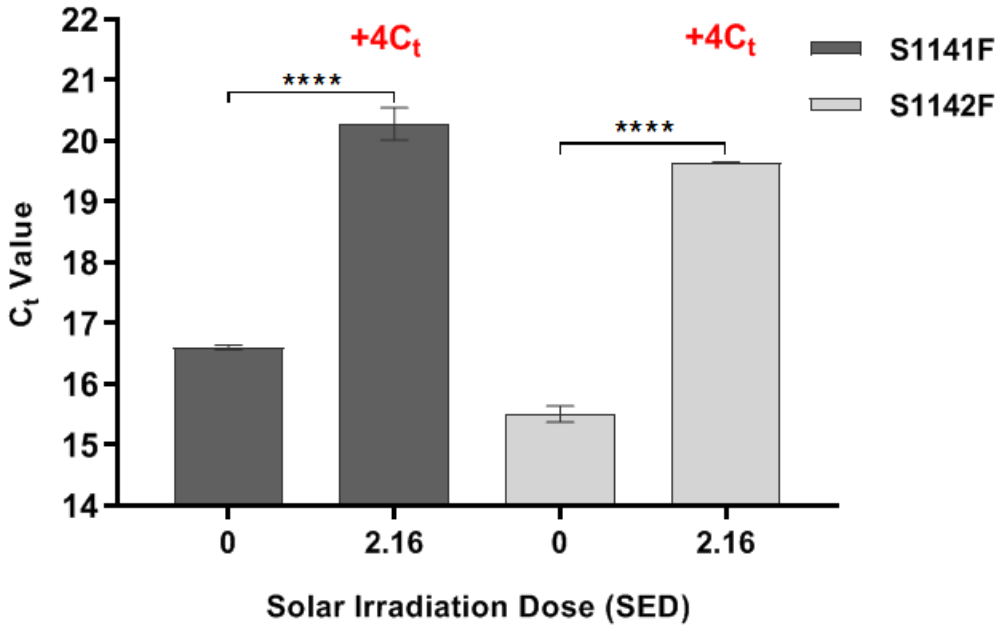

Figure 5-14: Detection of solar radiation induced mtDNA damage in CELLnTEC skin equivalents using 11kb qPCR assay. Skin equivalents were irradiated with 2.16 SED (see 2.2.2.). The standard erythemal dose (SED, J.m-2) is equivalent to an erythemal radiant exposure of 100 J.m-2. Mean ± SD data from one human skin equivalent per donor (S1141F (male - age 40), S1142F (male – age 17). Statistical difference determined by one-way ANOVA with Tukey's post-hoc test. **** p <.0001, N=1, n=3

5.3.3 Pilot study #3: CELLnTEC skin equivalent scaling between insert sizes, fresh/frozen medium comparison, and multiphoton live imaging trial

In the third pilot study, keratinocytes and reticular fibroblasts isolated from one adult foreskin donors (S1147F – male, age 53) were used to grow donor-matched and scaffold-free full thickness human skin equivalents with CELLnTEC medium in three sizes (24-, 12- and 6-well). As each 12-well size skin equivalent requires 120,000 keratinocytes, a 24-well size was trialled because it would be an important option for smaller skin samples (e.g. facial) which produce reduced numbers of keratinocytes. A 6-well size skin equivalent was trialled only to attempt live imaging, so that the microscope objective could be accommodated. A comparison was also made between two commercial brands of hanging inserts (Greiner and Millipore) to grow 12 well size skin equivalents. This was because CELLnTEC switch between these brands,

but report discrepancies between the PET membrane of individual batches. A more critical comparisons was made between 'fresh' and 'frozen' CELLnTEC medium, because once a medium bottle is thawed it is only viable for 6 weeks at 4°C before the nutrients/supplements are depleted. The medium was thawed at 4°C protected from light, but some was portioned into 50ml aliquots and re-frozen. For each size (6-, 12-, 24-well), two skin equivalents was grown with the 'fresh' medium and two with the 'frozen' aliquots. One of each was used for live imaging (Figure 5-16), and the other embedded in FFPE and OCT for standard histology.

In this pilot, both cell types were thawed and expanded in their cell-specific CELLnTEC epithelium or fibroblast proliferation medium before seeded into hanging inserts. It was observed that cells revived and proliferated very well in this medium, regardless of whether the medium had been re-frozen. Countess II Cell Counter (Invitrogen) readings confirmed almost identical cell counts and >90% live cells for flasks with 'fresh' or 'frozen' medium.

However, after this point it was found that skin equivalents developed compact and well defined as 24-well size. Unfortunately the FFPE comparison tissue for '24-well size + frozen medium' was lost in processing as a result of the cassette holes being too large. However, an OCT section of this skin equivalent was reviewed and was considerably thinner than 'fresh' with limited dermis. The same pattern was found for the 12-well skin equivalent grown in 'frozen' medium, although the skin equivalent in OCT had a thicker dermis. No 6-well insert slices looked formed in FFPE or OCT sections. From this data it appears that both fresh media and a 24 size are the best conditions for skin equivalents, but even that model is not as good as those produced from the skin cells of other donors. As this was only performed on one donor, the findings are inconclusive.

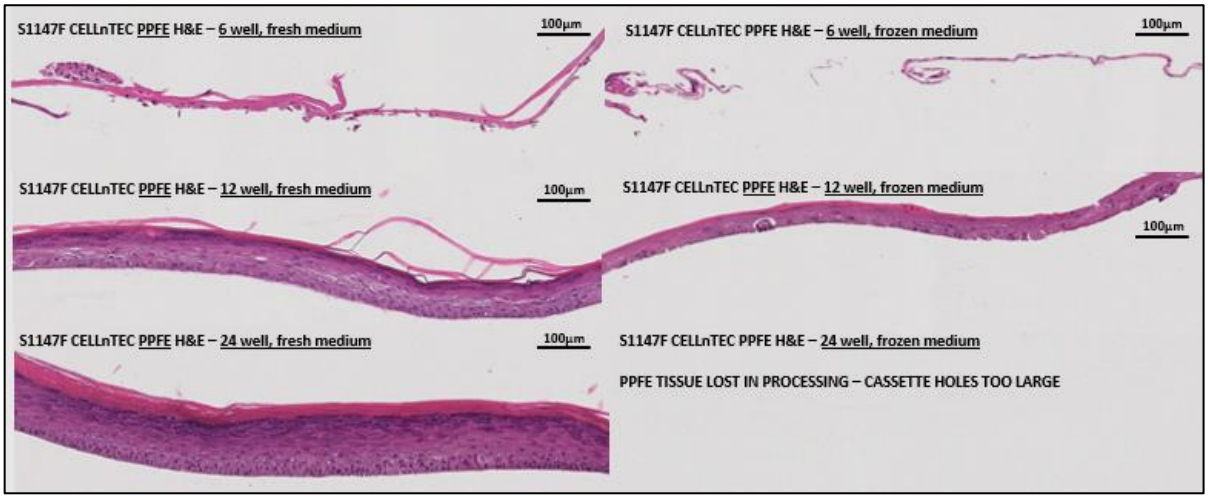

Figure 5-15: Histological H&E staining of skin equivalents developed using CELLnTEC commercial medium and foreskin-derived adult keratinocytes and reticular fibroblasts from donor S1147F. Skin equivalents were grown in three insert sizes (6-, 12-, 24-well) and in fresh or frozen aliquots of CELLnTEC prime medium. One FFPE skin equivalent was lost in tissue processing due to the biopsy cassette hole size. H&E staining was performed on three sections per FFPE-embedded skin equivalent. N=1, n=3.

As both autofluorescence and second harmonic generation (SHG) signal of the collagen had been viewed well in a skin equivalent cryosection (S1074F donor, Figure 5-9), live label-free imaging was trialled on these skin equivalents using the multiphoton system (see 5.2.3.4), with Dr Glyn Nelson of Newcastle Bio-Imaging Facility.

The 6-well size inserts could not accommodate any available objectives. If an objective did fit within the insert, it would only be able to image the middle portion of the skin equivalent. An InverterScope™ was used to invert the objective and attempt to image from underneath, but it was difficult to optimise through the PET membrane. We next tired removing the 12-well (fresh) skin equivalent from the insert onto a glass slide, with the stratum corneum dry and facing upwards. A drop of water was required underneath to keep the skin equivalent from dehydrating and curling inwards**.** Some second harmonic collagen signal was attained, but it was very dim, and the structures all appeared to run vertically (Figure 5-16). Given that the H&E imaging in Figure 5-18 was acquired after this live SHG trial, the dim signal was likely attributed to inadequate model formation from this donor.

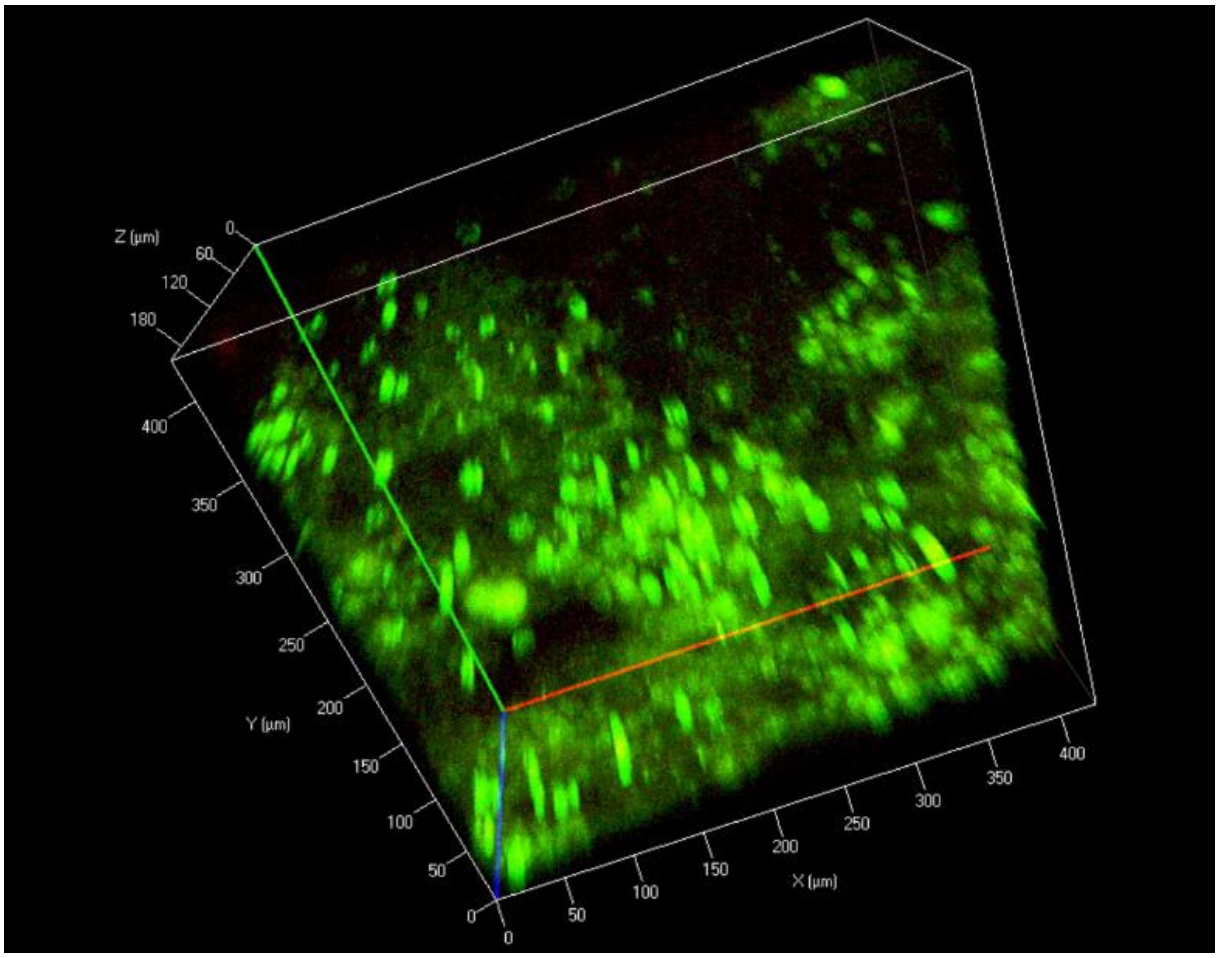

Figure 5-16: Second harmonic generation of skin equivalent collagen using live label-free multiphoton microscopy. Live SHG multiphoton imaging of dermal pan-collagen in non-fixed skin equivalents developed using CELLnTEC commercial medium and foreskin-derived adult keratinocytes and reticular fibroblasts from donor S1147F. Image from a 12-well size skin equivalent grown with fresh medium and removed from its insert for imaging.

5.3.4 Pilot study #4: CELLnTEC skin equivalent antioxidant cream application, and analysis of equivalents development by ELISA testing media

Initially a young (S1142F, male – age 17), middle age (S1151F, male – age 35) and older donor (S1146F, male – age 76) were selected to establish skin equivalents for a time-scale AOX protection study using topical application of test formulations. The fibroblasts proliferated well when thawed and were passaged once before seeding into inserts. They grew for 10 days while keratinocytes simultaneously proliferated to confluence post-thaw. Accutase™ was used instead of Trypsin-EDTA for keratinocyte passaging because it was recommended by CELLnTEC, it is a gentler enzyme, and doesn't require neutralising/centrifugation. However, when the keratinocytes were passaged with Accutase™ they did not adhere to the new flask surface, and the majority subsequently died by the following morning. When the medium was moved to a new flask, some viable cells did adhere but were no longer the correct morphology. The study was repeated with remaining donor-matched cell stocks. Donors S1141F (male - age 40) and S1151F (male – age 35) were used to grow skin equivalents to compare against commercial Labskin™. Donor S1154F (male – age 44) was also intended for use but failed to thaw viable proliferative fibroblasts. This is a rare phenomenon that occurs with some donors, although they are generally always older than 70 years old. Although S1141F and S1151F keratinocytes were thawed on the same day, S1141F proliferated twice as fast as S1151F. As such S1141F had to be passaged at day 5, but when treated with Accutase™ the same problem with flask adherence arose. Another vial of S1141F keratinocytes was thawed which was reasonably confluent after 5 days, for seeding onto the dermis. Neither donor was passaged between thawing and seeding onto the dermis layer, but it was noted that keratinocytes are centrifuged to change medium type so all Accutase™ was removed. Future work should therefore also centrifuge the keratinocytes to remove Accutase™ when passaging to new flasks. Unfortunately, when histology was performed on PPFE and OCT embedded skin equivalents, none had formed into 3D skin models (data not included). In addition when DNA was extracted from the skin equivalents for qPCR there was only 0.2-0.8µg, which was considerably less than the 8-11µg extracted from previous skin equivalents grown with donor S1141F (Figure 5-13).

Media was collected throughout skin equivalent development on days 4, 9, 14, 19, 24 and 29 (Figure 5-17). This was stored at -80^{o}C and used for protein ELISA of pro-collagen I, fibronectin and hyaluronan. The ELISA data was used to compare inter-donor and inter-skin equivalent variability between two donors, with three skin equivalents per donor as demonstrated in Figure 5-17. Over the 29-day period, donor S1141F produced a mean 4.4 times more pro-collagen I, 4.5 times more fibronectin, and 3.4 times more hyaluronan than S1151F who was similar in age. The inter-skin equivalent reproducibility was much better conserved in

S1151F skin equivalents. However, both donors followed the same trend throughout skin equivalent establishment with pro-collagen I and fibronectin relatively stable throughout dermis establishment, increasing upon the addition of keratinocytes, and stabilising again throughout cornification at the air-liquid interface. Hyaluronan had more of a peak and trough pattern for both donors, peaking greatly when skin equivalents were first raised to the air-liquid interface. However, it was unusual that the medium required only 1:4-1:16 dilution after ELISA standard curves were performed. Previously the dilutions were a minimum 1:1000 to fit within the range of standard concentrations used. This was an indication that the models were producing much less protein, and therefore the cells mustn't be forming standard skin equivalents. This concern was confirmed when histology confirmed this batch of skin equivalents had not formed into 3D models (data not included). However this experiment did prove that the ELISA technique could be used to sensitively detect inter-donor and inter-skin equivalent variability.

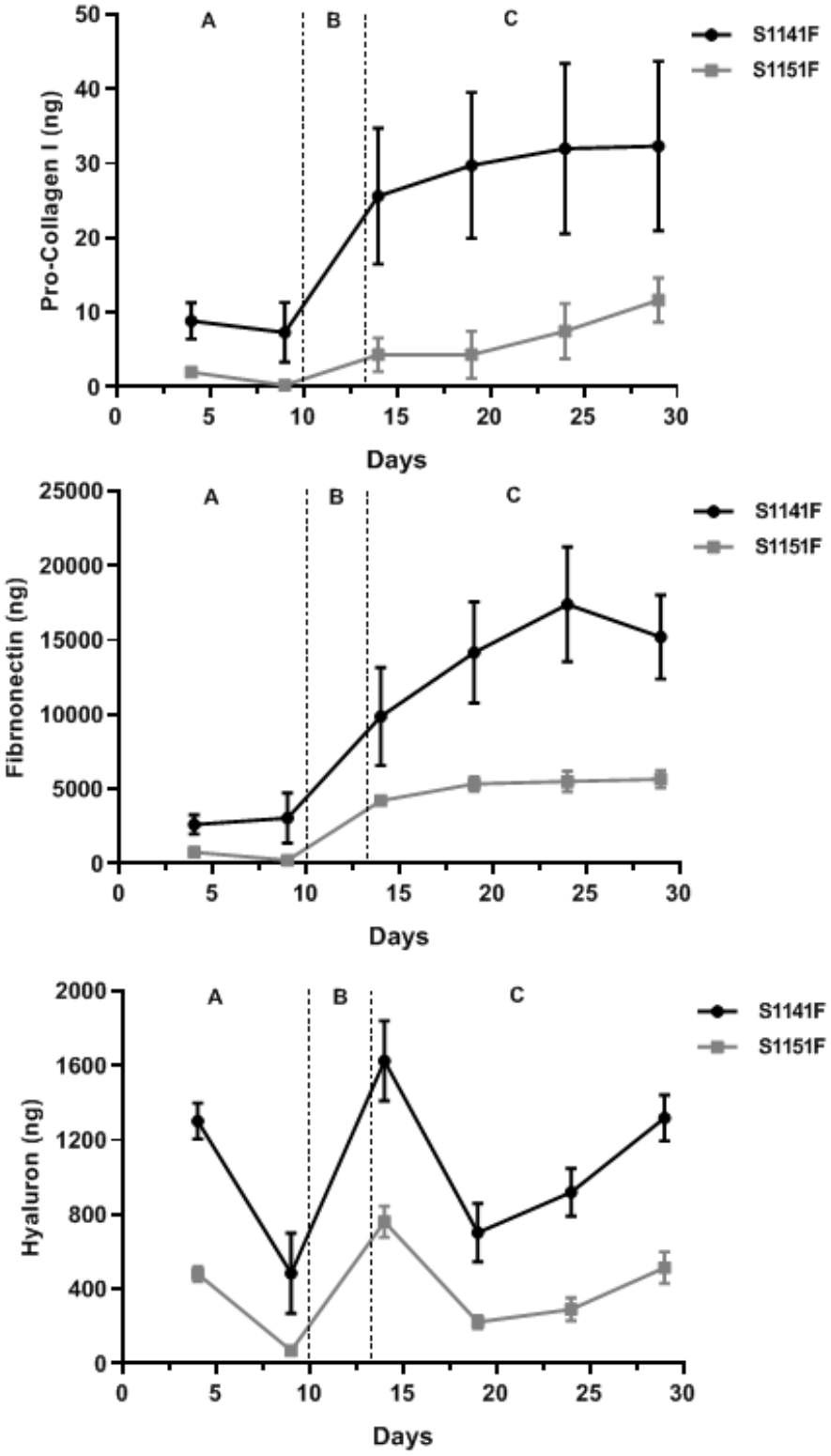

Figure 5-17: Mean ELISA quantification of pro-collagen I, fibronectin, and hyaluronan proteins produced by developing CELLnTEC full thickness human skin equivalent. Media samples were collected at days 4, 9, 14, 19, 24 and 29. Skin equivalents were grown with donor-matched foreskin-derived adult keratinocytes and reticular fibroblasts from donors S1141F (male – age 40) or S1151F (male – age 35). Skin equivalent development is grouped in three phases: dermis growth (A; 10 days, CnT-PRF medium), addition of keratinocytes in submerged culture (B; 3 days, CnT-FTAL medium), and air-liquid interface (C; 12 days, CnT-FTAL medium). ELISA was performed to measure inter-donor and inter-skin equivalent variability. There is therefore no requirement to normalise for increasing cell number over time. ELISA was performed in duplicate for each sample. Mean ± SEM data obtained from three skin equivalents per donor, whereby error bars represent inter-skin equivalent variability. N=1, n=3.

5.3.5 Comparison of skin fibroblast ECM production from thick (abdomen) versus thin (foreskin) donor sites, using CELLnTEC medium

It was queried if skin equivalents thickness was a result of the two skin equivalents only containing two cell types, or that the fibroblasts of thin skin (i.e. foreskin) produce less extracellular matrix (ECM) than thicker skin sites. A pilot comparison was made between skin fibroblasts of thick abdomen and thin foreskin. As multisite skin samples were unavailable from the same donor, two donors were selected of the same age (56), sex (male), and cell passage number (2). The foreskin donor (S1197F) was isolated from dermis in-house, and the abdominal donor fibroblasts (RVI07) were kindly provided by Dr Peter Hanson of Newcastle University. Initially cells were seeded within hanging inserts to grow into human dermis equivalent (as for a full thickness skin equivalent) but visualising and removing them from the membrane was ineffective. Cells were then grown in monolayers within a 12-well plate, with six wells per donor. To determine if foreskin fibroblasts ECM production could be increased (to make a thicker dermis layer), they were treated with CELLnTEC ECM production medium according to manufacturer's online protocol.

Standard curves for each ELISA kit were performed on high protein samples (supplementary Figure 9-6) to determine a working dilution. As Figure 5-16 demonstrates, foreskin fibroblasts produced more pro-collagen I, but approximately 50% less fibronectin/hyaluronan than abdominal fibroblasts (in CELLnTEC fibroblast proliferation medium (PR-F)).

The commercial CELLnTEC ECM boost medium did increase pro-collagen I production by 5-fold in both cell types, but not fibronectin and hyaluronan. A western blot was confirmed the collagen I was laid down as extracellular matrix protein (Figure 5-17). Initially a QuickZyme™ total collagen kit was used (as per CELLnTEC recommendations), but despite several optimisation attempts it could not detect collagen within the standards provided.

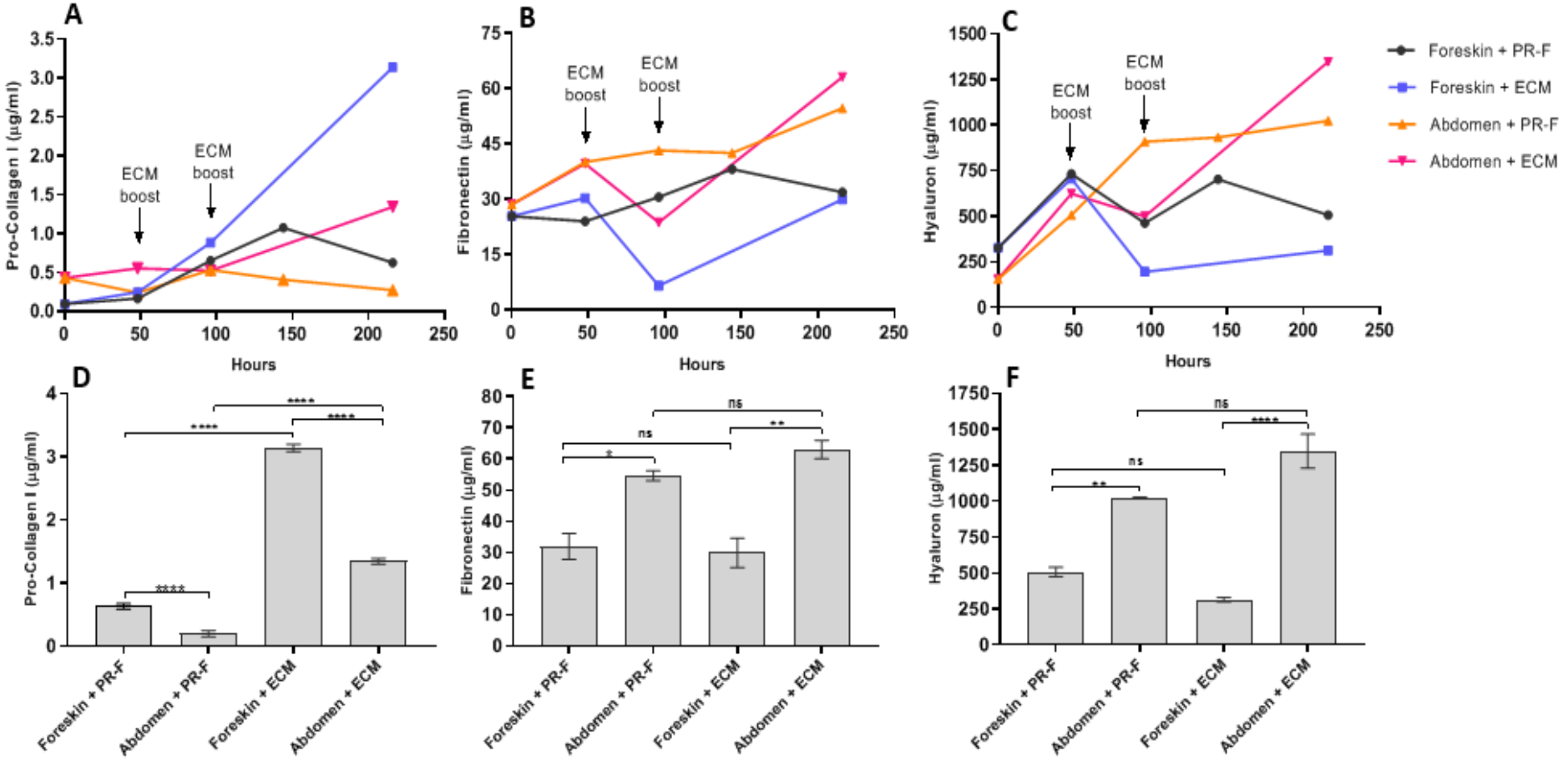

Figure 5-16: Mean ELISA quantification of pro-collagen I, fibronectin, and hyaluronan produced by reticular fibroblasts of one foreskin and one abdominal skin donor. Both sources of reticular fibroblasts were isolated 56-year-old male donors (S1197F and RVI07). Media samples were collected at 0, 24, 48, 96, 144 and 216 hours (A-C). Six wells of each donor were grown in CELLnTEC prime fibroblast proliferation medium (PR-F) for 48 hours before half were switched to CELLnTEC prime ECM production medium (ECM) for the remaining 168 hours, with one medium change at 96 hours as indicated by arrows on A-C. Time-points at 216 hours were used for statistical comparison between foreskin and abdomen, as well as each donor with/without extracellular matrix (ECM) boost medium (D-F). Statistical difference determined by one-way ANOVA with Tukey' s post-hoc test (D-F). **** p<.0001, **p<0.008, *p<.03, ns p>.05,N=1, n=3

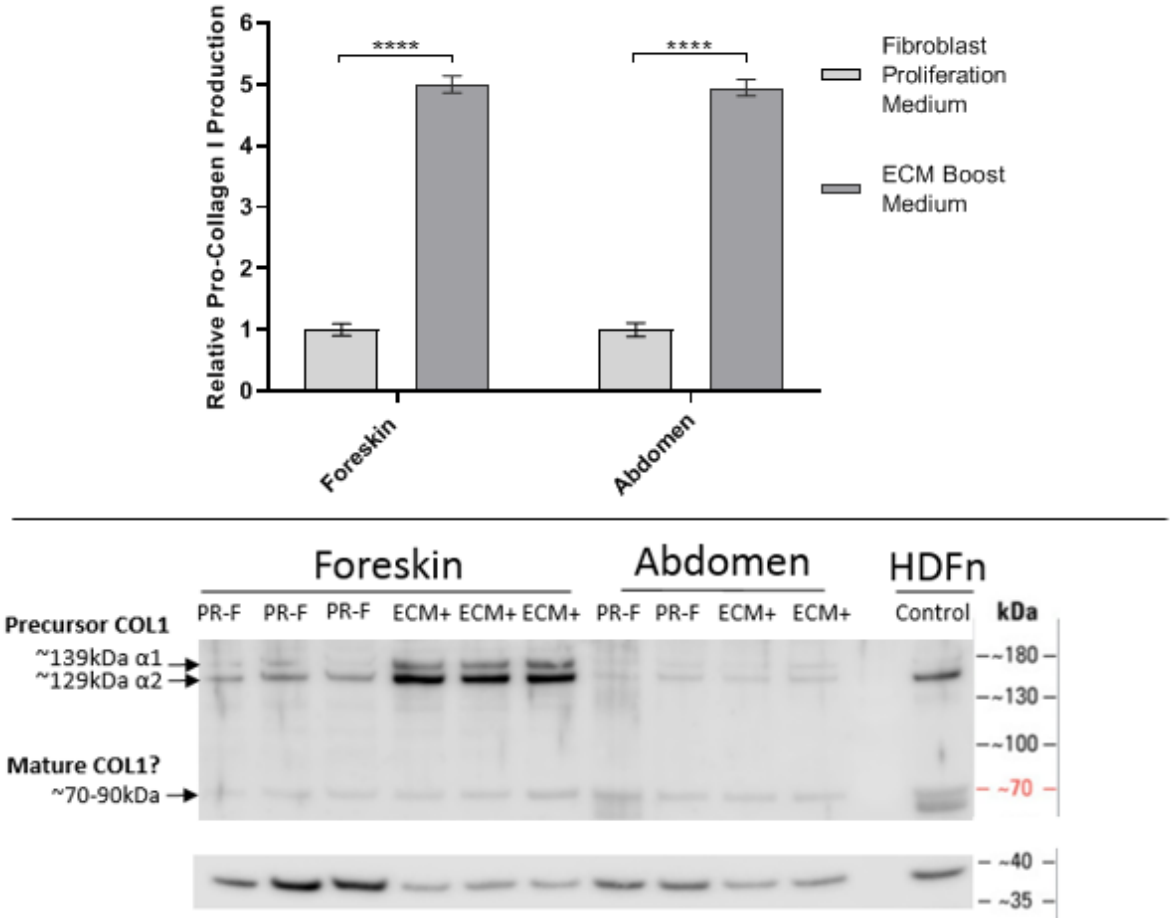

Figure 5-17: Five-fold fibroblast collagen increase with CELLnTEC commercial 'ECM boost' medium. Top: Relative mean ELISA showing 5-fold pro-collagen I (COLA1) increase in skin fibroblasts after 216 hours incubation with commercial CELLnTEC medium designed to increase/'boost' extracellular matrix (ECM) production (top). Data from reticular fibroblasts of one foreskin (S1197F - male, age 56) and one abdominal (RVI07 - male, age 56) skin donor. Bottom: Western blot for collagen I (alpha-1/alpha-2 bands; ~129-139kDa), with GAPDH (37kDa) loading control. There were bands at ~70-90kDa, which could be mature collagen I (COL1). ELISA performed in duplicate for all samples. ELISA statistical difference determined by one-way ANOVA with Tukey's post-hoc test **** p<.0001, N=1, n=3.

5.3.6 Optimisation of facial skin cell isolation, culture and cryopreservation

It was found that performing skin Dispase treatment on the same day as surgical removal provided better cell yields than storing overnight in storage medium at 4°C. Eighteen donors were used as outlined in Table 2-2. For additional method detail, see section 2.1.

5.3.6.1 *Processing and Dispase treatment*

Flame sterilised surgical scissors were used to remove adipose and a no. 11 shape scalpel was used to make 45^0 angle cuts into the rigid hypodermis to allow for Dispase penetration (which was a 1:8 dilution instead of 1:10). The epidermis was easily removed with surgical tweezers after overnight Dispase incubation. The hypodermis could not be removed from the dermis.

5.3.6.2 *Facial keratinocytes*

A direct comparison of keratinocyte culture with and without ROCK (apoptosis) inhibitor demonstrated that while some donors could establish a P0 starter culture without it, more donors would establish one with it. The use of ROCK inhibitor is discussed further in section 5.4. Due to the rapid metabolism of ROCK inhibitor, the media volume per 25cm^2 flask was increased to 10ml, which was changed at three regularly spaced weekly intervals. For the first 7-9 days (longer without ROCK) the morphology appeared as dots before small colonies were observed. These would reach confluency between days 10-14, at which point they could be frozen or split into two 25cm^2 flasks. The keratinocytes came off the flask surface readily with Accutase™. Removing ROCK inhibitor at the first passage and/or moving to a 75cm^2 flask was detrimental. However, if keratinocytes were frozen they could be thawed into CELLnTEC medium that did not contain ROCK. They proliferated well in CELLnTEC CnT-PR medium, but this was not directly compared to Epi-life™ medium because of limited cell numbers. It was generally observed that facial keratinocytes proliferated much faster than foreskin, but this wasn't recorded as quantitative data.

5.3.6.3 *Facial fibroblasts*

Fibroblasts migrated from dermis adhered to the flask surface but would not proliferate from these sites when the dermis was removed. To investigate if they required more glucose for proliferation, DMEM was additionally supplemented with 1% GlutaMAX™ but this did induce proliferation and the fibroblasts looked unhealthy. Having the colony sites closer together in a 25cm^2 flask (instead of the usual 75cm^2 flask) did not help proliferation. The thicker dermis-hypodermis meant that pieces were lost at each media feed as they dislodged very easily from the surface. Attempts to readhere them were unsuccessful. A direct comparison between 25cm^2 flask and 6-well plates did not improve the outcome, with the tissue even less adherent to 6 well plates with each media change. Moreover, the migrated fibroblasts adhered so strongly to the surface that they could not be removed with trypsin-EDTA, Accutase™, or with manual agitation. It was found that coating a 25cm^2 flask with 0.1% gelatine improved tissue adherence and enabled cell removal with Accutase™. Optimised tissue adherence followed dermis incubated overnight with 100% FBS (1ml), and the following morning a small ~2ml volume of media was added gently to provide some nutrition. On day 3, this was replaced with 5ml media which ensured the tissue had firmly adhered. Increasing the media volume above 5ml increased the likelihood of tissue lifting off. When adherence was optimised and proliferation remained non-evident, the number of dermis adherence sites was increased to maximise overall cell number. From donors 2740-2748 (see Table 2-2), the entire dermis was cut into small pieces,

which were individually placed onto the 0.1% gelatine coated 25cm^2 flask(s) with approx. 1 cm spacing between pieces. The dermis was placed with the papillary dermis facing upwards, so that reticular fibroblasts were acquired by migration from the tissue onto the coated flask base. At day 14 the tissue was removed as it decayed when left attached any longer. Media was changed for another 5-7 days (as longer meant the gelatine coating degraded), and Accutase™ was used to remove the fibroblasts for cryopreservation. Of the initial pilot (2624-2626), only donor 2625 yielded viable proliferating fibroblasts when thawed into CELLnTEC PR-F medium within a 25cm^2 flask. No donors successfully thawed viable cells until the optimisation of 0.1% gelatine coated 25cm^2 flasks. However, although all donors 2740-2748 had viable thawed cells of correct morphology, they also had a yeast infection of unknown cause and were discarded.

Facial skin fibroblast cryovials were additionally obtained from Public Health England (PHE; Oxford, UK), but none of the thawed vials contained viable cells and had a significant amount of debris. However the skin donors used by PHE were predominantly geriatric, and these older skin cells tend to behave abnormally in culture.

5.3.7 Pilot study #5: Full thickness facial skin equivalent using CELLnTEC methodology

Donor 2625 (female, 52yrs) was used for the pilot facial skin equivalent, with both keratinocytes and fibroblasts thawing well and proliferating to confluency in cell specific CELLnTEC medium. Fibroblasts were passaged once before seeding into 24-well inserts. The dermis establishment of 10 days, submerged keratinocyte co-culture of 3 days, and initial keratinocyte exposure to the air liquid interface (ALI) were completed. However, from day 4 at the interface the medium below some inserts was visibly white and cloudy (Figure 5-19, A+B). When swirled and held against a dark surface, the white clouds were visible as deposits (Figure 5-19, A). More inserts followed over the next few days, and a medium test proved that contact with the skin equivalent was necessary to produce this effect (see Figure 5-19, B). By day 12 the media had changed from a cloudy liquid to form a gelatinous consistency, which thickened further over the next 6 days (Figure 5-19, C to E). Attempts at harvesting the skin equivalents confirmed that a majority had completely degraded (Figure 5-19, D+E) and media samples tested negative for mycoplasma infection. However, some formalin-fixed and fresh-frozen skin equivalents did have histological remnants, with the most intact shown in Figure 5-18. It visually confirmed the suspicion that the dermal matrix was degrading, as witnessed by the gelatinous media in Figure 5-19.

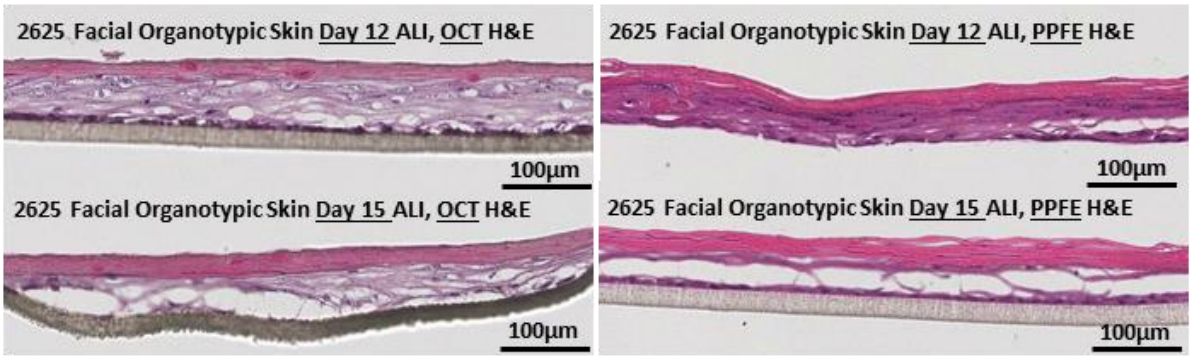

Figure 5-18: Histological H&E staining of skin equivalents developed using CELLnTEC commercial medium and facial skin-derived adult keratinocytes and reticular fibroblasts from donor 2625. Despite signs of ongoing degradation whilst at the air-liquid interface (ALI), key skin equivalent components did form. There is a keratinised stratified epidermis (~0.019mm), attached to a dermal layer (~0.05mm) which showed some ECM production by the facial reticular fibroblasts. Day 12 at the ALI is the standard duration for a completed skin equivalent, with Day 15 ALI representative of three days in culture. Histology was comparative in fixed- (PPFE) or frozen- (OCT) skin equivalent sections, with both confirming that the ECM was degrading. H&E staining was performed on three sections per FFPE/OCT-embedded skin equivalent. N=1, n=3.

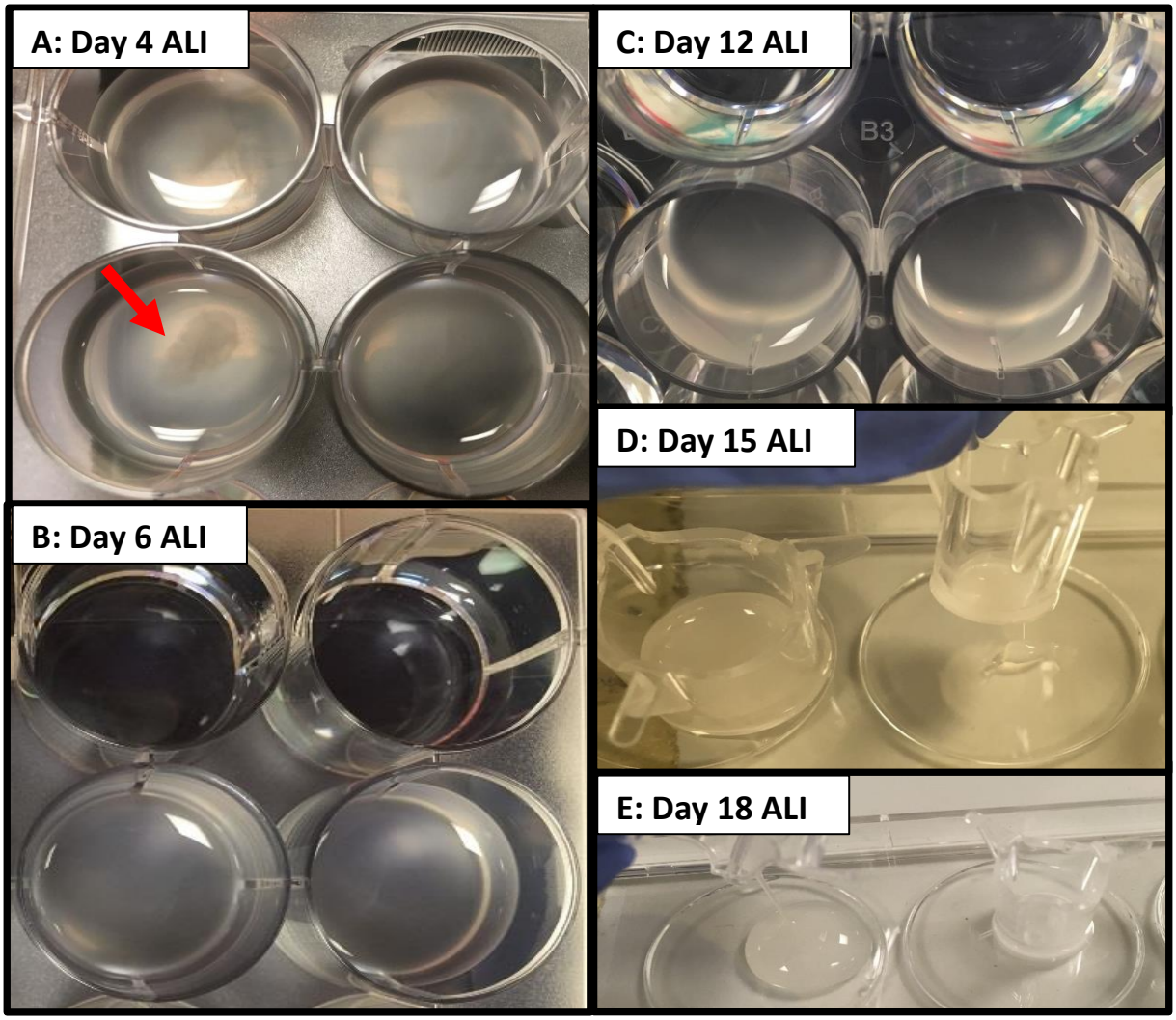

Figure 5-19: Photographs of facial skin equivalents at air-liquid interface (ALI) days 4, 6, 12, 15 and 18. Skin equivalents developed using CELLnTEC commercial medium and facial skin-derived adult keratinocytes and reticular fibroblasts from donor 2625. All skin equivalent development stages had been completed until they were raised to the ALI, and four days later the media began to present as cloudy-white (A+B). Media incubated in empty wells did not turn cloudy-white (top wells, B). At ALI day 12 the media had become a gelatinous consistency (C), which progressively increased in solidity until ALI day 18 (D+E). Failed attempts to harvest skin equivalents from the wells containing gelatinous material confirmed they had degraded.

5.3.8 Comparative overview of all CELLnTEC skin equivalent pilot studies

Investigation of the use of CELLnTEC media and methodology with in-house derived adult skin cells can be broadly grouped into five pilot studies (see Table 5-2). Overall it was evident that cells should be a low passage, with best results seen from seeding passage number 2 fibroblasts (freshly isolated and not cryopreserved) and passage number 2 keratinocytes (cryopreserved at passage number 0, revived and used). However difficulty arose with fibroblast transition from DMEM flask media to CELLnTEC proliferation medium (for skin equivalent inserts), as this was proposed by CELLnTEC as a causative factor in the pilot 2 skin equivalent contraction. Thawing passage number 0 fibroblasts into CELLnTEC proliferation medium is an alternative option, where they are expanded once before seeding into inserts as passage number 2 cells. In the skin equivalents there was variability in the dermal layer thickness, whereby the thickest models came from donors of a young age greater (S1074F – age 28 and S1142F – age 17). However not enough donors were tested to conclude this is a statistically true association. Skin equivalents could be scaled between insert sizes, but grew best in 12-well or 24-well size (possibly best as 24-well). Although there was no difference in cell proliferation and viability with frozen aliquots of medium, the histology of skin equivalents grown with 'fresh' medium showed thicker layers. However this was only tested in one donor (S1147F), the fibroblasts were passage number 4 at time of insert seeding, and the fibroblasts did not make a thick ECM in any condition tested. Moreover in pilot 4 both donors failed to display histology of a fully formed equivalent. Several factors aside from frozen aliquots of medium could have contributed to the pilot 4 result. The donor S1141F had also performed sub-optimally in pilot 2, and S1151F has not been tested before. However these were the last remaining donor-matched skin cell cryovials. The fibroblasts of these cells were also passage number 4 when seeded into inserts. In monolayer, the prolferation rate decreases rapidly from passage number 4 to 6 but they do divide. To lay down enough ECM, it is preferable to prioritise younger passage number fibroblasts in optimal proliferative condition, over extending the culture time to obtain more fibroblasts that are a higher passage number.

Donor	Adult skin cell source	Donor age at surgical date	Pilot	Number of models established	Fibroblasts – isolated& expanded in DMEM	Fibroblasts – passage number when frozen	Fibroblasts – media expanded in post thaw	Fibroblasts – Passage (P) number seeded into insert [Insert brand; well size]	Keratinocytes– isolated& expanded in Epi-life	Keratinocytes – passage number when frozen	Keratinocytes – media expanded in post thaw	Keratinocytes – Passage (P) number seeded into insert	Model contraction evident
S1073F	Foreskin	65	1	2	Yes	N/A – not frozen	N/A – not frozen	**P2** [Millipore; 12 well]	Yes	P0	Epi-life	P2	No
S1074F	Foreskin	28	1	2	Yes	N/A – not frozen	N/A – not frozen	**P2** [Millipore; 12 well]	Yes	P0	Epi-life	P2	No
S1141F	Foreskin	40	2	14	Yes	N/A – not frozen	N/A – not frozen	**P2** [Millipore; 12 well]	Yes	P1	Epi-life	P3	Yes
S1142F	Foreskin	17	2	14	Yes	N/A – not frozen	N/A – not frozen	**P2** [Millipore; 12 well]	Yes	P1	Epi-life	P3	Yes
S1145F	Foreskin	51	2	12	Yes	N/A – not frozen	N/A – not frozen	**P2** [Millipore; 12 well]	Yes	P1	Epi-life	P3	Yes
S1147F	Foreskin	53	3	14	Yes	P1	CNT-PRF	**P4** [Greiner; 6 well (x4), 12 well (x6), 24 well (x4)]	Yes	P1	CNT-PR	P3	No
S1141F	Foreskin	40	4	15	Yes	P1	CNT-PRF	**P4** [Greiner; 12 well]	Yes	P1	CNT-PR	P3	No
S1151F	Foreskin	35	4	15	Yes	P1	CNT-PRF	**P4** [Greiner; 12 well]	Yes	P1	CNT-PR	P3	No
2625	Facial	52	5	13	Yes	P0	CNT-PRF	**P2** [Greiner; 24 well]	Yes	P1	CNT-PR	P3	No

Table 5-2: Comparative summary of 3D CELLnTEC skin equivalent pilot studies

5.4 Discussion

The successful growth of a full thickness donor-matched human skin equivalent without the use of artificial scaffold is both exciting and highly novel. As previously detailed in section 1.3, most in-house methods and commercial skin equivalents incorporate a scaffold material.

Meloni *et al.* (2010) and Groeber *et al.* (2011) describe how a multi-layered skin equivalent is a welcomed mediator between conventional cell culture monolayers (lacking physiological conditions and complex cell-cell/ECM interactions), skin explants (high variability, difficult to obtain/maintain) and *in vivo* animal models (ethical considerations and anatomical/metabolism differences). A primary advantage of in-house skin equivalents is that the cellular composition is controlled by the researcher (Groeber *et al.*, 2011). The donor-matched layers, fibroblast-derived dermal matrix and stratified epidermis of the CELLnTEC skin equivalent implicate wide-ranging applications.

As fibroblasts are critical to wound healing, their natural function of extracellular matrix production (Tracy *et al.*, 2016) has been encouraged by the CELLnTEC media. Fibroblasts surrounded by their own secreted microenvironment influence epidermal growth (El Ghalbzouri *et al.*, 2009).

It is found throughout the pilots that a well-developed dermis of CELLnTEC derived skin equivalents correlated with low passage number fibroblasts. Janson *et al.* (2013) reported that using serially passaged fibroblasts in full thickness equivalents produced thinner dermis, and elevated senescence-associated biomarkers. The cells used for their equivalents were extracted from healthy surplus skin of female donors (aged 44, 56, 60 years), and their dermal layer established without scaffold in CELLnTEC media. They found that several (but not all) characteristics of aged skin can be recreated through the fibroblast passage number.

Deeper analysis of the skin equivalent morphology incorporated immunostaining for epidermal and dermal biomarkers. Cytokeratin 14 was used as a general epidermal marker (Figure 5-7) and stained positive in the skin equivalent. Skin collagen distribution alters with dermis depth (Tracy *et al.*, 2016). To visualise how the fibroblasts had structurally arranged their ECM, dermal structural proteins (collagen I and fibrillin) and the epidermal-dermal junction (collagen IV) were positively staining (Figures 5-5 to 5-7). Due to the matrix being a 3D structure, it was necessary to image several cross-sections and compress the z-stack to generate these figures.

A comparison was made with antibody labelling of collagen and the label free approach of second harmonic generation (SHG) (Figures 5-9 and 5-16). Both were performed on a cryosection of the same embedded sample, but consultation of the results with Dr Glyn Nelson (Newcastle University) did not find any distinct advantages from visualising collagen with SHG. Any advantage would be related to saving time or antibody. Whilst SHG was successful

in a section of frozen-embedded skin equivalent, it was much less successful in an attempt to generate live signal from a 3D intact skin equivalent (Figure 5-16). However this may benefit from being repeated with a well-established skin equivalent, as the one used from donor S1147F did not have a good dermis (Figure 5-15). It was clear that the skin equivalent would have to be removed from the hanging insert, so repeat live imaging throughout an extended experiment would not be feasible. To generate strong imaging for marketing purposes and localised data relating to test compounds, a better approach would be the use of label-free MALDI-MS imaging. In the last few years, this method has emerged in the skin literature relating to topical AOX penetration and distribution profiles of metabolites, lipids and proteins (Enthaler *et al.*, 2013; Mitchell *et al.*, 2016; Hochart *et al.*, 2019; Vanickova *et al.*, 2019). Innovenn have published using MALDI-MS imaging to assess wound-healing in Labskin™ commercial skin equivalent (Lewis *et al.*, 2018). Innovenn kindly supplied some Labskin™ skin equivalents for this work. Unfortunately they stained weak or negative for dermal matrix proteins, yet both cytokeratin 14/collagen I stained positive in the epidermal layer (Figure 5-8). It appeared that suspending fibroblasts within a fibrin gel (Bojar, 2015) had inhibited their capacity to secrete matrix proteins into the inter-cell space. It appeared as if the collagen I was pushed out of the matrix into the epidermis, sitting atop the fibrin gel. Publications of Labskin™ that include immunostaining or MALDI-MS imaging focus on epidermal labelling, and advocate Labskin™ for use in skin barrier associated areas such as psoriasis (Harvey *et al.*, 2016), wound-healing (Lewis *et al.*, 2018), and microbiome (Bojar, 2015).

The barrier properties of full thickness skin equivalents are closer to *in vivo* skin than epidermal equivalents, and contain all human skin lipids (Mathes *et al.*, 2014). Whilst a dry stratum corneum was visible on CELLnTEC skin equivalents and present in H&E histology sections, it was unexpected that a common lipid stain (Oil red O) didn't have positive stratum corneum staining of skin equivalents or control samples of *ex-vivo* foreskin (data not included). Despite various protocol comparisons and amendments, this negative staining could not be explained. However a recent publication had positive Oil red O lipid staining of a foreskin cell derived full thickness skin equivalent with two key protocol differences: the fixation step was 1 hour and the mountant was 50% glycerol (Muresan *et al.*, 2019). Nevertheless, the dry stratum corneum of the CELLnTEC skin equivalent was suitable for formulation application and surface irradiation with solar light. After solar irradiation, there was a 16-fold (4 C_t) increase in mtDNA damage compared to a foil-protected skin equivalent from the same donor (Figure 5-14).

The final area of skin equivalent development surrounded the sources of donated skin. A majority of commercial skin equivalents, primary cells and cell lines in the literature are sourced from adult or neonatal foreskin. Generally these resources are also pooled from multiple donors.

A common secondary source of surplus skin is from breast or abdominal surgery, but it is more technically difficult to isolate viable cells from these regions. Yet, these three areas are rarely exposed to environmental stressors (covered by clothing), are not typical sites for skin diseases (e.g. psoriasis, eczema), and are not the intended site of application for cosmetic formulations. It is recognised that skin around the body and even within the same region (e.g. face) differs in laxity, thickness, topology, pH, temperature, moisture and microbiology (Wong *et al.*, 2016). In addition, these factors are also affected by race, age, sex, lifestyle (e.g. obesity), and pathologies (Wong *et al.*, 2016).

It was observed that foreskin derived skin equivalents were thin, and it was queried if this was a result of 1) human skin equivalents containing only two cells types and no accessory structures/hypodermis, or 2) that the fibroblasts of thin skin (e.g. foreskin) secreted a reduced or different composition of matrix to fibroblasts of thicker skin (e.g. abdomen). To test this hypothesis a pilot was designed to compare the fibroblasts of adult foreskin and abdomen in the CELLnTEC medium used to support dermal layer formation (Figures 5-18, 5-19). Abdomen-derived fibroblasts were used because access to facial skin was not available at the time of this experiment. In this experiment some fibroblasts were treated with a commercial 'extracellular matrix boost' medium to see if the secreting capacity could be upregulated, and if this increase would lay down as protein (Figure 5-19). Unfortunately, we were unable to obtain two samples from the same donor, but two donors were chosen for their matched age, sex, ethnicity, and cell passage number. ELISA successfully detected differences between the donor sites, and the commercial medium induced 5X more collagen I production (but not fibronectin or hyaluronan). Whilst it is not definitive if the differences in this data were a result of donor- or site- variability, the techniques used in this pilot were successful at detecting differences. If samples were obtained from multiple sites on the same donor, this would be highly novel and informative data for the dermatology field. There is one research group that has published on the differing mechanical properties of dermal fibroblasts from different sites (Kuang *et al.*, 2015; Xu *et al.*, 2017). The only other research found on multi-site comparison was a study investigating the effect of fibroblast donor site on epidermal differentiation in a full-thickness skin equivalent (Konstantinova *et al.*, 1998). They used foreskin derived keratinocytes and fibroblasts isolated from the breast, trunk, arm, face, and earlobe of fifteen normal skin donors. The fibroblasts were seeded into rat collagen, and keratinocytes seeded onto the gel-based dermal layer. In addition, they sourced eyelid fibroblasts from nine donors, and found all supported the formation of a well differentiated and stratified epidermis. It is worth noting from this study that whilst all facial fibroblast donors supported epidermal development, other regions (e.g. breast and arm) had differences between donor capabilities to support this

development. However, beyond this study there is a lack of information understanding the role of regional skin cells on skin equivalent function. As a result, there are questions surrounding what area of skin we are representing in skin equivalents and the translational impact of this on the data generated.

To address this, a comparison between facial and foreskin derived skin equivalents was designed to investigate if the same data was obtained with antioxidant product testing. To our knowledge, there has been no data published with 100% facial skin cell-derived skin equivalents and it is unknown if a working protocol exists.

Protocols for isolation and culture of primary skin cells had to be optimised for facial skin (see 5.3.6). The use of ROCK (apoptosis) inhibitor (Y-27632) to increase the yield of facial-skin derived keratinocytes is controversial. The advantage is that it ensures that proliferative keratinocytes will be isolated from facial skin, even if the sample is very small. Chapman *et al.*, (2014) analysed the gene expression of adult human keratinocytes cultured with or without 10μM Y-27632 ROCK inhibitor, which is the same compound used in this thesis for facial keratinocyte starter culture. The study found that the genes most significantly down-regulated are necessary for keratinocyte differentiation, but that this was reversible when Y-27632 was removed (Chapman *et al*., 2014). Mi *et al*. (2019) showed that addition of Y-27632 for two days in the starter culture of primary melanocytes dramatically increased the yield, and that this could be attributed to their finding that Y-27632 significantly upregulating keratinocyte stem cell factor expression. There is concern that the addition of Y-27632 selects for highly proliferative progenitor (stem cell-like) keratinocytes, but that you may be selecting for holoclones at the expense of meroclones and paraclones (Barrandon, Y. and Green H. (1985); Dellambra *et al*. (2000); Nanba, D. (2019), Generally it raises the question of keratinocyte population functional quality over quantity. However as Y-27632 was only incubated for a short duration, it remains an option for isolating keratinocytes from small skin samples that are difficult to obtain e.g. face.

There were observational differences in the culture of foreskin and facial skin cells. Whilst the facial site information was requested (e.g. cheek, eyelid etc.), the donor consent form only recorded and disclosed the sex and age (Table 2-2). Facial keratinocytes proliferated at a greater rate, and facial fibroblasts appeared to prioritise matrix production over cellular proliferation as they could not be removed from the flask surface (unless pre-coated with gelatine). There was substantial variability between facial donors for the capacity to isolate proliferative primary cell cultures, but this doesn't account for the fact that foreskin samples were more readily available than facial skin samples. Therefore the statistical variability between facial and foreskin donors may not be as prominent when the sample size is accounted for. Only one facial

donor completed the entire skin equivalent process, but there was breakdown of the dermal matrix over time (Figures 5-20, 5-21). This had never been seen in-house with foreskin donors, but Konstantinova *et al.* (1998) allude to a similar phenomenon with their skin equivalents (facial fibroblast/foreskin keratinocyte-derived) when they describe a short experiment time of 14 days because '*the proliferative rate of the cells decreases after 14 days, and by day 21 a thick stratum corneum remains but there is no dermis layer'*. It is also interesting that eyelid-fibroblasts produced a skin equivalent almost twice as thick as that from normal skin-fibroblasts of other regions (Konstantinova *et al.*, 1998). It is worth noting that this paper describes how the stratum corneum thickens over time, which was also observed in pilot #2 (Figure 5-11) of this thesis. This is inevitable given that no skin equivalent to date undergoes desquamation. The implications of this for time-course experiments in equivalents is to be noted, whereby an experiment with repeat topical applications would be affected by the continued thickening of the stratum corneum. Indeed, Asselineau *et al.* (1986) reported that unlike in-vivo epidermis, the reconstructed epidermis continues to stratify (and thicken) for as long as 20 days.

As facial skin samples are typically small and produce limited cell numbers, the skin equivalent was successfully scaled down to 24 well size. Relative to the standard 12-well, 24-well foreskin- and facial- derived skin equivalents were more compact, slightly thicker and easier to process for histology. In addition, having several 24-well skin equivalents produces less artefact than separating each 12-well skin equivalent into sections by scalpel. Whilst most commercial inserts are available as a 24-well size, corresponding 24-well plates for raising skin equivalents to the air-liquid interface are not available from leading companies (Millipore, Greiner, CELLnTEC). However, towards the end of this work, Thermo Fisher filled this gap in the market with their Nunc™ consumables range. This is a practical option that would save on the required volumes of expensive CELLnTEC media.

To determine the extent of inter-donor and inter-skin equivalent variability, ELISA was used to compare levels of secreted proteins in the medium (Figure 5-17). This is a useful technique for quality control purposes of skin equivalent batches. This technique could also be used to address a limiting factor of this work whereby it was unknown which donors would produce good skin equivalents. An overview of all trials (see Table 5-2 and section 5.3.8) determined that the best donors were of young biological age and had low passage number cells. However, in this research group the consent forms are collected and sent monthly. This means that the donor age mightn't always be accessible before the fibroblasts are ready to be seeded for skin equivalents, and successful skin equivalent formation remains unknown until histological analysis. As such, considerable time and resources are used inefficiently. For future work I recommend the use of protein ELISA to screen fibroblast donors for their secretory capacity of ECM protein (e.g.

collagen I) in the proliferative monolayer stage (70% confluent) at passage number 0 or 1. Alternatively, as this work was performed in an external ELISA equipped lab, a student project could be to find an alternative protein detection assay. Whilst the QuickZyme™ kit was not sensitive enough to detect collagen within the provided range of standards, there may be alternative options. This would give an indication if the fibroblasts of a donor should be seeded into inserts for 3D skin equivalents, frozen for future 3D skin equivalents, or passaged further for different experiments. In addition, until the rate of inter-skin equivalent variability is established, it is advised to continue with three skin equivalents per condition as throughout this thesis and in some literature e.g. Konstantinova *et al.* (1998).

Whilst facial fibroblasts were the limiting factor for continuation of this work on facial-derived skin equivalents, a large stock of facial keratinocytes were preserved as a result of this work. These could be used for reconstructed human epidermis skin equivalents (see 5.2.2. and supplementary Figure 9.4) or seeded on top of a foreskin fibroblast derived dermis (of a donor similar in biological age).

Overall, the successful growth of human skin derived skin equivalents that are scaffold-free, donor-layer matched, and 100% human derived in <1% serum medium is an exciting and novel outcome. Several immunostaining, ELISA, western, and cell culture protocols have been generated from this work. Experiments combining the antioxidants introduced in chapter 4, skin equivalents outlined in this chapter, and transition to topical applications are discussed in chapter 6.

5.5 Summary of findings

- CELLnTEC commercial medium and protocol for the establishment of full-thickness human skin equivalents worked successfully with in-house derived cells
- The CELLnTEC skin equivalents were all scaffold-free, with donor-matched layers, and antibiotic/serum-free medium
- Fibroblasts secreted the dermal structural matrix, with the thickness and robustness limited by donor biological age and fibroblast passage number
- The keratinocyte passage number should match the fibroblast, with both at P0 or P1 upon seeding
- CELLnTEC derived skin equivalents had correct histology (H&E) and stained positive for key biomarkers indicative of a fibroblast secreted extracellular matrix
- Immunostaining of commercial Labskin™ determined a lack of extracellular matrix proteins in the dermal compartment

- Label-free imaging of CELLnTEC skin equivalent collagen could be performed on frozen sections using second-harmonic-generation (SHG), but not in skin equivalents within their inserts
- CELLnTEC skin equivalents were successfully scaled to 24-well insert sizes
- Protein ELISA of collagen, fibronectin and hyaluronan in stored cell medium demonstrated differences between donors and anatomical sites
- Western blot confirmed that ELISA data for collagen secretion is laid down in the skin equivalent
- A protocol for the isolation and culture of facial skin cells was created
- Facial keratinocytes are highly proliferative in culture, and facial skin equivalents may need a reduced number of days stratifying at the air-liquid-interface (ALI)
- A pilot of facial skin cell derived skin equivalents had progressive dermal degradation throughout the air-liquid interface phase
- Recommendations for future advancement are outlined in the chapter discussion e.g. MALDI-MS imaging, donor screening for skin equivalent suitability etc.

Chapter 6: Antioxidant formulation testing in whole skin ex-plant and full thickness skin equivalents

6.1 Chapter overview and aims

Antioxidant formulation testing was performed using acellular sun protection factor (SPF) testing in response to solar simulated light, alongside topical application to human skin equivalents and human ex-plant skin (foreskin and facial). These skin equivalents were tested for the antioxidant capacity to protect against solar light induced damage to mitochondrial DNA in human skin. This work also aimed to investigate if the protection seen in skin cell monolayers with direct antioxidant exposure (Chapter 4) translated through to more complex 3D model systems with antioxidants delivered in cream formulation.

6.2 Chapter specific methods

6.2.1 Human skin equivalent culture conditions

Labskin™ (Innovenn) full thickness human skin equivalents arrived within 24 hours of dispatch at room temperature within solidified medium gel. They were transferred to a Greiner ThinCert™ 12-well deep culture plate containing 4.5ml/well of Labskin™ maintenance medium (supplemented with 1% PSA) and acclimatised overnight at 37^{o}C, 5% CO_2. The medium was replaced on day 2 (i.e. skin equivalent day 29, see Figure 6-10) immediately prior to formulation application. In-house full thickness human skin equivalents were grown using CELLnTEC commercial medium and methodology as described in Chapter 5. Experiments were performed the day after skin equivalent completion (day 29, see Figure 6-10) with CELLnTEC PR-FTAL medium (supplemented with 1% PSA) replaced prior to formulation application.

6.2.2 Human ex-plant skin culture conditions

Tissue was used if collected on the day of surgical removal, where it was stored at 4^{o}C submerged in transport media (DMEM with 2% PSA). Subcutaneous tissue and vasculature were removed from skin submerged in PBS-2% PSA prior to taking 4mm diameter punch biopsies. Individual biopsies were placed "epidermis-up" in 24 well ThinCert™ 0.4µm PET transparent hanging inserts (Greiner), suspended above 500µl DMEM, and acclimatised to culture conditions overnight at 37^{o}C, 5% CO_2. Experiments were performed the following day.

6.2.3 Human ex-plant skin metabolic viability testing

To detect skin metabolic viability the culture medium underneath the hanging insert was replaced with 500µl 3-(4, 5-dimethylthiazol-2-yl)-2,5-diphenyltetrzaolium bromide (MTT; Sigma M2128) at a final concentration of 1mg/ml (diluent: complete DMEM) for 2 hours at

37°C, 5% CO_2. Formed formazan (purple) was dissolved by free-floating the biopsy in a 15ml tube containing 700µl freshly made acidified isopropanol (1µl 37% (12M) HCL per 1ml isopropanol). This was parafilmed twice and stored overnight at 4°C. Absorbance was read at 570nm with SpectraMax™ (Molecular Devices), and blank corrected for acidified isopropanol.

6.2.4 Irradiation of human ex-plant skin and full thickness human skin equivalents

Skin equivalents within hanging inserts were transferred to a standard well plate containing room temperature PBS instead of media. They were irradiated with a solar simulator as described in section 2.2.2 and immediately placed onto wet ice prior to harvesting (see 6.2.1.6).

6.2.5 Confirmation of skin barrier integrity using lucifer yellow stain

To determine barrier integrity post-solar irradiation, ex-plants were stained with lucifer yellow as follows. Lucifer yellow CH salt (L0259, Sigma) was dissolved to 1mM solution in PBS, 0.22µm sterile filtered, and stored light protected at 4°C. The stain was pipetted onto the stratum corneum and incubated for 2 hours at 37°C. The sample was formalin fixed overnight at 4°C within a cassette, washed with PBS and OCT embedded. Cryosections (8µm) air-dried for 1 hour at room temperature in the dark, were briefly rinsed with distilled water and mounted with ProLong™ Diamond Antifade with DAPI (Invitrogen). Images were acquired with Dr Glyn Nelson at Newcastle Bio-Imaging Unit using a Nikon A1R confocal microscope equipped with a 10x 0.45NA objective. DAPI was excited with 406nm diode laser and lucifer yellow with the 457nm line from an Argon laser as sequential images with 425-475 and 570-620nm bandpass filters respectively. PMT gains, pixel dwell time and density were kept constant for all images.

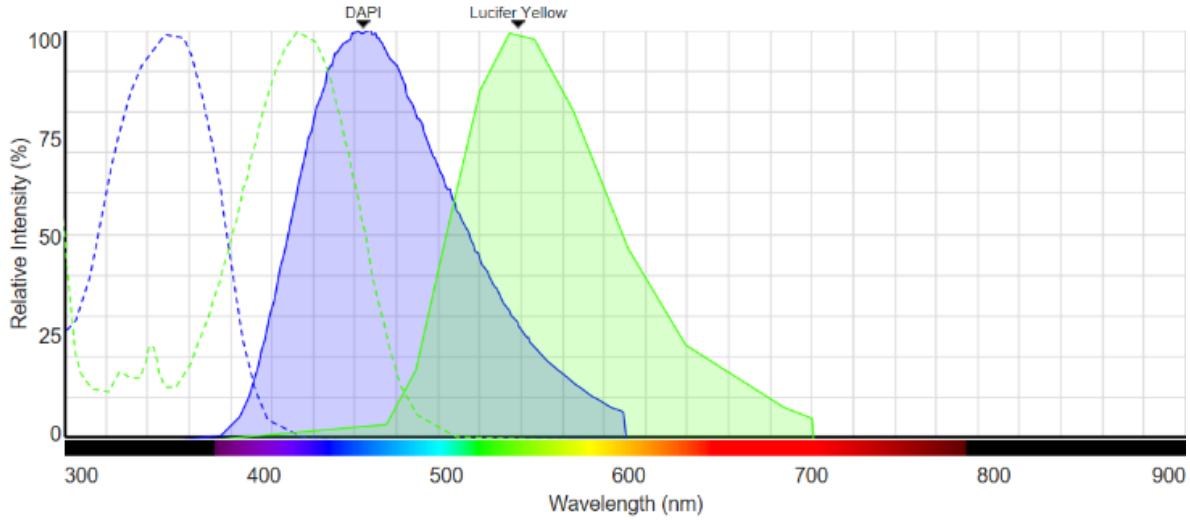

Figure 6-1: Schematic of lucifer yellow excitation and emission spectra, alongside DAPI excitation and excitation spectra. To account for skin autofluorescence in the spectrum green region, Lucifer yellow was excited at 457nm whilst DAPI was excited at 405nm. Image source: Florescence SpectraViewer on ThermoFisher.com.

6.2.6 Harvesting of human ex-plant skin and full thickness human skin equivalents

Ex-plant skin equivalents were immediately snap frozen on dry ice and stored at -80°C pending DNA extraction as outlined in section 2.3.

Labskin™ skin equivalents were harvested as outlined in Figure 6-2, whereby half of each equivalent had a different cream applied. Therefore the middle quadrants were used for DNA extraction because they had the least surface area contact with the opposite testing side (Figure 6-2). CELLnTEC skin equivalents were also harvested in this manner, but the epidermis was not removed. After solar irradiation, individual skin equivalents were removed from their inserts by scalpel, divided and peeled into layers (if appropriate) with flame-sterilised fine surgical tweezers. Samples were immediately snap-frozen on dry ice and transferred to -80°C. Skin equivalents remained chilled on wet ice while individually processed as quickly as possible. OCT embedding was performed last over liquid nitrogen, with blocks stored at -80°C.

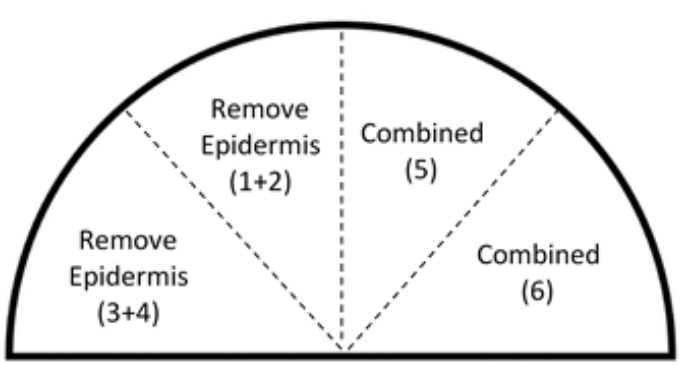

1. Epidermis -> Snap freeze & store at -80°C for DNA extraction
2. Dermis -> Snap freeze & store at -80°C for DNA extraction
3. Epidermis -> Snap freeze & store at -80°C for reference material
4. Dermis -> Snap freeze & store at -80 for reference material
5. Combined -> Snap freeze & store at -80°C for DNA extraction
6. Combined -> OCT embedding

Figure 6-2: Schematic of Labskin™/CELLnTEC skin equivalent harvest, whereby half of each skin equivalent was used per cream. Whilst Labskin™ epidermis could be removed, CELLnTEC skin equivalents remained as combined layers.

6.2.7 Formulation composition, storage and dose

Formulations were synthesized by GSK collaborators (Weybridge, UK), which were stored light protected at 4°C. The formulation composition and experimental IDs are summarised in Table 6-1.

Comparative market standards were La Roche Posay Anthelios™ XL Sun Lotion (SPF 50+), Olay Total Effects™ Anti-Ageing Moisturiser (SPF 15), and Olay Regenerist™ 3 Point Super Age Defying Moisturiser (SPF 0). Creams were used at 2mg/cm^2 for SPF testing and application to human skin equivalent surfaces, but 20mg/cm^2 for ex-plants due to the minute surface area and minimum weighing capacity of 1mg. See 6.2.8 for more information.

Function	Ingredient	EXP142169-13	EXP142169-14	EXP142169-15	EXP142169-16
Water	Aqua	75.63	75.78	75.53	75.88
Functional ingredient	Sabiwhite	0.25	0	0.25	0
Functional ingredient	Pterowhite	0	0.1	0.1	0
Functional ingredient	Niacinamide	4	4	4	4
Humectant	IPD	1.5	1.5	1.5	1.5
Humectant	Glycerin	5	5	5	5
Humectant	Panthanol	1.5	1.5	1.5	1.5
Humectant / Stabiliser	Pentylene Glycol	5	5	5	5
Stabiliser	Hydroxyacetophenone	0.5	0.5	0.5	0.5
Emulsion Lipids	Isostearyl Isostearate	0.256	0.256	0.256	0.256
Emulsion Lipids	Cetyl Alcohol	0.426	0.426	0.426	0.426
Emulsion Lipids	Behenic Acid	0.256	0.256	0.256	0.256
Emulsion Lipids	Behenic Alcohol	1.207	1.207	1.207	1.207
Emulsion Lipids	Dicapryl Carbonate	4	4	4	4
Emulsion Lipids	Hydrogenated Lecithin	0.355	0.355	0.355	0.355
Polymer	Sepimax Zen	0.12	0.12	0.12	0.12

Table 6-1: GlaxoSmithKline formulation composition ingredients. Each contain a base functional antioxidant niacinamide (NAM; 4%) alongside test antioxidants of interest tetrahydrocurcumin (THC; Sabiwhite™, 0.25%) and/or pterostilbene (PTERO; Pterowhite™, 0.1%). To protect GSK proprietary information, these formulations were given identification codes before dispatch to Newcastle University e.g. EXP142169-13. All values represent percentage composition (% w/w).

6.2.8 Application to human skin ex-plant

Creams were weighed (0.00125g per half 4mm biopsy) by dipping sterile 200µl pipette tips into formulation and transferring into small plastic weigh boats on a KERN analytical balance (model: ABT 100-5M). They were immediately applied by placing the biopsy onto the cream with the stratum corneum (SC) facing downwards. Using fine surgical tweezers, the biopsy was rotated in a circular motion ten times in each direction with applied pressure. The biopsy was turned SC-upwards, returned to the insert and left for 10 minutes to allow for permeation of the formulation before returned to culture conditions.

6.2.9 Application to human skin equivalents

Formulation spreaders were prepared by rapidly rotating each glass pasteur pipette (between hands) over a blue flame to create a rounded bulb end. These were sterilised by oven baking at 100^{o}C for 24 hours within a metal container. A Gilson Microman M25 (3-25µl) positive displacement pipette (with Gilson CAP PISTONS CP25 tips) was used to transfer creams onto the stratum corneum, after establishing the volume (µl) equating to 2.2mg on a KERN analytical balance (model: ABT 100-5M). For 12-well size skin equivalents (Labskin™ and CELLnTEC), half a skin equivalent (1.1cm^2) was dosed with 4µl GSK formulations, 3.5µl La Roche Posay, or 4.5µl Olay. Once applied, it was immediately rubbed in circular motions with the spreader. After 10 minutes skin equivalents were returned to culture conditions.

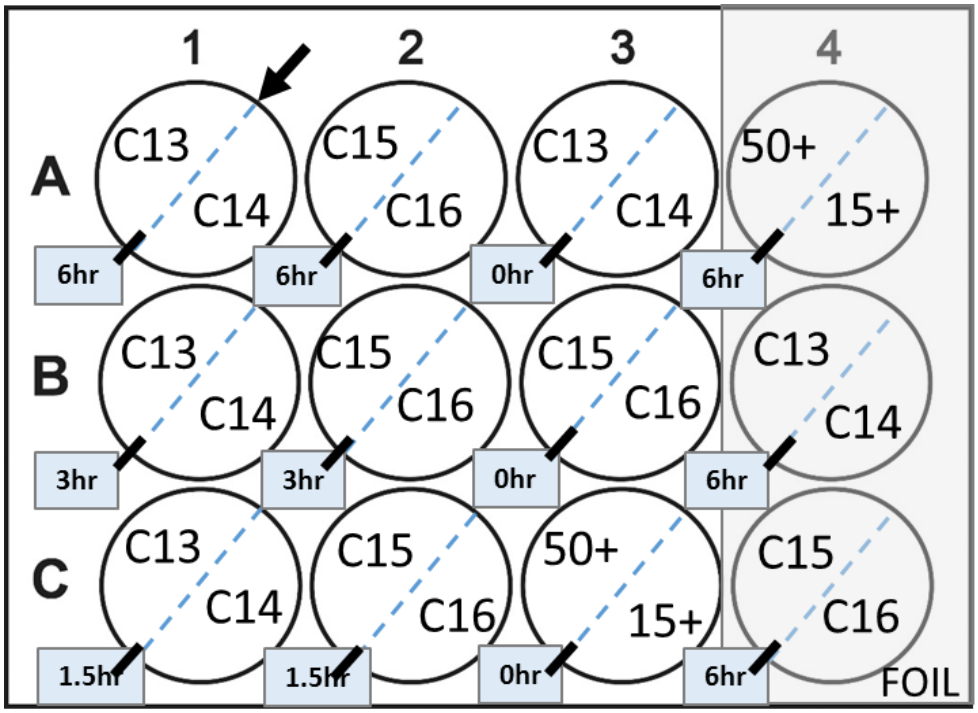

Figure 6-3: Schematic of Labskin™/CELLnTEC skin equivalent cream application, whereby half of each skin equivalent was used per cream. Cream formulations were pre-incubated on skin equivalents for 0, 1.5, 3 or 6 hours prior to solar irradiation with 2.16 SED (CELLnTEC), 5 SED (Labskin™) or foil protection (0 SED). The standard erythemal dose (SED, J.m-2) is equivalent to an erythemal radiant exposure of 100 J.m-2. Labskin™ required the same irradiation dose as whole skin due to its physical thickness (See Table 6.2). A niacinamide base (C16) was compared to niacinamide + tetrahydrocurcumin (C13), pterostilbene (C14), or both (C15). Market controls included 50+ or 15 SPF.

6.2.10 Acellular formulation solar irradiation (broad spectrum SPF testing)

Formulations were applied at 2mg/cm^2 onto Transpore surgical tape coated quartz dish or PMMA plate. This was evenly spread in circular motion with a gloved finger, and immediately irradiated with a Newport solar simulator as previously described (see 2.2.2). To determine if the formulations could absorb/physically block some of the UV, live irradiance data (mAmp) was recorded from the radiometer directly underneath the quartz dish/PMMA plate. Test formulations were compared to market standards of known SPF (0, 15 and 50+).

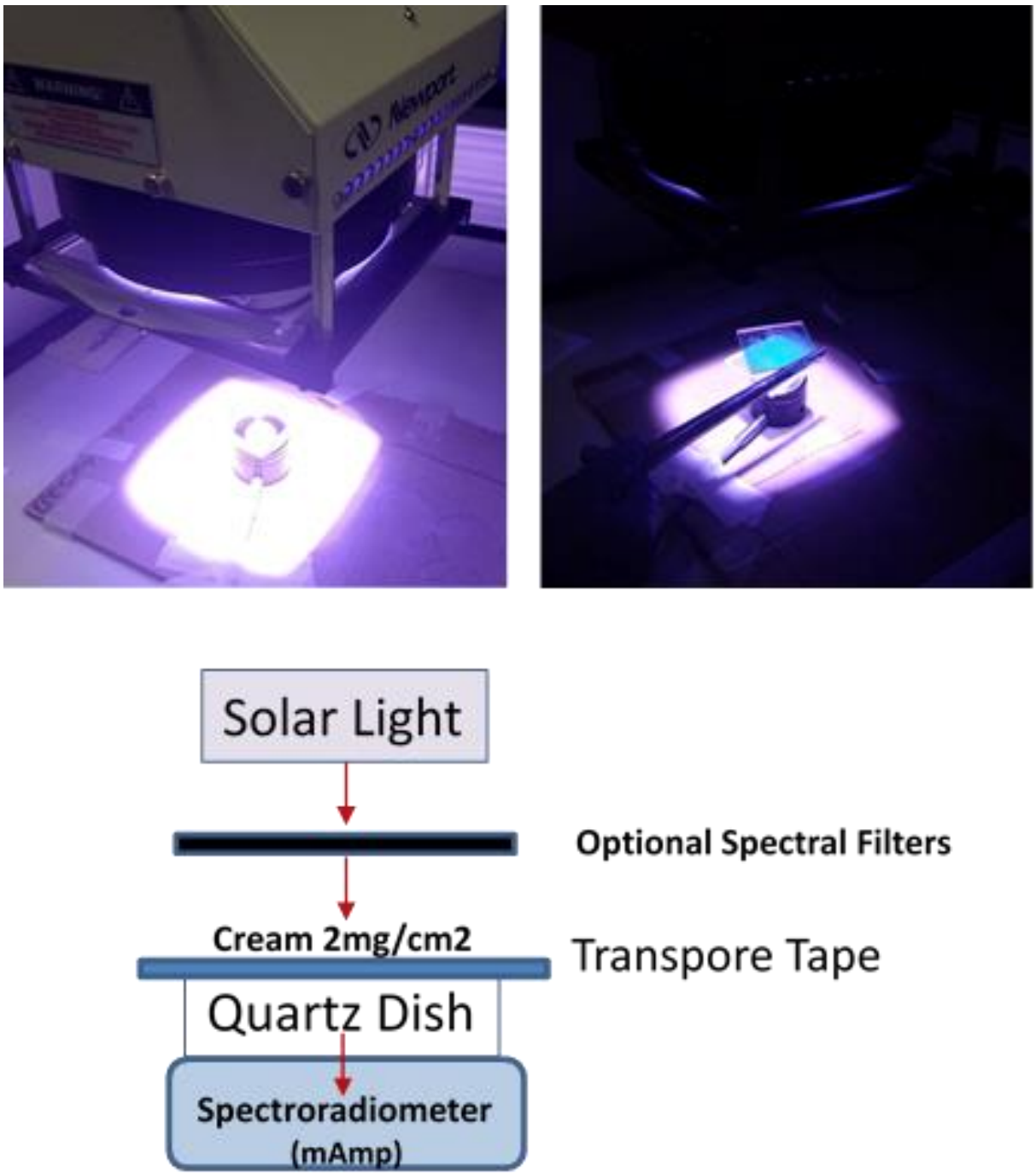

Figure 6-4: Schematic/photographs of *in-vitro* solar protection factor (SPF) testing method. Solar simulated light from a Newport simulator is passed through a quartz dish onto a spectroradiometer. The quartz dish is coated with Transpore surgical tape (with negligible blocking capacity), which topical applications can be applied across the surface area at a recommended dose of 1-10mg/cm^2. Filters can be used to block specific parts of the solar spectrum e.g. infrared.

6.2.11 Data analysis of mitochondrial DNA protection

Formulations applied to human skin equivalents or ex-plant skin were testing for mitochondrial DNA damage using the qPCR methods outlined in Chapter 3. The formulations were not removed prior to DNA analysis because the application method chosen (see 6.2.8-6.2.9) ensured it was absorbed ('rubbed' in) and therefore was not sitting on the surface. Data for each donor (CELLnTEC skin equivalents or ex-plant biopsies) was generated from one qPCR plate, with housekeeping qPCR run immediately beforehand to ensure equal starting levels of mtDNA in diluted samples. Labskin™ was the one experiment where the number of samples did not fit onto one qPCR plate. As it required three qPCR plates, one DNA control sample was re-run on all plates to determine inter-run variation, and controls from all plates were grouped for analysis.

Statistical analysis was performed with reference to Yuan *et al.* (2006) and performed on raw C_t values, whereby all non-irradiated controls were first grouped as a control column. Each donor was analysed individually. A one-way ANOVA with Dunnett's post-hoc test was used to determine significance between the mean treated and control C_t values.

To generate a graph, C_t differences for each donor were converted to relative fold change ratio ($2^{\Delta Ct}$) and presented as mean±95% confidence intervals. The mean of controls was first subtracted from each treated condition ($\Delta C_{t\,=}\, \Delta C_{t\,(treated)} - \Delta C_{t\,(control)}$). In addition, the mean ± standard deviation of grouped donor C_t values were used to illustrate variation and overall trend.

6.3 Results

6.3.1 Optimisation of whole skin ex-plant model system

6.3.1.1 *Whole skin ex-plant experiments are best performed at their metabolic peak (day 1), after overnight acclimatisation to culture conditions*

Ex-plant biopsies were taken from two foreskin and one facial skin sample on the day of surgical removal. As whole foreskin is a shared departmental resource and facial skin is a small sample, with 8 punch biopsies required per donor this was the minimum number of samples required to confirm that the biopsies acclimatise to culture conditions overnight and are therefore viable for experimentation. Each were maintained in hanging inserts as outlined in 6.2.2, with metabolic viability determined by the tissue capacity to reduce MTT to formazan (see 6.2.3). Viability was calculated relative to the day 0 baseline metabolic capacity of each donor, with metabolic peak maintained at day 1 for all tissues tested. After day 1, two foreskin donors metabolism decreased by approximately 25% every 24 hours until a plateau at around day 5. Although they shared the same trend (%), individual raw data demonstrated that the 27-year-old donor (14552) produced more formazan than the 41-year-old (14551) from days 0-2. The facial donor maintained metabolic capacity in culture for the entire 7 days.

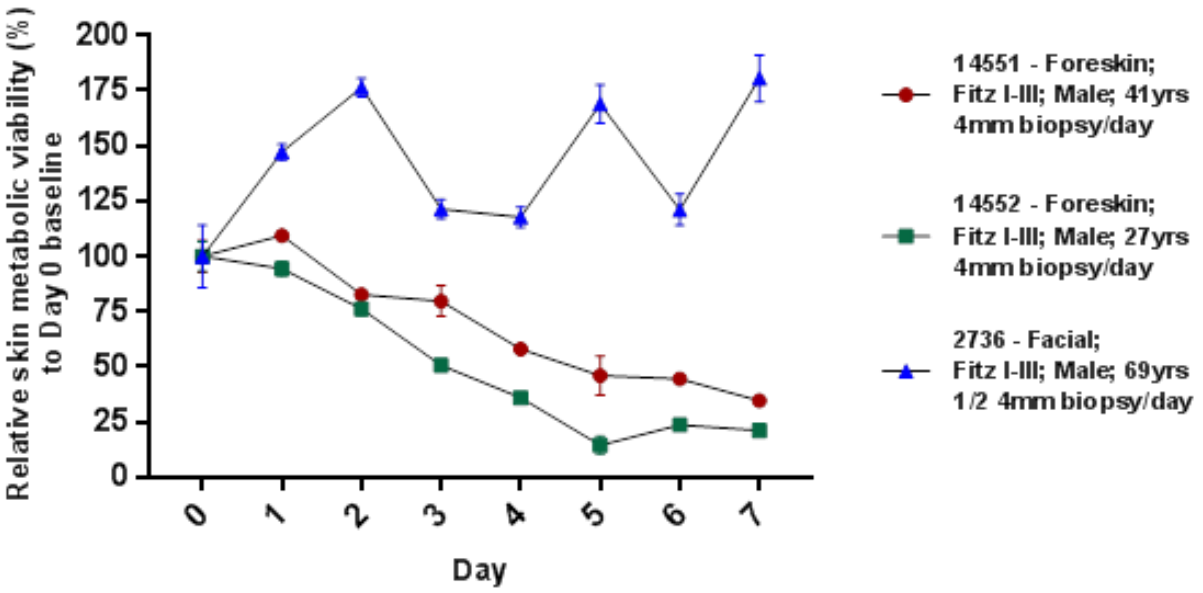

Figure 6-5: Mean skin metabolic viability over 7 days in culture. Viability relative to a day 0 baseline performed on the day of surgical removal. Whole skin explant 4mm punch biopsies from two foreskin (14551 – male, age 41, 14552 – male, age 27) and one facial (2736 – male, age 69) donors were maintained in culture, with one punch biopsy tested every day for its' capacity to reduce MTT to formazan. Data presented as mean ± SD; N=1, n=3 per donor.

6.3.1.2 *Foreskin explant (4mm) obtained significant mtDNA damage from ≥4 SED complete solar irradiation*

Ex-plants from three foreskin donors were acclimatised to culture conditions overnight and irradiated as described in 6.2.4 (and 2.2.2) in a dose dependent manner of 0, 2, 4, 6, and 8 SED, whereby 1 standard erythemal dose (SED, J.m-2) is equivalent to an erythemal radiant exposure of 100 J.m-2. The 2 SED dose routinely used for monolayer and thin human skin equivalents did not induce a detectable amount of mtDNA damage in whole skin ex-plants. However, a mean 2.2 C_t (5-fold) was detected at 4 SED, with a marginal increase to 2.5 C_t (5.7-fold) at 6 SED. Only 2 of 3 donors were able to detect damage at 8 SED as one donor (14526 – age 46) was particularly susceptible to solar irradiation and did not have enough intact mtDNA to produce 11kb amplicons in the qPCR assay of Chapter 3 (as demonstrated by melt product temperature). To account for donor variability in damage susceptibility as well as a representative solar exposure dose, 5 SED was chosen from this data as an optimal experimental dose.

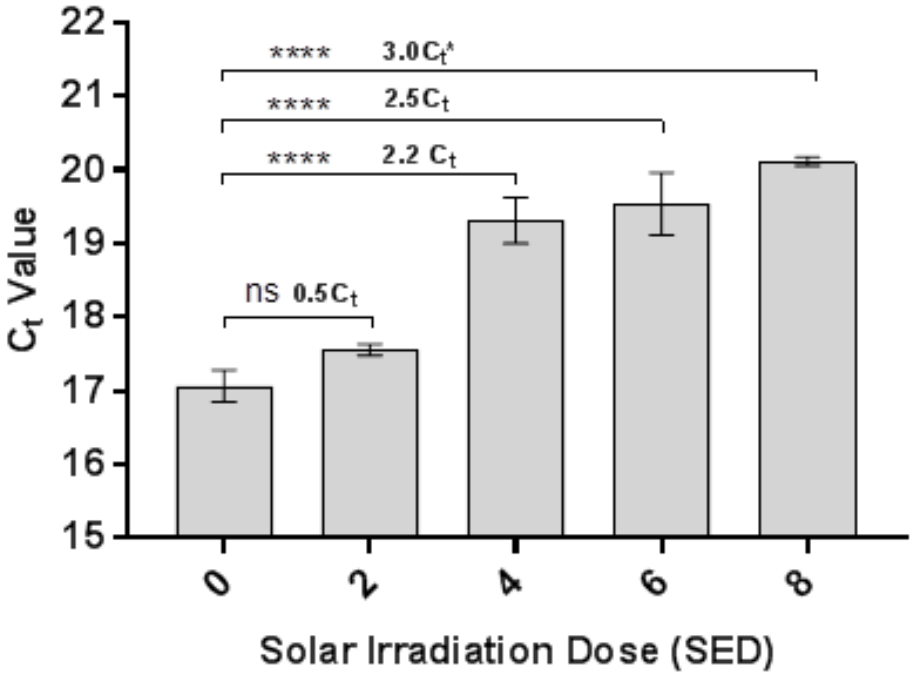

Figure 6-6: Dose response of solar irradiation (0-8 SED) on mtDNA damage to whole skin foreskin ex-plants. Significant damage was detected from 4 SED, with the maximum damage capacity for one donor reached by 8 SED. A dose of 5 SED was determined an optimal solar irradiation dose, for detection by 11kb qPCR assay. The standard erythemal dose (SED, J.m-2) is equivalent to an erythemal radiant exposure of 100 J.m-2. Total DNA was analysed for mtDNA damage by the housekeeping and 11kb qPCR assays of Chapter 3. Mean ± SEM generated from three adult male foreskin donors (14525 – age 56), 14526 (age - 46), 14527 (age 67) for 0-6 SED (N=3, n=9) or 8 SED (N=2, n=6). Significant difference to 0 SED detected by one-way ANOVA with Dunnett's post-hoc test **** $p<.0001$ ns $p>.05$

6.3.1.3 *A solar simulated dose of 5 SED does not damage skin barrier integrity or diminish metabolic viability*

Ex-plants from three adult male foreskin donors (14525 – age 56, 14526 – age 46, 14527 – age 67) were acclimatised to culture conditions overnight and irradiated in a dose dependent manner of 0, 2.5, 5, and 7.5 SED (see 6.3.2 and 2.2.2). The standard erythemal dose (SED, J.m-2) is equivalent to an erythemal radiant exposure of 100 J.m-2. These were tested for barrier integrity with lucifer yellow stain and metabolic viability with MTT assay. An experimental dose of 5 SED solar irradiation did not disrupt barrier integrity or reduce metabolic viability of the skin (Figure 6-7).

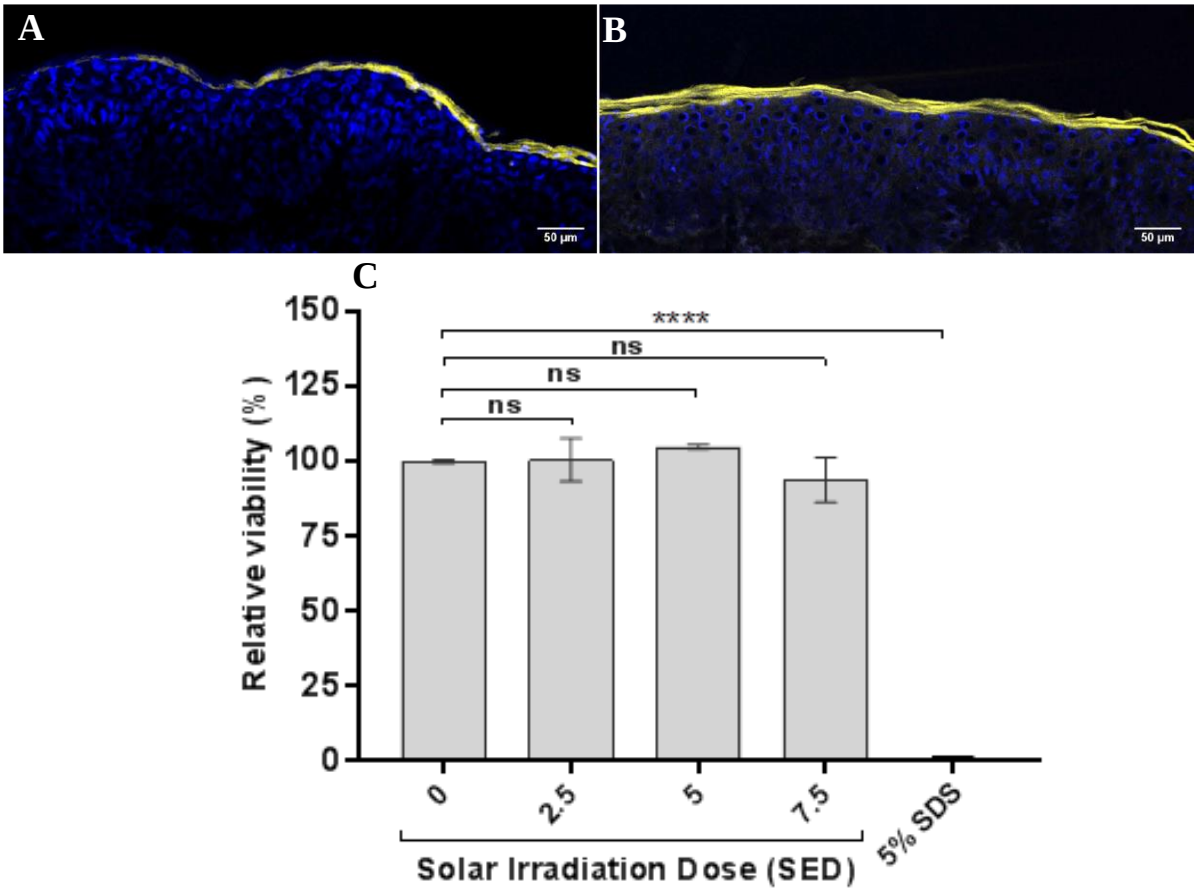

Figure 6-7: Solar irradiation does not damage barrier integrity or diminish metabolic viability. A+B) Adult foreskin donor 14527 (age 67) irradiated with 0 SED (A) or 5 SED (B) both maintained Lucifer yellow within intact stratum corneum. Scale bar 50µm, nuclei stained with DAPI. C) Dose response solar irradiation (0 - 7.5 SED) on whole skin foreskin ex-plants did not reduce metabolic viability (as determined by MTT conversion to formazan). Significant damage was detected by 1% SDS positive control. The standard erythemal dose (SED, J.m-2) is equivalent to an erythemal radiant exposure of 100 J.m-2. Total DNA was analysed for mtDNA damage by the housekeeping and 11kb qPCR assays of Chapter 3. Mean ± SEM generated from three adult foreskin donors (14525 - age 56, 14526 - age 46, 14527 – age 67y). Significant difference to 0 SED detected by one-way ANOVA with Dunnett's post-hoc test ****p<.0001 ns p>.05, N=3, n=9

6.3.1.4 *Solar irradiation variation across surface area does not largely affect the experimental dose (SED)*

A UV-photometer was used to measure solar irradiation (mAmps) over each well of a 24 well plate, which was placed in the central solar radiation area (see 2.2.2). Solar radiation readings were taken with/without a VIS-IR filter, as the filter is used to determine solar irradiation dose but removed for the irradiation treatment. Raw data obtained by Miss Maria Zakhour (undergraduate student). The solar irradiation values without a filter (Figure 6-8, A) demonstrate a mean of 16.82mAmps, which range between 16.25-17.52mAmps reaching each well. Negligible difference (0 – 0.06 mAmps) was found when the UV-VIS filter was washed before the repeat on a different day. The mean plate solar irradiation data (with filter, 8.87 mAmps; n=24) was used to represent 5 SED, whereby 1 standard erythemal dose (SED, J.m-2) is equivalent to an erythemal radiant exposure of 100 J.m-2 Relative variation was calculated where the lowest dose relatively equated to 4.81 SED and the highest dose relatively equated to 5.17 SED (Figure 6-8, B).

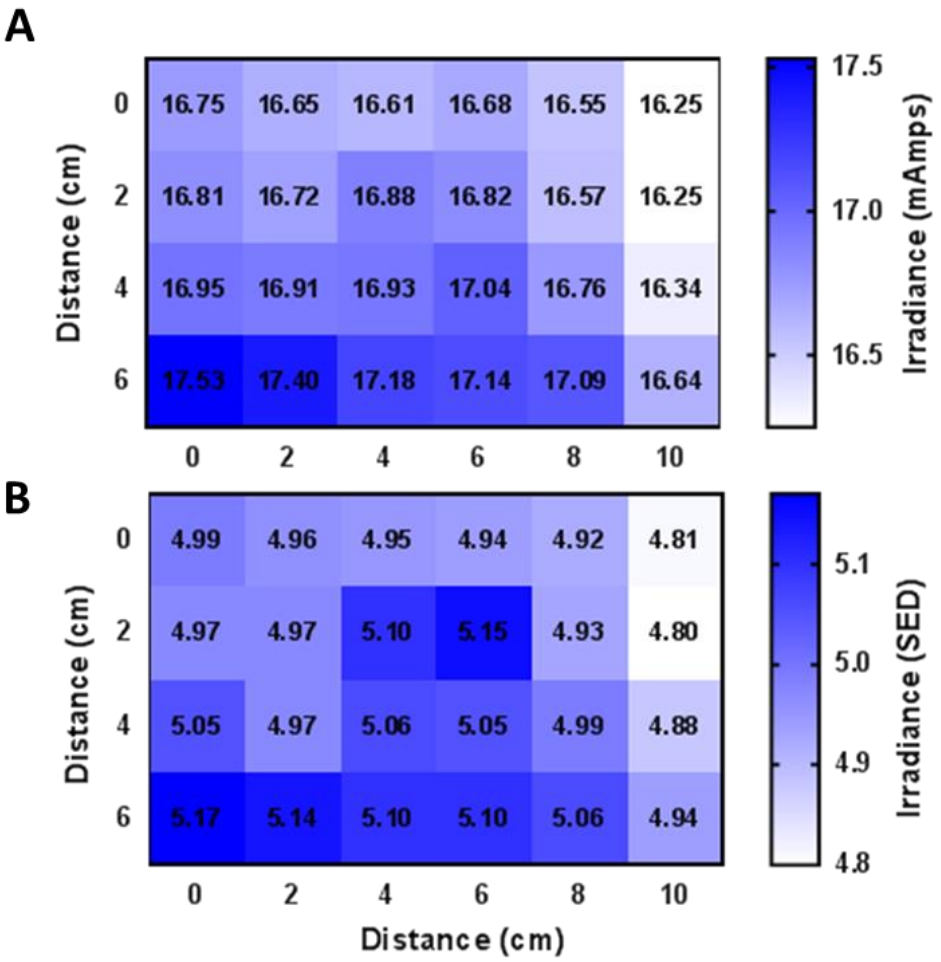

Figure 6-8: Solar irradiation over surface area. A: Solar irradiation (mAmps, without VIS-IR filter) of each well on standard 24 well plate in centre of irradiation area (see 2.2.2). The surface area is not homogenous as it ranges between 16.25-17.53mAmps, with a mean of 16.81mAmps (n=24). B: Solar irradiation dose (SED) calculated from data (mAmps) with VIS-IR filter, demonstrating range between 4.81 - 5.17SED, whereby 1 standard erythemal dose (SED, J.m-2) is equivalent to an erythemal radiant exposure of 100 J.m-2. Mean well values calculated from two independent repeats, N=2, n=1.

6.3.2 AOX formulation testing

6.3.2.1 *Test formulations did not physically block live solar light irradiance*

AOX and placebo test formulations did not physically block complete solar simulated light (Figure 6-9). Raw data obtained by undergraduate student Miss Maria Zakhour. The relative data did not change when filters where used to eliminate UV or visible and infrared components of solar light (data not shown). There was no difference to the data obtained through a quartz dish or industry standard PMMA plate for SPF testing (PMMA data not shown). Experimental controls demonstrated that covering the test system with foil blocked all irradiance, and Transpore surgical tape itself blocked only minimal light (<2 mAmp; data not shown). Market standards of known broad spectrum SPF significantly blocked irradiance by 85-90%. Both GSK placebo cream and Olay Regenerist™ SPF 0 contain niacinamide with no UV filter ingredients. Olay Regenerist™ offered marginally more protection than placebo alone (<10%). The addition of THC, PTERO, or combination to a niacinamide-containing placebo did not block any solar irradiance.

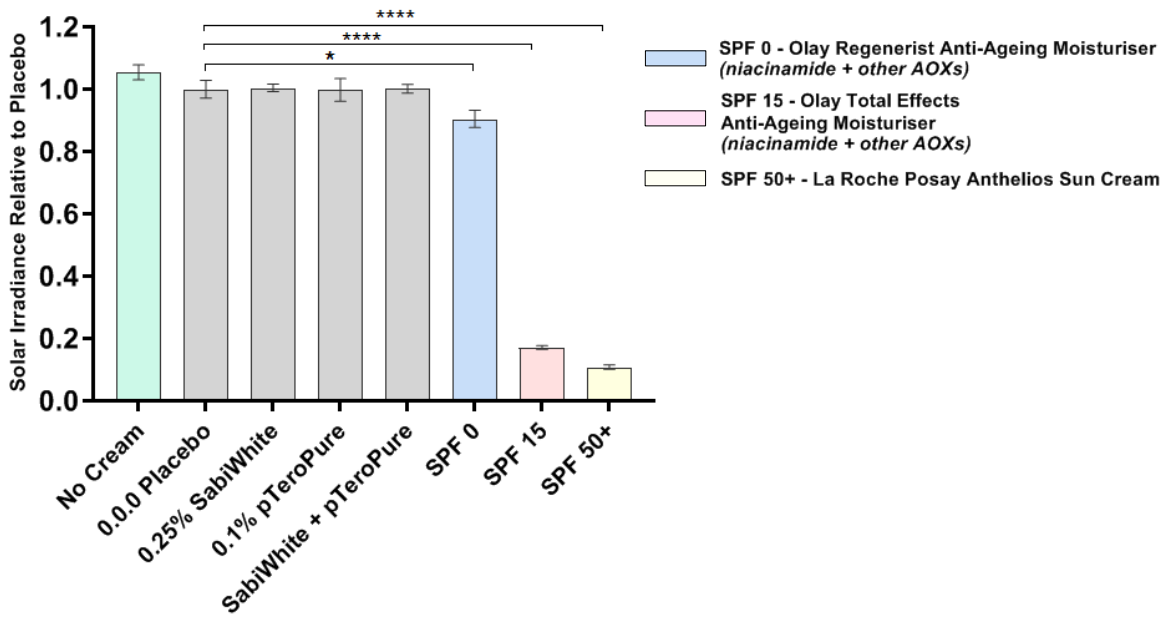

Figure 6-9: SPF testing of AOX formulations against market standards. Formulations with/without AOX(s) and SPF 0/15/50+ market standards were tested for their ability to physically block solar light transmission to a radiometer (mAmp). Mean ± SEM from three independent repeats. Significant difference relative to placebo determined by one-way ANOVA with Dunnett's post-hoc test **** p<.001, *p<.05, N=3, n=1 per condition

6.3.3 Human skin equivalent formulation testing

6.3.3.1 *Comparative summary of commercial Labskin™ and in-house CELLnTEC skin equivalents technical characteristics*

The primary difference between in-house and commercial skin equivalents is the ability to control the source of keratinocytes and fibroblasts used. Labskin™ uses adult fibroblasts derived from one donor foreskin, but pools keratinocytes from several neonatal foreskin donors. In-house skin equivalents can use donor-matched keratinocytes and fibroblasts. The second key difference is that the CELLnTEC skin equivalent uses no dermal scaffold, whereas Labskin™ uses a fibrin gel which fibroblasts are seeded into. This makes Labskin™ skin equivalents approximately 10X thicker. A third relevant difference is that Labskin™ epidermis can be manually removed, whereas CELLnTEC skin equivalents have a robust basement membrane. Labskin™ is available in 6-well and 12-well sizes, whereas one in-house pilot found CELLnTEC was best grown as 12- or 24-well size skin equivalents (see Chapter 5).

Model Characteristics	Labskin[1.1]	CELLnTEC
Surface Area (12 well)	1.1cm^2	1.1cm^2
Thickness	5-6mm	0.2-0.5mm
Insert permeable membrane pore size	3.0µm	0.4µm
Insert permeable membrane pore density	2x10^6 cm^2	1x10^{8}cm^2
Insert brand	Greiner	Greiner/Millipore
Insert sizes	6 or 12 well	12 or 24 well
Human foreskin-derived keratinocytes	Pooled donors: neonatal epidermis	Single donor: adult epidermis
Human foreskin-derived reticular fibroblasts	Single donor: adult dermis	Single donor - adult dermis
Donor matched layers	No	Yes
Dermal layer scaffold	Fibrin gel	No
Days at air-liquid interface (ALI)	7-12 (two shipping dates)	12
Media serum	Serum-free	<1% FBS or serum-free
Antibiotics/Antifungals during growth	No	No
Antibiotics/Antifungals were added post ALI	Yes	Yes
Phenol containing medium	Yes	No
Histology confirms one dermal & four epidermal layers	Yes	Yes
Epidermis can be manually removed	Yes	No (robust basement membrane)
Formulation can be applied to stratum corneum	Yes	Yes
Solar irradiation to induce 4-fold mtDNA damage	5 SED (500J/m^2)	2.16 SED (216J/m^2)

Table 6-2: Comparative summary of Labskin™ and CELLnTEC full thickness skin equivalent characteristics. Labskin™ data taken from company website, certificate of analysis (batch 190103) and first-hand technical experience. CELLnTEC skin equivalents derived in-house with media and technical protocol obtained from company website. **ALI – air liquid interface*

Asides from Labskin™ maintenance medium containing phenol, all other characteristics such as establishment time/method remain as standard for these skin equivalent types. Labskin™ construction timeline information was sourced from a publicly available presentation slide, which has since been taken offline (supplementary Figure 9-3).

There are two key differences in the timelines of Labskin™ and CELLnTEC construction, although both take the same total time of approximately 6 weeks. Labskin™ grows its dermal equivalent in 6 days, compared to CELLnTEC 10 days. In addition, Labskin™ completes cornification by air-liquid interface (ALI) day 7, though CELLnTEC protocol takes ALI 12 days (+5 days). Both skin equivalents decrease in viability over time in culture (1-10 days), although CELLnTEC was tested for 12 days after air-liquid interface completion.

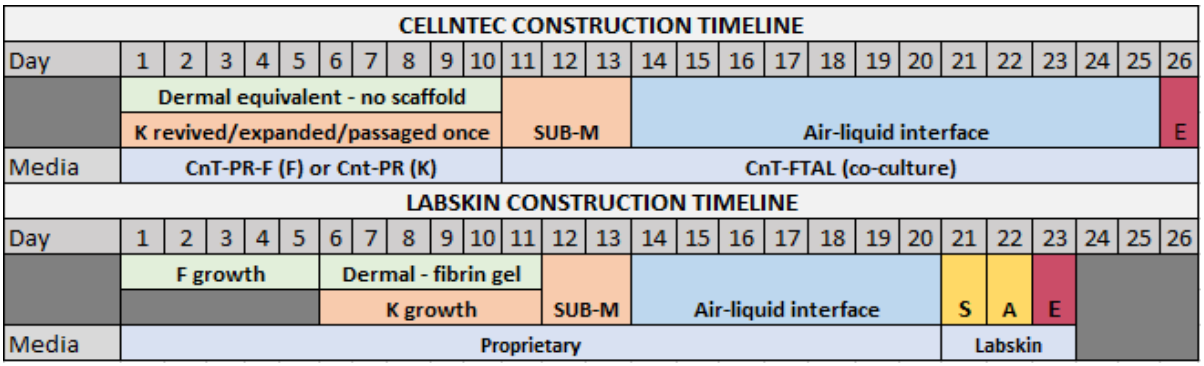

Figure 6-10: Comparative schematic of CELLnTEC and Labskin™ construction timeline. K- Keratinocytes, F – Fibroblasts, SUB-M – submerged co-culture, S – shipping date, A – arrival/acclimatisation, E – experiment day.

6.3.3.2 *Labskin™ skin equivalents pre-incubated (0, 1.5, 3 & 6 hours) with AOX or SPF formulations demonstrated sensitive time-dependent protection in the epidermis (limited in dermis or combined layers)*

A comparison was made between the sensitivity of the 11kb qPCR assay (see Chapter 3) at determining mtDNA damage (and protection) in commercial human skin equivalent Labskin™ with combined layers and manually separated epidermis and dermis (Figures 6-11, 6-12). A solar dose of 5 SED was chosen because this skin equivalent is ~5-6mm mm thick and this had proven sufficient in whole skin (Figure 6-6). Two NAM base creams were applied per skin equivalent and grouped as: THC/PTERO, SPF 50+/15+, placebo/combination (see Figure 6-3). All samples were tested for homogenous mtDNA content immediately prior to 11kb testing, with 18/24 dermis samples requiring normalisation (additional total DNA) to equate to the mtDNA content of the epidermis and combined samples. Only 3/24 epidermis and 3/24 combined samples required marginal normalisation.

Overall there was greater sensitivity in the amount of damage detected in the epidermis, compared to dermis and combined layers. However, the epidermis 3-hour data for placebo and combination was not obtained because the epidermis of one skin equivalent (of x12) did not adequately separate and minimal DNA was extracted (~1ng/µl). In the combined epidermis and dermis, the distinctive trend seen with epidermis is visibly diluted when the multi-layer mtDNA is pooled together.

The epidermis trend demonstrated that all test formulations had the lowest amount of damage at 0 hour (immediate application), and this increased with time. Whilst PTERO had the highest amount of damage at each time-point, in combination with THC this was reduced. The addition of test AOXs did not improve the protection seen with NAM base cream.

In the epidermis only one market control (SPF 15) protected against mtDNA damage induced by solar light, and this was also seen in the combined sample. However, this was reversed in the dermis sample, whereby SPF 50 protected and SPF 15 did not. Nevertheless, the overall amount of damage detected in the dermis samples was very low, as the qPCR fold change range lay predominantly between 1 to 3-fold (Figure 6-12, B).

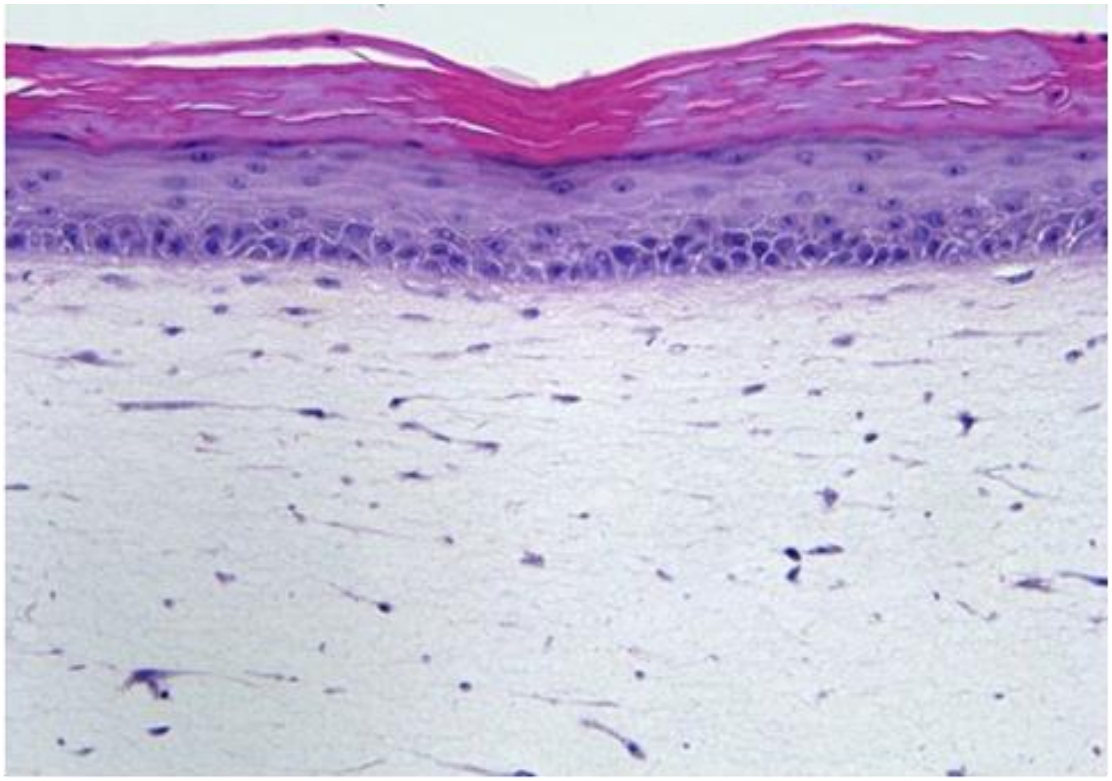

Figure 6-11: Labskin™ H&E histology. H&E histology of Labskin™ batch 190103, demonstrating stratum corneum, epidermis and dermis. Histology provided by Labskin within accompanying quality control documentation.

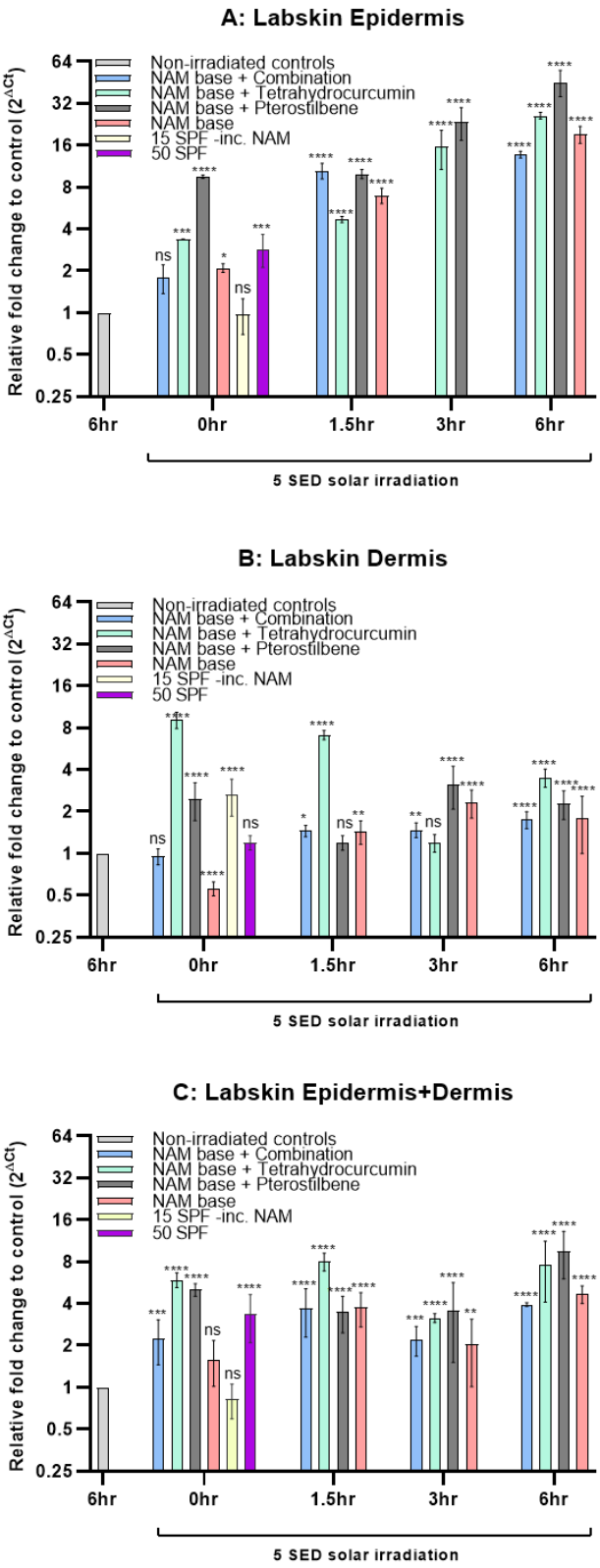

Figure 6-12: Labskin™ commercial skin equivalents were tested for mtDNA protection from 5 SED solar light, after pre-incubation (0-6 hours) with AOX formulations. Formulations contained 4% niacinamide (NAM), NAM+0.25% tetrahydrocurcumin, NAM+0.1% pterostilbene, or NAM+combination. Market controls of known SPF 15/50 were included, where the SPF 15 formulation contains NAM. A comparison was made by adjacent portions of skin equivalent whereby separated epidermis (A) and dermis (B) were compared to combined (C) layers. In graph A, the 3-hour data for NAM and NAM+combination was not obtained because the epidermis of one skin equivalent did not adequately separate and minimal DNA was extracted. Total DNA was analysed for mtDNA damage by the housekeeping and 11kb qPCR assays of Chapter 3. The standard erythemal dose (SED, J.m-2) is equivalent to an erythemal radiant exposure of 100 J.m-2. Statistical difference from controls determined by one-way ANOVA with Dunnett's post-hoc test on raw C_t value data. ****p<.0001, ***p<.001, **p>.001, *p>.01, ns p>.05, N=1, n=3 per sample

6.3.3.3 *Labskin™ experiment repeated on CELLnTEC skin equivalents produced incomparable data due to inadequate batch formation*

As outlined in section 5.3.4, it became apparent after the formulation application experiment that this batch of skin equivalents had not formed into layers and produced significantly less DNA when compared to previous pilot studies. However, a dry stratum corneum surface was available for topical application. Total DNA was analysed for mtDNA damage by the housekeeping and 11kb qPCR assays of Chapter 3. The housekeeping assay amplified 83bp amplicons for all skin equivalents from both S1141F and S1151F donors, and they all had equal mtDNA content. However 2.16 SED solar irradiation induced such significant damage in S1151F donor skin equivalents that 11kb amplicons of intact mtDNA could not be amplified from any irradiated samples using long range qPCR assay. However they did amplify in DNA samples from S1141F donor skin equivalents (Figure 6-13). Although all irradiated samples had significant difference to non-irradiated controls, the SPF 15 and 50 control formulations did demonstrate a reduced damage than other samples.

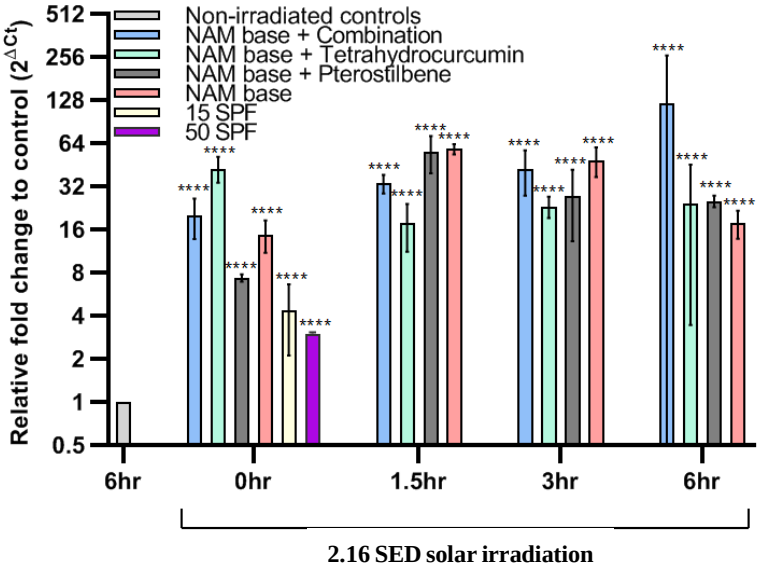

Figure 6-13: CELLnTEC skin equivalents were tested for mtDNA protection from 2.16 SED solar light, after pre-incubation (0-6 hours) with AOX formulations. Skin equivalents were derived from foreskin-derived adult keratinocytes and reticular fibroblasts from donor S1141F (age 40). Formulations contained 4% niacinamide (NAM), NAM+0.25% tetrahydrocurcumin, NAM+0.1% pterostilbene, or NAM+combination. Market controls of known SPF 15/50 were included, where the SPF 15 formulation contains NAM. Total DNA was analysed for mtDNA damage by the housekeeping and 11kb qPCR assays of Chapter 3. The standard erythemal dose (SED, J.m-2) is equivalent to an erythemal radiant exposure of 100 J.m-2. Statistical difference from controls determined by one-way ANOVA with Dunnett's post-hoc test on raw C_t value data. ****p<.0001, N=1, n=3 per sample

6.3.4 Ex-plant skin formulation testing

It was investigated if the 11kb assay (see Chapter 3) could sensitively determine mtDNA damage (and protection) in ex-plant foreskin and facial skin. It was not possible to remove the epidermis (as for Labskin™, Figure 6-12), without risking further damage caused by an enzyme or heat treatment separation methods. Each 4mm biopsy was manually cut in two, with one formulation applied per half biopsy (see 6.2.8). The AOX formulations tested contained 4% niacinamide (NAM) base cream with/without a combination of 0.25% tetrahydrocurcumin (THC) and 0.1% pterostilbene (PTERO). All samples per donor were analysed on one qPCR plate, having been tested for homogenous mtDNA content immediately prior to 11kb testing.

6.3.4.1 *Adult foreskin pre-incubation with AOX formulations indicated a protective trend in some donors from solar light induced mtDNA damage*

Four adult male foreskin donors were used to compare a 4% NAM base cream with/without a combination of 0.25% THC and 0.1% PTERO (Figures 6-14, 6-15). Six pre-incubation time points ranged from 0 to 6 hours. Three of these donors had enough tissue to perform three time points (0, 2, 4 hours) on niacinamide base creams containing tetrahydrocurcumin or pterostilbene (Figure 6-15).

Consistent with Figure 6-6, there was an induction of ~5-fold mtDNA damage in all four donors irradiated with 5 SED and no cream formulation.

There was a protective trend that increased with pre-incubation time in donors 14567 (NAM base), 14563 and 14566 (NAM base ± combination) (Figure 6-14). In some instances the amount of mtDNA damage was almost as low as the non-irradiated controls, and these were indicated as non-significant (ns) or only marginally different (*). There was not a clear improvement to mtDNA protection with the addition of THC and PTERO to NAM base. Donors 14566 (age 77) and 14563 (age 21) had an immediate protection with NAM base ± THC that decreased in a time dependent manner.

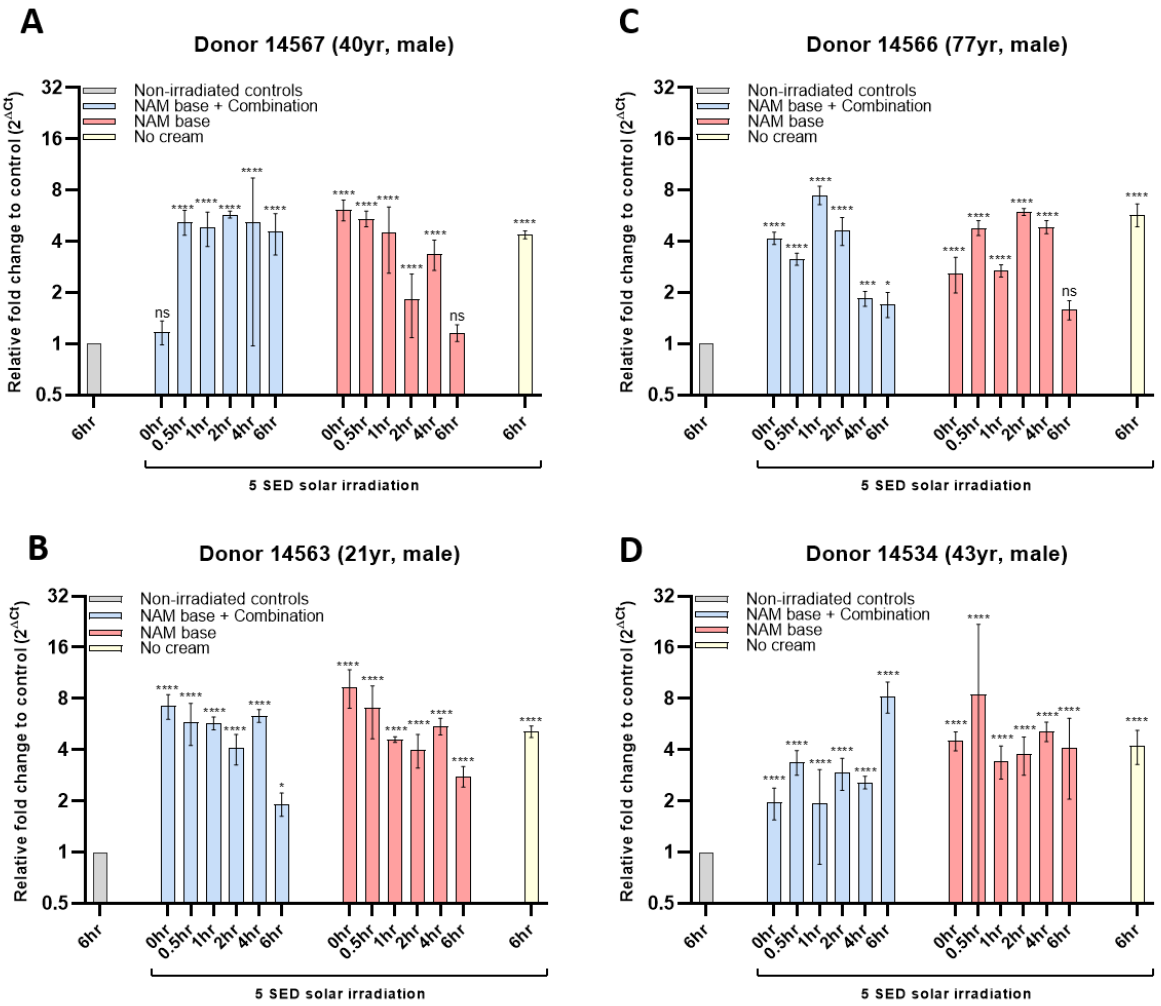

Figure 6-14: Protection against solar induced mtDNA damage of ex-plant foreskin with AOX formulations. Total DNA was analysed for mtDNA damage by the housekeeping and 11kb qPCR assays of Chapter 3. Solar irradiation (5 SED) induced a detectable window of mtDNA damage within a DNA pool of all skin layers. The standard erythemal dose (SED, J.m-2) is equivalent to an erythemal radiant exposure of 100 J.m-2. Pre-incubation (0-6 hours) of ½ 4mm skin biopsies with 4% niacinamide (NAM) base formulation ± 0.25% THC/0.1% PTERO combination gave variable mtDNA protection (A-D; mean ± 95% CI). Statistical difference from controls determined by one-way ANOVA with Dunnett's post-hoc test on raw C_t value data. ****p<.0001, ***p<.001, **p>.001, *p>.01, ns p>.05, N=1, n-3 per sample

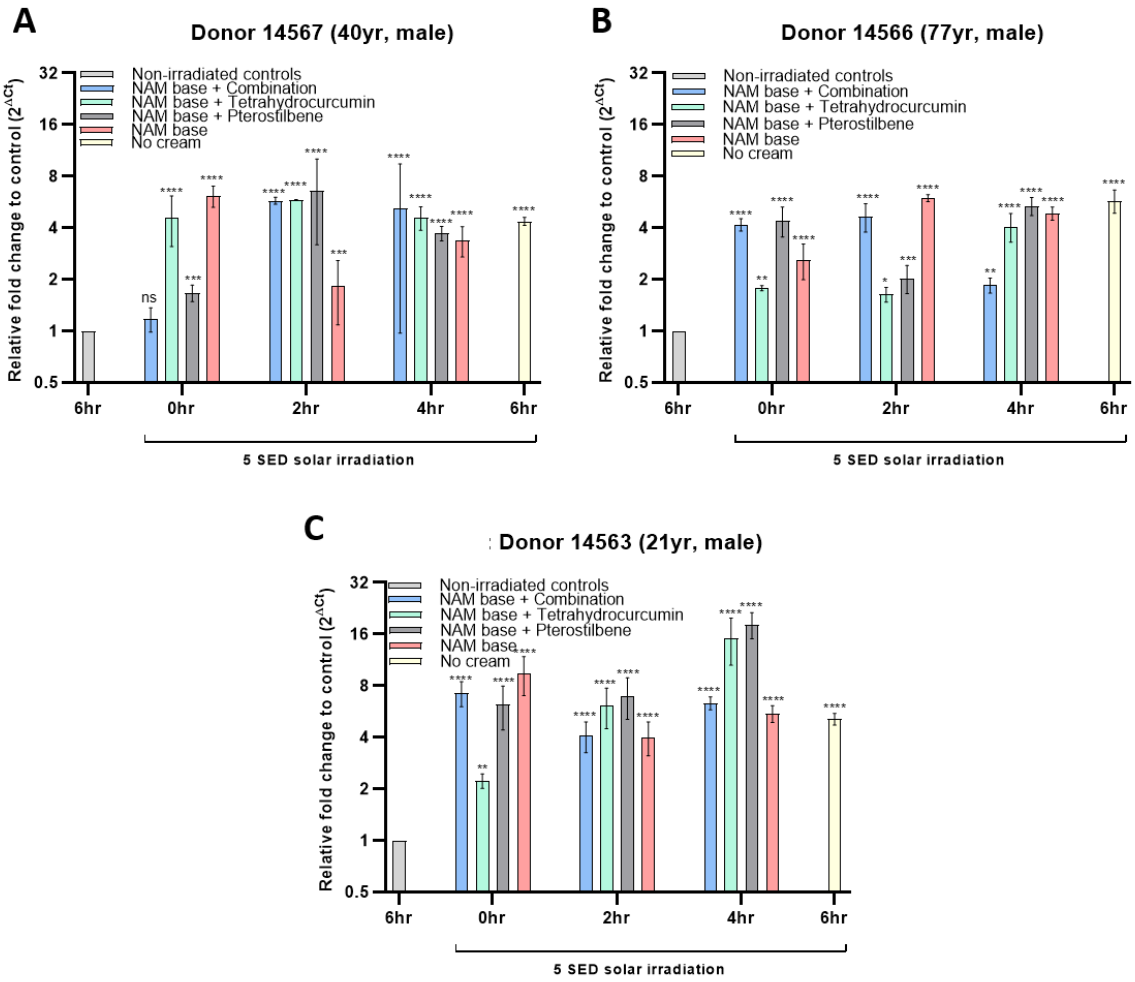

Figure 6-15: Protection against solar induced mtDNA damage of ex-plant foreskin with AOX formulations. Total DNA was analysed for mtDNA damage by the housekeeping and 11kb qPCR assays of Chapter 3. Solar irradiation (5 SED) induced a detectable window of mtDNA damage within a DNA pool of all skin layers. The standard erythemal dose (SED, J.m-2) is equivalent to an erythemal radiant exposure of 100 J.m-2. Pre-incubation (0-6hours) of ½ 4mm skin biopsies with 4% niacinamide (NAM) base formulation±0.25% tetrahydrocurcumin, 0.1% pterostilbene or a combination gave variable mtDNA protection (A-C; mean ± 95% CI). Statistical difference from controls determined by one-way ANOVA with Dunnett's post-hoc test on raw C_t value data. ****p<.0001, ***p<.001, **p>.001, *p>.01, ns p>.05, N=1, n=3 per sample

6.3.4.2 *Adult facial skin pre-incubated with AOX formulations indicated inconclusive protection against solar light induced mtDNA damage*

Three adult male donors were used to compare a 4% NAM base cream with/without a combination of 0.25% THC and 0.1% PTERO (Figures 6-16, 6-17). Six pre-incubation time points ranged from 0 to 6 hours. Two of these donors had enough tissue to perform three time points (0, 2, 4 hours) on NAM base creams containing THC or PTERO (Figure 6-17).

There was insufficient facial skin to perform a dose-response solar irradiation experiment as with foreskin in Figure 6-6. As facial skin is markedly thicker than foreskin, 5 SED solar irradiation induced approximately half the mtDNA damage in all donors irradiated without cream formulation.

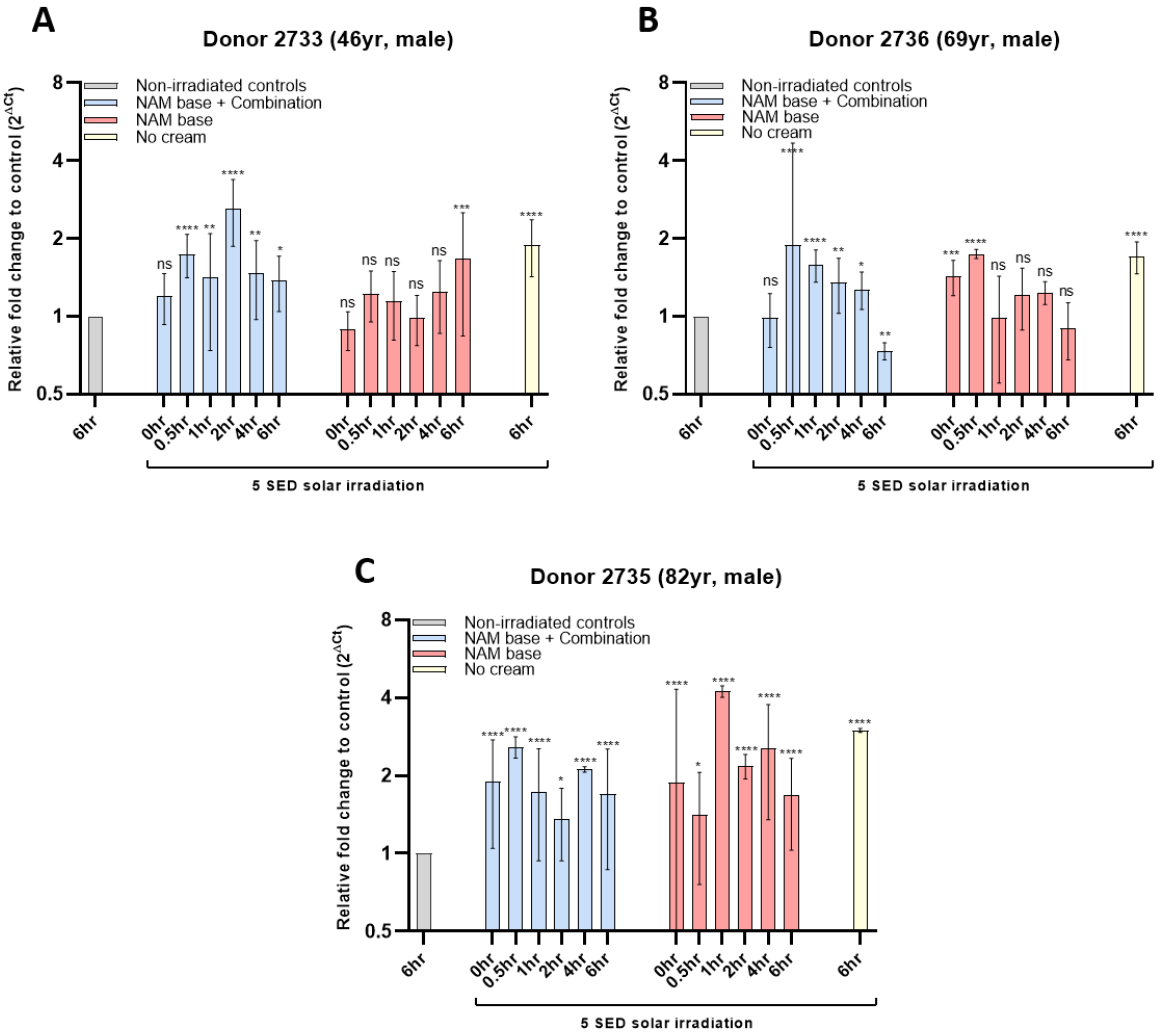

Figure 6-16: Protection against solar induced mtDNA damage of ex-plant adult facial skin with AOX formulations. Total DNA was analysed for mtDNA damage by the housekeeping and 11kb qPCR assays of Chapter 3. Solar irradiation (5 SED) did not induce a detectable window of mtDNA damage within a DNA pool of all skin layers. The standard erythemal dose (SED, J.m-2) is equivalent to an erythemal radiant exposure of 100 J.m-2. Pre-incubation (0-6 hours) of ½ 4mm skin biopsies with 4% niacinamide (NAM) base formulation ± 0.25% THC/0.1% PTERO combination gave variable mtDNA protection (A-C; mean ± 95% CI). Statistical difference from controls determined by one-way ANOVA with Dunnett's post-hoc test on raw C_t value data.. ****p<.0001, ***p<.001, **p>.001, *p>.01, ns p>.05; N=1, n=3 per sample

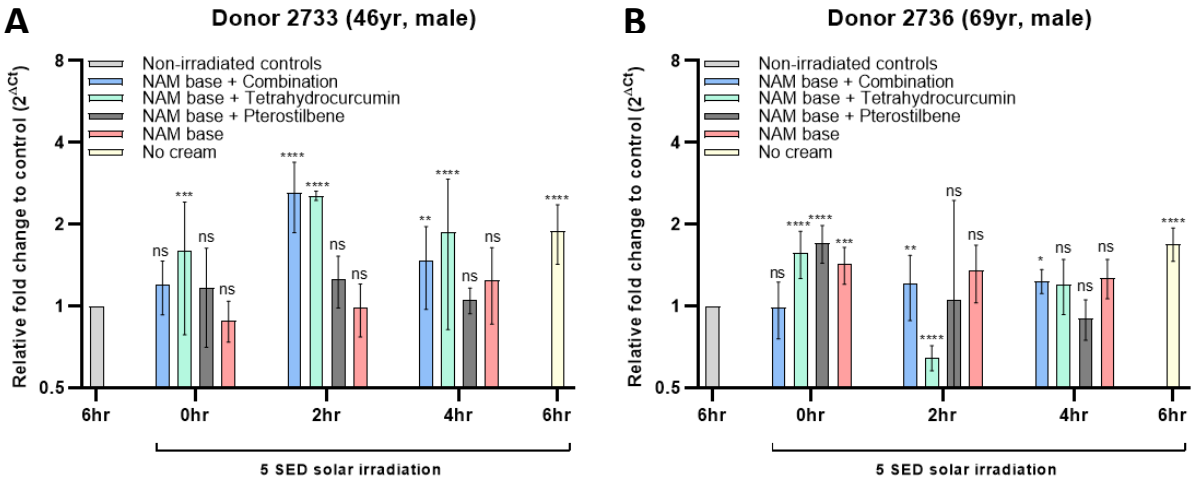

Figure 6-17: Protection against solar induced mtDNA damage of ex-plant facial skin with AOX formulations. Total DNA was analysed for mtDNA damage by the housekeeping and 11kb qPCR assays of Chapter 3. Solar irradiation (5 SED) did not induce a detectable window of mtDNA damage within a DNA pool of all skin layers. The standard erythemal dose (SED, J.m-2) is equivalent to an erythemal radiant exposure of 100 J.m-2. Pre-incubation (0-6 hours) of ½ 4mm skin biopsies with 4% niacinamide (NAM) base formulation±0.25% tetrahydrocurcumin, 0.1% pterostilbene or a combination gave variable mtDNA protection (A-B; mean ± 95% CI). Statistical difference from controls determined by one-way ANOVA with Dunnett's post-hoc test on raw C_t value data. ****p<.0001, ***p<.001, **p>.001, *p>.01, ns p>.05; N=1, n=3 per sample

6.3.4.3. Grouped donor analysis of foreskin or facial skin protection against solar induced mtDNA damage by AOX formulations.

Although statistics were performed on raw C_t comparisons between samples of the same donor, raw data was grouped in Figure 6-18. Although donor variation is evident by large standard deviation bars, statistical difference could not be calculated on mean C_t values of multiple donors (see 6.2.11). In Figure 6-18 the lower dashed line indicates the mean C_t value of non-irradiated controls, whereas the higher dashed line indicates the mean Ct value of irradiated skin without any cream application. The distance inbetween represents the 'window of damage' to visually identify which conditions showed some mtDNA protection from solar irradiation. This window is markedly smaller for facial skin (Figure 6-18, B), where 5 SED solar irradiation didn't induce as much damage as thinner foreskin. There are some trends seen with foreskin (Figure 6-18, A) that are indicative of protection e.g. THC + 0 hour, but more donors are required to draw strong conclusions.

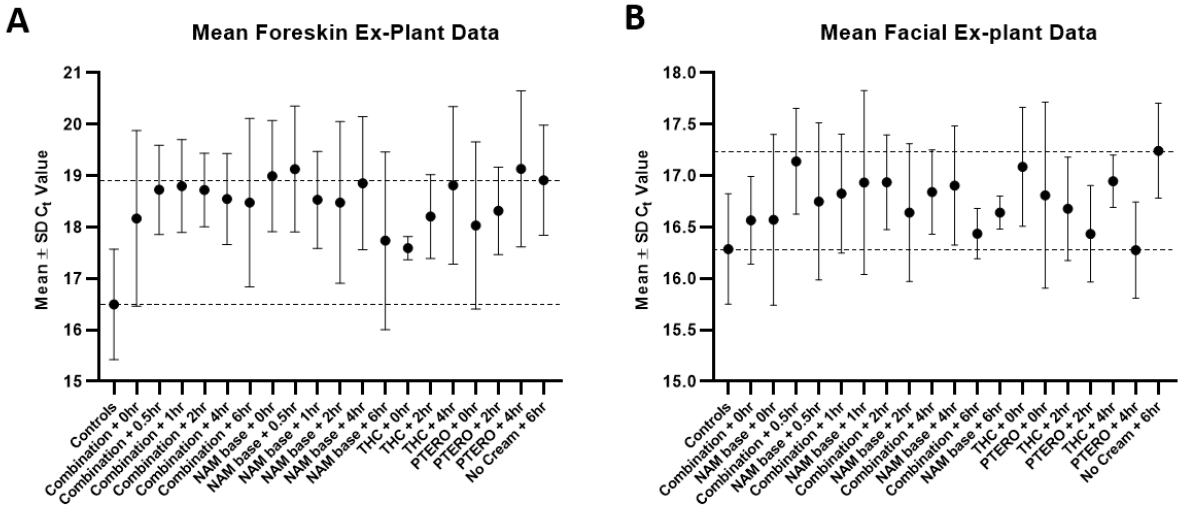

Figure 6-18: Mean protection against solar induced mtDNA damage of ex-plant foreskin or facial skin with AOX formulations. Total DNA was analysed for mtDNA damage by the housekeeping and 11kb qPCR assays of Chapter 3. Pre-incubation (0-6 hours) of adult foreskin (A) or facial skin (B) ½ 4mm skin biopsies with 4% NAM base formulation ± 0.25% THC , 0.1% PTERO or a combination. Data is mean raw C_t values ± SD for the foreskin and facial donors of Figures 6-14 to 6-17. The lower dashed line indicates the mean C_t value of non-irradiated controls, whereas the higher dashed line indicates the mean Ct value of irradiated skin without any cream application. The distance inbetween represents the 'window of damage' to visually identify which conditions showed some mtDNA protection from solar irradiation. The standard deviation bars represent donor variability. Statistical difference could not be calculated on mean C_t values of multiple donors (see 6.2.11). N=3, n=9 per data point.

6.4 Discussion

This chapter investigated if the protection seen in skin cell monolayers with direct antioxidant (AOX) exposure (Chapter 4) was reproduced in 3D skin model systems with AOXs delivered in cream formulation. The human skin equivalents outlined in Chapter 5 were used for formulation testing and compared to whole skin ex-plant from foreskin and facial sources. These skin equivalents were tested for the AOX capacity to protect against solar light induced damage to mitochondrial DNA in human skin, using the qPCR method (Chapter 3). In accordance with international cosmetic protocols (e.g. COLIPA), a formulation dose of $2mg/cm^2$ was applied in experiments (Lionetti and Rigano, 2017).

Initial acellular experiments were performed on the emulsion formulations provided by GSK, that have a Physiogel™ (Stiefel) chassis/base formulation inclusive of a core AOX ingredient (niacinamide) and test antioxidants tetrahydrocurcumin, pterostilbene, or combination (Table 6-1). Although niacinamide was not included in monolayer experiments (chapter 4), it would be included in a cosmetic product due to its established efficacy and popularity with consumers. As such, two Olay products that contain niacinamide (0 or 15 SPF) were included as market controls, alongside a high SPF positive control (La Roche Posay sun cream). The test formulations contain no UV filters, and neither the chassis nor AOX ingredients provided any physical blocking capacity of simulated sunlight (Figure 6-9). As outlined in the chapter 4 discussion, it was expected that phenolic antioxidants would offer protection by biological mechanisms over physical absorbance of UV wavelengths. Sirerol *et al.* (2015) also found that while pterostilbene compound has an absorbance peak in the UVB range, the pterostilbene formulation had a very low *in-vitro* SPF rating. However, this knowledge is useful for two reasons. It confirms that any protection seen in model systems has a biological basis and avoids a delayed product launch as a result of the legal requirement for sun protection product testing (e.g. Cosmetics Regulation (EC no. 1223/2009)).

To optimise an organ culture method for ex-plant skin, biopsies from three donors were incubated at air-liquid interface for 1-7 days and tested for their capacity to metabolise MTT (Figure 6-5). Facial skin was better sustained over time than foreskin, but it is unclear if this is attributed to donor or site variability. Whilst all tissue was used for experiments on day 1 (after overnight acclimatisation), the tissue viability could perhaps be extended for longer studies with a different medium. For long term organ culture of human scalp skin, Lu *et al.* (2007) compared supplemented serum-free William's E medium with a commonplace serum-containing MEM medium. They found that serum-free medium allowed prolonged and enhanced human skin and hair follicle survival beyond three weeks, with one donor reported to survive 88 days. Zhou *et*

al. (2018) reviews human skin organ culture and the approach in this thesis (DMEM+10% FBS, air-liquid interface) is concurrent with culture conditions for the majority of skin sites. However they advocate the use of a serum-free or human-serum approach in lieu of bovine-serum.
It was reassuring that an environmentally relevant dose of 5 SED (500 J/m^2) induced a level of mtDNA damage in ex-plant foreskin that could be detected by the qPCR method (chapter 3). Whilst this equates to a relatively intense dose of 5 hours Mediterranean summer sun, it is not outside the feasibility of a single or accumulative dose to human skin. As seen in Figures 6-6 and 6-7, this dose did not disrupt the skin barrier or reduce metabolic activity in the cultured skin. The solar irradiation dose was optimised using foreskin, but it was unexpected that 5 SED would only induce half the amount of mtDNA damage in facial biopsies (Figures 6-16, 6-17, 6-18(B)). This narrowed the detection window for AOX protection to the limit of qPCR assay sensitivity (1 C_t), making it difficult to draw conclusions from Figure 6-18 (B). In addition, the facial skin had a rigid hypodermis that made it technically difficult to divide biopsies evenly in half and sit upright on the insert membrane. The unequal division of facial biopsies likely explains the viability peaks and troughs in Figure 6-5, whereby a slightly smaller piece would produce less formazan.

The final chapter area pertains to AOXs formulation testing using the human skin equivalents characterised in chapter 5. These include the in-house derived CELLnTEC skin equivalent (Figure 6-13) and commercial Labskin™ (Figure 6-12). Technical characteristics of these skin equivalents are compared in Figure 6-10 and Table 6-2. Unlike the CELLnTEC skin equivalent, Labskin™ epidermis could be manually separated from the dermal compartment. However the Labskin™ fibrin hydrogel dermis ruptured and released liquid when divided with a scalpel. To investigate where most of the solar light induced mtDNA damage was located, a comparison was made between separated and combined Labskin™ epidermis-dermis (Figure 6-12). The data confirmed the theory that a limiting factor for qPCR assay mtDNA damage detection is comparative sample size. A standardised surface area and thickness of tissue sample is required. Relative to pooled mtDNA from all skin layers, a higher proportion of damage would be detected in pooled mtDNA from the thinner epidermis. In Figure 6-12 the same trend is found in epidermis and combined, but the level of damage (bar height) has been reduced (or 'diluted'). This 'dilution' effect is not as prevalent in Labskin™ as other human skin equivalent/*ex-vivo* skin because there are few fibroblasts in the dermal compartment, and a thickened stratum corneum. The skin equivalent is substantially thicker than physiological skin and it was unclear if 5 SED simulated solar light had penetrated through the dermis. The 'dilution' effect was more evident in the foreskin and facial skin studies (Figures 6-14 to 6-18) and the qPCR assay could

not distinguish clear trends between test conditions. To increase sensitivity, epidermal separation of ex-plant skin would be feasible by Dispase (enzyme) or heat treatment methods (Zou and Maibach, 2018). However, it is more likely that DNA/RNA/protein quality would be preserved through the separation method of a 30-minute epidermis-up (free-floating) incubation in ice-cold 0.5M ammonium thiocyanate phosphate buffer (Baris *et al.*, 2011). The intention was to repeat the ex-plant/Labskin™ AOX formulation studies with CELLnTEC skin equivalents, but they failed to establish (see 5.3.8). It was expected that as these in-house skin equivalents were of a similar thickness to thin physiological skin (but without additional cell types/organ structures), that the qPCR assay would be suited to distinguish between conditions.

6.5 Summary of main findings

- Organ culture of human foreskin and facial skin punch-biopsies were maintained at the air-liquid interface
- A dose-response solar irradiation of ex-plant foreskin determined 5 SED induced mtDNA damage detectable with the qPCR assay
- A dose of 5 SED did not disrupt the skin barrier integrity or skin metabolic function
- GSK test formulations tested as SPF 0 in acellular *in-vitro* assay
- Formulations were topically applied at 2mg/cm^2 to commercial Labskin™ and in-house CELLnTEC skin equivalents. Formulations were topically applied at 2mg/cm^2 to commercial Labskin™ and in-house CELLnTEC skin equivalents
- Labskin™ could be manually separated and a greater sensitivity of mtDNA was detected in isolated epidermis.
- CELLnTEC skin equivalents failed to establish correctly for this experiment, but some DNA was attained and it had a sensitive detection of mtDNA damage
- An organ culture system, solar irradiation, formulation application and isolation techniques (DNA/RNA/protein etc.) were optimised for whole skin, making it suitable for other analytical methods
- Pooled mtDNA from whole skin ex-plant provided a damage range detectable by the qPCR assay in foreskin, but not the thicker facial skin
- Separation of the epidermis from whole skin (by enzyme or heat treatment) should provide a pool of mtDNA that the qPCR assay can sensitively detect damage within

Chapter 7: Detection of mtDNA damage in donor-matched BCC and non-BCC facial skin

7.1 Chapter overview and aims

Mitochondria are becoming increasingly associated with human cancers whereby cellular metabolic reprogramming is thought to have a key role in tumour initiation and progression (Hosseini *et al.*, 2017). Environmental stressors such as UV result in accumulative damage to mtDNA in human skin, and skin cancer rates of incidence are rising. However, it remains unclear why only portions of environmentally exposed skin become cancerous, and the adjacent skin remains physiologically intact. A proof of concept study was designed to see if the qPCR assay (Chapter 3) could be applied to the detection of mtDNA damage in donor-matched basal cell carcinoma (BCC) and non-BCC tissue. The effect of simulated solar radiation on these tissues was also investigated. In collaboration with Dr Sarah Felton of Oxford University Hospital NHS Trust and Public Health England (PHE; Oxford, UK), 21 donors were included in this pilot study.

7.2 Chapter specific methods

Skin samples were sourced from Mohs micrographic surgical patients of Dr Sarah Felton. Total DNA samples were sourced in collaboration with Dr Ken Raj and Dr Graham Holliman of PHE. Skin processing, solar irradiation, and DNA extractions were performed by Dr Holliman at PHE on donor-matched whole skin from excised facial BCC and its non-cancerous standing cone (see Table 7-1 footnote for definition). Donor information is summarised in Table 7-1 whereby 21 donors (16 females, 5 male) were analysed for mtDNA damage with sequential housekeeping and 11kb mtDNA assays, as outlined in Chapter 3. Housekeeping was used to check donor-matched BCC and non-BCC samples had equal mtDNA copy number (C_t values). Data from the 11kb assay was analysed as outlined in 6.3.3, except for the following differences. Data was grouped into two categories per donor, whereby non-BCC represents $C_{t\ (control)}$ and the BCC represented $C_{t\ (treated)}$ in the $2^{\Delta Ct}$ (treated-control) formula calculating relative fold change. Welch's t-test was performed on the raw C_t values of all samples per donor (Fagerland and Sandvik, 2009).

Donor ID	Sex	Site(s)	Age*	BCC** DNA	Non-BCC*** DNA	Notes/Thesis Figure(s)
190717-58M	M	Back	58	Yes	Yes	Fig 7-3
190717-61F	F	Cheek	61	Yes	Yes	Fig 7-3
190717-69F	F	Nose	69	Yes	Yes	Fig 7-3
190717-86F	F	Nose	86	Yes	Yes	Fig 7-3
260717-56F	F	Chin	56	Yes	Yes	Fig 7-3
260717-82F	F	Forehead	82	Yes	Yes	Fig 7-3
260717-62F	F	Nose	62	Yes	Yes	Fig 7-3
260717-47F	F	Lip	47	Yes	Yes	Fig 7-3
260717-79M	M	Temple	79	Yes	Yes	Suspected SCC^{+}, Fig 7-3
260717-92F	F	Chin & Forehead	92	Yes - both	Yes - both	Figs. 7-1, 7-3
300817-85FA	F	Nose	85	Yes	Yes	Fig 7-3
300817-85FB	F	Nose	85	Yes	Yes	non-BCC may be scar tissue, Fig 7-3
181017-81F	F	Nose, lip/cheek, and eyelid	81	Yes - nose	Yes - nose, lip/cheek, eyelid	Figs. 7-1, 7-3
181017-91F	F	Nose	91	Yes	Yes	Fig 7-3
181017-82M	M	Nose	82	Yes	Yes	Fig 7-3
181017-87F	F	Eyelid	71	Yes	Yes	non-BCC was not supplied so manually separated, Fig 7-3
041017-76F	F	Lip	76	Yes	Yes	Fig 7-3
011117-70F	F	Nose & lip	70	Yes - both	Yes - both	≠ Figs. 7-1, 7-3
011117-61F	F	Nose	61	Yes	Yes	≠ Fig 7-3
131217-79M	M	Ear	79	Yes	Yes	Fig 7-3
131217-88M	M	Cheek	88	Yes	Yes	Fig 7-3
Excluded samples						
041017-71M	M	Ear	71	Yes	No	
131217-51M	M	Nose	51	Yes	No	
300817-70M	M	Neck	70	No	Yes	
011117-XXF	F	Ear	?	No	Yes	≠
011117-61F	F	Nose	61	Yes	No	

Table 7-1: Demographics of donor DNA samples provided in collaboration with Public Health England and Oxford University Hospital NHS Trust. Two donors were excluded from analysis as no comparative material was available. *Age on date of surgery, **BCC – basal cell carcinoma excised by Mohs surgery, ***non-BCC – Mohs surgical standing cone or 'dog ears' are skin adjacent to the excision site that are removed for smooth wound closure, $^{+}$SCC - squamous cell carcinoma ≠Sample used to compare DNA extracted 'fresh' or stored overnight at 4ºC (15h) 'dog-ear' from BCC.

7.3 Results

7.3.1 Sensitive detection of relative mtDNA damage across multiple facial sites.

There were three female donors who had multiple excisions from different facial sites (260717-92F, 181017-81F, 011117-70F, see Table 7-1). Total DNA was analysed for mtDNA damage by the housekeeping and 11kb qPCR assays of Chapter 3. The non-BCC samples were compared to determine if mtDNA damage had accumulated to the same extent across their face. Differences were detected in all donors, with highest damage seen at the lip/cheek and chin areas.

/

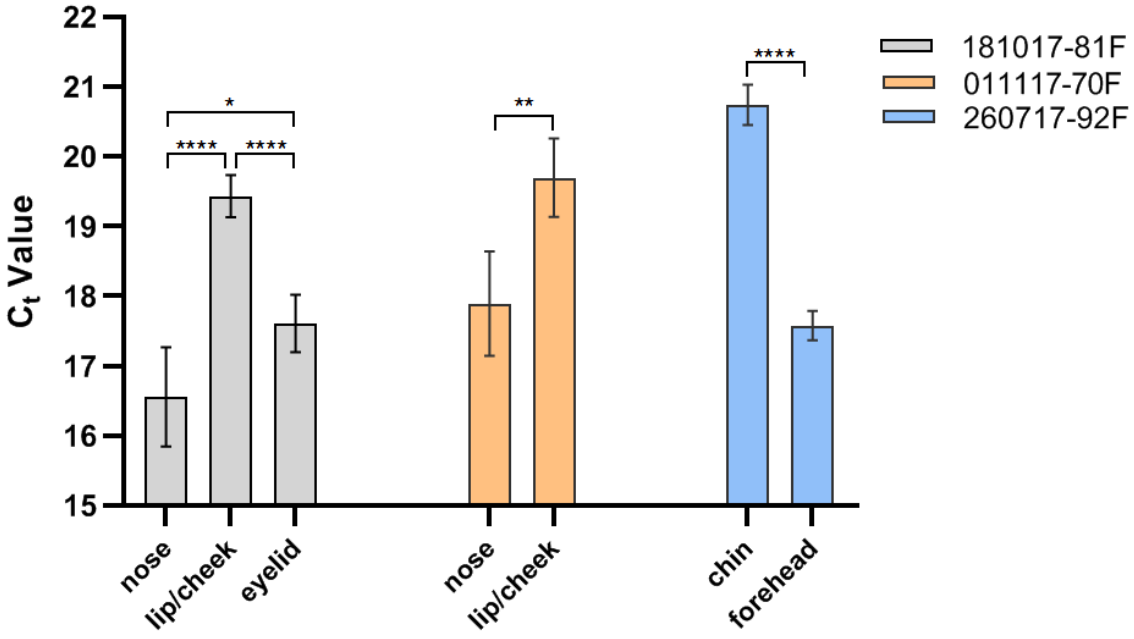

Figure 7-1: Sensitive detection of mtDNA damage across multiple facial sites in three female donors. Total DNA was analysed for mtDNA damage by the housekeeping and 11kb qPCR assays of Chapter 3. Statistical difference determined by two-tailed unpaired t-test with Welch's correction. Mean C_t ± SD, ****p<.0001, **p=.026, *p=.01; N=1, n=3 per sample.

7.3.2 Solar irradiation methods did not induce detectable differences in mtDNA damage

To determine if there was a difference in BCC susceptibility to solar light induced mtDNA damage, Dr Graham Holliman (PHE) manually divided all donor samples (BCC and non-BCC) exposing half to irradiation using a Hönle solar simulator. Various solar irradiation doses were used but mtDNA damage was not induced (data not included). A PHE spectroradiometer was sent to Newcastle University and various traces of the Newport Solar Simulator were captured using SpectraSuite software. The equipment was returned to PHE and repeated on their solar simulator. The data was analysed at PHE by Dr Holliman and showed that the Newport model represented 'summer' sunlight compared to the 'winter'-like sun of the Hönle solar simulator. This is represented in Figure 7-2 where the Newport model has a much higher amount of UV, with the Hönle producing comparatively lower UVA and negligible UVB.

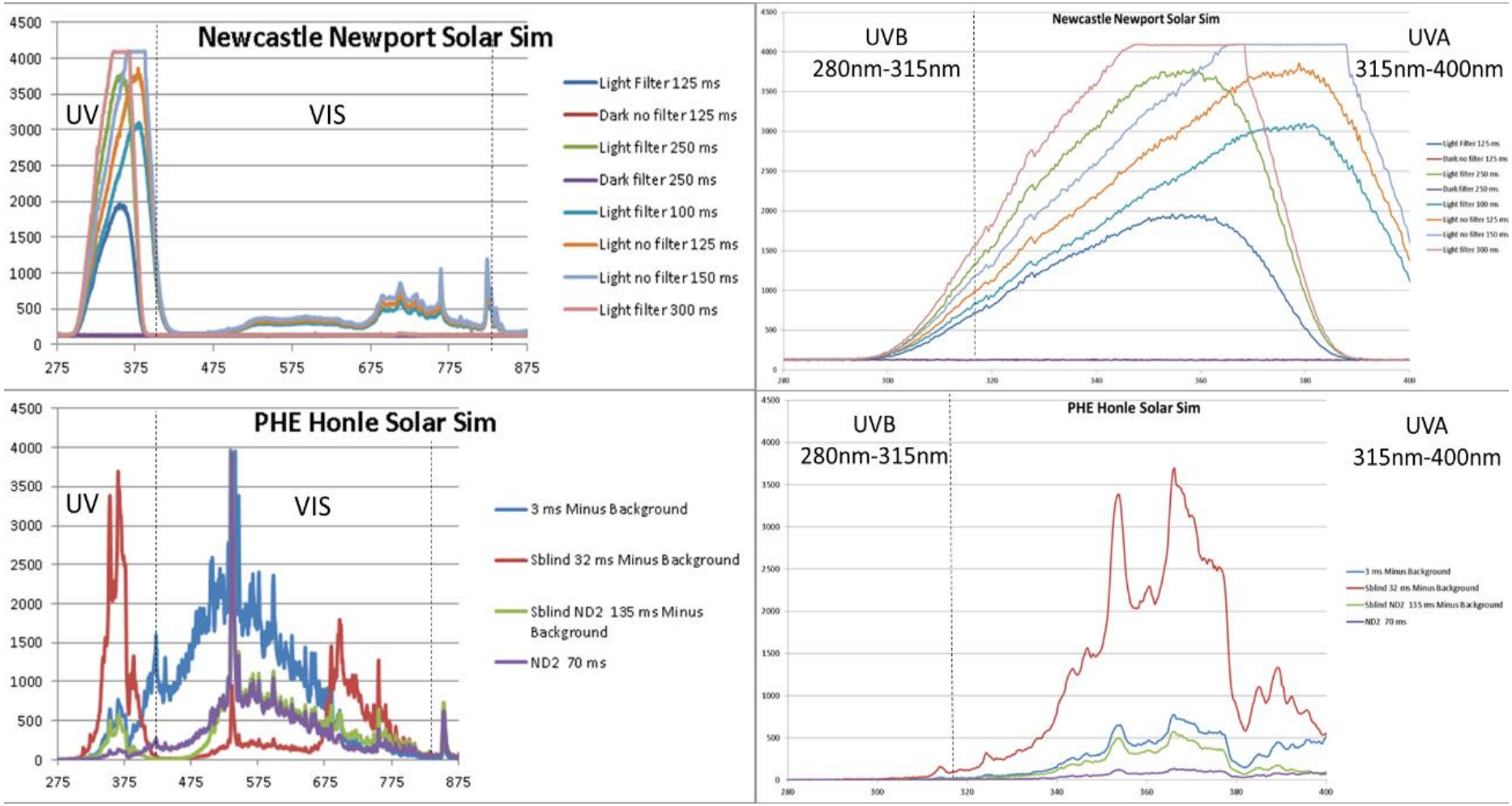

Figure 7-2: Spectral irradiance traces of Newport and Hönle solar simulators. The Newport model better represents summer light, with a high dose of UVB and UVA. Control filters include a dark filter (to block all light), and light filter (to block viable and infrared).

7.3.3 Detection of differences in donor-matched BCC and non-BCC mtDNA damage

Total DNA was analysed for mtDNA damage by the housekeeping and 11kb qPCR assays of Chapter 3. The mtDNA damage fold change ($2^{\Delta Ct}$) of BCC relative to non-BCC per donor is illustrated in Figure 7-3. Of the 22 donors analysed, a majority were from the nose (n=9), followed by lip (n=3), cheek/chin/forehead (n=2/region), and eyelid/ear/temple/back (n=1/region). The BCC had less mtDNA damage than non-BCC in 8/22 donors, but more than non-BCC in 5/22. The levels were within 2-fold of one another in 9/22 donors.

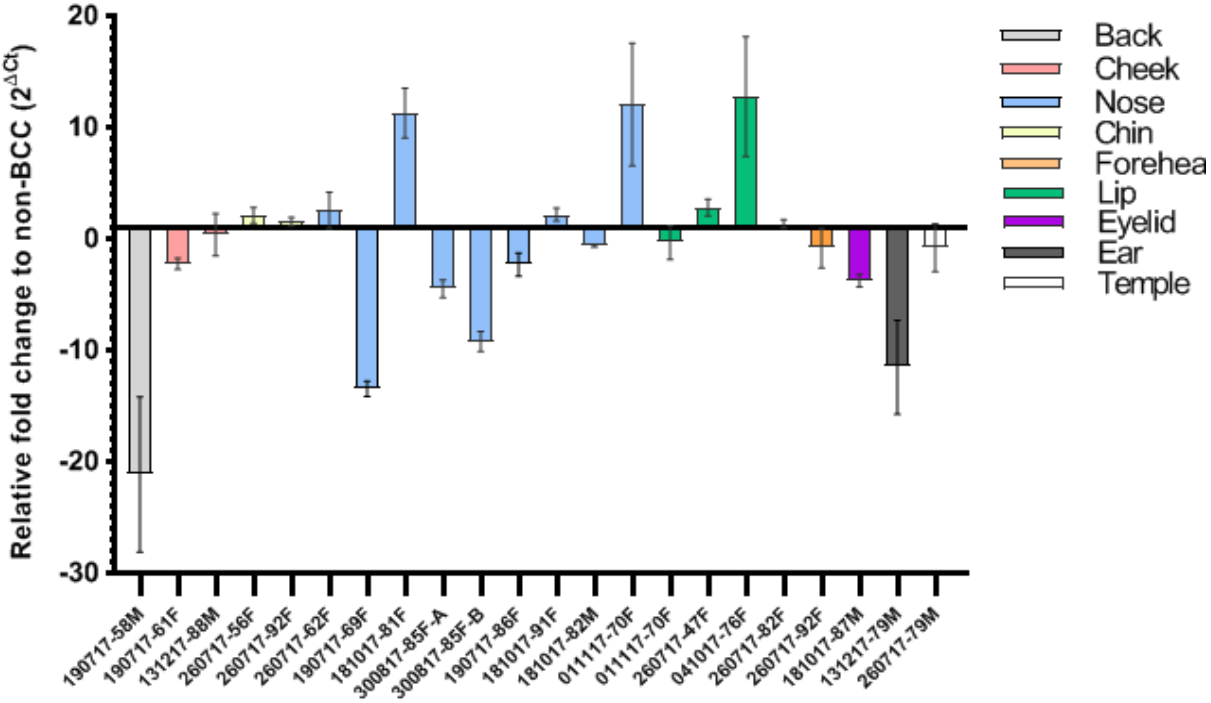

Figure 7-3: Detection of mtDNA damage in donor-matched BCC and non-BCC skin samples. Total DNA was analysed for mtDNA damage by the housekeeping and 11kb qPCR assays of Chapter 3. The skin sites are grouped by colour, and all but one sample are facial skin. The relative fold change of BCC mtDNA damage to non-BCC control are graphed as mean ± 95% CI; N=1, n=3 per sample

7.4 Discussion

Traditionally nuclear DNA (nDNA) has been widely studied in cancer research, and the carcinogenic effect of UVR on skin nDNA is well defined in the skin cancer field (Schallreuter *et al*., 2002; Fajuyigbe *et al*., 2018). However, mitochondria are becoming increasingly associated with human cancers because cellular metabolic reprogramming is thought to have a key role in tumour initiation and progression (Penta *et al.*, 2001; Giampazolias and Tait, 2016; Zong *et al.*, 2016; Hosseini *et al.*, 2017). To date a majority of the research pertaining to mitochondria and epithelial carcinomas have focused on other organ systems such as renal, gastric, and colorectal (Penta *et al.*, 2001; Hosseini *et al.*, 2017). Yet skin cancer rates of incidence are rising, and environmental stressors such as UV cause accumulative damage to mtDNA in human skin cells (Hosseini *et al.*, 2017). Basal cell carcinoma (BCC) is the most common skin tumour, although squamous cell carcinoma (SCC) is more aggressive (Fajuyigbe *et al*., 2018). There are established associations between intermittent sun-exposure (e.g. holidays) causing BCC and melanoma, whereas accumulative lifetime sun exposure is associated with SCC occurrence (Kimlin and Guo, 2012). It is hypothesized that BCC arises from mutation(s) to epidermal basal stem cells (Fajuyigbe *et al*., 2018), yet it remains unclear why only portions of environmentally exposed skin become cancerous and the perilesional skin is comparatively unaffected. Eshaghian *et al*., (2005) used long range PCR to investigate mtDNA in BCC/tumour-free skin margins and found a lower frequency of deletions in the tumours. Long range PCR can be biased to preferentially amplify smaller products (Eshaghian *et al*., 2005), which the qPCR assay (chapter 3) ameliorates through amplification of intact mtDNA. A proof of concept study was designed to see if the qPCR assay could be applied to the detection of mtDNA damage in donor-matched BCC and non-BCC tissue. The effect of simulated solar radiation on these tissues was also investigated. In collaboration with Dr Sarah Felton of Oxford University Hospital NHS Trust and Public Health England (PHE; Oxford, UK), 21 donors were included in this pilot study.

As three patients had multiple excisions, it was an opportunity to first investigate whether the qPCR assay could detect differences in the amount of mtDNA damage between their individual (non-BCC) facial regions. As well as confirming the suitability of the qPCR assay to detect acquired damage, it was interesting to review differences across the face where skin thickness is highly variable. Even in the context of this small study, it was clear that the incidence of nose BCC was more prevalent than other areas (Table 7-1). However, nose had significantly less mtDNA damage than thinner skin such as the eyelids and lips (Figure 7-1). Of the donors analysed, a majority were from the nose (n=9), followed by lip (n=3), cheek/chin/forehead

(n=2/region), and eyelid/ear/temple/back (n=1/region) (Figure 7-3). Pratt *et al.* (2017) describe how 70-90% of BCCs develop on sun-exposed head and neck regions, but 5-10% of all skin cancers are on the eyelids. Their study in Liverpool (UK) used UV imaging to show that facial areas prone to skin cancer are those missed during sunscreen application (particularly around the eyes and lips).

To investigate the effect of solar irradiation on BCC and non-BCC skin, each skin sample was divided in half and treated with 2 SED solar simulated light. This dose was chosen by Dr Holliman of PHE, but this did not induce any differences to mtDNA that could be detected by the qPCR assay (data not included). Calibration equipment was sent from PHE to compare solar irradiation equipment (Figure 7-2), which indicated that 2 SED from the Newport 'summer' solar simulator would induce much more damage than a Hönle 'winter' sun simulator. Later studies determined that 2 SED is an insufficient dose for induction of damage in whole skin (Chapter 6). It would perhaps be better to focus on repeated dosing in an organ culture system (Chapter 6), but as this was a secondary question focus was shifted towards the primary objective of comparing mtDNA damage (Figure 7-3).

As seen in Figure 7-3, BCC had less mtDNA damage than non-BCC in 8/22 donors, but more than non-BCC in 5/22. The levels were within 2-fold of one another in 9/22 donors.

Whilst it is not unexpected that a cohort could stratify in groups, concerns arose around this data. It became apparent with the transition from cell (chapter 4) to more complex human skin models (chapter 6), that the qPCR assay comparative nature requires consistency between the volume of sample used to isolate DNA. Whilst the housekeeping protocol ensures equal mtDNA content between samples, the tissue surface area and depth require standardisation. In a cell or skin swab experiment, sample standardisation is more naturally embedded in the methodology. In this collaboration there were additional logistical factors relating to sample collection, transport and processing, that could have affected mtDNA damage. In future studies it is recommended to create robust protocols that detail consistency in sample storage method/duration, processing, and DNA isolation. Whilst surface area is easily standardised by a punch biopsy of chosen diameter (mm), excision depths vary between procedures. To control for this, reference material could be embedded so data can be grouped by histological depth measurements and/or facial region mapping. The non-uniformity of facial skin suggests an approach that groups donor data by region so that thin skin (e.g. lip/eyelid) is not grouped with thicker cheek or nose. It is also necessary to group by skin phototype (Fajuyigbe *et al*., 2018).

Overall, this area of research using donor-matched BCC/non-BCC skin is novel and worth developing. As the qPCR assay was scaled down in Chapter 3, a small punch-biopsy of donor

tissue provides enough DNA for mtDNA screening. This allows for several further investigations to be performed on the DNA/RNA/protein of remaining tissue from an extremely valuable resource.

7.5 Summary of findings

- The qPCR assay (chapter 3) can detect mtDNA damage in human skin
- The Newport Solar Simulator has a different spectral profile than PHE lamps. This is a consideration for future collaborative project protocols incorporating solar irradiation
- To induce a detectable level of induced solar light damage in facial skin, a very high single dose or repeated dosing of organ cultured skin are most likely to be effective
- Collaborative protocols should be standardised for future studies pertaining to sample storage, transport, DNA isolation, sample punch-biopsy size (surface area), sample biopsy depth, and facial location mapping

Chapter 8: Discussion

8.1 Overview

To drive development of skin products, it is essential to understand how AOX ingredients interact and behave. Human skin is exposed to daily oxidative stress from environmental stressors. This project aimed to demonstrate if phenolic AOXs tetrahydrocurcumin (THC) and pterostilbene (PTERO) could protect skin mtDNA from environmental sun exposure. There are numerous publications relating to curcumin and resveratrol, but extremely limited studies on their enhanced synthetic derivatives. Furthermore, there are no studies that use these derivatives in combination.

To accomplish this, a sensitive assay was optimised to detect protection of mtDNA, and a representative full thickness skin equivalent was developed that comprised donor-matched layers and no scaffold material. In addition, an organ culture method was optimised for human skin.

A limiting factor in scientific research is the capacity for basic research to translate to clinical or commercial application. To investigate, this project incorporated a novel transitional approach from previously obtained human cell line data to 2D primary cell monoculture, full-thickness skin equivalents, and whole skin ex-plants. Applications of the qPCR assay were tested in models of different complexities and its use for detection of acquired mtDNA damage was investigated by novel comparison of donor-matched basal cell carcinoma (BCC) and non-BCC facial skin.

8.1 AOX stability: THC and PTERO

Acellular investigations of THC and PTERO photo-stability in solar simulated light, revealed PTERO (but not THC) sustained dose dependent photo-degradation. Although AOX absorbance data in UV-visible light are commonplace, the effect of solar light on AOX stability and chemical structure is infrequently reported. This data concurs with studies by Sirerol *et al.* (2015) who reported PTERO absorbance in the UVB range (275, 290, 305nm; 1mM), and Silva *et al.* (2013) who found the amount and rate of trans-resveratrol degradation was highest after exposure to the combined UV-VIS (200-600nm) spectrum, rather than UV (254nm) or VIS (≥365nm) in isolation. Dr Robert Lucas of GSK hypothesized that the photo modulated PTERO may be pro-oxidative (see supplementary chapter 9.2.4). Moreover it was a patented liposome encapsulated PTERO that was found to confer remarkable protective effects against the production of skin cancer tumours in UVB treated hairless mice (Estrela, J. and Asensi, M. 2009; Sirerol *et al.*, 2015). Yet a study by Dujic *et al.* (2007) reported UVA or VIS photoactivation of low level curcumin in HaCaTs was required to stimulate antiproliferative

effects. These simple experiments provide valuable information relating to strategic combinations of AOXs (or other AOX ingredients) and give considerations for vehicles in formulation design. While THC and PTERO had positive UV absorbance data, this was not translated to a physical blocking (SPF) capacity within a Physiogel™ formulation. Sirerol *et al.* (2015) also found that while PTERO compound has an absorbance peak in the UVB range, the PTERO formulation had a very low *in-vitro* SPF rating. A low SPF rating can sometimes be viewed positively because legislation (e.g. Cosmetics Regulation EC no. 1223/2009) requires extensive testing for a cosmetic to be classified with sun protection status. It is preferable for the AOX ingredients to achieve protection or repair via biological mechanisms.

8.2 Optimisation of the qPCR assay to assess AOX protection of mtDNA

The comparative qPCR assay optimised in this project effectively scaled down the required amount of DNA (by 76%) and reaction volume (by 60%). This meant that more sample types could be economically screened, and smaller samples could be included. This method has been published (Hanna *et al.*, 2019) and applied to other studies which are intended for publication. This assay is a powerful screening tool for assessing AOX protection of mtDNA from solar simulated light. However, some instances have been detected where this assay is not appropriate.

If a sample contains so much mtDNA damage that intact copies cannot amplify, then a shorter mtDNA amplicon should be chosen. An example of this would be a skin swab (where considerable damage is in the top layers of skin), or where monolayers are excessively damaged by high or repeated dosing of solar irradiation. In this instance primer dimer will amplify instead of 11kb mtDNA amplicons, which has a characteristic lower melt temperature of 79-80^{o}C.

The second instance relates to sample standardisation if the experimental model is tissue. As a comparative assay, the housekeeping protocols compare relative mtDNA content (irrespective of damage). However, the proportion of mtDNA damage within the total mtDNA pool is influenced by the volume of original sample. Relative to pooled mtDNA from all skin layers, a higher scale of damage would be detected in pooled mtDNA from the thinner epidermis. Therefore they could not be directly compared with this assay. An example of this was in the whole skin studies where a solar dose of 5 SED induced a higher range of mtDNA damage in foreskin, than thicker facial skin. In a cell or skin swab experiment, sample standardisation is more naturally embedded in the methodology. In a collaborative pilot study with Public Health England (PHE), this qPCR method was used to compare the mtDNA damage of donor-matched BCC/non-BCC skin. Whilst this research is highly novel, recommendations were made in the Chapter 7 discussion that would improve sample standardisation for future use with this

sensitive assay. This would add confidence to this preliminary data ahead of any publications. In order to induce a detectable amount of mtDNA damage in models of various thickness, the solar irradiation dose varied in this thesis, e.g. a 2.16 SED dose was used for monolayers, but 5 SED was required for whole skin. The standard erythemal dose (SED, J.m-2) is equivalent to an erythemal radiant exposure of 100 J.m-2 and equates to one hour of Mediterranean summer sun. The doses used were therefore not outside the remit of a physiological dose acquired over one or multiple accumulative sunlight exposures.

8.3 Protective capacity of THC and PTERO in primary human skin cells exposed to solar simulated light

Foreskin-derived adult keratinocytes, differentiated keratinocytes and fibroblasts were pre-incubated with THC and PTERO to test their protective capacity when irradiated with solar simulated light. Human skin cell lines are widely used to assess the protective capacity of AOXs, but the findings do not always translate with the same potency or mechanism in primary cell cultures. In addition, there is often variability in donor response which is more representative of the diverse consumer population. As such, information can be acquired from primary cell data pertaining to efficacy for market demographics such as sex, age, or skin-type. Although given that the most widely used and available resource of human skin is foreskin, this can skew these demographics. Each AOX was pre-incubated with three or four different adult foreskin donors. THC (but not PTERO) protected mtDNA in 2 of 3 fibroblast donors, and a combination gave greater protection in a further 2 of 3 different fibroblast donors. This is indicative of the previous point where not all donors respond in the same way, or to the same degree. However, it can be difficult to economically test enough donors to draw clear conclusions. With this in mind, it would be beneficial to incorporate design of experiments (DOE) statistical methods in order to identify the minimum number of donors to test and standardise study design. Mignon *et al.* (2018) advocate this approach after demonstrating how variations in technical parameters and cell culture protocols affect fibroblast response to solar irradiation.

There are some skin cell studies with THC or PTERO that propose mechanisms for their AOX and anticarcinogenic properties, such as upregulation of endogenous AOX enzymes (via NRF2 pathway), and increasing mitochondrial membrane potential (Ayli *et al.*, 2010; Kosuru *et al.*, 2016; Chen *et al.*, 2017; Trivedi *et al.*, 2017; Zhou *et al.*, 2019). A resonating point from Kosuru *et al.* (2016) is that low concentrations of PTERO drive protective AOX effects, and high concentrations have a pro-oxidant effect by increasing ROS as a means of inducing apoptosis to prevent carcinogenesis. Whilst AOX doses used in this thesis were selected for being high

(but non-toxic), a lower dose of PTERO was included in the later fibroblast experiments to investigate if this in-fact had a greater protective effect. Halving the dose did not enhance or diminish the mtDNA protection, so future studies on AOX efficacy should aim to find the lowest effective dose.

There is limited evidence in current literature in relation to the protective capacity of THC, PTERO or their combination against mtDNA damage. The protection of skin fibroblast mtDNA from solar light induced damage is novel and worthy of future study.

8.4 AOX formulation testing in 3D human skin models

To investigate whether the mtDNA results from skin cell monolayers could be replicated in more complex 3D model systems, AOXs were delivered in a Physiogel™ (Stiefel) moisturising cream formulation. The skin equivalents developed in Chapter 5 were used for formulation testing and compared to whole skin ex-plant from foreskin and facial sources. In accordance with international cosmetic protocols (e.g. COLIPA), a formulation dose of 2mg/cm^2 was applied (Lionetti and Rigano, 2017). A technical difficulty relating to ≤4mm skin punch biopsies is that they can be difficult to dose with minute volumes of formulation. However, this was overcome by using a positive displacement pipette.

It was not anticipated during the initial monolayer experiments that later formulations would contain niacinamide. As this is a core ingredient of future products, it would be worthwhile to investigate the impact of niacinamide with THC, PTERO, and THC/PTERO combination in monolayer experiments. The incorporation of two Olay positive control products (Chapter 6) worked well, as both contain ~4% niacinamide but vary in SPF status (0 or 15 SPF).

The formulations and market controls were tested on the in-house derived CELLnTEC skin equivalent and commercial Labskin™. Both skin equivalent types were simultaneously characterised with immunostaining, to compare the volume and organisation of extracellular matrix. Whilst the in-house skin equivalent stained positively, the Labskin™ dermis was not as physiologically representative. There was a low fibroblast density and it appeared that embedding fibroblasts within a gel limits their ability to secrete extracellular matrix. Klicks *et al*. (2017) refer to the use of hydrogel-based scaffolds in their review of 3D *in-vitro* skin equivalent systems, but don't comment on the functional capacity of fibroblasts embedded within it. It is unclear how readily fibroblasts can communicate with each other in this environment, or with keratinocytes. As collagen I stained within the Labskin™ epidermis, it appeared to visually suggest that the fibroblasts had pushed it out of the gel. In immunostaining and western blots, this antibody has proved highly specific and it is not expected to be non-specific binding. In published literature, Labskin™ is marketed towards epidermal studies

surrounding wound-healing or skin microbiome but fails to disclose thorough characterisation data. In addition, the model is substantially thicker than physiological skin and raises concerns about the translation of data relating to the dermis or whole skin. One advantage of the dermis design was that the epidermis could be manually removed. To investigate where most of the solar light induced mtDNA damage was located, a comparison was made between separated and combined Labskin™ epidermis-dermis. The same trend was found in epidermis and combined, but the level of damage (bar height) in the latter has been reduced (or 'diluted'). It was unclear if 5 SED simulated solar light had penetrated through the dermis.

This study used one batch of Labskin™ but data relating to inter-model and inter-batch variability is currently unavailable. Mitchell *et al.* (2016) tested the lipid distribution of Physiogel™ on Labskin™ skin equivalents using MALDI-MS imaging. It would be interesting to use this method to investigate the distribution of AOXs throughout human skin equivalent or ex-plant skin. This would be a strong method to visualise the penetrative capacity of THC and PTERO and establish if they reach the fibroblasts. This would add substantial merit to the protection seen with this combination and monolayer fibroblasts. If the product was to be classified as a day cream, consideration for AOX encapsulation would also be worth investigating with MALD-MSI. Friedrich *et al.* (2015) formulated resveratrol and curcumin within lipid-core nanocapsules and compared the penetration to 'free' compound solutions applied to human abdominal skin. Irrespective of encapsulation, resveratrol and curcumin had different penetrative profiles, although both penetrated the dermis and entered the fibroblasts. Kakkar *et al.* (2018) substantially increased the bioavailability and penetrative capacity of THC by trapping it in lipid nanoparticles and formulating a hydrogel that was tested on porcine ear skin. Both studies infer that with the right Physiogel™ formulation, the protective effects seen with THC/PTERO combination in fibroblasts could be achieved through product application to skin.

8.5 CELLnTEC medium: an effective commercial tool for producing human skin equivalents

Based on the pilot comparing fibroblasts from different skin regions, it would be highly valuable to apply the techniques to a study where donor skin was sourced from multiple body sites. This would eliminate inter-donor variability and make an important contribution to the field of dermatology.

It was not possible to repeat the ex-plant/Labskin™ formulation studies with CELLnTEC skin equivalents due to technical challenges establishing this batch of skin equivalents. However, an evaluation of all pilots was performed in and discussed in chapter 5. Considering the technical

recommendations outlined in chapter 5, it is unlikely that this event will reoccur in future experiments.

It is expected that as these skin equivalents are of a similar thickness to thin physiological skin (but without additional cell types/organ structures), that the qPCR assay is suited to sensitively distinguish between conditions. As such this experiment is worth repeating with future test formulations.

Preliminary work made promising strides in the adaptation of these skin equivalents to represent target areas of application (e.g. face). Such skin equivalents are commercially unavailable, and the highly proliferative nature of facial keratinocytes suggests the data obtained from formulation testing may be different to that from foreskin. Successfully scaling the skin equivalents to 24 well size makes it feasible to produce enough skin equivalents from small facial skin samples. Furthermore, a valuable resource of (mostly female donor) cryopreserved facial keratinocytes remain and could readily be grown into reconstructed human epidermal skin equivalents. Another option would be to seed atop dermis constructed from foreskin cell fibroblasts, but this is likely to complicate data interpretation. It is worth noting that the age of these donors (undergoing Mohs surgery) was typically from older female donors, who are likely to have accumulative sun exposure. As skin from older donors does not typically produce robust primary cell cultures, this could be a limiting factor to both producing facial skin derived skin equivalents and subsequently treating with solar irradiation.

Commercial media typically has higher levels of vitamins than are found physiologically, and both the ingredients and concentration are proprietary. To study AOXs this is an important factor to consider. CELLnTEC were co-operative in recognising that this could be detrimental to effective AOX dosing and shared the following concentrations as examples to consider: 2µM niacinamide, 0.1µM riboflavin, 0.3µM B12, and 0.2µM folic acid. CELLnTEC additionally state that their medium is free from phenol/cholera toxin/animal products, and composed of 21 amino acids, 19 minerals and trace elements (selenium, manganese, zinc), 14 vitamins, 10 other ingredients (glucose, pyruvate, buffers), and 6 growth factors/co-factors (insulin, hydrocortisone, epidermal growth factor, fibroblast growth factor) - https://cellntec.com/products/resources/tech/formulation/. For future work it may be worthwhile to perform a literature search of the physiological levels and role of media nutritional elements in the blood, hair and skin.

8.6 Future work

8.6.1 Human skin equivalents and organ culture system

Promising strides were made with the facial skin equivalent trial after optimisation of cell isolation and culture methodologies. Whilst it seems feasible that facial keratinocytes would readily develop into reconstructed human epidermis (RHE), it would be extremely worthwhile to trial the full-thickness skin equivalent in other donors. Given the keratinocytes proliferative rate, adaptations to the usual timeline are likely to be required. A contact at CELLnTEC communicated that keratinocytes will fail to attach or displace fibroblasts if the dermal layer has not established. If feasible, it may be useful to take histological sections of the dermis before and after keratinocytes are added.

To characterise skin equivalent similarity to whole skin, punch-biopsies of reference skin was kept for RNA/protein and a custom panel of skin-specific markers was designed. If time had allowed, this would have potentially been a powerful publication pertaining to the similarity of donor skin and skin equivalents derived from it. In particular, the genes of components from metabolic and AOX pathway were included to determine if skin equivalents have the machinery to behave in a physiological manner. This would infer how useful they are for elucidating AOX mechanisms of action. NanoString technology is an economical intermediary between TaqMan™ and RNAseq. As NanoString probes are directly incubated with RNA there is no cDNA amplification step, RNA quality is not a limiting factor, and data can be rapidly attained at Newcastle University NanoString facility. Functional characterisation has been performed on some commercial skin equivalents such as metabolic enzymes in SkinEthic™ (Eilstein *et al.*, 2014), but they were not compared to donor-matched skin.

Growth of skin equivalents is a long and expensive process. To better identify the donors most suitable for skin equivalents, it would be a worthy trial to begin collecting media samples from passage number 0-1 fibroblasts. These would be analysed by protein ELISA for high levels of extracellular matrix proteins, as the pilot in Chapter 5 showed that high levels in the media did correlate with larger western blot bands (indicative that it will lay down more protein). The aim would be to identify the best day to take a media sample and screen a donor for its likelihood to be shortlisted for skin equivalents or best used for another purpose.

In addition, studies pertaining to the stratum corneum are required. Asides from acquiring imaging and a lipid profile, MALD-MS imaging could compare Physiogel™ permeation through the CELLnTEC skin equivalent and a punch-biopsy of skin from the same donor (using the optimised organ culture system) (Mitchell *et al.* (2016)). Optimisation of a MALDI-MSI protocol with these skin equivalents would be highly advantageous for future testing of novel

compounds, as there would be visual identification of which layer(s) of skin they permeate and provide powerful visual evidence of damage protection for intellectual property and marketing purposes.

A limiting factor in this work was the low sample numbers in some experiments. Future work should aim to use statistical power calculations to determine the number of donors to use for each experiment, with consideration for grouping of biological age and body site.

8.6.2 Nuclear DNA (nDNA) protection

Another area of intended study would involve reanalysis of the DNA samples from this thesis for nDNA protection. As the qPCR assay uses mtDNA specific primers and only a very small amount of DNA, there is clear opportunity to analyse both genomes within the same sample. This would be highly novel and build a comprehensive picture of the AOX role in the intracellular space. There is known functional interplay between both genomes, including repair mechanisms and autophagy/mitophagy (Fang et al., 2016; Gammage and Frezza, 2019). A technique that could be easily optimised and offer rapid screening would be DNA ELISA for biomarkers of UV-induced damage such as 8-hydroxy-2'-deoxyguanosine (8-OHdG) (Cooke *et al*., 2003; Drake *et al.*, 2019). The only limiting factor might be the amount of DNA required (ng), which could be reduced by using half-area 96 well plates (as for protein ELISA in this thesis). Commercial kits are widely available, but it would be more economical to optimise an in-house protocol.

8.6.3 AOX mechanisms of action

There are many commercial AOXs of interest, and it is known that strategic combinations are key to enhance endogenous cell function (Burke. K.E, 2007; Bogdan and Baumann, 2008; Dinkova-Kostova & Abramov, 2015; Burke. K.E, 2018). Collaboration with experts in computational predictive modelling could help stratify these for testing in cellular systems. When using primary cells (which introduce donor variability), consultation with a Bayesian method expert (statistician) could help create a design of experiments (DOE) approach to determine the number of donors required for testing, alongside the number of variables and replicates required to draw meaningful conclusions (Collins *et al*., 2009; Holder, D.J. and Marino, M.J. (2017); Murray *et al*., (2017).

The primary cell AOX studies followed on from pilot in-house data obtained in skin cell lines. Dr Matthew Jackson (Newcastle University) pre-incubated HDFn cell lines with THC and PTERO for 12 hours before solar irradiation (2.16 SED). The cDNA was analysed with a human oxidative stress microarray (Qiagen) to assess the effects on 84 genes related to oxidative stress and antioxidant response. This work was preliminary and requires additional validation, but

future experiments could expand on the pathways identified (through the up/down-regulated genes) in primary skin cells and more complex models. The mechanisms of resveratrol and curcumin are propagated throughout the literature, and some studies have extended to their synthetically enhanced derivatives PTERO and THC (see sections 1.6.3 and 4.4). These are a valued resource to shortlist potential mechanisms worth investigating in our skin equivalent systems.

8.7 Closing summary

Physiogel™ moisturisers have proven capacity to help dryness, redness and skin irritation (Santos-Caetano *et al.*, 2019; Nisbet *et al.*, 2019; Santos-Caetano *et al.*, 2020). These symptoms typically present with compromised skin barrier integrity, increasing susceptibility to environmental stressors which drive their severity. It is hoped that the sensitive mtDNA assay and highly representative human skin equivalent model optimised in this thesis can be used to enhance product development and understanding. The data obtained in this thesis pertaining to THC/PTERO, in combination with what is known in the literature is highly indicative that these active ingredients could contribute anti-inflammatory, anticarcinogenic and AOX properties to the product range.

Chapter 9: Appendix

9.1 PhD publications, presentations and awards

Portions of this work have resulted in two peer-reviewed publications:

- Hanna, R., Crowther, J.M., Bulsara, P.A., Wang, X., Moore, D.J. and Birch-Machin, M.A. (2019) 'Optimised detection of mitochondrial DNA strand breaks', *Mitochondrion*. 46, pp.172-178.
- Naidoo, K., Hanna, R. and Birch-Machin Mark, A. (2018) 'What is the role of mitochondrial dysfunction in skin photoaging?', *Experimental Dermatology*, 27(2), pp. 124-128

This work has been presented at several conferences:

- North East Postgraduate Conference: engagement style presentation. Newcastle UK; 9th November 2018: **oral presentation**
- 8th International Conference on Oxidative Stress in Skin Medicine and Biology, Andros, Greece; 6-9th September 2018: **oral presentation**
- 11th Annual GSK PhD Science Symposium (Consumer Healthcare: Oral & Skin), Weybridge UK; 13-14th June 2018: **oral presentation**
- British Society of Investigative Dermatology (BSID) Conference, London UK; 26-28th March 2018: **travel bursary award and poster presentation**
- DMDG Skin Metabolism Meeting, Sunderland University, UK; 27th-29th November 2017: **networking event**
- Society of Investigative Dermatology (SID) Conference, Portland, OR, USA; 25th-29th April 2017: **poster presentation**
- Stratified Medicine Category, Director's Research Day, Institute of Cellular Medicine, Newcastle University; 26th June 2017: **poster presentation prize**
- Stratified Medicine, Biomarkers and Therapeutics Meeting, Newcastle University; 23rd May 2017: **poster presentation**

This work has been orally presented at internal and collaborative meetings:

- Institute of Cellular Medicine Seminars, Newcastle University, UK; annual oral presentation 2016-2018
- GSK Project Update Teleconference Calls; 2015-2019; 4-6 week intervals

9.2 Supplementary information

9.2.1 Composition of EpiLife™ Medium, with 60 µM calcium chloride

EpiLife™ medium (with 60µM calcium chloride; item MEP1500CA, Thermo Scientific) was used to isolate and culture adult foreskin-derived epidermal keratinocytes. The individual components are listed in the Table 9.1, but the concentrations are proprietary. The medium was additionally supplemented with Human Keratinocyte Growth Serum (HKGS), with the composition listed under 9.2.2. The formulation information was sourced from: https://www.thermofisher.com/uk/en/home/technical-resources/media-formulation.275.html.

Components	Molecular Weight	Concentration (g/L)
Amino Acids		
Glycine	75	confidential
L-Alanine	89	confidential
L-Arginine hydrochloride	211	confidential
L-Asparagine-H2O	150	confidential
L-Aspartic acid	133	confidential
L-Cysteine	121	confidential
L-Glutamic Acid	147	confidential
L-Glutamine	146	confidential
L-Histidine hydrochloride-H2O	210	confidential
L-Isoleucine	131	confidential
L-Leucine	131	confidential
L-Lysine hydrochloride	183	confidential
L-Methionine	149	confidential
L-Phenylalanine	165	confidential
L-Proline	115	confidential
L-Serine	105	confidential
L-Threonine	119	confidential
L-Tryptophan	204	confidential
L-Tyrosine	181	confidential
L-Valine	117	confidential
Vitamins		
Choline chloride	140	confidential
D-Pantothenic Acid	238	confidential
Folic Acid	441	confidential
Myo-Inositol	180	confidential
Niacinamide	122	confidential
Pyridoxal hydrochloride	206	confidential
Riboflavin	376	confidential
Thiamine hydrochloride	337	confidential
Vitamin B12	1355	confidential
d-Biotin	244	confidential

Inorganic Salts		
Ammonium Molybdate ((NH4)6Mo7O24-4H2O)	1236	confidential
Ammonium metavanadate (NH4VO3)	117	confidential
Calcium Chloride (CaCl2-2H2O)	147	confidential
Cupric sulfate (CuSO4-5H2O)	250	confidential
Ferric sulfate (FeSO4-7H2O)	278	confidential
Magnesium Chloride (MgCl2-6H2O)	203	confidential
Manganese Sulfate (MnSO4-H20)	169	confidential
Nickelous Chloride NiCl2 6H2O	238	confidential
Potassium Chloride (KCl)	75	confidential
Sodium Bicarbonate (NaHCO3)	84	confidential
Sodium Chloride (NaCl)	58	confidential
Sodium Meta Silicate Na2SiO3 9H2O	284	confidential
Sodium Phosphate dibasic (Na2HPO4-7H2O)	268	confidential
Sodium Selenite (Na2SeO3)	173	confidential
Tin Chloride (SnCl2.2H2O)	226	confidential
Zinc sulfate (ZnSO4-7H2O)	288	confidential
Other Components		
Adenine.HCl	172	confidential
D-Glucose (Dextrose)	180	confidential
DL-alpha-Lipoic Acid	206	confidential
Ethanolamine	61	confidential
HEPES	238	confidential
O-Phosphorylethanolamine	141	confidential
Phenol Red	376.4	confidential
Putrescine 2HCl	161	confidential
Sodium Pyruvate	110	confidential
Thymidine	242	confidential

Table 9-1: Composition of EpiLife™ Medium, with 60 µM calcium chloride.

9.2.2 Composition of Human Keratinocyte Growth Serum (HKGS; EpiLife™ supplement)

EpiLife™ medium (see 9.2.1) was supplemented with HKGS (item S0015, Thermo Scientific) before used in the isolation and culture of adult foreskin-derived epidermal keratinocytes. The individual components are listed in the Table 9.2. The information was sourced from: https://www.thermofisher.com/order/catalog/product/S0015#/S0015

Components	Stock concentration (100X)	Final concentration (1X)
Proteins		
Human epidermal growth factor	200ng/ml	0.2µg/ml
Human insulin-like growth factor-I	1µg/ml	0.01µg/ml
Bovine transferrin	500µg/ml	5µg/ml
Other Components		
Bovine pituitary extract (BPE)	20% v/v	0.2% v/v
Hydrocortisone	18µg/ml	0.18µg/ml

Table 9-2: Composition of Human Keratinocyte Growth Serum (HKGS; EpiLife™ supplement)

9.2.3 Composition of Dulbecco's Modified Eagle Medium (DMEM)

DMEM medium was used in the isolation and culture of adult foreskin-derived dermal fibroblasts. DMEM was developed in 1969 and is a modification of Basal Medium Eagle (BME) that differs from BME and MEM by the following characteristics:

- Vitamins 4X greater than MEM. Vitamins and amino acids greater than BME.
- Types and quantities of amino acids greater than MEM and BME
- Iron (ferric nitrate)

Individual components are listed in the Table 9.3. The information was sourced from:

- https://knowledge.lonza.com/media?id=20&search=
- https://www.sigmaaldrich.com/life-science/cell-culture/learning-center/media-formulations/dme.html

Components	Concentration (g/L)
Amino Acids	
L-Arginine • HCl	0.084
L-Cystine • 2HCl	0.0626
L-Glutamine	0.584
Glycine	0.03
L-Histidine • HCl • H2O	0.042
L-Isoleucine	0.105
L-Leucine	0.105
L-Lysine • HCl	0.146
L-Methionine	0.03
L-Phenylalanine	0.066
L-Serine	0.042
L-Threonine	0.095
L-Tryptophan	0.016
L-Tyrosine • 2Na • 2H2O	0.10379
L-Valine	0.094
Vitamins	
Choline Chloride	0.004
Folic Acid	0.004
myo-Inositol	0.0072
Niacinamide	0.004
D-Pantothenic Acid (hemicalcium)	0.004
Pyridoxal • HCl	0.004
Riboflavin	0.0004
Thiamine • HCl	0.004
Inorganic Salts	
Calcium Chloride	0.2
Ferric Nitrate • 9H2O	0.0001
Magnesium Sulfate (anhydrous)	0.09767
Potassium Chloride	0.4

Sodium Chloride	6.4
Sodium Phosphate Monobasic (anhydrous)	0.109
Sodium Bicarbonate	3.7
Other Components	
D-Glucose	4.5
Phenol Red • Na	0.0159
Pyruvic Acid • Na	0.11

Table 9-3: Composition of Dulbecco's Modified Eagle Medium (DMEM)

9.2.4 Hypothesized ROS production as a result of UV light exposure to PTERO.

Supplementary information to Chapter 4. Diagram produced by Dr Robert Lucas of GlaxoSmithKline, UK.

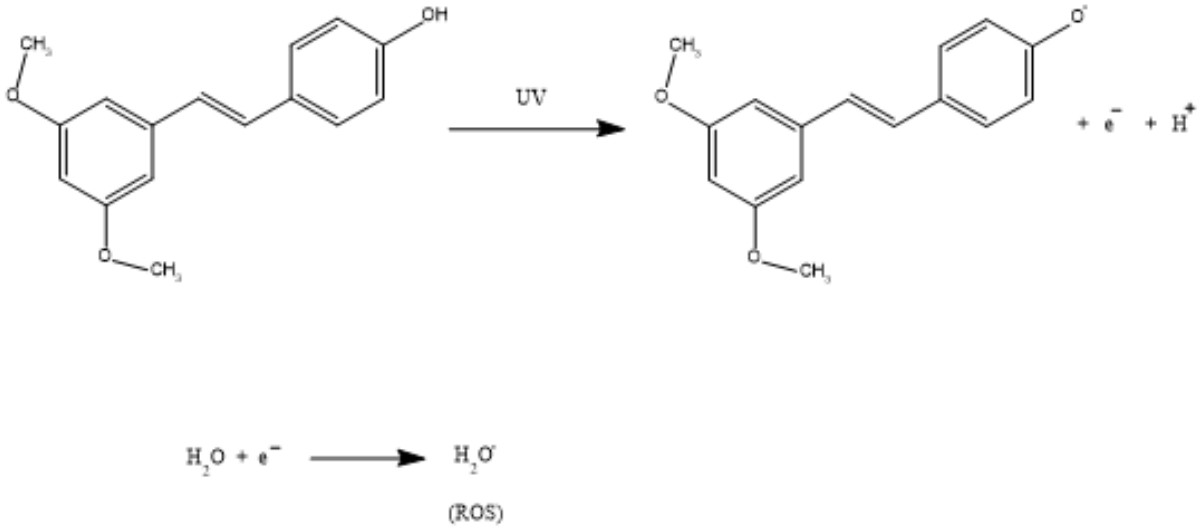

Figure 9-1: Hypothesized ROS production as a result of UV light exposure to PTERO.

9.2.5 Fixative reagent options for immunofluorescence

Supplementary information to Chapter 5.

Source: https://www.leica-microsystems.com/science-lab/how-to-prepare-your-specimen-for-immunofluorescence-microscopy/

	Fixative	Effect	Advantages	Disadvantages
Chemical crosslinkers	Formaldehyde	Crosslink proteins via their free amino groups	Preserves well cellular morphology. Good for already present fluorescent proteins.	Antigens might also be crosslinked
	Glutaraldehyde		Preserves well cellular morphology. Good for already present fluorescent proteins.	Antigens might also be crosslinked High autofluorescence
Organic solvents	Methanol	Fixation by dehydrogenation and protein precipitation. Cells will simultaneously become permeabilized.	Good preservation of cellular architecture. Faster procedure in comparison to chemical crosslinkers.	Strong negative effect on many epitopes. Not suitable for fluorescent proteins. Soluble and lipid components are getting lost.
	Acetone		Less damaging to epitopes. Faster procedure	Not suitable for fluorescent proteins. Soluble and lipid components are getting lost.

Figure 9-2: Fixative reagent options for immunofluorescence

9.2.6 Labskin™ construction timeline

Screenshot of a CELLnTEC conference presentation slide which was publicly available online in 2018 but has since been removed. Batch 1910123 used in this study was shipped on day 21 and received on day 22. After overnight acclimation the experiment was performed on day 3 after shipping, representing the green zone i.e. skin equivalents in optimal condition/viability.

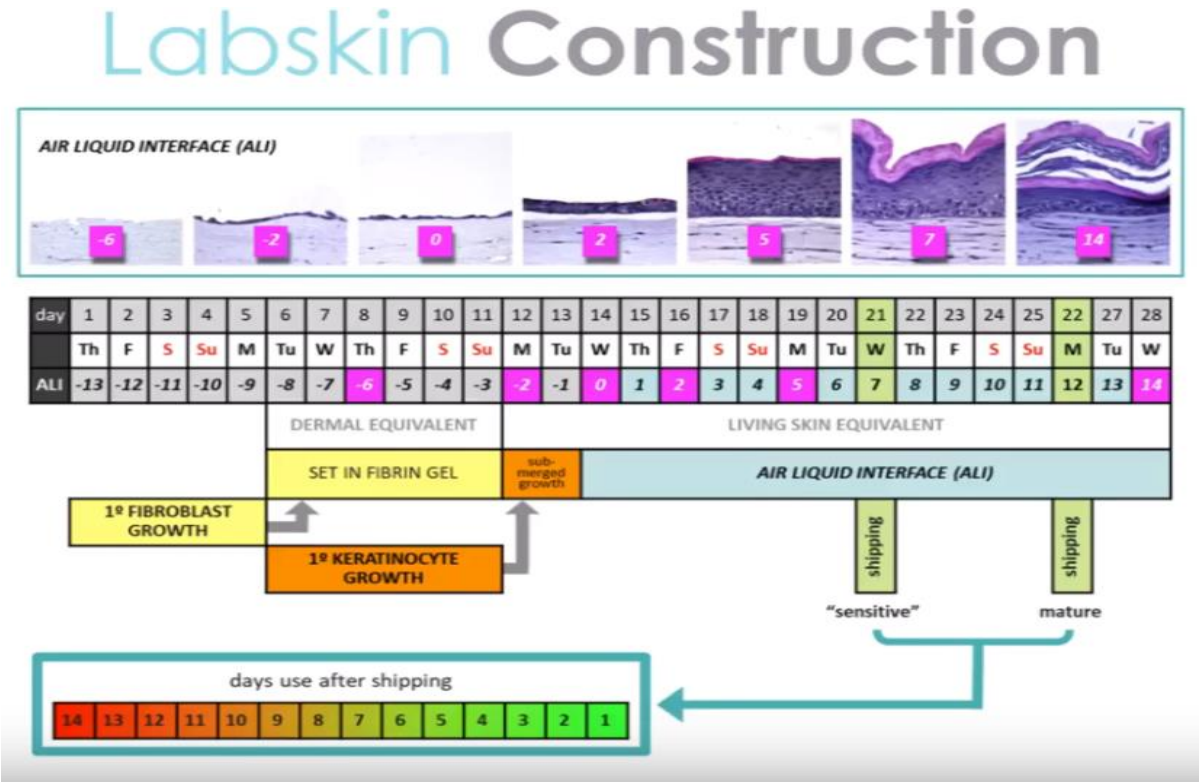

Figure 9-3: Labskin™ construction timeline

9.2.7 Comparative histological H&E of promotional CELLnTEC skin equivalent alongside in-house reconstructed human epidermis and full thickness skin equivalents.

Skin equivalents grown from foreskin-derived adult keratinocytes and reticular fibroblasts from male donors S1073F and S1074F. Measurements (mm) of stratum corneum, epidermis and dermis have been calculated using the scale bars for all skin equivalents, alongside the CELLnTEC promotional image.

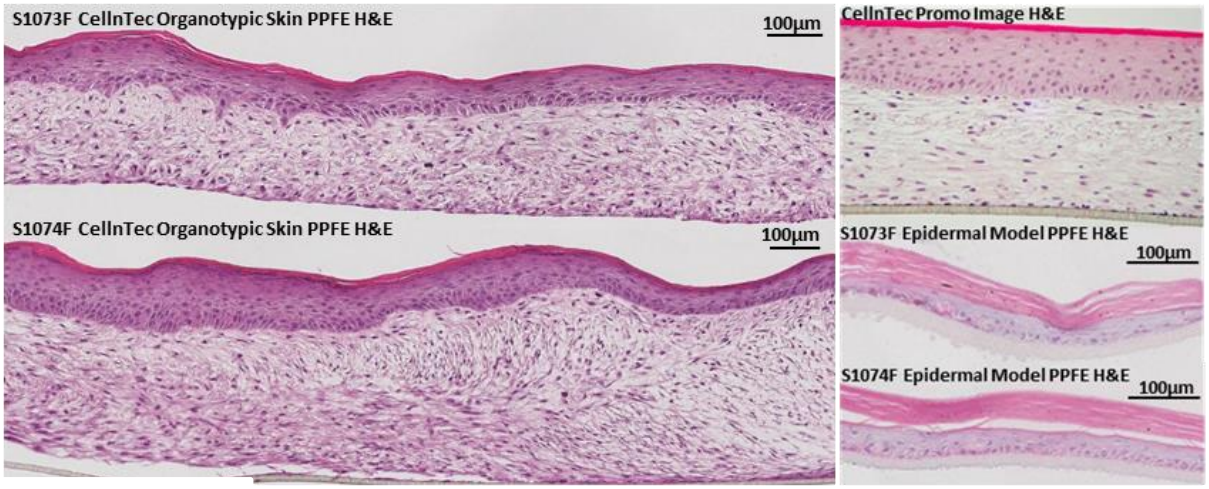

	Epidermal Model		CellnTec FT Organotypic Skin Model			*Ex-vivo* Adult Human Foreskin		
	S1073F	**S1074F**	**Promo Image**	**S1073F**	**S1074F**	**S1141F**	**S1142F**	**S1145F**
Stratum Corneum (mm)	0.033-0.040	0.033-0.040	0.006	0.005-0.011	0.006-0.017	0.005-0.014	0.070-0.014	0.07-0.015
Epidermis (mm)	0.040-0.046	0.040-0.046	0.075	0.042-0.105	0.047-0.117	0.023-0.136	0.069-0.138	0.052-0.138
Total Epidermis (mm)	0.073-0.086	0.073-0.086	0.081	0.047-0.116	0.053-0.134	0.028-0.150	0.138-0.152	0.122-0.153
Dermis (mm)	N/A	N/A	0.119	0.142-0.210	0.259-0.370	N/A	N/A	N/A
Dermis-Hypodermis (mm)	N/A	N/A	N/A	N/A	N/A	0.075-0.900	0.455-0.564	0.364-0.500
Total Model Depth (mm)	N/A	N/A	0.281	0.189-0.325	0.311-0.505	0.103-1.050	0.594-0.716	0.486-0.653

Figure 9-4: Comparative histological H&E of promotional CELLnTEC skin equivalent alongside in-house reconstructed human epidermis and full thickness skin equivalents. Skin equivalents grown from foreskin-derived and donor-matched adult keratinocytes and reticular fibroblasts of S1073F (male – age 65) and S1074F (male – age 28). Keratinocytes were also seeded into epidermal skin equivalents as a technical control of cell quality. Skin equivalents have formed an anatomically correct keratinised stratified epidermis, attached to a thicker dermal layer. The structural matrix was created by the fibroblasts, without artificial scaffold. A dermo-epidermal junction is visible, and fibroblasts are evident within the dermal layer. Measurements (mm) of stratum corneum, epidermis and dermis have been calculated using the scale bars for both skin equivalents, alongside the CELLnTEC promotional image and three ex-vivo whole foreskin donors (S1141F – male, ag 40, S1142F – male, age 17, S1145F – male, age 51; see supplementary Figure 9.4). Reference skin from S1073F and S1074F was unavailable. H&E staining was performed on three sections per skin equivalent from each PPFE and OCT block. Images shown are one PPFE section per donor, with PPFE providing better imaging than OCT. *FT - full thickness.* Scale bars are 100µm.

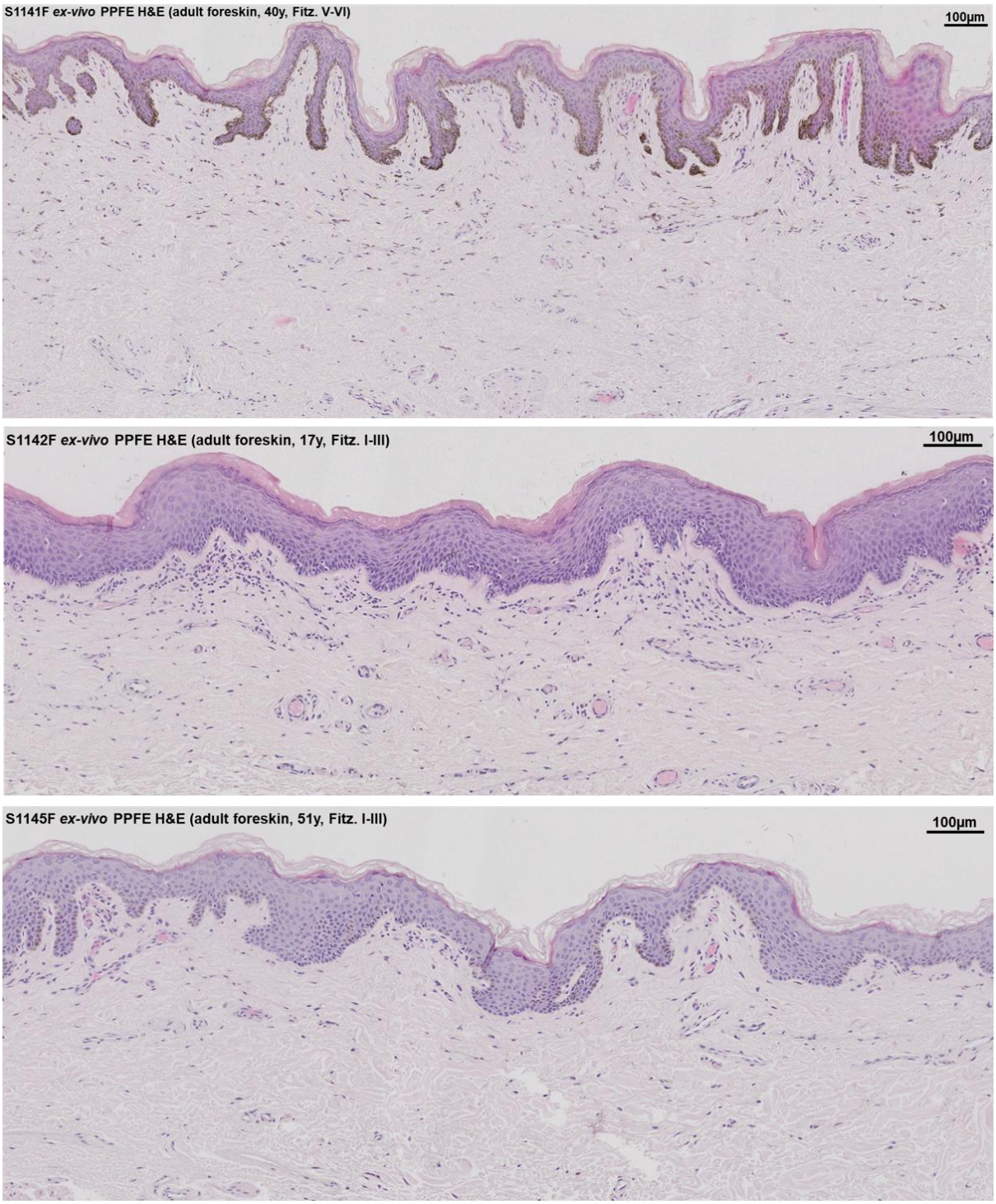

Figure 9-5: H&E histology of ex-vivo adult foreskin. Ex-vivo whole foreskin donors: S1141F – male, age 40, S1142F – male, age 17, and S1145F – male, age 51. *Fitz – Fitzpatrick classification of skin phototype*. Scale bars are 100µm.

9.2.8 ELISA standard curves for collagen I, fibronectin and hyaluronan detection in skin fibroblast medium.

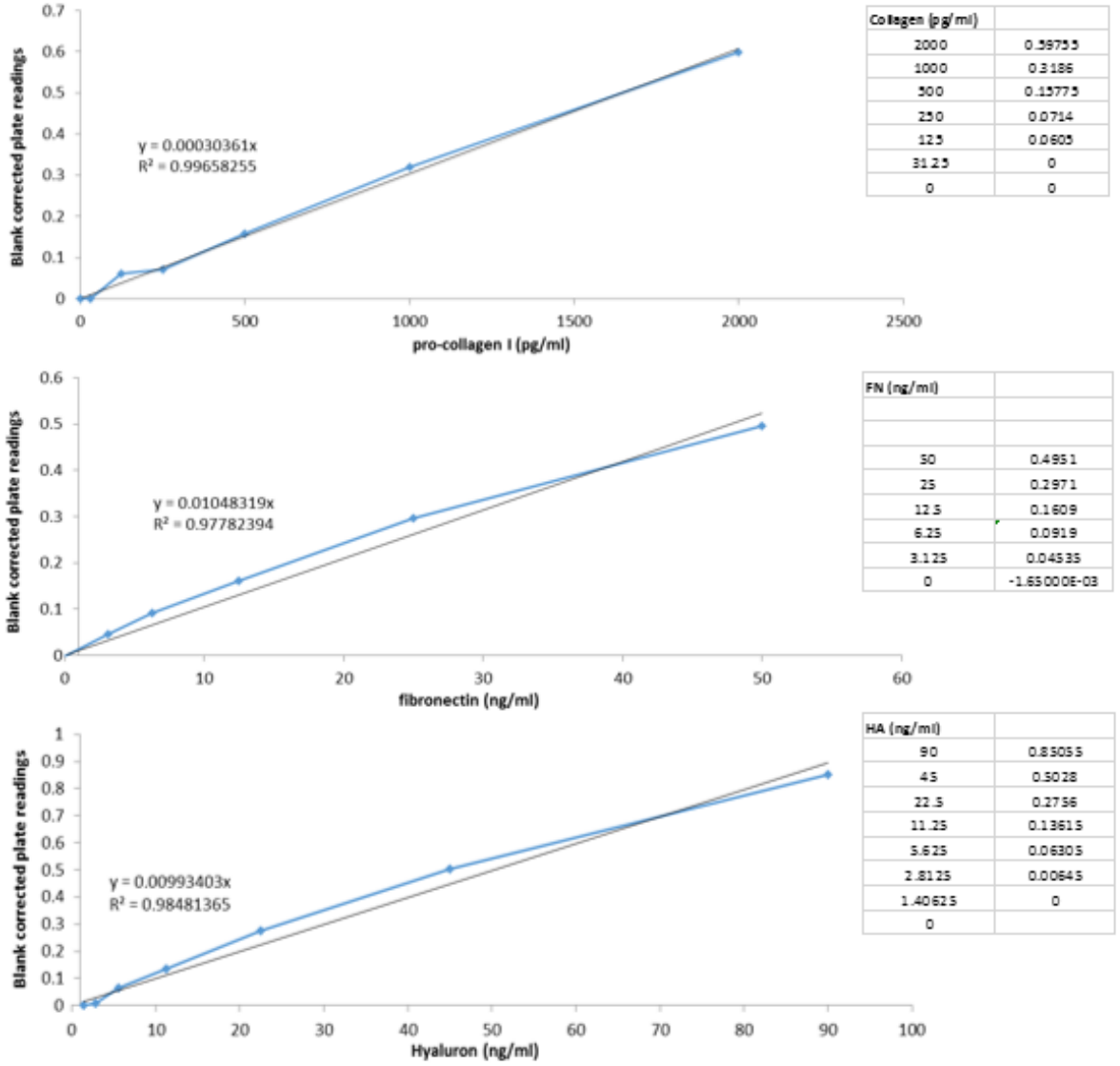

Figure 9-6: ELISA standard curves for collagen I, fibronectin and hyaluronan detection in skin fibroblast medium.

Chapter 10: References

Aggarwal, B.B., Deb, L. and Prasad, S. (2014) 'Curcumin differs from tetrahydrocurcumin for molecular targets, signaling pathways and cellular responses', *Molecules (Basel, Switzerland)*, 20(1), pp. 185-205.

Alanko, J., Riutta, A., Holm, P., Mucha, I., Vapaatalo, H. and Metsä-Ketelä, T. (1999) 'Modulation of arachidonic acid metabolism by phenols: relation to their structure and antioxidant/prooxidant properties', *Free Radical Biology and Medicine*, 26(1), pp. 193-201.

Anderson, A., Bowman, A., Boulton, S.J., Manning, P. and Birch-Machin, M.A. (2014) 'A role for human mitochondrial complex II in the production of reactive oxygen species in human skin', *Redox Biology*, 2, pp. 1016-1022.

Asselineau, D., Bernard, B.A., Bailly, C., Darmon, M. and Pruniéras, M. (1986) 'Human Epidermis Reconstructed by Culture: Is It "Normal"?', *Journal of Investigative Dermatology*, 86(2), pp. 181-186.

Atsumi, T., Fujisawa, S. and Tonosaki, K. (2005) 'Relationship between intracellular ROS production and membrane mobility in curcumin- and tetrahydrocurcumin-treated human gingival fibroblasts and human submandibular gland carcinoma cells', *Oral Diseases*, 11(4), pp. 236-242.

Ayli, E.E., Dugas-Breit, S., Li, W., Marshall, C., Zhao, L., Meulener, M., Griffin, T., Gelfand, J.M. and Seykora, J.T. (2010) 'Curcuminoids activate p38 MAP kinases and promote UVB-dependent signalling in keratinocytes', *Experimental Dermatology*, 19(6), pp. 493-500.

Baris, O. R., Klose, A. , Kloepper, J. E., Weiland, D. , Neuhaus, J. F., Schauen, M. , Wille, A., Müller, A. , Merkwirth, C. , Langer, T. , Larsson, N. , Krieg, T. , Tobin, D. J., Paus, R. and Wiesner, R. J. (2011) 'The Mitochondrial Electron Transport Chain Is Dispensable for Proliferation and Differentiation of Epidermal Progenitor Cells', *STEM CELLS*, 29, pp. 1459-1468.

Barrandon, Y. and Green H. (1985) 'Cell size as a determinant of the clone-forming ability of human keratinocytes' *Proceedings of the National Academy of Science*, 82(16), pp. 5390-5394

Bellas, E., Seiberg, M., Garlick, J. and Kaplan, D.L. (2012) 'In vitro 3D full thickness skin equivalent tissue model using silk and collagen biomaterials', *Macromolecular bioscience*, 12(12), pp. 1627-1636.

Berneburg, M., Plettenberg, H. and Krutmann, J. (2000) 'Photoaging of human skin', *Photodermatology, Photoimmunology & Photomedicine*, 16(6), pp. 239-244.

Birch-Machin, M.A. and Bowman, A. (2016) 'Oxidative stress and ageing', *British Journal of Dermatology*, 175(S2), pp. 26-29.

Birch-Machin, M.A. and Swalwell, H. (2010) 'How mitochondria record the effects of UV exposure and oxidative stress using human skin as a model tissue', *Mutagenesis*, 25(2), pp. 101-107.

Bogdan A. and Baumann L. (2008) 'Antioxidants used in skin care formulations', *Skin Therapy Letter*, 13(7), pp5-9

Bojar, R.A. (2015) 'Studying the Human Skin Microbiome Using 3DIn VitroSkin Models', *Applied In Vitro Toxicology*, 1(2), pp. 165-171.

Brohem, C.A., da Silva Cardeal, L.B., Tiago, M., Soengas, M.S., de Moraes Barros, S.B. and Maria-Engler, S.S. (2011) 'Artificial Skin in Perspective: Concepts and Applications', *Pigment cell & melanoma research*, 24(1), pp. 35-50.

Burke, K. E. (2007), Interaction of vitamins C and E as better cosmeceuticals. *Dermatologic Therapy*, 20: 314-321.

Burke, K.E. 2018, 'Mechanisms of aging and development - A new understanding of environmental damage to the skin and prevention with topical antioxidants', *Mechanisms of Ageing and Development*, 172(1), pp. 123–30.

Chapman, S., McDermott, D. H., Shen, K., Jang, M. K., and McBride, A. A. (2014). The effect of Rho kinase inhibition on long-term keratinocyte proliferation is rapid and conditional. *Stem cell research & therapy*, *5*(2), pp. 60-71

Chen, R.-J., Ho, C.-T. and Wang, Y.-J. (2010) 'Pterostilbene induces autophagy and apoptosis in sensitive and chemoresistant human bladder cancer cells', *Molecular Nutrition & Food Research*, 54(12), pp. 1819-1832.

Chen, R.-J., Lee, Y.-H., Yeh, Y.-L., Wu, W.-S., Ho, C.-T., Li, C.-Y., Wang, B., Jr. and Wang, Y.-J. (2017) 'Autophagy-inducing effect of pterostilbene: A prospective therapeutic/preventive option for skin diseases', *Journal of Food and Drug Analysis*, 25(1), pp. 125-133.

Collins, L. M., Dziak, J. J., & Li, R. (2009). Design of experiments with multiple independent variables: a resource management perspective on complete and reduced factorial designs. *Psychological methods*, 14(3), pp. 202–224

Cooke, M.S., Podmore, I.D., Mistry, N., Evans M.D., Herbert K.E., Griffiths H.R. and Lunec J. (2003) 'Immunochemical detection of UV-induced DNA damage and repair', *Journal of Immunological Methods*, 280(1-2), pp. 125-133,

Costa-Almeida R., Gomez-Lazaro M., Ramalho C., Granja P.L., Soares R., and Guerreiro S.G. (2015) 'Fibroblast-endothelial partners for vascularization strategies in tissue engineering'. *Tissue Engineering, Part A*, 21(5-6), pp. 1055-65.

de la Lastra, C.A. and Villegas, I. (2007) 'Resveratrol as an antioxidant and pro-oxidant agent: mechanisms and clinical implications', *Biochemical Society Transactions*, 35(5), pp. 1156-1160.

Dellambra, E., Golisano, O., Bondanza, S., Siviero, E., Lacal, P., Molinari, M., D'Atri, S., and De Luca, M. (2000) 'Downregulation of 14-3-3σ Prevents Clonal Evolution and Leads to Immortalization of Primary Human Keratinocytes'. *Journal of Cell Biology*, 149(5), pp. 1117–1130.

Diffey, B.L. (1991) 'Solar ultraviolet radiation effects on biological systems', *Physics in Medicine and Biology*, 36(3), p. 299.

Dinkova-Kostova, A.T. and Talalay, P. 2008, 'Direct and indirect antioxidant properties of inducers of cytoprotective proteins', *Molecular Nutrition and Food Research*, 52(1), pp. S128-38.

Drake D.M., Shapiro A.M., and Wells P.G. (2019) Measurement of the Oxidative DNA Lesion 8-Oxoguanine (8-oxoG) by ELISA or by High-Performance Liquid Chromatography (HPLC) with Electrochemical Detection. In: Hansen J., Winn L. (eds) Developmental Toxicology. Methods in Molecular Biology, vol 1965. Humana, New York, NY

Dujic, J., Kippenberger, S., Hoffmann, S., Ramirez-Bosca, A., Miquel, J., Diaz-Alperi, J., Bereiter-Hahn, J., Kaufmann, R. and Bernd, A. (2007) 'Low Concentrations of Curcumin Induce Growth Arrest and Apoptosis in Skin Keratinocytes Only in Combination with UVA or Visible Light', *Journal of Investigative Dermatology*, 127(8), pp. 1992-2000.

Działo, M., Mierziak, J., Korzun, U., Preisner, M., Szopa, J. and Kulma, A. (2016) 'The Potential of Plant Phenolics in Prevention and Therapy of Skin Disorders', *International journal of molecular sciences*, 17(2), pp. 160-160.

Eilstein, J., Léreaux, G., Budimir, N., Hussler, G., Wilkinson, S. and Duché, D. (2014) 'Comparison of xenobiotic metabolizing enzyme activities in ex vivo human skin and reconstructed human skin models from SkinEthic', *Archives of Toxicology*, 88(9), pp. 1681-1694.

El Ghalbzouri, A., Commandeur, S., Rietveld, M.H., Mulder, A.A. and Willemze, R. (2009) 'Replacement of animal-derived collagen matrix by human fibroblast-derived dermal matrix for human skin equivalent products', *Biomaterials*, 30(1), pp. 71-78.

Enthaler, B., Trusch, M., Fischer, M., Rapp, C., Pruns, J.K. and Vietzke, J.-P. (2013) 'MALDI imaging in human skin tissue sections: focus on various matrices and enzymes', *Analytical and Bioanalytical Chemistry*, 405(4), pp. 1159-1170.

Eshaghian. A, Vleugels. R, A,Canter. J, A, McDonald. M, A, Stasko. T, Sligh. J, E (2005) 'Mitochondrial DNA Deletions Serve as Biomarkers of Aging in the Skin, but Are Typically Absent in Nonmelanoma Skin Cancers', *Journal of Investigative Dermatology*, 126(2), pp. 336 - 344

Estrela. J, A. and Asensi, M. A (2009) Pterostilbene (pter) for use in the prevention and/or treatment of skin diseases, damages or injuries. Green Molecular, WO 2011/051483 Al.

Fagerland, M.W. and Sandvik, L. (2009) 'Performance of five two-sample location tests for skewed distributions with unequal variances', *Contemporary Clinical Trials*, 30(5), pp. 490-496.

Fajuyigbe. D, Lwin. S, M., Diffey. B, L, Baker. R, Tobin. D.J, Sarkany. R, and Young. A,R (2018) 'Melanin distribution in human epidermis affords localized protection against DNA photodamage and concurs with skin cancer incidence difference in extreme phototypes' *The FASEB Journal* 32(7), pp. 3700-3706

Fang, E.F., Scheibye-Knudsen, M., Chua, K.F., Mattson, M.P., Croteau, D.L. & Bohr, V.A. 2016, 'Nuclear DNA damage signalling to mitochondria in ageing', *Nature Reviews Molecular Cell Biology*, 17(5), pp. 308–21

Forbat, E., Al-Niaimi, F. and Ali, F.R. (2017) 'Use of nicotinamide in dermatology', *Clinical and Experimental Dermatology*, 42(2), pp. 137-144.

Forrester, A.R., Elias, M.S., Woodward, E.L., Graham, M., Williams, F.M. and Reynolds, N.J. (2014) 'Induction of a chloracne phenotype in an epidermal equivalent model by 2,3,7,8-tetrachlorodibenzo-p-dioxin (TCDD) is dependent on aryl hydrocarbon receptor activation and is not reproduced by aryl hydrocarbon receptor knock down', *Journal of Dermatological Science*, 73(1), pp. 10-22.

Friedrich, R.B., Kann, B., Coradini, K., Offerhaus, H.L., Beck, R.C.R. and Windbergs, M. (2015) 'Skin penetration behavior of lipid-core nanocapsules for simultaneous delivery of resveratrol and curcumin', *European Journal of Pharmaceutical Sciences*, 78, pp. 204-213.

Gammage, P.A. and Frezza, C. (2019) 'Mitochondrial DNA: the overlooked oncogenome?', *BMC Biology*, 17(1), p. 53.

Ganesan, P. and Choi, D.K. (2016) 'Current application of phytocompound-based nanocosmeceuticals for beauty and skin therapy', *International journal of nanomedicine*, 11, pp. 1987-2007.

Giampazolias, E. and Tait, S.W.G. (2016) 'Mitochondria and the hallmarks of cancer', *The FEBS Journal*, 283(5), pp. 803-814.

Godic, A., Poljšak, B., Adamic, M. and Dahmane, R. (2014) 'The role of antioxidants in skin cancer prevention and treatment', *Oxidative medicine and cellular longevity*, 2014, pp. 860479-860479.

Groeber, F., Holeiter, M., Hampel, M., Hinderer, S. and Schenke-Layland, K. (2011) 'Skin tissue engineering — In vivo and in vitro applications', *Advanced Drug Delivery Reviews*, 63(4), pp. 352-366.

Halliwell, B., Clement, M.V. and Long, L.H. (2000) 'Hydrogen peroxide in the human body', *FEBS Letters*, 486(1), pp. 10-13.

Handique, J.G. and Baruah, J.B. (2002) 'Polyphenolic compounds: an overview', *Reactive and Functional Polymers*, 52(3), pp. 163-188.

Hanna, R., Crowther, J.M., Bulsara, P.A., Wang, X., Moore, D.J. and Birch-Machin, M.A. (2019) 'Optimised detection of mitochondrial DNA strand breaks', *Mitochondrion*, 46, pp. 172-178.

Harvey, A., Cole, L.M., Day, R., Bartlett, M., Warwick, J., Bojar, R., Smith, D., Cross, N. and Clench, M.R. (2016) 'MALDI-MSI for the analysis of a 3D tissue-engineered psoriatic skin model', *PROTEOMICS*, 16(11-12), pp. 1718-1725.

Hochart, G., Bonnel, D., Stauber, J. and Stamatas, G.N. (2019) 'Biomarker Mapping on Skin Tape Strips Using MALDI Mass Spectrometry Imaging', *Journal of The American Society for Mass Spectrometry*.

Holder, D.J., & Marino, M.J. (2017) 'Logical experimental design and execution in the biomedical sciences.' *Current Protocols in Pharmacology*, 76, A.3G.1– A.3G.26

Hosseini, M., Kasraian, Z. and Rezvani, H.R. (2017) 'Energy metabolism in skin cancers: A therapeutic perspective', *Biochimica et Biophysica Acta (BBA) - Bioenergetics*, 1858(8), pp. 712-722.

Hudson, L., Bowman, A., Rashdan, E. and Birch-Machin, M.A. (2016) 'Mitochondrial damage and ageing using skin as a model organ', *Maturitas*, 93, pp. 34-40.

Janson, D., Rietveld, M., Willemze, R. and El Ghalbzouri, A. (2013) 'Effects of serially passaged fibroblasts on dermal and epidermal morphogenesis in human skin equivalents', *Biogerontology*, 14(2), pp. 131-140.

Kakkar, V., Kaur, I.P., Kaur, A.P., Saini, K. and Singh, K.K. (2018) 'Topical delivery of tetrahydrocurcumin lipid nanoparticles effectively inhibits skin inflammation: in vitro and in vivo study', *Drug Development and Industrial Pharmacy*, 44(10), pp. 1701-1712.

Kandola, K., Bowman, A. and Birch-Machin, M.A. (2015) 'Oxidative stress – a key emerging impact factor in health, ageing, lifestyle and aesthetics', *International Journal of Cosmetic Science*, 37, pp. 1-8.

Kaul, S., Gulati, N., Verma, D., Mukherjee, S. and Nagaich, U. (2018) 'Role of Nanotechnology in Cosmeceuticals: A Review of Recent Advances', *Journal of Pharmaceutics*, 2018, p. 19.

Kawagishi, H. and Finkel, T. (2014) 'Unraveling the Truth About Antioxidants: ROS and disease: finding the right balance', *Nature Medicine*, 20, p. 711.

Kazak, L., Reyes, A. and Holt, I.J. (2012) 'Minimizing the damage: repair pathways keep mitochondrial DNA intact', *Nature Reviews Molecular Cell Biology*, 13, p. 659.

Kimlin, M.G. and Guo, Y. (2012) 'Assessing the impacts of lifetime sun exposure on skin damage and skin aging using a non-invasive method', *Science of The Total Environment*, 425, pp. 35-41.

Klicks, J., von Molitor, E., Ertongur-Fauth, T., Rudolf, R. & Hafner, M. (2017), 'In vitro skin three-dimensional models and their applications', *Journal of Cellular Biotechnology*, 3(1), pp. 21–39.

Konstantinova, N.V., Lemak, N.A., Duong, D.-M.T., Chuang, A.Z., Urso, R. and Duvic, M. (1998) 'Artificial Skin Equivalent Differentiation Depends on Fibroblast Donor Site: Use of Eyelid Fibroblasts', *Plastic and Reconstructive Surgery*, 101(2), pp. 385-391.

Kosuru, R., Rai, U., Prakash, S., Singh, A. and Singh, S. (2016) 'Promising therapeutic potential of pterostilbene and its mechanistic insight based on preclinical evidence', *European Journal of Pharmacology*, 789, pp. 229-243.

Kuang, R., Wang, Z., Xu, Q., Liu, S. and Zhang, W. (2015) 'Influence of mechanical stimulation on human dermal fibroblasts derived from different body sites', *International journal of clinical and experimental medicine*, 8(5), pp. 7641-7647.

Laurent, M. (2018) 'Pollution and Sun Exposure: A Deleterious Synergy. Mechanisms and Opportunities for Skin Protection', *Current Medicinal Chemistry*, 25(40), pp. 5469-5486.

Lewis, E.E.L., Barrett, M.R.T., Freeman-Parry, L., Bojar, R.A. and Clench, M.R. (2018) 'Examination of the skin barrier repair/wound healing process using a living skin equivalent model and matrix-assisted laser desorption-ionization-mass spectrometry imaging', *International Journal of Cosmetic Science*, 40(2), pp. 148-156.

Li, H., Jiang, N., Liang, B., Liu, Q., Zhang, E., Peng, L., Deng, H., Li, R., Li, Z. and Zhu, H. (2017) 'Pterostilbene protects against UVB-induced photo-damage through a phosphatidylinositol-3-kinase-dependent Nrf2/ARE pathway in human keratinocytes', *Redox Report*, 22(6), pp. 501-507.

Li, H., Liu, D., Lu, J. and Bai, Y. (2012) 'Physiology and pathophysiology of mitochondrial DNA', *Advances in experimental medicine and biology*, 942, pp. 39-51.

Lionetti, N. and Rigano, L. (2017) 'The New Sunscreens among Formulation Strategy, Stability Issues, Changing Norms, Safety and Efficacy Evaluations', *Cosmetics*, 4(2), p. 15.

Lu, Z., Hasse, S., Bodo, E., Rose, C., Funk, W. and Paus, R. (2007) 'Towards the development of a simplified long-term organ culture method for human scalp skin and its appendages under serum-free conditions', *Experimental Dermatology*, 16(1), pp. 37-44.

MacNeil, S. (2007) 'Progress and opportunities for tissue-engineered skin', *Nature*, 445(7130), pp. 874-880.

Mailloux, R.J. and Harper, M.-E. (2012) 'Mitochondrial proticity and ROS signaling: lessons from the uncoupling proteins', *Trends in Endocrinology & Metabolism*, 23(9), pp. 451-458.

Malik, A.N., Shahni, R., Rodriguez-de-Ledesma, A., Laftah, A. and Cunningham, P. (2011) 'Mitochondrial DNA as a non-invasive biomarker: Accurate quantification using real time quantitative PCR without co-amplification of pseudogenes and dilution bias', *Biochemical and Biophysical Research Communications*, 412(1), pp. 1-7.

Manevski, N., Swart, P., Balavenkatraman, K.K., Bertschi, B., Camenisch, G., Kretz, O., Schiller, H., Walles, M., Ling, B., Wettstein, R., Schaefer, D.J., Itin, P., Ashton-Chess, J., Pognan, F., Wolf, A. and Litherland, K. (2015) 'Phase II Metabolism in Human Skin: Skin Explants Show Full Coverage for Glucuronidation, Sulfation, N-Acetylation, Catechol Methylation, and Glutathione Conjugation', *Drug Metabolism and Disposition*, 43(1), pp. 126-139.

Mathes, S.H., Ruffner, H. and Graf-Hausner, U. (2014) 'The use of skin models in drug development', *Advanced Drug Delivery Reviews*, 69-70, pp. 81-102.

McBride, H.M., Neuspiel, M. and Wasiak, S. (2006) 'Mitochondria: More Than Just a Powerhouse', *Current Biology*, 16(14), pp. R551-R560.

Mehta, S.K. and Gowder, S.J.T. (2015) 'Members of Antioxidant Machinery and Their Functions', in *Basic Principles and Clinical Significance of Oxidative Stress*.

Meloni, M., Farina, A. and de Servi, B. (2010) 'Molecular modifications of dermal and epidermal biomarkers following UVA exposures on reconstructed full-thickness human skin', *Photochemical & Photobiological Sciences*, 9(4), pp. 439-447.

Metodiewa, D., Jaiswal, A.K., Cenas, N., Dickancaité, E. and Segura-Aguilar, J. (1999) 'Quercetin may act as a cytotoxic prooxidant after its metabolic activation to semiquinone and quinoidal product', *Free Radical Biology and Medicine*, 26(1), pp. 107-116.

Mi, J., Feng, Y., Wen, J., Su, Y., Xu L., Zu T., Liu C., Fisher, D.E., and Wu, X. (2019) 'A ROCK inhibitor promotes keratinocyte survival and paracrine secretion, enhancing establishment of primary human melanocytes and melanocyte–keratinocyte co-cultures.' *Pigment Cell and Melanoma Research*, 33(1), pp. 16-29

Mignon, C., Uzunbajakava, N.E., Castellano-Pellicena, I., Botchkareva, N.V. and Tobin, D.J. (2018) 'Differential response of human dermal fibroblast subpopulations to visible and near-infrared light: Potential of photobiomodulation for addressing cutaneous conditions', *Lasers in Surgery and Medicine*, 50(8), pp. 859-882.

Mikesh, L.M., Aramadhaka, L.R., Moskaluk, C., Zigrino, P., Mauch, C. and Fox, J.W. (2013) 'Proteomic anatomy of human skin', *Journal of Proteomics*, 84, pp. 190-200.

Mitchell, C.A., Donaldson, M., Francese, S. and Clench, M.R. (2016) 'MALDI MSI analysis of lipid changes in living skin equivalents in response to emollient creams containing palmitoylethanolamide', *Methods*, 104, pp. 93-100.

Muresan, X.M., Narzt, M.-S., Woodby, B., Ferrara, F., Gruber, F. and Valacchi, G. (2019) 'Involvement of cutaneous SR-B1 in skin lipid homeostasis', *Archives of Biochemistry and Biophysics*, 666, pp. 1-7.

Murray, J.E, Barrett, S.T, Brock, R.L, and Rick A. Bevins, R.A. (2017) 'Caring about Power Analyses.' *ACS Chemical Neuroscience*, 8 (11), pp. 2352-2354

Naidoo, K., Hanna, R. and Birch-Machin, M.A. (2018) 'What is the role of mitochondrial dysfunction in skin photoaging?', *Experimental Dermatology*, 27(2), pp. 124-128.

Nanda, D. (2019) ' Human keratinocyte stem cells: From cell biology to cell therapy', *Journal of Dermatological Science*, 96(2), pp. 66-72

Nisbet, S., Targett, D., Rawlings, A.V., Qian, K., Wang, X., Lin, C.B., Thompson, M.A., Bulsara, P.A. and Moore, D.J. (2019) 'Clinical and in vitro evaluation of new anti-redness cosmetic products in subjects with winter xerosis and sensitive skin', *International Journal of Cosmetic Science*, 0(ja).

Okada, K., Wangpoengtrakul, C., Tanaka, T., Toyokuni, S., Uchida, K. and Osawa, T. (2001) 'Curcumin and Especially Tetrahydrocurcumin Ameliorate Oxidative Stress-Induced Renal Injury in Mice', *The Journal of Nutrition*, 131(8), pp. 2090-2095.

Oyewole, A.O. and Birch-Machin, M.A. (2015) 'Mitochondria-targeted antioxidants', *The FASEB Journal*, 29(12), pp. 4766-4771.

Oyewole, A.O., Wilmot, M., Fowler, M. and Birch-Machin, M.A. (2014) 'Comparing the effects of mitochondrial targeted and localized antioxidants with cellular antioxidants in human skin cells exposed to UVA and hydrogen peroxide', *The FASEB Journal*, 28(1), pp. 485-494.

Panich, U., Sittithumcharee, G., Rathviboon, N. and Jirawatnotai, S. (2016) 'Ultraviolet Radiation-Induced Skin Aging: The Role of DNA Damage and Oxidative Stress in Epidermal Stem Cell Damage Mediated Skin Aging', *Stem cells international*, 2016, pp. 7370642-7370642.

Passos, J.F., Saretzki, G., Ahmed, S., Nelson, G., Richter, T., Peters, H., Wappler, I., Birket, M.J., Harold, G., Schaeuble, K., Birch-Machin, M.A., Kirkwood, T.B.L. and von Zglinicki, T.

(2007) 'Mitochondrial Dysfunction Accounts for the Stochastic Heterogeneity in Telomere-Dependent Senescence', *PLOS Biology*, 5(5), p. e110.

Penta, J.S., Johnson, F.M., Wachsman, J.T. and Copeland, W.C. (2001) 'Mitochondrial DNA in human malignancy', *Mutation Research/Reviews in Mutation Research*, 488(2), pp. 119-133.

Phillips, J., Moore-Medlin, T., Sonavane, K., Ekshyyan, O., McLarty, J. and Nathan, C.-A.O. (2013) 'Curcumin Inhibits UV Radiation–Induced Skin Cancer in SKH-1 Mice', *Otolaryngology–Head and Neck Surgery*, 148(5), pp. 797-803.

Poljšak, B. and Fink, R. (2014) 'The protective role of antioxidants in the defence against ROS/RNS-mediated environmental pollution', *Oxidative medicine and cellular longevity*, 2014, pp. 671539-671539.

Prasad, S., Tyagi, A.K. and Aggarwal, B.B. (2014) 'Recent developments in delivery, bioavailability, absorption and metabolism of curcumin: the golden pigment from golden spice', *Cancer research and treatment : official journal of Korean Cancer Association*, 46(1), pp. 2-18.

Pratt, H., Hassanin, K., Troughton, L.D., Czanner, G., Zheng, Y., McCormick, A.G. and Hamill, K.J. (2017) 'UV imaging reveals facial areas that are prone to skin cancer are disproportionately missed during sunscreen application', *PLOS ONE*, 12(10), p. e0185297.

Rahal, A., Kumar, A., Singh, V., Yadav, B., Tiwari, R., Chakraborty, S. and Dhama, K. (2014) 'Oxidative stress, prooxidants, and antioxidants: the interplay', *BioMed research international*, 2014, pp. 761264-761264.

Ray, A.J., Turner, R., Nikaido, O., Rees, J.L. and Birch-Machin, M.A. (2000) 'The Spectrum of Mitochondrial DNA Deletions is a Ubiquitous Marker of Ultraviolet Radiation Exposure in Human Skin', *Journal of Investigative Dermatology*, 115(4), pp. 674-679.

Rojo de la Vega, M., Krajisnik, A., Zhang, D.D. and Wondrak, G.T. (2017) 'Targeting NRF2 for Improved Skin Barrier Function and Photoprotection: Focus on the Achiote-Derived Apocarotenoid Bixin', *Nutrients*, 9(12), p. 1371.

Salehi, B., Mishra, A.P., Nigam, M., Sener, B., Kilic, M., Sharifi-Rad, M., Fokou, P.V.T., Martins, N. and Sharifi-Rad, J. (2018) 'Resveratrol: A Double-Edged Sword in Health Benefits', *Biomedicines*, 6(3), p. 91.

Santos-Caetano, J.P, Gfeller, C.F., Mahalingam, H., Cargill, M., Thomson, M., Moore, D., Vila, R. and Doi, R. (2019) 'Cosmetic benefits of a novel biomimetic lamellar formulation containing niacinamide in healthy females with oily, blemish-prone skin in a randomised proof-of-concept study', *International Journal of Cosmetic Science*, 42(1), pp. 29-35.

Santos-Caetano, J.P., Vila, R., Gfeller, C.F., Cargill, M. and Mahalingam, H. (2020) 'Cosmetic use of three topical moisturizers following glycolic acid facial peels', *Journal of Cosmetic Dermatology*, 19(1), pp. 660-670.

Santos, J.H., Meyer, J.N., Mandavilli, B.S. and Van Houten, B. (2006) 'Quantitative PCR-Based Measurement of Nuclear and Mitochondrial DNA Damage and Repair in Mammalian Cells', in Henderson, D.S. (ed.) *DNA Repair Protocols: Mammalian Systems*. Totowa, NJ: Humana Press, pp. 183-199.

Schallreuter K, U, Tobin D, J, Panske A, (2002) 'Decreased Photodamage and Low Incidence of Non-Melanoma Skin Cancer in 136 Sun-Exposed Caucasian Patients with Vitiligo.' *Dermatology* 204, pp. 194-201

Schon, E.A., DiMauro, S. and Hirano, M. (2012) 'Human mitochondrial DNA: roles of inherited and somatic mutations', *Nature Reviews Genetics*, 13, p. 878.

Siebert, K.J. (2009) 'Chapter 2 Haze in Beverages', in *Advances in Food and Nutrition Research*. Academic Press, pp. 53-86.

Siebert, K.J., Troukhanova, N.V. and Lynn, P.Y. (1996) 'Nature of Polyphenol−Protein Interactions', *Journal of Agricultural and Food Chemistry*, 44(1), pp. 80-85.

Silva, C.G., Monteiro, J., Marques, R.R.N., Silva, A.M.T., Martínez, C., Canle L, M. and Faria, J.L. (2013) 'Photochemical and photocatalytic degradation of trans-resveratrol', *Photochemical & Photobiological Sciences*, 12(4), pp. 638-644.

Sirenko, O., Mitlo, T., Hesley, J., Luke, S., Owens, W. and Cromwell, E.F. (2015) 'High-content assays for characterizing the viability and morphology of 3D cancer spheroid cultures', *Assay and drug development technologies*, 13(7), pp. 402-414.

Sirerol, J.A., Feddi, F., Mena, S., Rodriguez, M.L., Sirera, P., Aupí, M., Pérez, S., Asensi, M., Ortega, A. and Estrela, J.M. (2015) 'Topical treatment with pterostilbene, a natural phytoalexin, effectively protects hairless mice against UVB radiation-induced skin damage and carcinogenesis', *Free Radical Biology and Medicine*, 85, pp. 1-11.

Tan, D.-X., Manchester, L.C., Esteban-Zubero, E., Zhou, Z. and Reiter, R.J. (2015) 'Melatonin as a Potent and Inducible Endogenous Antioxidant: Synthesis and Metabolism', *Molecules*, 20(10), pp. 18886-18906.

Taylor, S., Wakem, M., Dijkman, G., Alsarraj, M. and Nguyen, M. (2010) 'A practical approach to RT-qPCR—Publishing data that conform to the MIQE guidelines', *Methods*, 50(4), pp. S1-S5.

Tobin, D.J. (2006) 'Biochemistry of human skin—our brain on the outside', *Chemical Society Reviews*, 35(1), pp. 52-67.

Tracy, L.E., Minasian, R.A. and Caterson, E.J. (2016) 'Extracellular Matrix and Dermal Fibroblast Function in the Healing Wound', *Advances in wound care*, 5(3), pp. 119-136.

Trivedi, M.K., Gangwar, M., Mondal, S.C. and Jana, S. (2017) 'Protective effects of tetrahydrocurcumin (THC) on fibroblast and melanoma cell lines in vitro: it's implication for wound healing', *Journal of food science and technology*, 54(5), pp. 1137-1145.

Tückmantel, W., Kozikowski, A.P. and Romanczyk, L.J. (1999) 'Studies in Polyphenol Chemistry and Bioactivity. 1. Preparation of Building Blocks from (+)-Catechin. Procyanidin Formation. Synthesis of the Cancer Cell Growth Inhibitor, 3-O-Galloyl-(2R,3R)-epicatechin-4β,8-[3-O-galloyl-(2R,3R)-epicatechin]', *Journal of the American Chemical Society*, 121(51), pp. 12073-12081.

Tulah, A.S. and Birch-Machin, M.A. (2013) 'Stressed out mitochondria: The role of mitochondria in ageing and cancer focussing on strategies and opportunities in human skin', *Mitochondrion*, 13(5), pp. 444-453.

Vanickova, L., Guran, R., Kollár, S., Emri, G., Krizkova, S., Do, T., Heger, Z., Zitka, O. and Adam, V. (2019) 'Mass spectrometric imaging of cysteine rich proteins in human skin', *International Journal of Biological Macromolecules*, 125, pp. 270-277.

Wallace, D.C. (2010) 'Mitochondrial DNA mutations in disease and aging', *Environmental and Molecular Mutagenesis*, 51(5), pp. 440-450.

Wisnovsky, S., Jean, S.R., Liyanage, S., Schimmer, A. and Kelley, S.O. (2016) 'Mitochondrial DNA repair and replication proteins revealed by targeted chemical probes', *Nature Chemical Biology*, 12, p. 567.

Wong, R., Geyer, S., Weninger, W., Guimberteau, J.-C. and Wong, J.K. (2016) 'The dynamic anatomy and patterning of skin', *Experimental Dermatology*, 25(2), pp. 92-98.

Xu, Q.-c., Kuang, R.-x., Wei, S.-q., Kang, Q., Wang, J.-j. and Wang, Z.-g. (2017) 'Analysis of Mechanical Behavior of Dermal Fibroblasts Obtained From Various Anatomical Sites in Humans', *Annals of Plastic Surgery*, 79(5), pp. 438-443.

Yang, S.-C., Tseng, C.-H., Wang, P.-W., Lu, P.-L., Weng, Y.-H., Yen, F.-L. and Fang, J.-Y. (2017) 'Pterostilbene, a Methoxylated Resveratrol Derivative, Efficiently Eradicates Planktonic, Biofilm, and Intracellular MRSA by Topical Application', *Frontiers in Microbiology*, 8(1103).

Yong, F., Xiao-Hui, H., Zhi-Gang, J., Mang-Hua, X., Zhu-Ying, G. and Feng-Hou, G. (2012) 'Tiron protects against UVB-induced senescence-like characteristics in human dermal fibroblasts by the inhibition of superoxide anion production and glutathione depletion', *Australasian Journal of Dermatology*, 53(3), pp. 172-180.

Yuan, J.S., Reed, A., Chen, F. and Stewart, C.N., Jr. (2006) 'Statistical analysis of real-time PCR data', *BMC bioinformatics*, 7, pp. 85-85.

Zhang, Z. and Michniak-Kohn, B.B. (2012) 'Tissue engineered human skin equivalents', *Pharmaceutics*, 4(1), pp. 26-41.

Zhou, J., Ci, X., Ma, X., Yu, Q., Cui, Y., Zhen, Y. and Li, S. (2019) 'Pterostilbene Activates the Nrf2-Dependent Antioxidant Response to Ameliorate Arsenic-Induced Intracellular Damage and Apoptosis in Human Keratinocytes', *Frontiers in pharmacology*, 10, pp. 497-497.

Zhou, L., Zhang, X., Paus, R. and Lu, Z. (2018) 'The renaissance of human skin organ culture: A critical reappraisal', *Differentiation*, 104, pp. 22-35.

Zong, W.-X., Rabinowitz, J.D. and White, E. (2016) 'Mitochondria and Cancer', *Molecular Cell*, 61(5), pp. 667-676.

Zou, Y. and Maibach, H.I. (2018) 'Dermal–epidermal separation methods: research implications', *Archives of Dermatological Research*, 310(1), pp. 1-9.